Mechanisms of Continental Lithosphere Thinning and Rifted Margin Formation

UNIVERSITY OF LIVERPOOL

Thesis submitted in accordance with the requirements of the University of Liverpool for the degree of Doctor in Philosophy

by Roseanna Fletcher

June 2009

Abstract

Mechanisms of Continental Lithosphere Thinning and Rifted Margin Formation

Roseanna Fletcher

This thesis investigates the mechanisms by which the continental lithosphere is thinned prior to continental rupture and the onset of seafloor spreading. Whilst the formation of many intracontinental rift basins can be explained by the model of depth-uniform pure-shear lithosphere thinning, many rifted continental margins and propagating rift tips exhibit depth-dependent stretching. The timing and mode of deformation which is responsible for depth-dependent stretching is not well understood. The Faroe-Shetland basin (FSB), on the NE Atlantic margin, is shown to have experienced depth-dependent lithosphere thinning in the Late Palaeocene. The FSB is often considered to be a Mesozoic rift basin formed by pure-shear lithosphere stretching and thinning. However, the magnitude of post-Palaeocene water-loaded tectonic subsidence in the basin, determined by flexural backstripping using palaeo-bathymetric constraints, suggest that a rift event with a stretching factor of more than 3 occurred in the Palaeocene, yet only minor Palaeocene or post-Paleocene upper crustal extension is observed (with stretching factors of less than 1.1). At Late Palaeocene times the FSB lay at the tip of the incipient North Atlantic, although continental breakup occurred to the north and west of the basin, at the Faroes and Møre margins. Late Palaeocene continental thinning in the FSB demonstrates that depth-dependent continental thinning is a syn-breakup process and suggests that continental lithospheric thinning can occur along multiple offset axes prior to breakup, leaving a 'failed breakup basin' once seafloor spreading begins. Pure-shear and thermal buoyancy-driven upwelling-divergent flow (UDF) models have been examined to investigate the effect of these modes of continental lithosphere thinning on subsidence, heatflow, finite strain and the production of melt during rifted margin formation. The UDF model predicts depth-dependent lithosphere thinning, unlike the pure-shear model. Often, where observations, such as of melt volumes, at rifted margins are different to those predicted by the pure-shear model of continental breakup, temperature or composition anomalies are invoked to explain the apparent discrepancy. The ratio of the axial upwelling velocity to the half-spreading velocity of the UDF model can be varied to give a range of rifted margin geometries with variable volcanic addition without requiring such anomalies. Low-velocity-ratio UDF models predict that wide zones of lower continental crust and continental mantle are exhumed prior to the onset of melting during continental breakup, as observed at non-volcanic margins. High-velocity-ratio UDF models predict that melting begins soon after deformation begins and that thick volcanic addition may be present close to the continental margin, as observed at volcanic margins. Pure-shear and UDF modes of deformation most likely both contribute to continental lithosphere thinning, with the importance of each mechanism varying with depth and time. Finally, dynamic modelling demonstrates that lateral viscosity contrasts associated with inherited water-content heterogeneities may allow induction of small-scale convection in the continental lithosphere. This small-scale convection preferentially thins the lithospheric mantle with respect to the upper crust prior to continental lithospheric rupture.

Acknowledgements

Firstly I would like to thank Nick Kusznir for his excellent supervision over the last four years. His enthusiasm, intelligence and advice have inspired me and it has been a pleasure to work with him.

Support from a NERC CASE studentship is gratefully acknowledged, and I also owe thanks to Alan Roberts from Badleys Geoscience and the representatives from iSIMM and MM2 partners(Amerada Hess, Anadarko, BG, BP, ConocoPhillips, ENI UK, Petrobras, Schlumberger Cambridge Research, StatoilHydro, Shell, TOTAL, WesternGeco, and NERC and the DTI), for financial support as well as their interest in my work. The sharing of knowledge, questions, challenges and ideas which arose from partner meetings have significantly improved this work. Particular thanks to the Faroes team at Statoil in London for making me welcome to their offices to work on the dataset for the Faroes-Shetland basin, for their interest in my ideas and for allowing some of their data to be reproduced in this thesis.

I also thank Marc Parmentier and Greg Hirth for inviting me to Brown University to work with and adapt their numerical model. I learned a lot from both of them and thoroughly enjoyed New England (cheers Jay). I also benefited considerably from numerous scientific discussions with many people at various conferences and bars. I would particularly like to remember Martin Casey, who always believed in my abilities and encouraged me to believe in myself.

Thank you to John Piper and Tony Watts for agreeing to read and examine this thesis.

To the Department of Earth and Ocean Sciences at Liverpool University - Thank you for making it a fantastic place to be. The people, particularly everyone on the fourth floor, have made the last four years fun and contributed to a very good working environment. Special mention to Vijay for being such a good mate that he even read most of this.

Thank you to my family - Mum, Tom, John, Nanny, Dad - for always supporting me in everything I do. I am also very grateful to many other good friends, especially my Liverpool girls Corallie, Rhiannon, Kerry, and Sarah.

And to Dave - Thanks for everything - You're amazing.

Contents

List of Figures

List of Tables

Chapter 1

Introduction and Aims

1.1 Introduction

Continental lithospheric extension and thinning results in the formation of rift basins and, in the case of lithospheric rupture, the formation of two rifted margins separated by an ocean basin. The aim of this thesis is to investigate the processes which occur during continental lithosphere thinning. What are the modes of deformation responsible for thinning? Are the processes and mechanisms responsible for intracontinental rift basin formation the same or different to those which occur during continental lithospheric rupture prior to the onset of seafloor spreading? This thesis addresses these questions using both observational and modelling approaches.

Many intracontinental rift basins have been successfully modelled using the pure-shear thinning model (McKenzie, 1978), which assumes that thinning of the lithosphere is uniform with depth, for example the Kenya Rift and the North Sea, (e.g. Steckler et al., 1988; Marsden et al., 1990; Kusznir et al., 1995). It is commonly assumed that continental lithospheric rupture and rifted margin formation also occur by depth-uniform thinning. However, recent discoveries indicate that at many rifted margins, the accommodation of extension is depth-dependent; the whole lithosphere has apparently been thinned much more than the upper crust (e.g. Royden and Keen, 1980; Driscoll and Karner, 1998; Davis and Kusznir, 2004). In addition, observations of wide zones of

exhumed continental mantle at some rifted margins (Boillot et al., 1987, 1989; Pickup et al., 1996; Dean et al., 2000) cannot easily be explained by the depth-uniform pure-shear model of continental thinning, suggesting that there may be other modes of extension which are active during continental breakup. Furthermore, rifted continental margins exhibit large variations in magmatic activity: at 'non-volcanic' margins, mantle exhumation has occurred with minor or no volcanism, whilst voluminous intrusive and extrusive volcanism may accompany breakup at 'volcanic' margins (e.g. White and McKenzie, 1989; Eldholm and Grue, 1994). The cause of the variability in the volume of volcanic material produced during continental breakup is debated: intrinsic variables such as mantle temperature anomalies can explain apparently anomalous volcanism if the pure-shear model is invoked (e.g. White and McKenzie, 1989; Bown and White, 1995; Minshull et al., 2001; Reston and Morgan, 2004). However, other authors question the applicability of the pure-shear model to rifted margin formation, and invoke, for example 'active' upwelling, to explain voluminous volcanism at some margins (e.g. Mutter, 1985; van Wijk et al., 2001; Korenaga et al., 2002). Additionally, the mechanism by which the change in the mode of extension from pure-shear continental extension to seafloor spreading is accommodated is not well understood. A more detailed review of models of continental lithospheric thinning and observations at rift basins and rifted margins is given in Chapter 2.

In this thesis the Tertiary evolution of the Faroe-Shetland basin (FSB) on the NE Atlantic margin is investigated. At Late Paleocene times the basin lay at the propagating tip of the incipient North Atlantic; but continental lithospheric rupture and the onset of seafloor spreading occurred to the west and north of the Faroe-Shetland basin, at the Faroes and Møre margins. Analysis of the distribution of extension in the FSB provides information about the mode of thinning which is active during this poorly-understood phase of continental lithosphere thinning, between intracontinental rifting and continental breakup.

I also investigate the implications of various modes of extension on the subsidence, heatflow and melt production history of continental rift basins and rifted continental

margins. In particular I investigate the effects of upwelling-divergent flow (UDF) within the continental lithosphere and asthenosphere - a process similar to that which occurs at mid-ocean ridges - during continental lithospheric thinning prior to breakup.
This thesis aims to investigate the processes and modes of deformation which occur during continental lithosphere thinning by addressing the following questions:

1. Does depth-dependent lithosphere stretching only occur at rifted margins, or can it be observed in continental rift basins, prior to complete rupture of the continental lithosphere?

2. What are the implications of depth-dependent modes of lithosphere deformation on subsidence, heatflow and volcanic addition for rift basins and rifted margins?

3. What predictions of margin geometry, subsidence and volcanic addition do models of continental lithospheric thinning leading to basin and margin formation by upwelling-divergent flow make? How do these predictions compare with predictions made by the pure-shear model, and how well do these models explain observations at rift basins and margins?

4. What physical processes and driving forces may be responsible for depth-dependent modes of extension and thinning during continental lithosphere thinning?

This thesis has two parts: 1) Examining the depth-dependence of extension in the Faroe-Shetland basin and 2) Forward modelling continental lithosphere thinning leading to basin and margin formation.

1.2 The Tertiary development of the Faroe-Shetland basin

The development of the Faroe-Shetland basin (FSB) is investigated in Chapters 3-6 of this thesis. This basin is located to the north of the UK on the NE Atlantic rifted margin. The basin experienced significant stretching and thinning in the Mesozoic, and the Mesozoic section of the basin exhibits a faulted basin geometry typical of intracontinental rifts. However, during the early Tertiary the basin lay at the tip

of the incipient Atlantic Ocean, and anomalous subsidence in the FSB is apparently synchronous with continental breakup which occurred to the north and to the west of the basin, at the Faroes and Møre margins. The basin is a candidate for a 'failed breakup basin'; a continental rift basin which almost, but did not, rupture. Thus it records an important phase in the continental lithospheric thinning process between intracontinental rifting and continental breakup and the onset of seafloor spreading.
In Chapters 3 to 6 the following subsidiary questions are addressed:

1. What is the magnitude and timing of the lithospheric-scale thinning of the Faroe-Shetland basin. Specifically, how has extension and thinning in the FSB been accommodated, and what is the distribution of thinning with depth?

2. Is the deformation history of the FSB compatible with a pure-shear (or modified pure-shear) model of continental lithospheric extension?

3. What factors or processes may be responsible for the anomalous subsidence history of the FSB?

4. What are the implications of a depth-dependent lithosphere stretching model for the formation of the FSB? How does depth-dependent stretching affect the subsidence, heatflow and melt-history of the basin?

5. If depth-dependent stretching occurred in the FSB, what processes may be responsible for this?

1.3 Forward modelling continental lithosphere thinning.

Kinematic modelling

In Chapters 7 and 8, the theoretical implications of kinematic end-member modes of accommodating extension in the continental lithosphere are examined: pure-shear and upwelling-divergent flow. The pure-shear model assumes that extension in the continental lithosphere is distributed uniformly with depth. Upwelling-divergent flow (UDF) was suggested by Davis and Kusznir (2004) to explain depth-dependent stretching and

the exhumation of continental mantle at rifted margins, and a number of rifted margins have been successfully modelled using the UDF, or a combined UDF and pure-shear, model of continental breakup (Healy and Kusznir, 2007; Kusznir and Karner, 2007). Observations of the response of the continental lithosphere to extension, at present day and ancient rifts, can be qualitatively and quantitatively compared to predictions made by models. This can give insights into the mode of deformation which operates in the continental lithosphere during thinning and breakup. Observational constraints from the Iberian margin and Faroe-Shetland basin are used in Chapters 9 and 10 respectively to try to determine the mode of deformation responsible for their formation.
The following subsidiary questions are addressed using the kinematic models:

1. How do the margin geometry, finite deformation, subsidence and heatflow histories predicted by a UDF model of continental lithosphere thinning differ from those predicted by a pure-shear model? How can the models be tested?

2. How does the melt production predicted by a UDF model of continental lithosphere thinning differ from that predicted by a pure-shear model?

3. Can UDF during rifted margin formation explain apparently anomalous melt production during continental breakup? What other explanations are there? How can these explanations be tested?

Dynamic modelling

In Chapter 11 a dynamic model is employed to address some questions about the driving forces responsible for continental lithosphere thinning:

1. What are the driving forces which may induce depth-dependent stretching and thinning during lithosphere thinning?

2. What are the effects of melting and compositional (water-content) heterogeneities on continental lithospheric thinning processes?

Chapter 12 discusses the findings of the thesis in terms of the key questions posed in this chapter. The conclusions are outlined and further work is identified.

Chapter 2

Continental lithospheric extension - a review

2.1 Introduction

Continental extension, and continental breakup and seafloor spreading initiation are a fundamental part of the theory of Plate Tectonics. Continental extension may be limited to minor lithospheric thinning or may involve complete lithospheric rupture and the onset of seafloor spreading. In this thesis an intracontinental rift basin is considered to be a region in which extension has been accommodated, but rupture of the continental lithosphere has not occurred. Examples include the North Sea (e.g Klemperer, 1988) and the Basin and Range (e.g. Stewart, 1971). A rifted continental margin is the remnant of continental breakup where continental lithosphere is adjacent to oceanic lithosphere. Continental breakup results in two conjugate rifted margins separated by an ocean basin.

Many rift basins have been successfully modelled using the model of pure-shear extension, proposed by Artemjev and Artyushkov (1971), and quantitatively described by McKenzie (1978). Seafloor spreading is generally considered to occur by upwelling-divergent flow of the mantle beneath the mid-ocean ridge (e.g. Reid and Jackson, 1981; Spiegelman and McKenzie, 1987). However the mechanism by which continental

stretching evolves into seafloor spreading is not well understood.

This thesis focuses on two aspects of the continental lithospheric thinning process:

1. How thinning and extension of the continental lithosphere is accommodated during rift basin and rifted margin formation.

2. Partial melting and the production of volcanic addition during continental lithospheric thinning and the onset of seafloor spreading.

The lithospheric geometry, geological history and presence or absence of volcanic addition in rift basins and at rifted margins provide information which allow the mode of deformation of the continental lithosphere to be constrained. Propagating rift tips, where a mid-ocean ridge meets continental lithosphere, and failed breakup basins provide particularly relevant information about the processes which occur in the continental lithosphere after the onset of extension but prior to continental rupture. Failed breakup basins are rift basins which once lay at the propagating tip of incipient seafloor spreading, but where continental lithospheric rupture did not occur, and so these basins may represent fossil propagating rift tips.

Rift basin and rifted margins contain important mineral and energy resources. Many of the untapped oil and gas reserves are in the deepwater regions of rifted margins, which may contain thick piles of sediment. Academic and oil industry exploration data have greatly improved our knowledge of the anatomy of rift basins and rifted margins, and are driven by an increasing need to understand their development.

In this chapter various models which have been proposed to explain the processes by which continental extension occurs are presented. An overview of some general features of rift basins, propagating rift tips and and rifted margins is then given, and observations are discussed in relation to the various models. The driving forces and physics responsible for continental extension and breakup are then briefly reviewed.

2.2 Measuring thinning of the continental lithosphere

The geometry of rift basins and rifted margins refers to the spatial variability of the thickness of the crust and the lithosphere, which indicate how extension has been distributed in the continental lithosphere during thinning and stretching. Strain is measured in terms of a stretching factor, β, which is:

$$\beta = \frac{t_0}{t_c} \tag{2.1}$$

where t_0 refers to the initial thickness of a layer (e.g. the crust) and t_c the present thickness of that layer.

β can also be measured in terms of horizontal extension:

$$\beta = \frac{length\ of\ profile}{length\ of\ profile - extension} \tag{2.2}$$

It is also useful sometimes to consider the thinning factor:

$$\gamma = 1 - \frac{1}{\beta} \tag{2.3}$$

The value of γ ranges from 0 to 1, with a thinning factor of zero indicating no thinning or extension, and a thinning factor of one corresponding to infinite extension or complete thinning and rupture.

Extension and thinning in the continental lithosphere can be measured at three levels (Figure 2.1):

1. the upper crust
2. the whole crust
3. the whole lithosphere.

Extension in the upper crust occurs by brittle deformation, where horizontal offset is accommodated on discrete fault surfaces. Fault analysis can indicate both the timing and magnitude of upper crustal extension. Lower crustal extension is usually considered

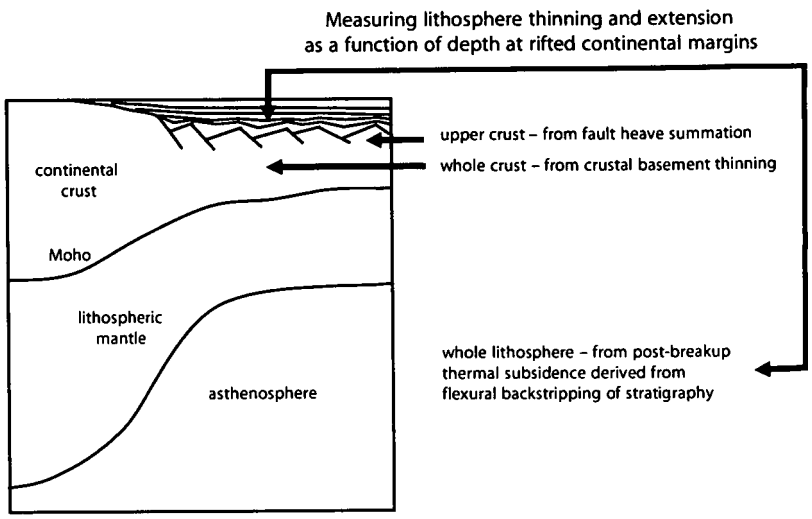

Figure 2.1: Measuring extension and thinning at continental rift basins and rifted margins, from Kusznir and Karner (2007).

to be accommodated by ductile deformation process. Thinning factors for the whole crust can be determined if the Moho depth is known; Moho depth can be determined using both seismic and gravity methods. Determining crustal thinning factors requires knowledge of the initial crustal thickness, which is usually inferred from adjacent unthinned regions. The timing and magnitude of lithospheric thinning can be determined by analysing subsidence histories derived from well-data. The subsidence history of a basin or margin can provide important information about the timing, magnitude and mechanism of continental thinning. However, subsidence and uplift may also occur as a result of processes not directly related to continental lithosphere thinning, for example, sea-level changes, dynamic topography associated with subduction zones and plume related uplift. Where possible the subsidence history of a basin or margin should be corrected to remove signals caused by these effects when investigating lithospheric thinning processes.

2.3 Melting during continental thinning

Melting and volcanism at the Earth's surface is caused by partial melting of upwelling material (e.g. Figure 2.2). The volume and composition of volcanism which occurs during continental thinning is dependent on the processes and conditions of lithospheric thinning. In this thesis volcanism in rift basins and at rifted margins is assumed to be mainly due to partial melting of mantle peridotite.

$$\textit{Upper mantle source reservoir (peridotite)} \longrightarrow \textit{Basalt} + \textit{Depleted mantle} \quad (2.4)$$

The melting properties of peridotite are well-understood from observations and geochemical measurements at mid-ocean ridges and ophiolites, from laboratory experiments and thermodynamic calculations. Published melt parameterisations (Klein and Langmuir, 1987; McKenzie and Bickle, 1988; Katz et al., 2003) are used in this thesis to calculate melt production during continental lithosphere thinning and rifted margin formation.

2.4 Kinematic models of continental lithospheric thinning

Various kinematic models of continental lithospheric stretching and thinning are described in this section and are illustrated in Figure 2.3. These kinematic models describe the mechanism by which continental lithosphere thinning may occur, and predict the resulting distribution of extension in rift basins and at rifted continental margins. Kinematic models define a set of relationships which describe how a system evolves, and are useful for understanding the response of a system to processes that are poorly constrained by geophysical or field data. Predictions made by kinematic models may be qualitatively and quantitatively compared to observations in order to assess whether a model is able to explain the formation of an individual basin or margin. Key parameters (for example extension rate) can be varied in order to quantitatively compare model predictions to observations on a case-specific basis, allowing the basin or margin history to be investigated or even inverted.

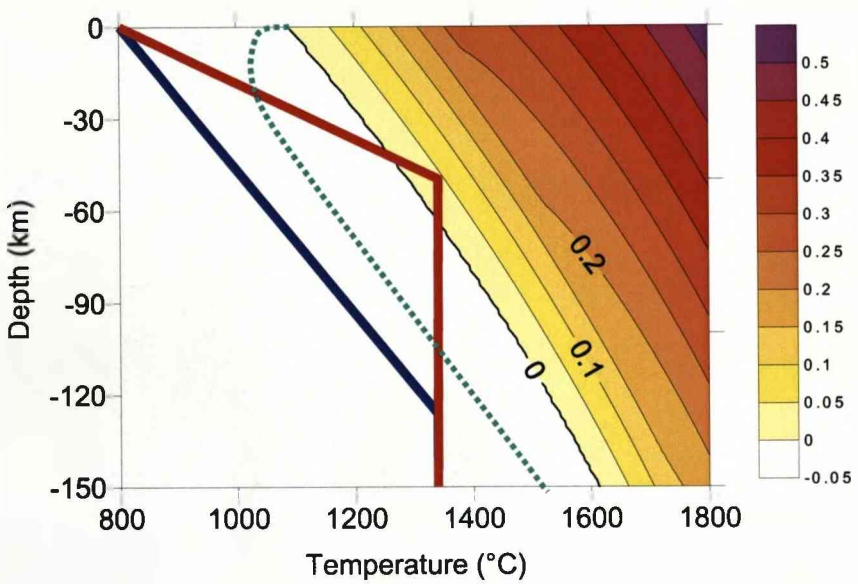

Figure 2.2: Melting of mantle peridotite. Black contours illustrate fraction of partial melt as a function of pressure and temperature for dry peridotite, calculated using parameterisation of Katz et al. (2003). Green line illustrates the approximate position of the solidus when the peridotite has a high water-content. The blue line represents a pre-rift continental geotherm where temperatures are below the solidus and no melting occurs. During continental thinning, temperatures in the lithosphere (e.g. the red line) may exceed the solidus and melting may begin.

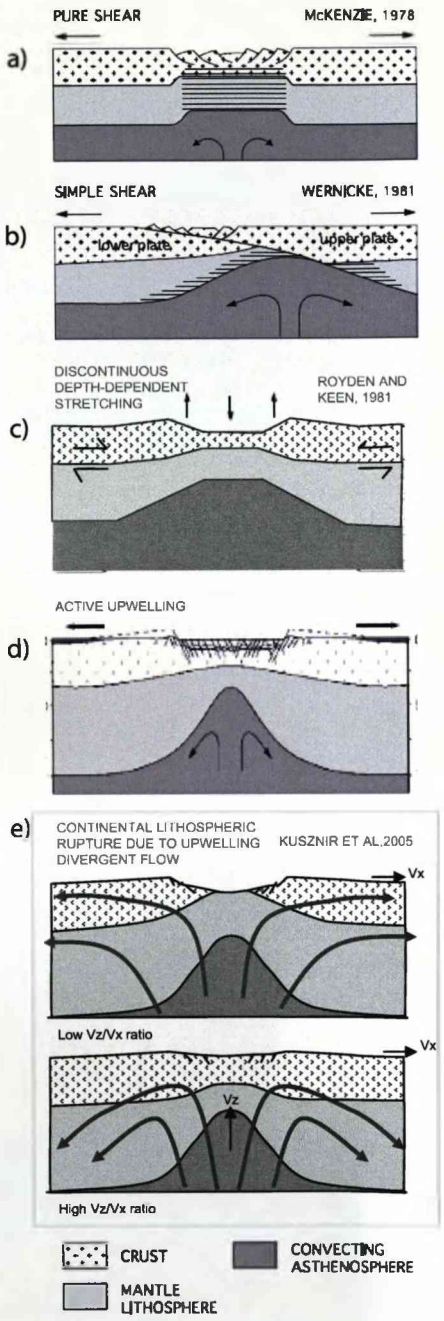

Figure 2.3: Conceptual diagram of various models of continental lithosphere thinning. (**a**) Pure-shear (McKenzie, 1978), (**b**) Simple-shear (Wernicke, 1985), (**c**) Discontinuous depth-dependent stretching (Royden and Keen, 1980), (**d**) Active upwelling (e.g. Mutter, 1985; Huismans et al., 2001a), (**e**) Upwelling-divergent flow (Davis and Kusznir, 2004; Kusznir et al., 2005; Kusznir and Karner, 2007). Figures (**a-d**) are modified from Ziegler and Cloetingh (2004).

Kinematic models do not explicitly offer insights into the driving mechanisms responsible for deformation of the continental lithosphere, but may offer insights into deformation modes which occur during continental lithosphere thinning, which then allow inferences about the driving forces to be made.

2.4.1 Pure-shear

The pure-shear model of continental extension and thinning (McKenzie, 1978, Figures 2.3a and 2.4) assumes that extension is uniform with depth. Instantaneous pure-shear extension of the lithosphere creates space into which asthenospheric material passively rises (Figure 2.4). The pure-shear model implicitly assumes that the lithosphere deforms as a continuum, although in the Earth the upper crust extends by brittle faulting, and this must be considered when comparing the predictions made by the model to observations. Relationships between extensional faulting, crustal thinning, heatflow and subsidence predicted by the pure-shear model can be derived analytically. The pure-shear model therefore has powerful predictive capabilities which can be used for calculating palaeoheatflow and palaeobathymetry information. The model has been developed to account for finite duration rifting (Jarvis and McKenzie, 1980), and it is simple to make corrections for regional effects such as uplift and subsequent subsidence caused by the transient presence of a mantle plume, or relative sea-level changes.

The cause of subsidence in rift basins and at rifted margins is illustrated in Figure 2.4, using the model of pure-shear thinning of McKenzie (1978). Lithospheric thinning has two isostatic effects: crustal thinning results in subsidence (Si_{ct}), and the thermal effects of thinning the whole lithosphere (and consequentially increasing the temperature gradient at the site of rifting) results in thermal uplift (Si_{th}). The net isostatic result of initial lithospheric thinning is referred to as initial subsidence (Si). After thinning, the lithosphere temperature perturbation associated with thinning conductively cools, and a second phase of slower (thermal) subsidence occurs. This is referred to as post-rift thermal subsidence (St).

The model of lithosphere thinning by pure-shear deformation (McKenzie, 1978) enables the magnitude of initial and thermal subsidence to be related to the magnitude of thinning (i.e. β) using simple mathematical formulae (detailed in Section 5.2). If continental thinning did not occur by pure-shear extensional deformation, then subsidence cannot necessarily be related to real stretching and thinning factors using the McKenzie (1978) formulae, although an apparent stretching factor can be a useful measure of the magnitude of thinning.

The volume and composition of melt predicted by the pure-shear model is dependent on the mantle potential temperature and the duration of thinning (McKenzie and Bickle, 1988; Bown and White, 1995). Comparisons of data to predictions made by the pure-shear model have been used to identify mantle thermal anomalies during continental breakup (e.g. White et al., 1992).

Although the pure-shear model and its derivatives have been successful in modelling many intracontinental rift basins (e.g. the Gulf of Suez (Steckler et al., 1988), the Kenya Rift and the North Sea, (Kusznir et al., 1995), the Jeanne d'Arc Basin (Kusznir et al., 1991)), a number of observations at rift basins and rifted margins are incompatible with the pure-shear model, which suggests that other lithosphere deformation processes play an important role during continental lithosphere thinning. In particular, observations of depth-dependent stretching are, by definition, contrary to the pure-shear model. In this section a number of alternative lithospheric-scale models of continental extension are briefly reviewed. It is useful to consider the predictions by each of the models in relation to the model of pure-shear, due to the latter's simplicity. The models described are not necessarily mutually exclusive to each other or to the pure-shear model, as more than one lithospheric-scale process may be occurring simultaneously, or become more or less important through time.

2.4.2 Simple-shear

Wernicke (1985) suggested that lithospheric extension may be accommodated by simple shear along low-angle lithosphere-scale detachments (see Figure 2.3b). Simple-shear

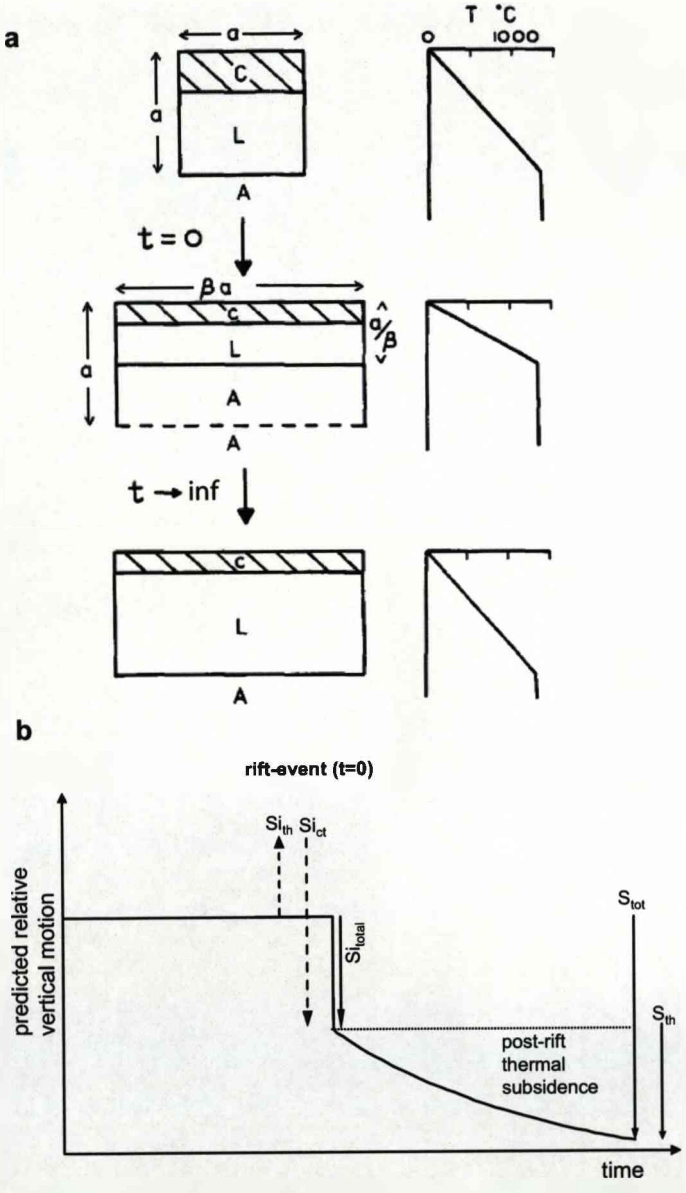

Figure 2.4: The depth-uniform stretching model, (after McKenzie, 1978), and schematic resulting subsidence history.

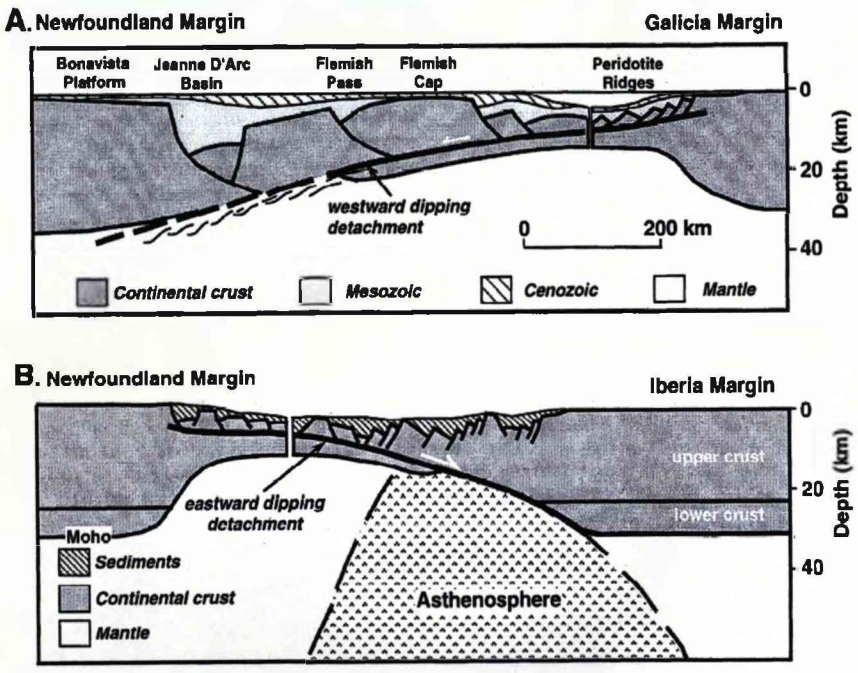

Figure 2.5: The upper plate paradox. Driscoll and Karner (1998) noted that pairs of conjugate margins had each been identified as the upper plate of a simple-shear conjugate margin pair. For the Newfoundland and Iberian-Galician margins, each showed a discrepancy between large regional subsidence (apparent stretching factors of 3.4 to 4.6) and much less upper crustal extension due to brittle deformation (apparent stretching factors of 1.6 to 1.9). From Driscoll and Karner (1998).

extension results in a lateral offset between the zone of thinnest crust and of maximum thermal uplift during the early stages of extension, and if breakup occurs, the model predicts that there will be one 'upper plate' and one 'lower plate' continental margin. The simple-shear model predicts less melting than the uniform extension model (Latin and White, 1990) for a given amount of extension. The asymmetric margins predicted by this model exhibit depth-dependent stretching, variations in syn- and post-rift subsidence relative to the pure-shear model and provide a simple mechanism for exhumation of lower crustal and lithospheric mantle rocks. However, Driscoll and Karner (1998) found that pairs of conjugate margins both appeared to be 'upper plate' margins (where lithosphere thinning exceeds upper crustal thinning), thus causing a fundamental reconstruction problem. They termed this discrepancy the 'upper plate paradox' (Figure 2.5).

2.4.3 Decoupled pure-shear

Royden and Keen (1980) observed that the apparent magnitude of mantle lithosphere thinning at the Labrador shelf was much greater than the magnitude of thinning of the crust. They proposed a simple 1–D model of depth-dependent stretching where the lithospheric mantle was stretched more than the crust (Figure 2.3). Although this model is able to explain observations and make valuable predictions about the implications of depth-dependent stretching, the model does not necessarily balance extension in 2–D. White and McKenzie (1988) suggested that this space problem could be resolved if extension was distributed over a wider zone in the upper crust than in the lower lithospheric layers, although this solution implies at least some decoupling between upper and lower lithospheric layers. A number of dynamic numerical models predict deformation by a process similar to decoupled pure-shear, where the distribution of extension varies in depth and with time (e.g. ter Voorde et al., 1998; Lavier and Manatschal, 2006; Huismans and Beaumont, 2008), depending on the initial rheological and temperature structure of the lithosphere.

2.4.4 Small-scale convection

Keen (1985) and Buck (1986) suggested that small-scale convection in the continental lithospheric mantle during extension and thinning may explain observations of depth-dependent stretching and rift flank uplift. Secondary convection may be a result of flow instability in the upper mantle and lower crust, induced by viscosity contrasts and thermal and melt buoyancy forces. Small-scale convection may occur in the lithospheric mantle whilst strain remains relatively distributed in the upper crust. This mode of deformation can explain depth-dependent stretching as the lithosphere and lower crust are preferentially removed from the basin axis and pushed outwards (Huismans et al., 2001a; Huismans and Beaumont, 2008). Dynamic models of continental extension have illustrated that small-scale convection may be an inherent part of the continental breakup processes, although this result is dependent on the initial conditions of the model. Secondary convection may also be able to explain voluminous pre- and syn-breakup magmatism without requiring that mantle temperature anomalies are present (Mutter, 1985; van Wijk et al., 2001; Korenaga et al., 2002), as small-scale convection results in an increased flux of material through the zone of melting. Additionally, small-scale convection is likely to be enhanced if a thermal anomaly is present in the mantle (Nielsen and Hopper, 2004). Small-scale convection has also been shown to preferentially remove the lithospheric mantle and lower crust even after surface extension has ceased, and may explain late-stage magmatism at some continental rift basins (Huismans et al., 2001b; Hernlund et al., 2008).

2.4.5 Upwelling-divergent flow

Davis and Kusznir (2004) suggest that upwelling divergent flow (UDF) may be used to describe the dominant process active during lithosphere thinning leading to continental breakup. The upwelling divergent flow field can be easily described analytically using the cornerflow solution of Batchelor (1967), maintains a balance of extensional strain, and is variable in its form. Upwelling divergent flow of the mantle occurs at

mid-ocean ridges, and the analytical UDF solution of Batchelor (1967) and its derivatives have previously been used to describe mid-ocean ridge processes (e.g. Reid and Jackson, 1981; Spiegelman and McKenzie, 1987; Braun et al., 2000); therefore the UDF model of continental lithospheric thinning evolves into a model of seafloor spreading. If upwelling-divergent flow is considered to occur only in the lower lithosphere then the flowfield resembles those predicted by dynamic models of small-scale convection.

Kusznir et al. (2005) showed the ability of the UDF model to explain depth-dependent stretching and the overall lithospheric-scale structure of volcanic and non-volcanic margins by varying the form of the upwelling diverging flowfield. The form of the UDF flowfield is defined by the ratio of the axial upwelling velocity V_z^0 to the half-spreading velocity V_x^0. Low flow ratios (V_z^0/V_x^0) result in a margin architecture which resembles a non-volcanic margin, whilst high velocity ratios imply that buoyant flow is important and results in margin geometry which resembles volcanic margins. Kusznir et al. (2005), Healy and Kusznir (2007) and Kusznir and Karner (2007) have successfully applied the model to a number of case-histories by matching observed bathymetry and gravity profiles to those predicted by the model.

In chapters 7 and 8 of this thesis I compare predictions of subsidence, heatflow, lithospheric geometry and melt production made by the upwelling-divergent flow model to those made by the pure-shear model.

2.5 Extension and rupture of the continental lithosphere

2.5.1 Rift basins

Rift basins are usually elongate tectonic depressions representing a region of continental extension and thinned crust (Olsen and Morgan, 1995). Regions of present day rifting are characterised by negative Bouguer gravity anomalies, high heat flow and variable amounts of volcanic activity, indicating that a thermal anomaly exists at depth (Allen and Allen, 2005). The duration of extension varies from a few to hundreds of Myr, and the width of rift zones varies from tens to hundreds of km. The age of dip-slip and

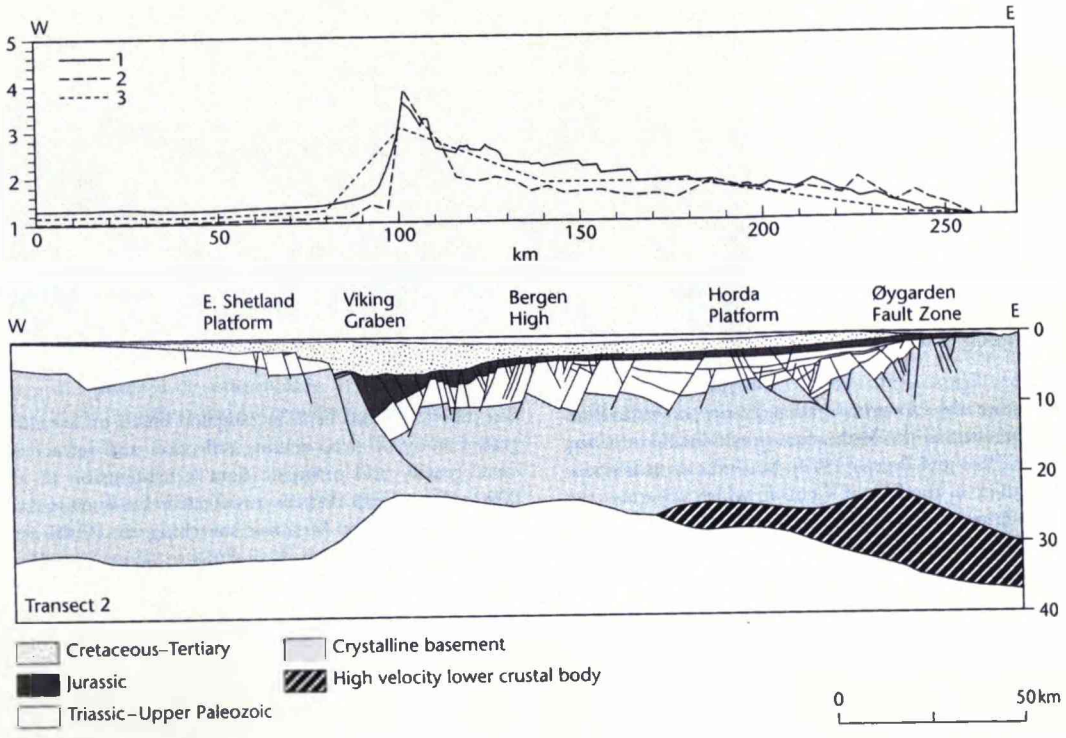

Figure 2.6: Crustal structure of the Viking graben. Upper crustal extension is accommodated by extensional faults, whilst in the lower crust the deformation is more distributed. Upper panel shows extension factors derived for the upper crust, whole crust and lithospheric mantle. Line 1 indicates crustal stretching factor assuming an initial thickness of 36km, line 2 is from reverse modelling and line 3 is from forward tectonostratigraphic modelling. From Skogseid et al. (2000). Stretching factors are relatively uniform with depth, illustrating the applicability of the pure-shear model to the basin.

variable strike-slip faults in the upper crust indicate the age of active extension of a rift basin, post-rift sediments are usually unfaulted and distributed over a wider region than the syn-rift sediments. The lower crust and lithospheric mantle extend by ductile deformation processes. An example of a crustal section through a continental rift is shown in Figure 2.6.

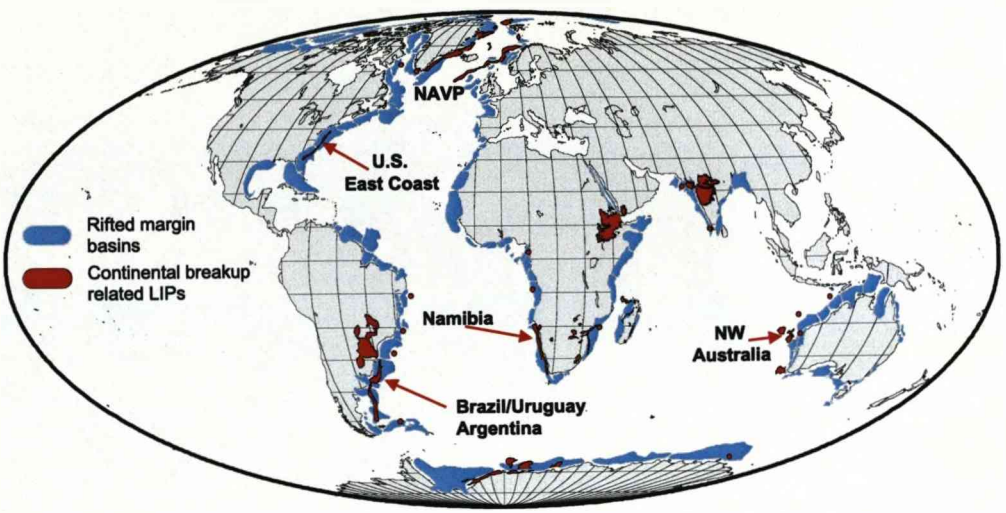

Figure 2.7: Map illustrating identified rifted continental margins, and the location of Large Igneous Provinces (LIPs) associated with continental breakup. Reproduced from Skogseid et al. (2000).

2.5.2 Rifted continental margins

A rifted continental margin is the landward edge of the continental lithosphere, formed during continental lithospheric rupture. A global map showing the location of rifted margins is shown in Figure 2.7. Rifted continental margins can be classified using a number of criteria, depending on the presence or absence or volcanism, width or symmetry. In this thesis I usually consider rifted continental margins in terms of the magmatism associated with their formation, and describe volcanic and non-magmatic/magma-poor margins separately in the following subsections. However I note that there is a continuum between the end-member volcanic and non-volcanic margins. I also note that it is sometimes useful to consider margins in terms of their relative width (wide or narrow) or symmetry (symmetric or asymmetric margins), and may discuss some findings in terms of these classifications.

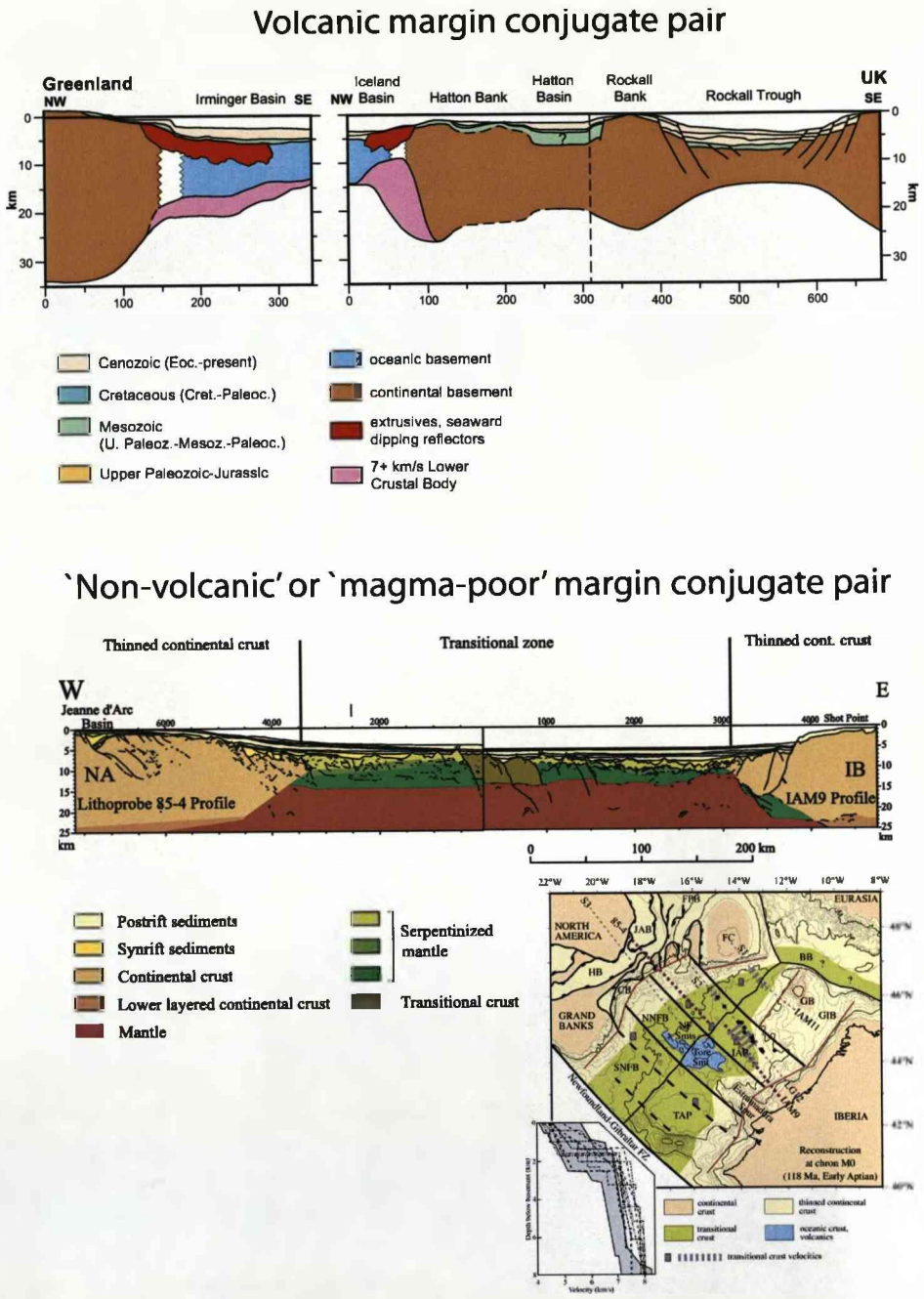

Figure 2.8: Examples of volcanic and non-volcanic margins. Top picture show the Greenland-Hatton bank conjugate volcanic rifted margins. From Tsikalas et al., In Press. For location map see Figure 2.15. Both margins have voluminous intrusive and extrusive volcanic rocks of breakup age. Lower picture shows the Iberia-Newfoundland conjugate non-volcanic margin pair reconstructed to chron M0 (from Sibuet et al. (2007)). The transition zone is thought to be exhumed continental peridotite which has been serpentenised. Map shows plate reconstruction of Iberia-Newfoundland at chron M0, location of section denoted by dotted red line. From Sibuet et al. (2007).

Volcanic margins

Volcanic margins may be associated with voluminous extrusive and intrusive volcanic activity which is usually synchronous with continental breakup, occurring over a period of a few Myr (e.g. White and McKenzie, 1989). This volcanism results in thicker than average oceanic crust at the onset of seafloor spreading, seaward dipping reflectors (SDRs) and often the presence of high velocity lower crust at the transition between continental and oceanic domains (e.g. White and McKenzie, 1989; Skogseid et al., 1992; Larsen and Marcussen, 1992; White et al., 2008). Most of the volcanism is basaltic, although silicic volcanism can also be observed, which may indicate partial melting of the lower crust or highly fractionated melt.

Examples of volcanic rifted margins include the North Atlantic rifted margins associated with Tertiary Igneous Provinces of Greenland, Britain and Norway; South Atlantic margins associated with Parana-Etendeka flood basalts; and the margins of southwest India and the Seychelles associated with the Deccan Traps. An example of the crustal structure of a volcanic conjugate margin pair is shown in Figure 2.8.

Volcanic margins are often associated with either uplift or the lack of rapid initial subsidence (e.g Roberts et al., 1984), which may be observed as a breakup unconformity. On the rift flanks some of this uplift may be permanent (as opposed to time-decaying thermal uplift), and many volcanic margin flanks are elevated, for example the Norwegian and Greenland margins and the southwest Indian margin.

White and McKenzie (1989) showed that a number of volcanic margins are related in space and time to Large Igneous Provinces, and suggest that the volume of melt produced during continental breakup can be explained by passive (pure-shear) rifting of continental lithosphere above a positive mantle thermal anomaly. However, others argue that high melt fluxes at volcanic margins can be caused by a period of active upwelling of the mantle during margin formation and may not always require a temperature anomaly (e.g. Mutter, 1985; van Wijk et al., 2001; Korenaga et al., 2002). Others have suggested that high melt production during continental breakup may be caused by a fertile mantle source region (Foulger and Anderson, 2005).

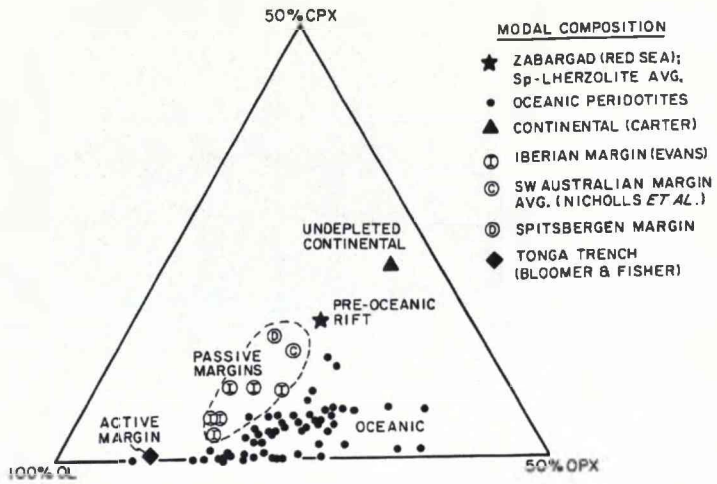

Figure 2.9: Modal composition of mantle peridotites from the Atlantic Ocean, the Iberian, southwestern Australian and Spitzbergen margins, from the Red Sea (a pre-oceanic rift), average of peridotites from the Tonga Trench and estimated undepleted continental lherzolites, from Bonatti and Michael (1989). Bonatti and Michael (1989) suggest that there is a systematic change in the bulk geochemistry going from undepleted continental lithospheric mantle to preoceanic rifts to passive margins to mature oceans, suggesting an increase in the degree of depletion through the Wilson cycle.

Possible reasons for enhanced volcanism at some rifted margins are investigated in chapter 8 of this thesis.

Non-volcanic margins

Non-volcanic, or magma-poor, margins may display a broad ocean-continent transition, up to 170km wide, of exhumed continental mantle separating oceanic crust from thinned continental crust (e.g. Boillot et al., 1987, 1989; Pickup et al., 1996; Dean et al., 2000). This exhumed mantle may be serpentenised as it comes into contact with seawater, and may display weak magnetic anomalies associated with the serpentenisation process (Sibuet et al., 2007) or the intrusion of gabbros to the lower crust during a process analogous to ultra-slow seafloor spreading (Srivastava et al., 2000). Bonatti and Michael (1989) showed that the geochemistry of peridotite exhumed at the seafloor at passive margins differs in geochemistry to oceanic peridotites. A systematic change in bulk oxide compositions going from undepleted continental lithospheric mantle to preoceanic

rifts to passive margins to mature oceans (Figure 2.9) suggests an increase in the degree of depletion and cooler equilibrium conditions as the upper mantle evolves through the Wilson cycle. Petrologic studies of transition zone peridotites suggest that the exhumed peridotites on the Newfoundland, Iberian, and Galician margins in the northern Central Atlantic have a heterogeneous, but depleted subcontinental origin. The peridotites at the Iberian and Galician margins appear to have been refertilized by melt infiltration syn- or post-break-up (Chazot et al., 2005; Muntener and Manatschal, 2006). A sharply defined breakup unconformity is not always obvious at non-volcanic margins. At the Iberian margin and at the incipient Woodlark basin, continental breakup occurs by complex polyphase magmatic and tectonic processes (Taylor et al., 1995; Peron-Pinvidic et al., 2007a; Jagoutz et al., 2007) which are distributed in both space and time.

A number of explanations have been proposed to explain the absence of volcanism at non-volcanic margins, including a cool geotherm (Reston and Morgan, 2004; Pérez-Gussinyé et al., 2006), slow extension and thinning (Whitmarsh et al., 1996) and the presence of depleted lithosphere (Pérez-Gussinyé et al., 2006). These explanations will be explored in more detail in chapter 8, and I will also consider the implications of upwelling-divergent flow as a mode of thinning the continental lithosphere on the prediction of melting during lithospheric thinning. In chapter 9 predictions of melt production made by kinematic models of lithospheric thinning are tested against observations at the Iberian margin.

Depth-dependent stretching at continental rifted margins

Numerous continental rifted margins exhibit depth-dependent stretching, where the lithosphere has apparently been thinned much more than the upper crust (e.g. the eastern Canada margin (Royden and Keen, 1980); the Norwegian margin (Roberts et al., 1997), the northwest Australian margin (Driscoll and Karner, 1998); in the Pearl River Mouth Basin in the South China Sea (Clift et al., 2001), Goban Spur, the Vøring margin and Galicia margin (Davis and Kusznir, 2004, Figures 2.10 and 2.11)). Depth-dependent stretching has been described at both volcanic and non-volcanic margins,

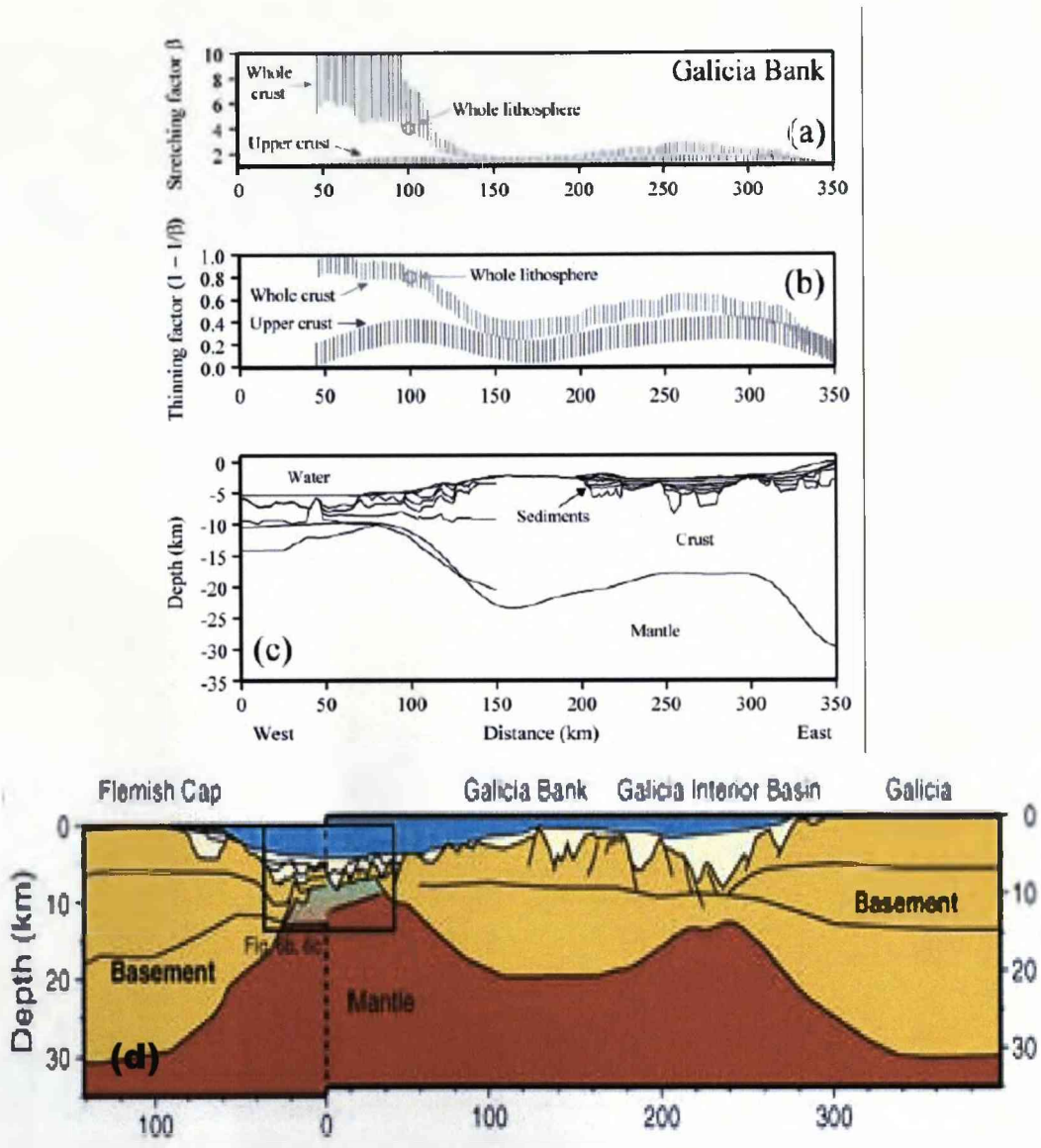

Figure 2.10: (**a**) Stretching and (**b**) thinning factors across (**c**) the Galicia margin and Galicia Interior basin illustrate the depth-dependent stretching which has occurred during and since continental breakup (from Davis (1999). (**d**) Crustal reconstruction across the Newfoundland-Galicia margins (from Hopper et al. (2006, using sections from Funck et al. (2003); Perez-Gussinye et al. (2003); Reston et al. (1996); Cordoba et al. (1987); Whitmarsh et al. (1996)).

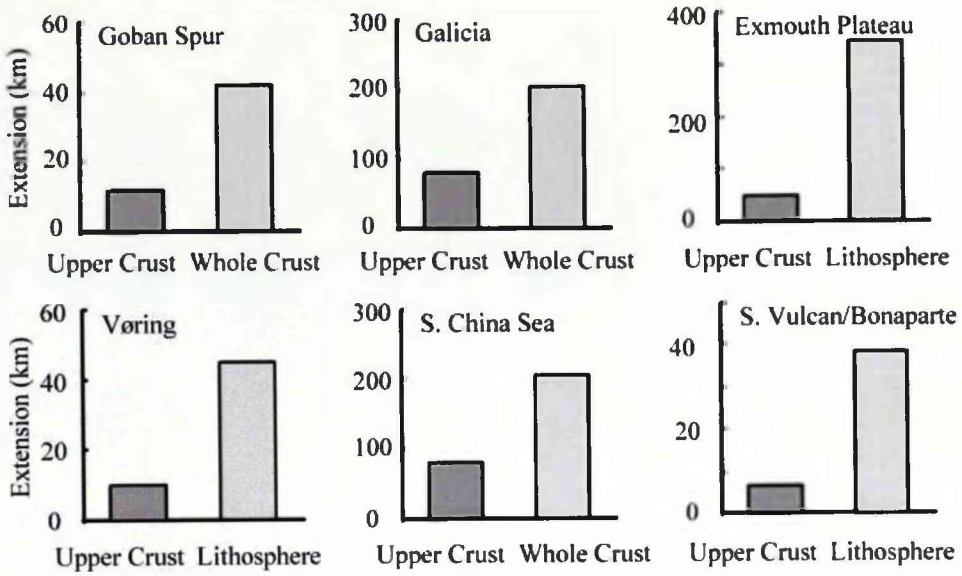

Figure 2.11: Total apparent extension calculated for six margins. In each case whole lithosphere or whole crust extension greatly exceeds extension of the upper crust. From Davis and Kusznir (2004)

including conjugate pairs. Preferential lithospheric mantle and lower crustal thinning with respect to upper crustal thinning has also been reported in the Vøring basin, 150km landwards of the Norwegian continental margin (Roberts et al., 1997), suggesting that the process of depth-dependent thinning can affect pre-breakup basins over a wide zone. Clift and Lin (2001) and Kusznir et al. (2004) demonstrated that depth-dependent stretching in the Pearl River Mouth basin and on the Norwegian margin respectively, is a syn-breakup phenomenon, suggesting that depth-dependent stretching is an inherent part of the breakup process, as opposed to a consequence of early seafloor spreading.

2.5.3 Propagating rift tips and failed breakup basins

Propagating rift tips generate deep basins ahead of young oceanic crust and newly ruptured continental crust. Failed breakup basins are basins which were perhaps once at the propagating tip or flank of an oceanic basin, but did not rupture. Examples of

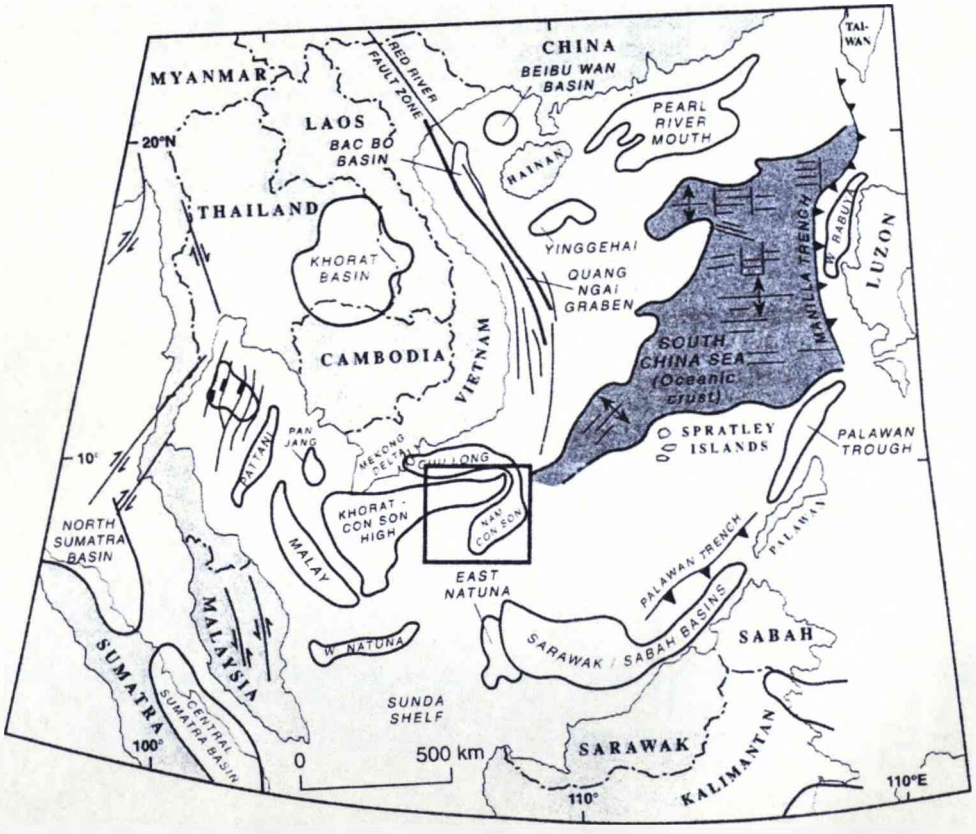

Figure 2.12: Tectonic map of the South China sea region. Note the location of the Nam Con Son basin at the palaeo-propagating tip of the ocean basin. The Pearl River mouth basin, also mentioned in the text, is also located on this map. From Matthews et al. (1997).

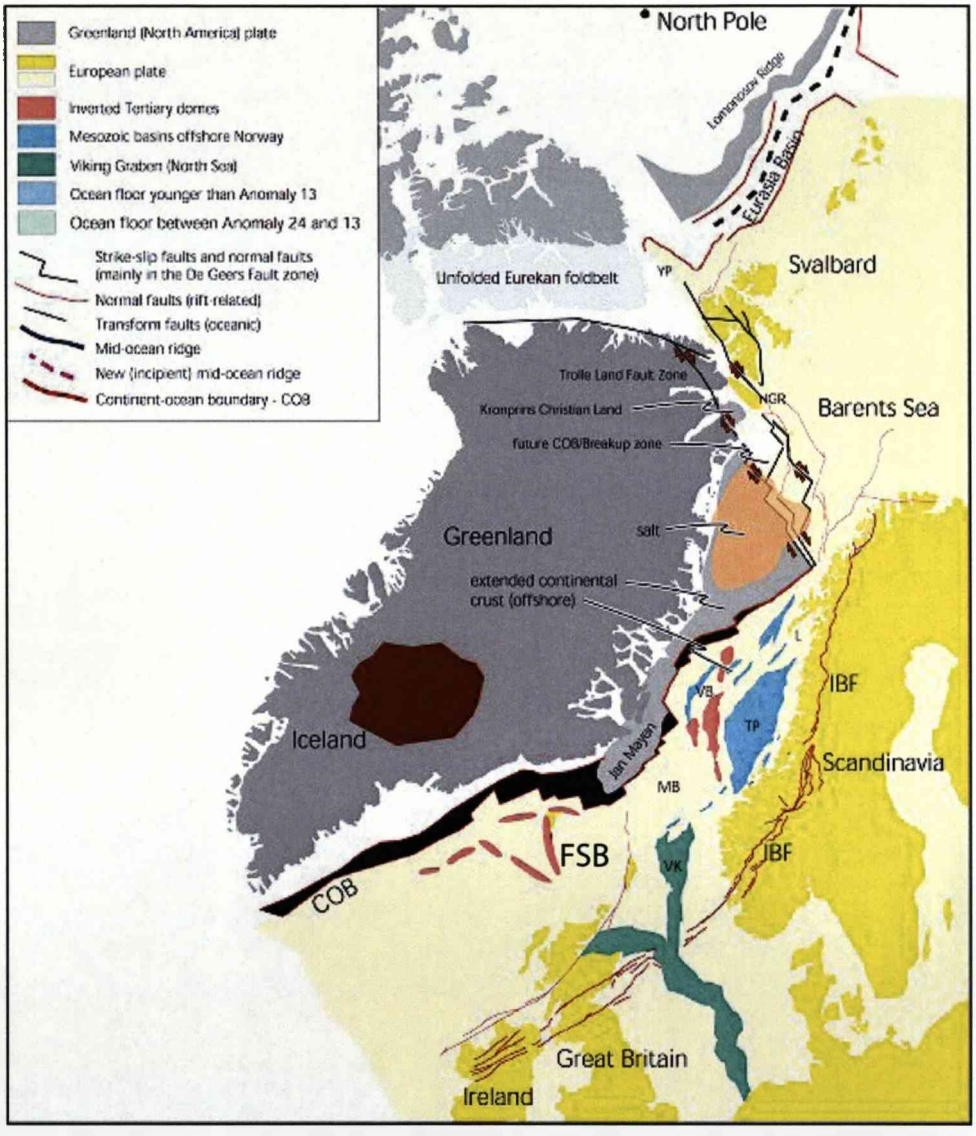

Figure 2.13: Reconstruction of the North Atlantic at magnetic anomaly 24 times (end Palaeocene, ~54Ma), just prior to the onset of seafloor spreading. Breakup of the North Atlantic was accompanied by voluminous volcanism, which may have been associated with a high-temperature mantle plume which enhanced the rate of upwelling beneath the incipient ridge (an inferred position for the plume is shown in dark red). Note the location of the Faroe-Shetland basin (FSB), which is coaxial with the Møre margin, and may have been thinned during Palaeocene continental breakup. Annotations: MB= Møre basin; COB = Continent-Ocean Boundary, HGR = Hovgaard Ryggen; IBF = Innermost boundary fault; TP = Trøndelag Platform; VB = Vøring Basin VK = Viking Graben; YP = Yermak Plateau. Adapted from Mosar et al. (2002).

present-day propagating rift tips include the Woodlark basin, and the Gulf of California. Candidates for failed breakup basins include the Nam Con Som basin (Clift et al., 2001, see Figure 2.12 for location) and the Santos basin (Scotchman et al., 2006). Both the Woodlark basin (Kusznir and Karner, 2007) and the Nam Con Son basin (Clift et al., 2001) have been shown to exhibit depth-dependent stretching, where preferential lithospheric and lower crustal thinning (with respect to the upper crust) occurs prior to the onset of seafloor spreading. This provides further evidence that the process responsible for continental lithospheric thinning and rupture is, or becomes, depth-dependent prior to the onset of seafloor spreading.

In this thesis I investigate the Tertiary evolution of the Faroe-Shetland basin (FSB). The subsidence in the FSB since the end of the Palaeocene suggests that substantial lithospheric thinning has occurred, whilst very little evidence for Palaeocene or post-Palaeocene upper crustal extension is observed. At late Paleocene times the basin lay close to the incipient north Atlantic (see Figure 2.13), but breakup occurred to the west of the Faroe-Shetland basin, at the Faroes margin. The basin is a candidate for a failed breakup basin, although various other explanations have been put forward for the anomalous subsidence history of the basin.

2.5.4 The spatial distribution of rifts

It was first observed by Wilson (1966) that continental rifting can occur close to old orogenic belts, for example breakup of the Atlantic occurred close to the Caledonian-Appalachian orogeny (Figure 2.14). A number of causes have been proposed to explain this phenomenon. Dunbar and Sawyer (1989) show that the increased crustal thicknesses associated with orogens can decrease lithospheric strength, providing a weak zone where later rifting can more easily occur. Vauchez et al. (1997) suggest that the inherited tectonic fabric in the continental lithospheric mantle induces strength anisotropy which influences the propagation of rifts so that they are parallel to orogenies. Clift and Lin (2001) speculate that continental extension may preferentially occur above an old arc-setting, due to the weakening effect that volatiles have on the lithosphere

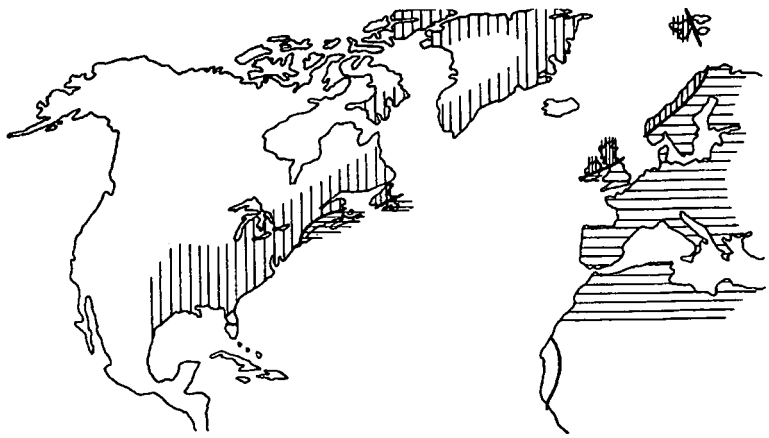

Figure 2.14: The reopening of the Atlantic. Map of the North Atlantic region showing distribution of Lower Palaeozoic fauna. 'Atlantic' type fauna shown by horizontal shading, 'Pacific' type fauna by vertical shading. This evidence led Wilson (1966) to suggest that the Atlantic opened close site of an old orogeny (thick black line). From Wilson (1966).

(Hirth and Kohlstedt, 1996). In chapter 12 of this thesis a preliminary test is carried out which assesses whether water-content heterogeneities associated with continental accretion could provide a weak zone that may be exploited during rifting.

A number of margins exhibit very wide zones of thinned continental crust between unequovical oceanic and continental domains. In some cases the thinned crust may be a result of an earlier extension event (e.g. Rockall Trough, Figure 2.8; Galicia Interior Basin, Figure 2.10), although it is possible that processes associated with continental breakup may also preferentially thin marginal basins (e.g. Roberts et al., 1997). Nevertheless, it often observed that the locus of continental rupture and seafloor spreading avoids regions of previously thinned crust. The map in Figure 2.15 illustrates that extensional processes in the North Atlantic region have been active since at least Palaeozoic times, but the direction and locus of rifting has shifted a number of times, and consequentially the marginal areas host a number of rift basins of variable ages. This can be explained by considering the integrated strength of the lithosphere. Where continental crust has been thinned and has had sufficient time to cool (or if thinning is slow), thinned lithosphere may be stronger than unthinned continental lithosphere,

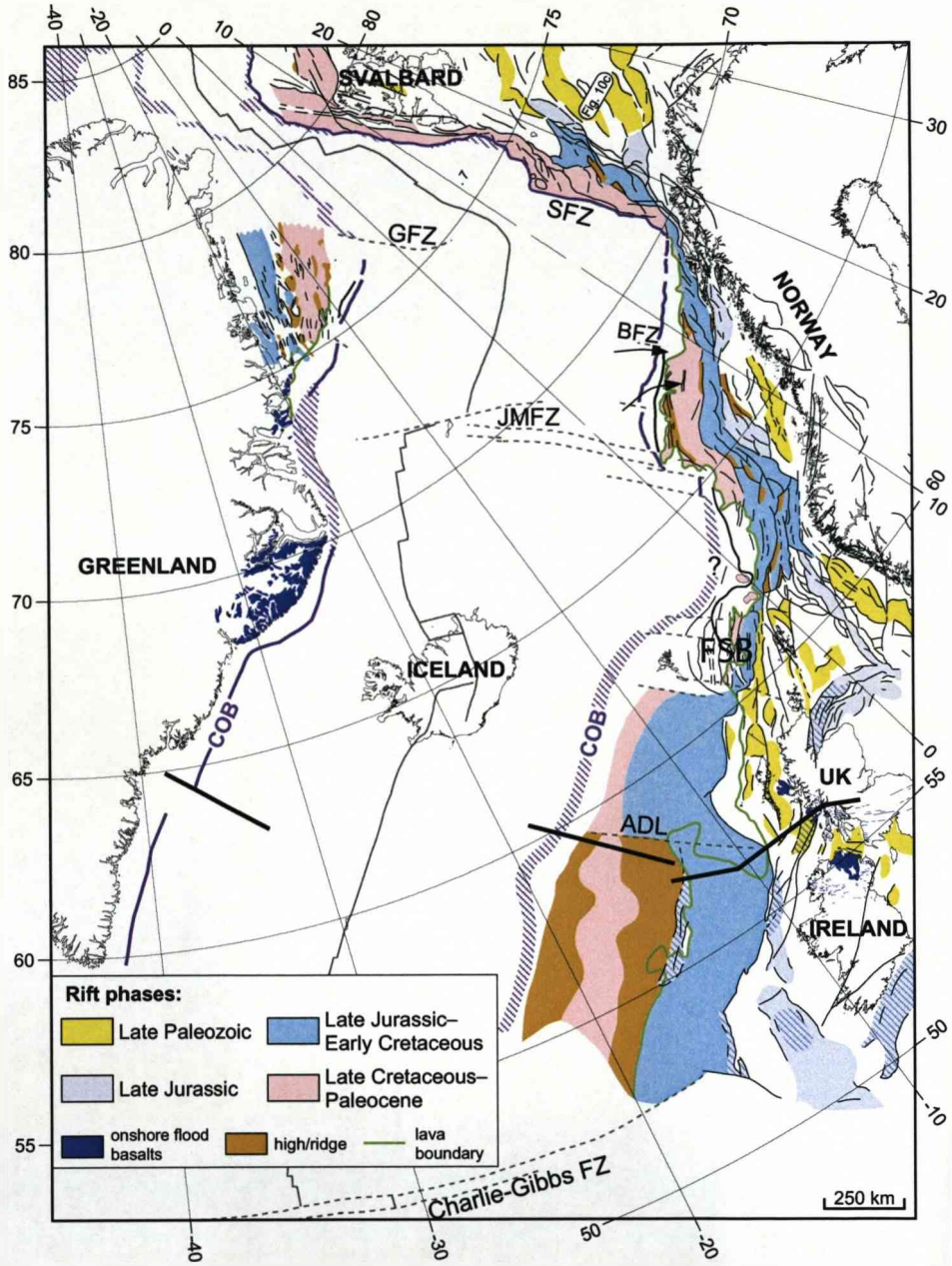

Figure 2.15: Tectonic map of the North Atlantic rift province, showing the location of the rifting phases which occurred prior to the opening of the Atlantic at late Palaeocene times. FSB denotes location of the Faroe-Shetland basin. Major transfer zones: ADL, Anton Dohrn Transfer/Lineament; BFZ, Bivrost Fracture Zone; JMFZ, Jan Mayen Fracture Zone; GFZ, Greenland Fracture Zone; SFZ, Senja Fracture Zone. Dark lines denote location of Greenland-Hatton-Rockall section in Figure 2.8. Adapted from Tsikalas et al., In Press.

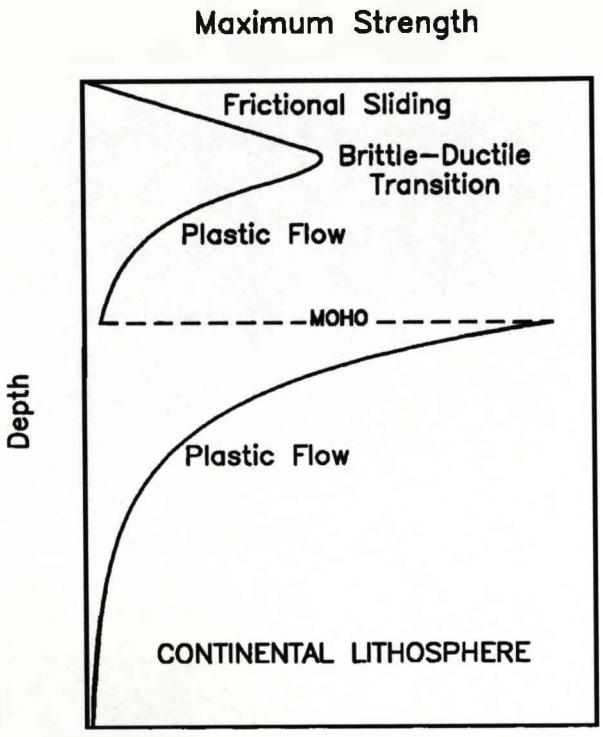

Figure 2.16: The yield strength envelope. Schematic illustration of rock strength as a function of depth for a two-layer continental lithosphere. The crust is assumed to be quartz dominated and the lithospheric mantle olivine dominated. Above the brittle-ductile transition the upper crust deforms according to Byerlee's Law, an experimentally-derived law which describes the failure stress of rocks. Below the brittle-ductile transition, deformation occurs by plastic flow. The strength discontinuity at the Moho is a result of the lithology discontinuity. After Kohlstedt et al. (1995).

and the locus of thinning may migrate or shift towards a weaker zone (e.g. England, 1983; Kusznir and Park, 1987; van Wijk and Cloetingh, 2002). Other factors may also influence the location of continental breakup, and are discussed in this thesis.

2.6 The strength of the continental lithosphere and the driving forces of thinning and breakup

The integrated strength of the continental lithosphere determines the total tectonic force required for lithospheric rupture. It is useful to consider the strength of the lithosphere in terms of a yield-stress envelope. The yield stress envelope can be calculated for a 1–D lithospheric column using equations for material failure determined by laboratory experiments and scaled to appropriate values for the lithosphere. A simple example is shown in Figure 2.16 for a two-layer lithosphere. The strength of the upper crust is determined by equations for brittle failure, whilst for the lower crust and the mantle the strength is determined according to ductile deformation laws. As the lithology of the crust and the mantle differ, a strength discontinuity occurs at the Moho. The integrated strength of the lithosphere is influenced by the initial temperature structure, crustal thickness, the composition of the crust and the mantle (e.g. see Kusznir and Park, 1982, 1987; Burov and Diament, 1995; Buck et al., 1999; Jackson, 2002; Ziegler and Cloetingh, 2004). Figure 2.17 illustrates the potential influence of water on the integrated strength of the lithosphere.

Although 1–D yield stress envelopes are useful for calculating the strength of the lithosphere, it is important to remember that continental lithosphere thinning is a 2– or 3–dimensional process, and as thinning and deformation begins, the deformation field is modified by the evolving temperature and strain rate fields, as well as the presence of melt.

The driving forces of continental rifting have usually been considered in terms of 'passive' and 'active' components. Passive rifting implies that extension is driven by far-field horizontal forces which arise due to plate-scale process such as slab-pull or slab-rollback (e.g. see Forsyth and Uyeda, 1975). During passive rifting the asthenospheric mantle upwells into the accommodation space created by the extension. The end-member model of active rifting implies that extension is driven by buoyant upwelling (e.g. of a mantle plume) which originates in the deep mantle, and impinges on the base of the

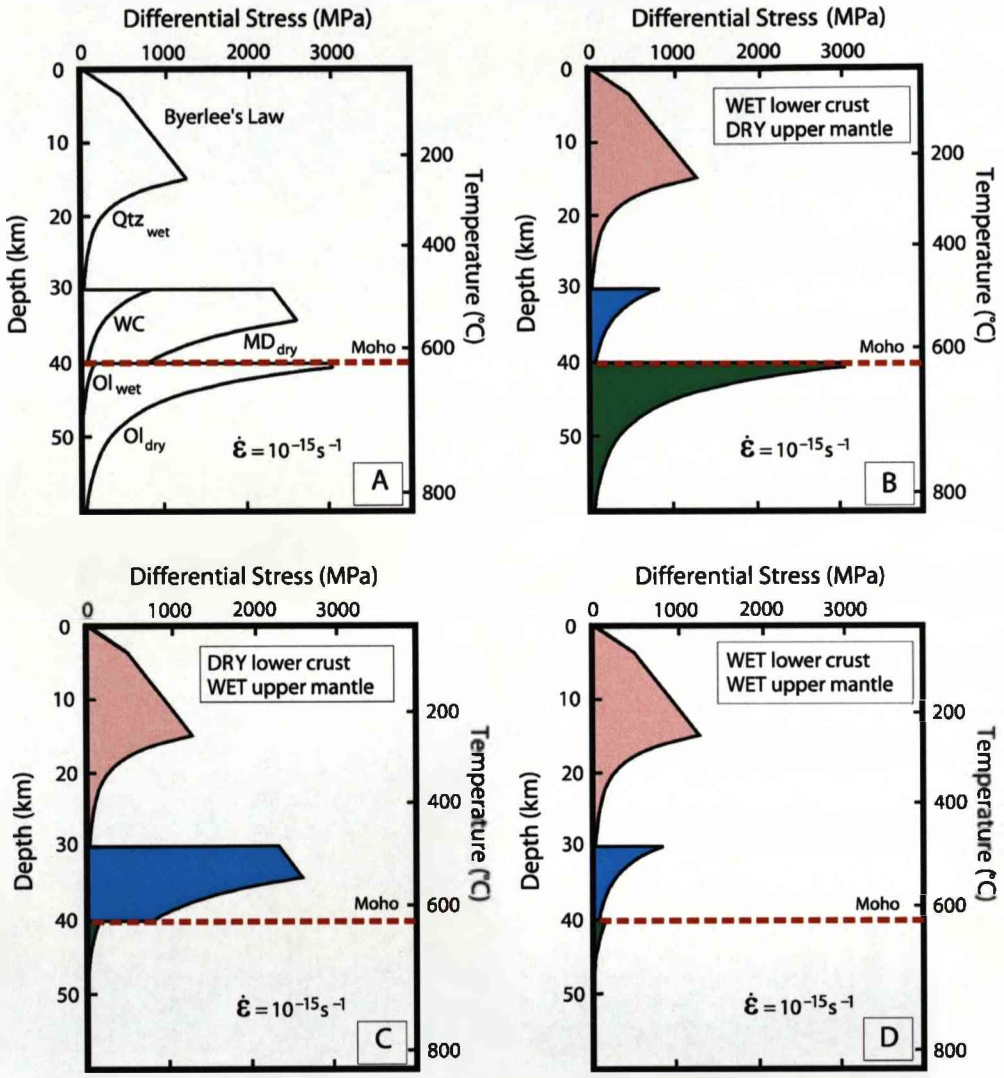

Figure 2.17: The effect of water on the Yield Stress Envelope. Strength envelopes of differential stress versus depth in the continental lithosphere, to illustrate the potential effects of water on the integrated yield strength and the distribution of strength with depth. From (Jackson, 2002).

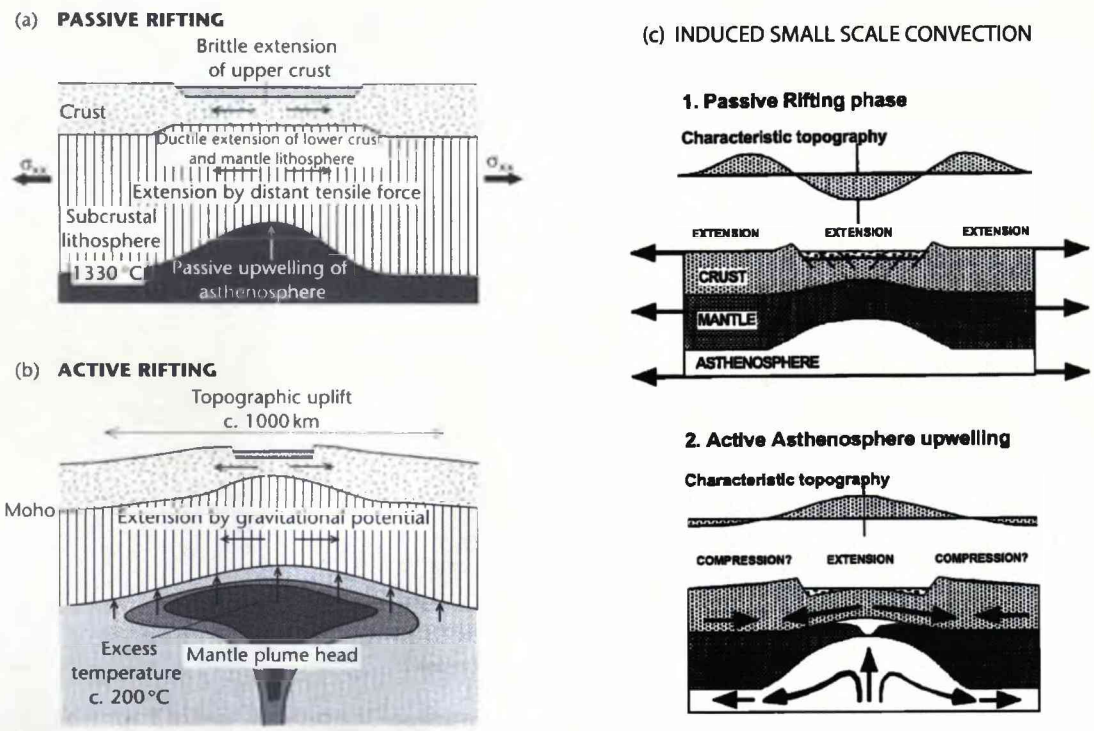

Figure 2.18: Schematic diagram of driving forces associated with **(a)** 'active' and **(b)** 'passive' rifting. From Allen and Allen (2005). **(c)** illustrates schematic representation of induced small-scale convection in the continental lithosphere. From Huismans et al. (2001a).

continental lithosphere causing topographic doming and weakening of the lithosphere leading to rifting. A summary of the active and passive rifting models is shown in Figure 2.18a and 2.18b .

However, both passive and active models of continental rifting fail to explain some aspects of rifting: Rifting and lithosphere breakup is not always associated with a mantle plume (e.g.Iberia-Newfoundland), and neither the active or passive model explain depth-dependent stretching.

As already described, a number of authors have shown the importance of induced small-scale convection during lithospheric thinning (Figure 2.18c). In these models small-scale convection is induced by viscosity and density contrasts which arise as a consequence of passive rifting. Induced small-scale convection may explain depth-dependent stretching and excess volcanism at volcanic margins, as described above. In addition depth-dependent stretching caused by preferential lithospheric thinning can increase the rift-push force, which encourages further extension. In this thesis 'active' rifting or flow is considered to refer to a style of rifting where upwelling of (hot and buoyant) material occurs faster or more vigorously than would be predicted by passive rifting. Induced small-scale convection is therefore considered to be an 'active' thinning process.

The evolution of rift basins and rifted margins is dependent on a number of intrinsic and extrinsic factors, including strain rate, mantle potential temperature, the rheological layering of the lithosphere and initial Moho and lithosphere topography (e.g. Dunbar and Sawyer, 1989; Corti et al., 2003; Nielsen and Hopper, 2004).

In chapter 11, I investigate some of the dynamic processes which may occur during continental lithospheric thinning. I assess the influence of melting and of compositional heterogeneities on the development of small-scale convection.

2.7 Summary

Continental lithospheric extension and thinning results in the formation of rift basins and, in the case of lithospheric rupture, the formation of two rifted margins separated

by an ocean basin. Rift basins and rifted margins exhibit a wide range of characteristics in terms of extension, width, and volcanism. Not all observations at rift basins and rifted margins are easily explained by a simple model of continental thinning by pure-shear extension, and variations in the mode of deformation and conditions of rifting have been proposed to account for these observations.

Many questions remain regarding continental rift basin and rifted margin formation. One key question is whether the processes which form continental rift basins are the same or different as those which ultimately cause continents to rupture and seafloor spreading to initiate. It is widely observed that many, maybe all, rifted margins experienced depth-dependent stretching during continental breakup, whereas the formation of many intracontinental rifts can be explained by the model of pure-shear stretching. Cochran and Karner (2007) observe that rifts which eventually rupture are characterised by syn-rift sag basins where lithospheric thinning appears to have occurred in the absence of upper crustal faulting, whilst rifts which are characterised by large offset fault systems generally will not proceed to breakup. They propose that the style of rifting and therefore the ultimate fate of the rift (whether or not it proceeds to breakup) may be influenced by the initial strength of the lithosphere. However, some rift basins appear to be sag basins which did not breakup (e.g. the Nam Con Son basin) - so a related question may be: was the process that formed these sag basins different to the processes which form more 'typical' intracontinental rifts (i.e. pure-shear)?

A number of explanations exist for the variability in volcanism at rifted margins, and the cause of both 'anomalously' high and low volumes of volcanic addition during lithospheric thinning is debated. Intrinsic variables such as mantle potential temperature can affect the volume and composition of melt during thinning, however the processes of continental lithospheric thinning (the mode of deformation) also has a significant influence on the production of volcanic addition.

The driving forces responsible for continental lithospheric thinning and rupture are also not completely understood. It is likely that the location of rifting is dependent on both pre-existing conditions and heterogeneities in the continental lithosphere and the forces

available to drive rifting.

This thesis aims to investigate the processes and mechanisms which are active during continental lithospheric thinning and breakup, and the manifestations of those mechanisms on the resulting basins and margins. In the next four chapters I focus my attention to the Faroe-Shetland basin, a candidate for a failed breakup basin which records an important phase of continental rifting between rift basin and rifted margin formation. In chapters 7 and 8 I compare predictions of continental margin geometry, subsidence, heatflow and melt production made by end-member models of continental lithospheric thinning and also investigate the influence of intrinsic variables (e.g. extension rate and mantle potential temperature) on predictions. To try to determine the mode and conditions of deformation for two case histories I then compare predictions made by models to observations at the Iberian margin (chapter 9) and in the Faroe-Shetland basin (chapter 10). In chapter 11 I present an investigation into some of the driving forces and processes which may be responsible for the initiation and mode of continental lithosphere thinning.

Chapter 3

The geological history of the Faroe-Shetland basin

3.1 Introduction

The Faroe-Shetland Basin (FSB), an apparent Mesozoic rift basin on the NE Atlantic margin (Figure 3.1) exhibits an anomalous Tertiary subsidence history (Nadin et al., 1997; Clift and Turner, 1998; Ceramicola et al., 2005; Champion et al., 2008). Post-rift subsidence from a series of Mesozoic rift events was interrupted by uplift in the Late Palaeocene, shortly before continental breakup and seafloor spreading initiation occurred at the Faroes and Møre continental rifted margins. Well-logs and seismic mapping show that large areas of the basin became subaerial at the time of continental breakup (Naylor et al., 1999; Smallwood and Gill, 2002; Ellis et al., 2002; Champion et al., 2008). Rapid subsidence occurred at the end of the Palaeocene and in the Eocene. Since the end of the Palaeocene the axis of the basin has experienced water-loaded tectonic subsidence of up to 2km (Turner and Scrutton, 1993; Nadin et al., 1997; Ceramicola et al., 2005). This magnitude of post-Palaeocene subsidence in the basin suggests that a major Late-Palaeocene rift event occurred, but very little tectonostratigaphic evidence for rifting (i.e. faulting) is observed in the upper crust (Turner and Scrutton, 1993; Ceramicola et al., 2005).

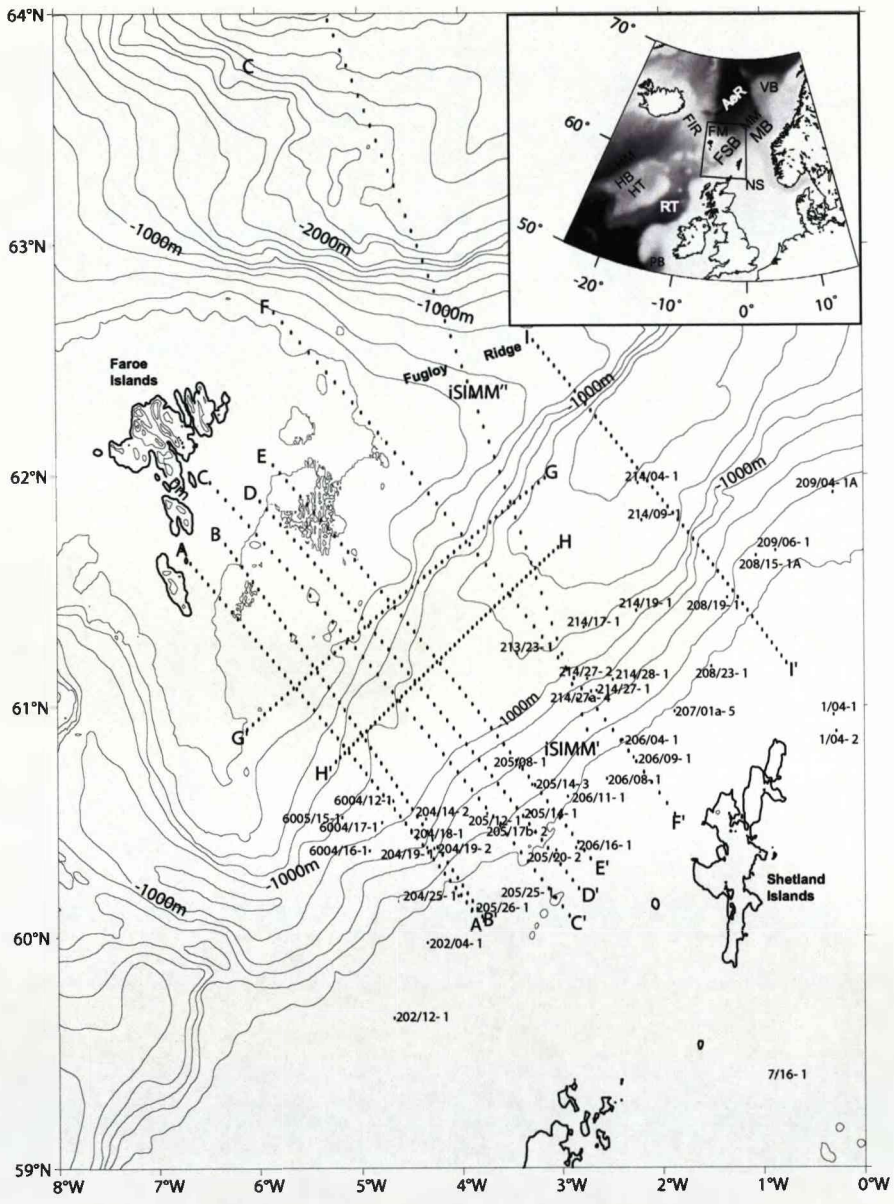

Figure 3.1: Bathymetric contour map of FSB area and location of profiles (A-I and iSIMM) and wells used in this study. Inset: Shaded bathymetry of NE Atlantic. Annotations: FSB=Faroe-Shetland basin; FM=Faroes margin; MB=Møre Basin; MM=Møre Margin; FIR=Faroes-Iceland Ridge; HB=Hatton bank; HT=Hatton Trough; RT=Rockall trough; PB=Porcupine Basin; VB=Vøring Basin; AeR=Ægir Ridge; NS=North Sea

Previous work has suggested that the anomalous Tertiary subsidence history can be attributed to transient uplift events caused by the proto-Iceland plume during continental breakup between Europe and North America (Nadin et al., 1997; Smallwood and Gill, 2002; Champion et al., 2008) or magmatic underplating associated with breakup on the Faroese margin (Clift and Turner, 1998). However, these previous analyses have generally focused on small areas of the basin where the palaeobathymetric control is good, and interpretations have not been tested over the whole basin. Hurst (2006) showed that the basin cannot be modelled using the pure-shear model of continental extension of (McKenzie, 1978) and suggested that the basin is a failed breakup basin associated with Atlantic breakup. Intense exploration by the petroleum industry and academia in the basin has yielded an extensive dataset of seismic reflection and refraction lines and well-logs. This dataset enables models of basin formation to be tested for a much larger area than previous studies.

This chapter contains a summary of the geological and tectonic history of the FSB. This is discussed in relation to a large amount of observational data which is available for the basin. A series of seismic reflection profiles across the basin were kindly provided by StatoilHydro, these had been interpreted and depth-converted using seismic velocity measurements from wells in the basin. A depth-converted profile from the iSIMM (integrated seismic imaging and modelling of margins) project, a joint industry-academia project carried out in 2002, is also presented. In addition, a series of simplified well-log maps, complied from well-logs and well reports provided by StatoilHydro, are presented, these illustrate the overall palaeobathymetric evolution of the basin. Estimates of crustal thickness derived from seismic refraction and gravity studies across the basin are also reviewed.

In Chapters 4-6, an analysis of the tectonic history of the basin is carried out, with a focus on events which occurred during the Late Palaeocene, the time of continental lithospheric rupture on the adjacent Faroes and Møre margins. In Chapter 4, the magnitude of thinning and extension in the basin is quantified. Extension of the upper

crust is determined by summing fault heaves imaged on seismic lines. Using palaeobathymetry data where available, the water-loaded tectonic subsidence in the basin is quantified using 1D and 2D flexural backstripping. In Chapter 5 these data are used to evaluate the applicability of the pure shear lithosphere thinning model of continental rift basin formation (McKenzie, 1978) to the basin. The McKenzie (1978) model assumes that lithosphere thinning occurs by pure shear, where stretching of the lithospheric layers is uniform with depth (see Figure 2.4). The magnitude of stretching of a layer (e.g. the crust) is usually quantified in terms of an extension factor β, where β is the ratio between the initial and final layer thicknesses:

$$\beta = \frac{initial\ layer\ thickness}{final\ layer\ thickness} \tag{3.1}$$

During lithosphere thinning, syn-rift subsidence (Si_{total}) occurs due to the net isostatic effect of crustal thinning (Si_{ct}) plus thermal uplift (Si_t). Post-rift subsidence (St) is predicted to follow an exponential decay curve with a time constant of around 62.8Myr (McKenzie, 1978) as the lithosphere cools by conduction and thermally contracts.

To assess the applicability of the pure-shear model of basin formation to the basin, the timing and magnitude of lithospheric thinning implied from the subsidence history of the basin is compared to stretching factors determined from extension accommodated on brittle faults in the upper crust and to apparent whole crustal stretching factors calculated from gravity studies and seismic refraction experiments which sample the Moho. Possible causes of anomalous subsidence in the FSB are considered and discussed. The basin is shown to have experienced depth-dependent thinning, where thinning of the lithospheric mantle and lower crust exceeds that of the upper crust, approximately synchronously with lithosphere rupture and the onset of seafloor spreading at the adjacent Faroes and Møre margins. The implications and timing of depth-dependent stretching and thinning are discussed in Chapter 6. In Chapter 10 two-dimensional models are employed to try to determine the mode of deformation responsible for the Tertiary development of the FSB.

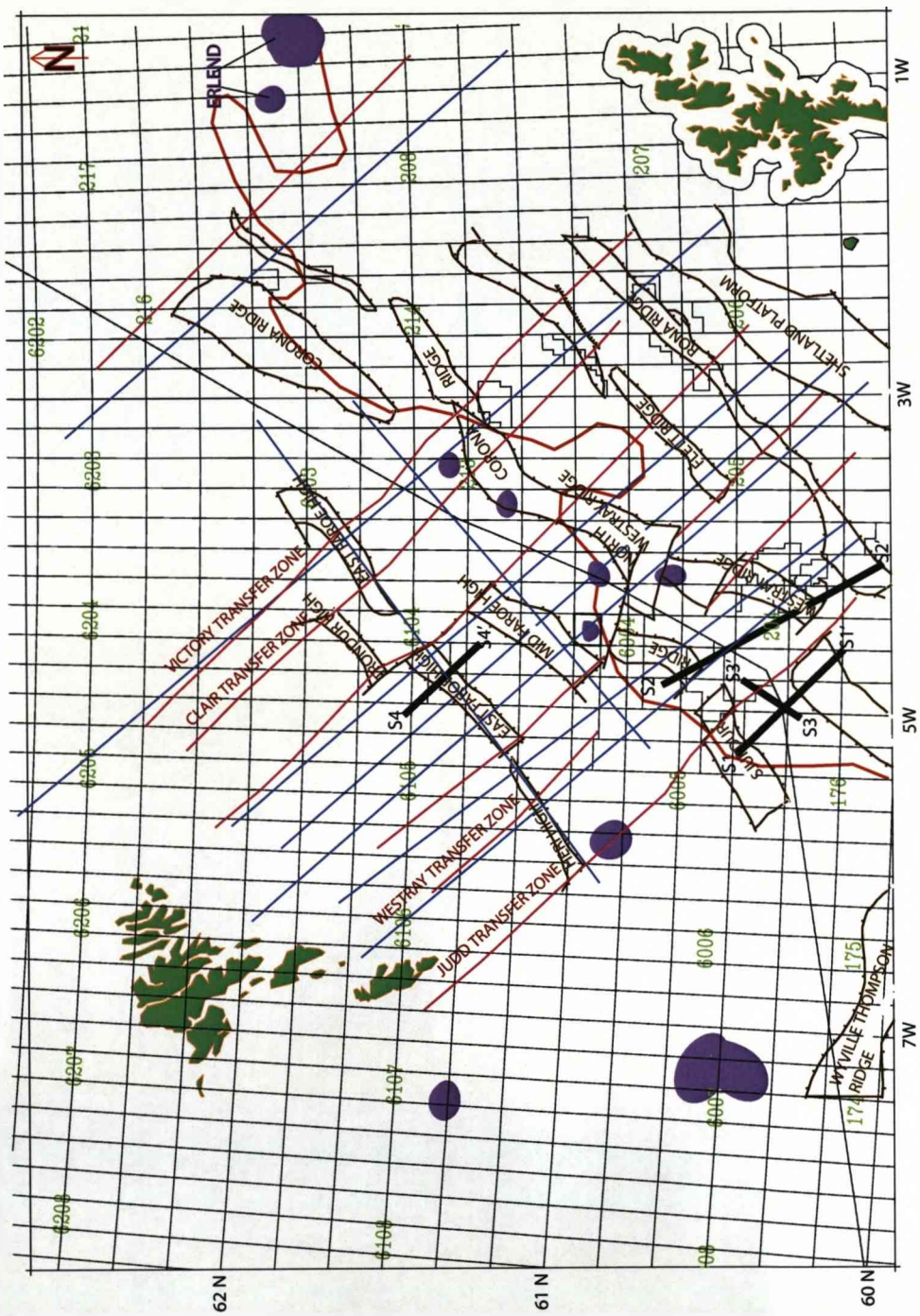

Figure 3.2: Structure map of the FSB. Location of profiles used in this study shown in blue, transfer zones shown in red, structural highs in brown and UK/Faroes border in black. Numbers in green denote quadrant numbers. Purple zones denote igneous intrusions, and red line shows eastwards limit of the Palaeocene Faroe Islands basalt series extrusives. Modified from StatoilHydro internal document. Approximate locations of profiles shown in Figure 3.12 illustrated in heavy black lines.

3.2 Tectonic setting and overview of the basin

The FSB (Figures 3.1 and 3.2) lies on the NE Atlantic passive volcanic rifted margin, in the region between unthinned continental crust and oceanic crust. The FSB is one of a series of basins on the northeast Atlantic margin (Figure 3.1), formed by continental extension since collapse of the Caledonide orogeny in the Devonian. A number of discrete but overprinting, generally NE-SW trending rifting events have been identified in the FSB between the Devonian and Early Cenozoic by various authors (e.g. Doré et al., 1999; Roberts et al., 1999; Dean et al., 1999; Hooper and Walker, 2002). Bathymetry within the FSB plunges northeast to a maximum depth of 1700m, where it reaches the Norwegian basin. The southeastern flank of the basin is the Shetland continental platform which extends northeastwards to the Norwegian margin. The northwestern flank of the basin, the Faroese continental block, is covered by thick basalt, which may be up to 5km thick (e.g. Richardson et al., 1999; Smallwood et al., 2001). Voluminous volcanism occurred between ~58 and ~54Ma during lithosphere rupture and the onset of seafloor spreading to the north and west of the FSB, on the Møre and Faroes margins (Waagstein, 1995, 1988). Total sediment thickness (Devonian-Present) in the basin reaches 8km (e.g. Roberts et al., 1999; Lamers and Carmichael, 1999). Sag subsidence (subsidence not associated with faulting) since the Late Palaeocene has given the sediments in the basin a 'steers head' geometry. Post break-up compression events, associated with plate reorganisations in the Atlantic, have affected the region causing minor reverse faulting and folding on the Faroes platform and Fugloy ridge (Boldreel and Andersen, 1993, 1998; Andersen et al., 2000; Davies et al., 2004). A more detailed review of the geologic history of the basin, with particular reference to palaeobathymetry and the timing of events in the Late Palaeocene, is given in Section 3.5

3.3 Crustal thickness

Seismic refraction data

There have been a number of seismic refraction experiments across the FSB and Faroes continental block (Clift and Turner, 1998; Richardson et al., 1998, 1999; Raum et al., 2005; Roberts, 2007) which have imaged the Moho beneath the basin (Figure 3.3a-f). Each of the profiles illustrates significant Moho upwarp and crustal thinning which correlate with the present day bathymetry of the basin (Figure 3.3a,b). The crust (Top basement - Moho) thins to a minimum of <11km in five of the six published profiles. Moho depth underneath the Shetland Platform reaches a depth of 32km, this provides a lower bound estimate of the initial crustal thickness in the area. Apparent crustal stretching factors (the ratio of initial to present day crustal thickness) indicate that the crust has been thinned to one third of its original thickness in the centre of the basin (Figure 3.3c). The profiles show a mismatch of crustal thicknesses at crossover points which are likely to be due to variable ray coverage, determination of 'top basement', processing and use of gravity and magnetic modelling to interpolate between and outside regions of ray coverage. High velocity lower crust has been imaged on the seaward side of the Fugloy ridge (Raum et al., 2005; Roberts, 2007, Figure 3.3a), probably indicating the presence of lower crustal intrusions associated with continental break-up of the volcanic Faroese margin, but this does not extend beneath the FSB.

Crustal thickness map from gravity inversion

Satellite gravity data can be used to determine the thickness of the crust. The method of Greenhalgh and Kusznir (2007) has been used to invert the gravity field for crustal thickness incorporates corrections for the thermal gravity anomaly from lithospheric thinning. N. Kusznir (pers. comm.) has calculated the apparent crustal thickness and thinning factors of the NE Atlantic region (Figure 3.5). This method predicts crustal thinning in the FSB which is continuous with the thin crust of the Møre basin, a wide, Mesozoic basin which lies inboard of the Møre margin. The gravity inversion assumes zero sediment thickness; consequently the crustal thicknesses shown in Figure 3.5a are

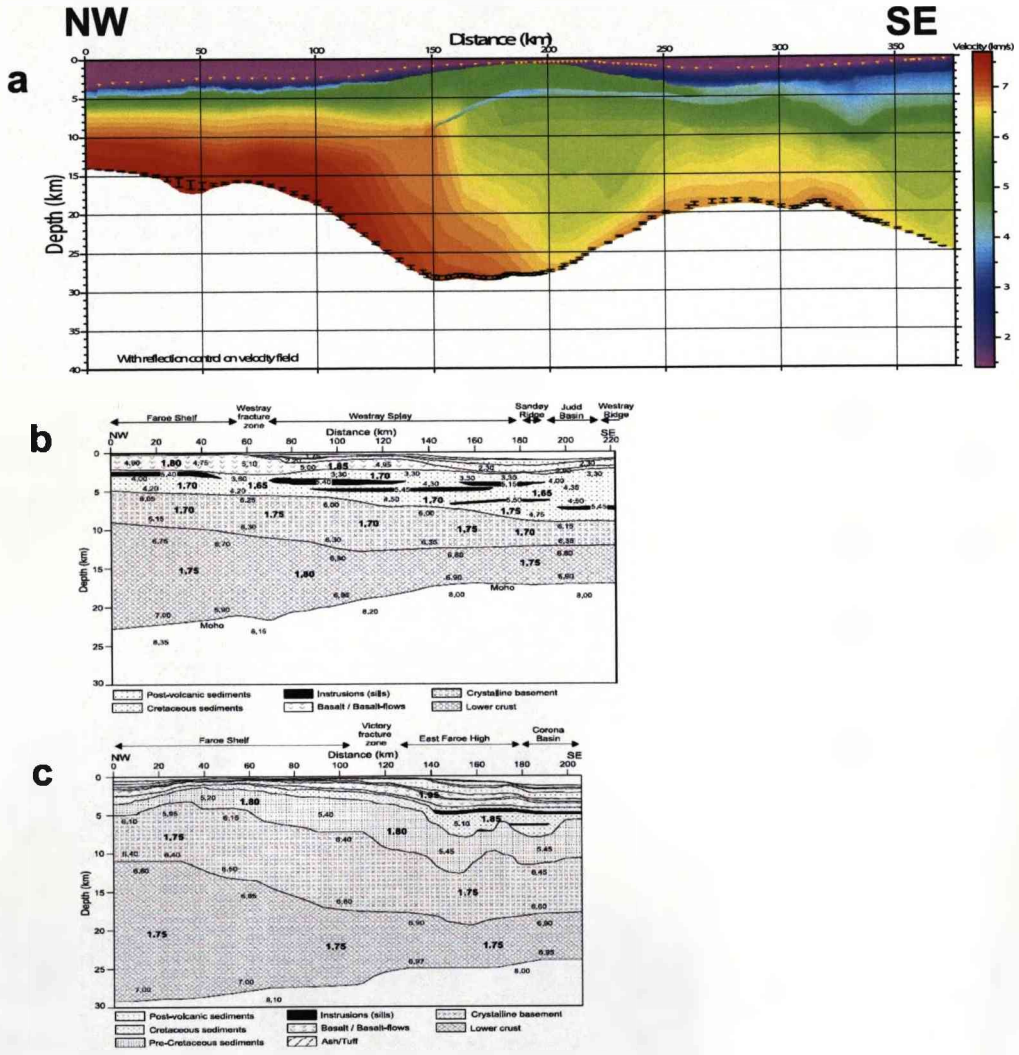

Figure 3.3: Compilation of published wide-angle seismic profiles and interpretations in the FSB.(**a**) iSIMM (Roberts, 2007); (**b**) Raum profile 2 (Raum et al., 2005); (**c**) Raum profile 1 (Raum et al., 2005). Continued on next page.

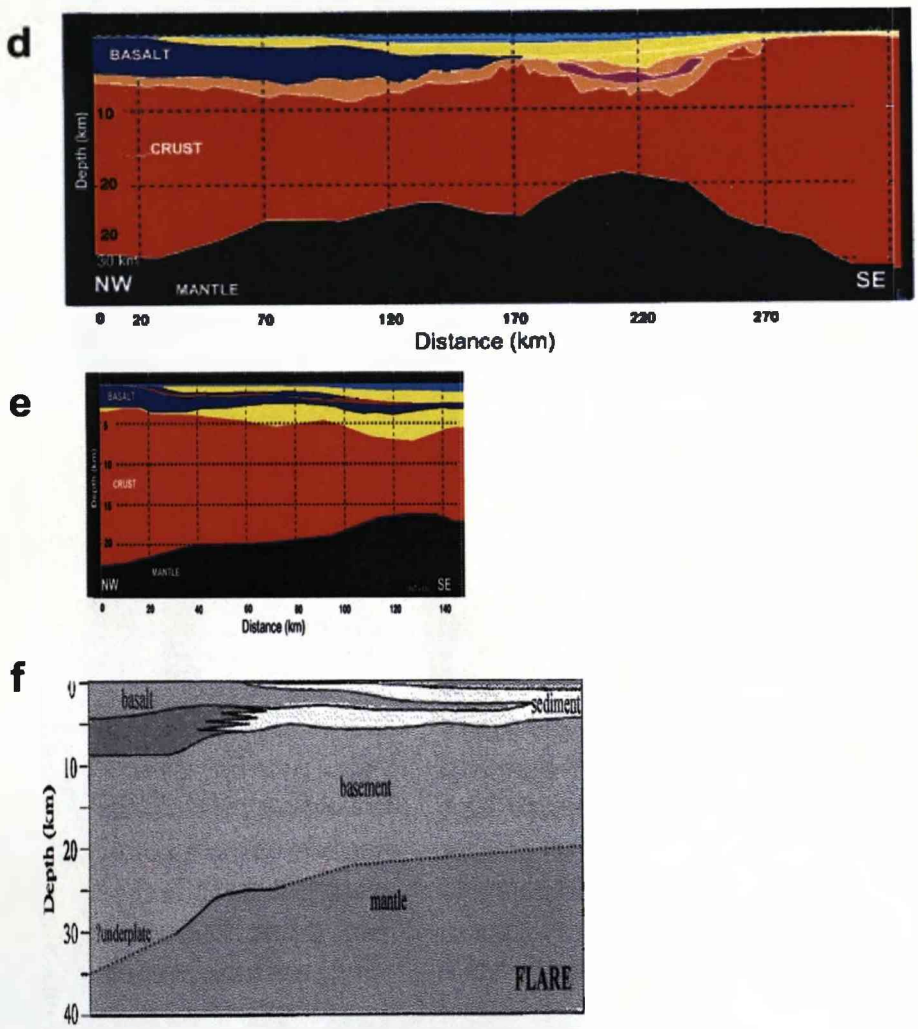

Figure 3.3: ..continued from previous page. Compilation of published wide-angle seismic profiles and interpretations in the FSB. (**d**) FAST (Smallwood et al., 2001); (**e**) OF94-23 (Smallwood et al., 2001); (**f**) FLARE (Richardson et al., 1999).

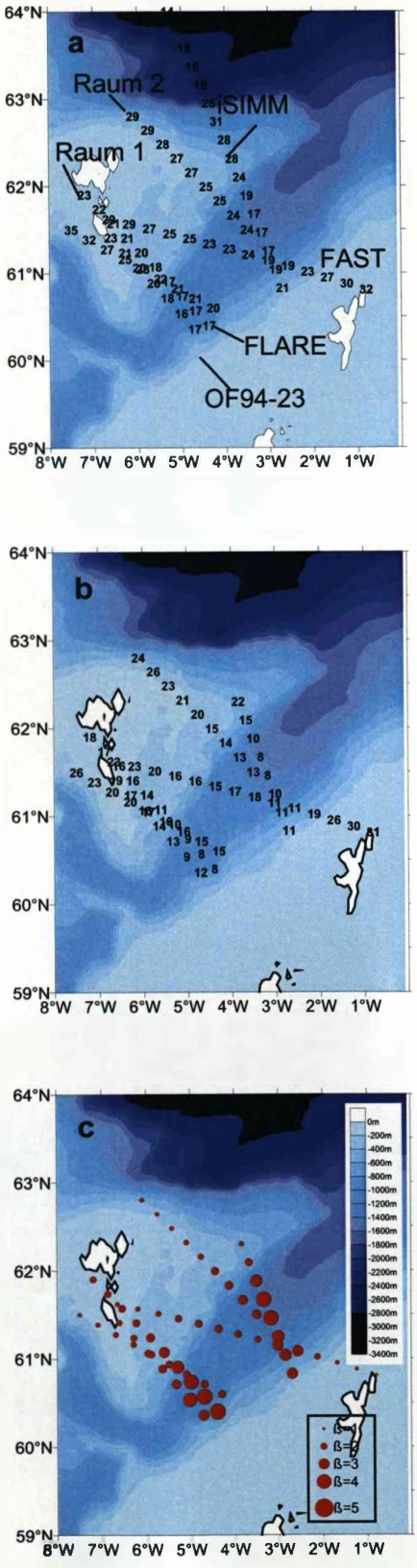

Figure 3.4: Crustal thickness in the FSB from seismic refraction profiles. (**a**) interpreted Moho depth and (**b**) crustal thickness (in km) respectively at 25km spacing along the profiles shown in Figure 3.3. Crustal thickness is defined as Top basement to Moho; Top basement depth taken from interpretations in Figure 3.3 except the iSIMM line, where Top basement is taken from a coincident seismic reflection profile (Figure 3.7 **j**). Values are superimposed on the present day bathymetry. (**c**) shows apparent whole crustal stretching factor β, at 25km spacing along the profiles. Stretching factors are calculated assuming an initially uniform crustal thickness of 35km and superimposed on the present day bathymetry.

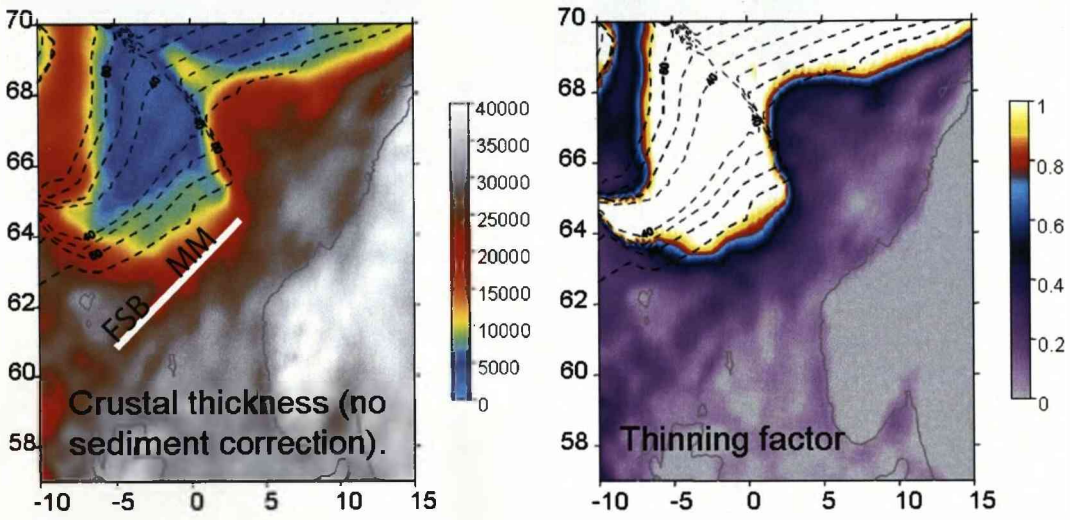

Figure 3.5: (**a**) Crustal thickness and (**b**) continental lithosphere thinning factor predicted by gravity inversion incorporating a lithosphere thermal gravity anomaly correction (Greenhalgh and Kusznir, 2007). Predicted ocean-continent transition location corresponds to thinning factor = 1. FSB = Faroes-Shetland Basin, MM = Møre Margin. The axis of the Faroes-Shetland Basin and its NE continuation onto the Møre margin are shown (white line). Ocean isochrons from (Muller et al., 1997) are superimposed (black dashed lines). The lithosphere thermal gravity anomaly correction assumes continental breakup at 55 Ma; ocean isochrons younger than 45 Ma only are used to condition the oceanic lithosphere thermal model. Gravity inversion assumes zero sediment thickness; thinning factors are consequentially lower bounds. Reference crustal thickness used in gravity inversion = 32.5 km. From N. J. Kusznir (pers. comm.)

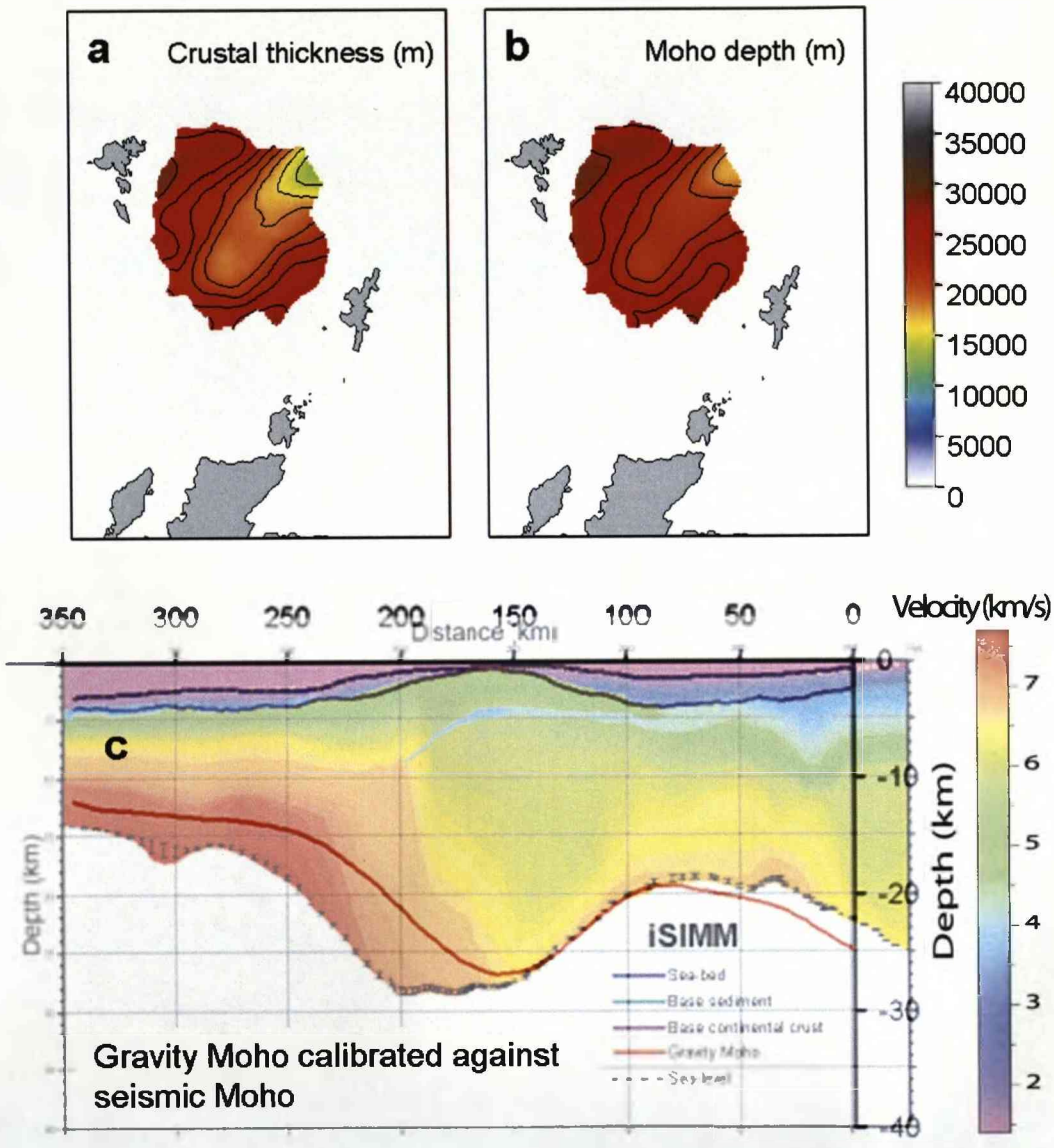

Figure 3.6: Crustal thickness and Moho depth from gravity inversion (in m), corrected for sediments above the basalt. (**a**) Crustal thickness and (**b**) Moho depth over the study area. The lithosphere thermal gravity anomaly correction assumes thinning event at 55 Ma. Gravity inversion corrects for sediments above Top Basalt (see Figure 3.8 for sediment distribution) and crustal thickness refers to Top Basalt - Moho thickness. Top basement is up to 7km beneath Top Basalt (see Figure 3.8), consequently crustal basement thicknesses are lower than suggested here. Reference crustal thickness used in gravity inversion = 32.5 km. From N. J. Kusznir (pers. comm). (**c**) Gravity-derived Moho compared to seismic refraction P-wave velocity model (Roberts, 2007) for the iSIMM line.

lower bounds.

When corrections for the post-Basalt sediment are also included in gravity inversion (Figure 3.6), the gravity inversion method predicts that the Moho has relief of 6-8km from the flanks to the centre of the basin, and crustal thickness (Top Basalt to Moho) in the axis decreases from around 22km in the southern axis to 14km in the northern part of the study area. The gravity inversion predicts a Moho depth similar to that derived using seismic refraction methods (Figure 3.6c). If the crustal thickness is defined as Top basement to Moho, the crustal thicknesses has a minimum thickness of 10-12km along the iSIMM line, corresponding to whole crustal thinning factors of between two and three in the axis of the basin.

3.4 Dataset used in this analysis

3.4.1 Seismic reflection data

A series of eight dip and two strike seismic profiles across the FSB are shown in Figure 3.7. Lines A-I are composite seismic profiles provided by StatoilHydro from a regional dataset. A series of ten regional horizons which could be correlated across the basin, were interpreted using available well ties by the Faroes team at StatoilHydro. Sub-basalt horizons were identified where possible using a high-frequency processing technique (Gallagher and Dromgoole, 2007) or inferred using gravity modelling. The interpreted profiles were depth-converted using interval velocities calibrated from well ties and are assumed to be constant for each layer. The sub-basalt horizon picks and velocities are uncalibrated by well data and therefore subject to higher uncertainty

Figure 3.7 *(following page)*: Regional composite seismic profiles used in this study. The Top Basalt reflector can be seen as a strong unbroken reflector, the basalt pinches out towards the SE of the basin. In the SE (West of Shetland area) side of the basin large fault blocks are imaged which are infilled with Devonian-Present Day sediments. A series of sills can be seen under the axis of the basin as strong discontinuous reflectors. The East Faroes high shows evidence for minor reverse faulting, which has influenced the architecture of the Eocene and younger stratigraphy. The strike lines G and H show the locations of transfer zones. Line locations are shown as inset

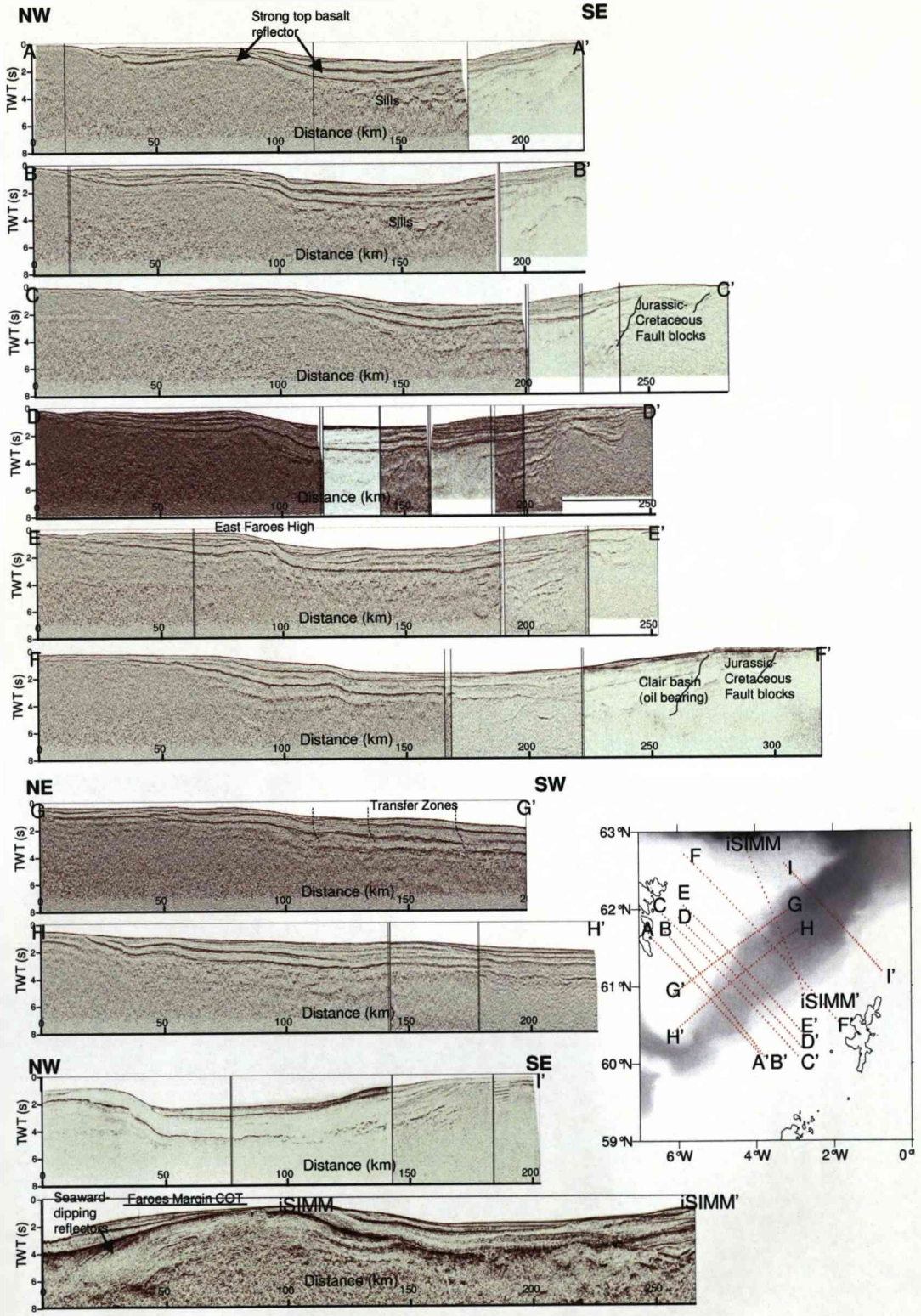
NW
SE
Strong top basalt reflector
A
A'
Sills
TWT (s)
Distance (km)
B
B'
C
C'
Jurassic-Cretaceous Fault blocks
D
D'
East Faroes High
E
E'
F
F'
Clair basin (oil bearing)
NE
SW
G
G'
Transfer Zones
H
H'
I
I'
Seaward-dipping reflectors
Faroes Margin COT
iSIMM
iSIMM'
63°N
62°N
61°N
60°N
59°N
6°W
4°W
2°W
0°

than picks in the eastern part of the basin where most of the wells have been drilled. The iSIMM profile was acquired and processed by Western Geco Q-streamer data as part of the iSIMM (integrated seismic imaging and modelling of margins) project, a joint industry-academia project, in 2002 (e.g. White et al., 2008). Seismic interpretation on the iSIMM profile was carried out using available well ties and correlated to the StatoilHydro dataset where reflectors were unclear. The mid-Eocene reflector was not interpreted on the iSIMM line as it is unclear. The interpreted iSIMM profile was depth-converted using the same interval velocities as for the other seismic profiles. Figure 3.8 shows the ten depth-converted profiles.

3.4.2 Well-log maps

Well-logs and reports from 42 wells were used to produce simplified well-logs (Figure 3.9) and well-log maps (Figure 3.10). Interpretive or descriptive information was assimilated for up to 33 time intervals in each well. Figure 3.11 illustrates a simplified tectono-stratigraphy for the Late Cretaceous-Early Eocene of the FSB. Where the stratigraphy used in the well reports was different to that in Figure 3.11, the relative ages of units were correlated using other published timescales (Mitchell et al., 1993; Turner and Scrutton, 1993; Clift and Turner, 1998; Lamers and Carmichael, 1999; Naylor et al., 1999; Smallwood and Gill, 2002).

For each stratigraphic unit sampled at a well, the well-log or report was used to assign a symbol illustrating the interpreted environmental conditions if available, or the lithology. Figure 3.10 show a series of well-log maps made for eight horizons that illustrate the basin history; these are discussed in the next section in relation to the overview of

Figure 3.8 *(following page)*: Interpreted and depth-converted profiles used in this study. For locations see Figure 3.1. All profiles are equivalent to the profiles in Figure 3.7 except the iSIMM line which was only depth-converted in the FSB, and not across the Faroes Margin. Unit age, initial porosity, decompaction constant, grain density, density* and seismic velocity for each layer listed in table. Density* indicates the in-situ (compacted) density for each layer, corresponding to the density calculated for a location 150km along profile A. For explanation of the effect of compaction on the density on sediments see section 4.3.3.

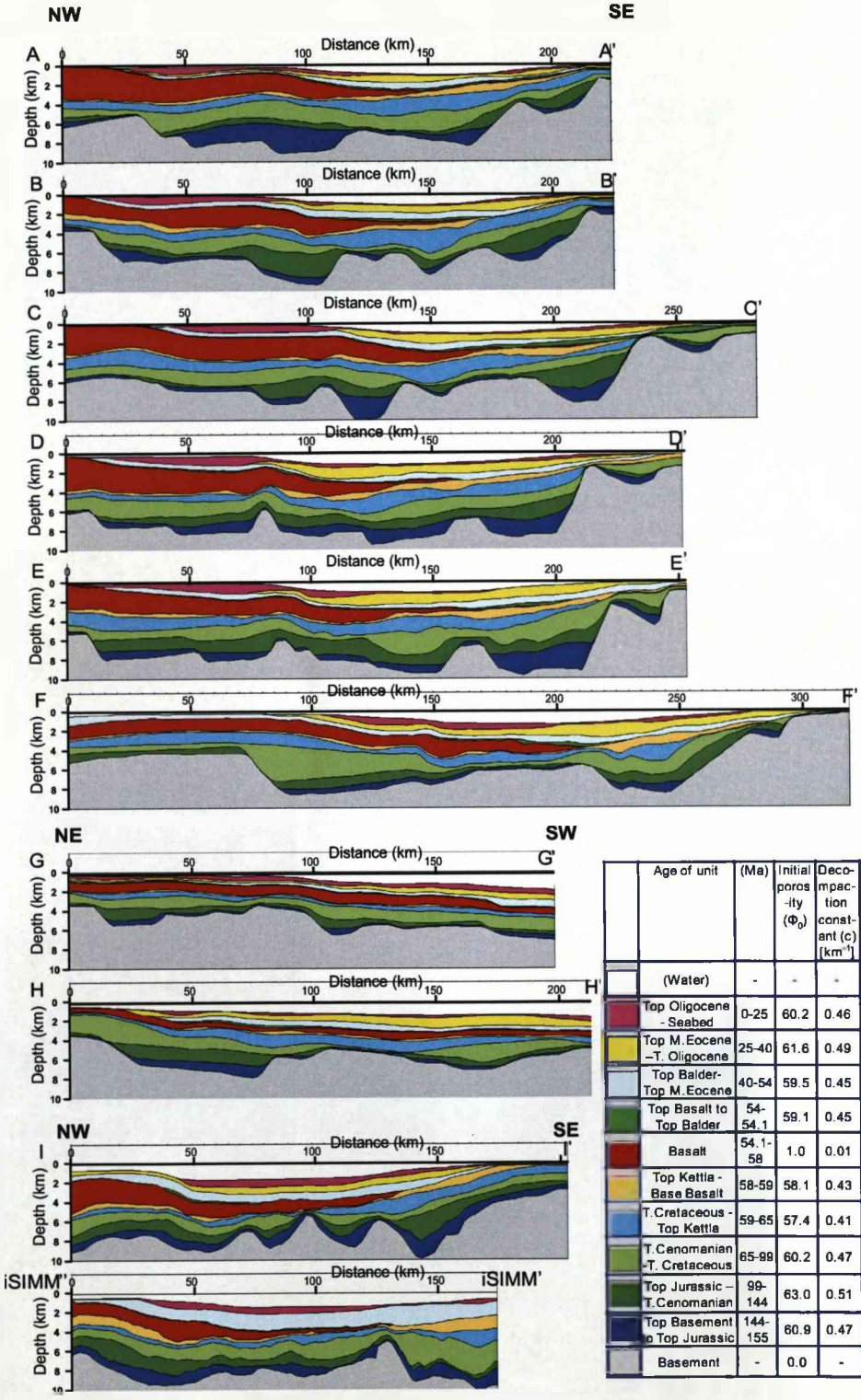

	Age of unit	(Ma)	Initial poros-ity (Φ_0)	Deco-mpac-tion const-ant (c) [km^{-1}]	Grain densi-ty (ρ_{grain}) [kgm^{-3}]	Densi-ty* (ρ_{sed}) [kgm^{-3}]	Seism-ic veloci-ty [ms^{-1}]
	(Water)	-	-	-	1000	1000	1490
	Top Oligocene - Seabed	0-25	60.2	0.46	2710	1120	2250
	Top M.Eocene –T. Oligocene	25-40	61.6	0.49	2710	1360	2250
	Top Balder-Top M.Eocene	40-54	59.5	0.45	2700	1720	2250
	Top Basalt to Top Balder	54-54.1	59.1	0.45	2700	1900	4500
	Basalt	54.1-58	1.0	0.01	2800	2770	3000
	Top Kettla - Base Basalt	58-59	58.1	0.43	2700	2030	3000
	T.Cretaceous - Top Kettla	59-65	57.4	0.41	2690	2230	3000
	T.Cenomanian -T. Cretaceous	65-99	60.2	0.47	2700	2530	3000
	Top Jurassic – T.Cenomanian	99-144	63.0	0.51	2720	2640	3500
	Top Basement to Top Jurassic	144-155	60.9	0.47	2710	2630	4500
	Basement	-	0.0	-	-	2850	-

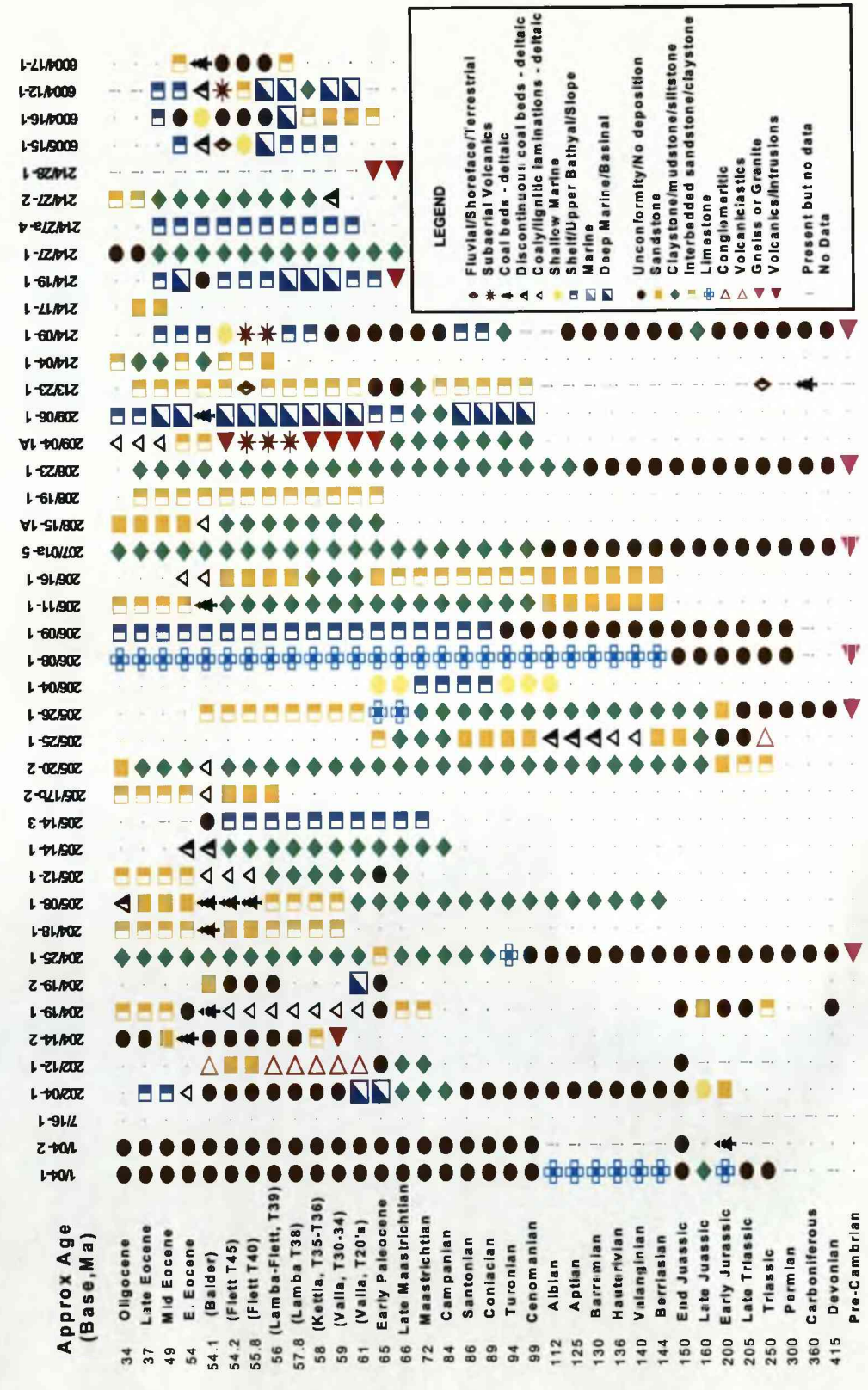

Figure 3.9: Simplified well-logs for wells in the FSB. For well locations see Figure 3.1

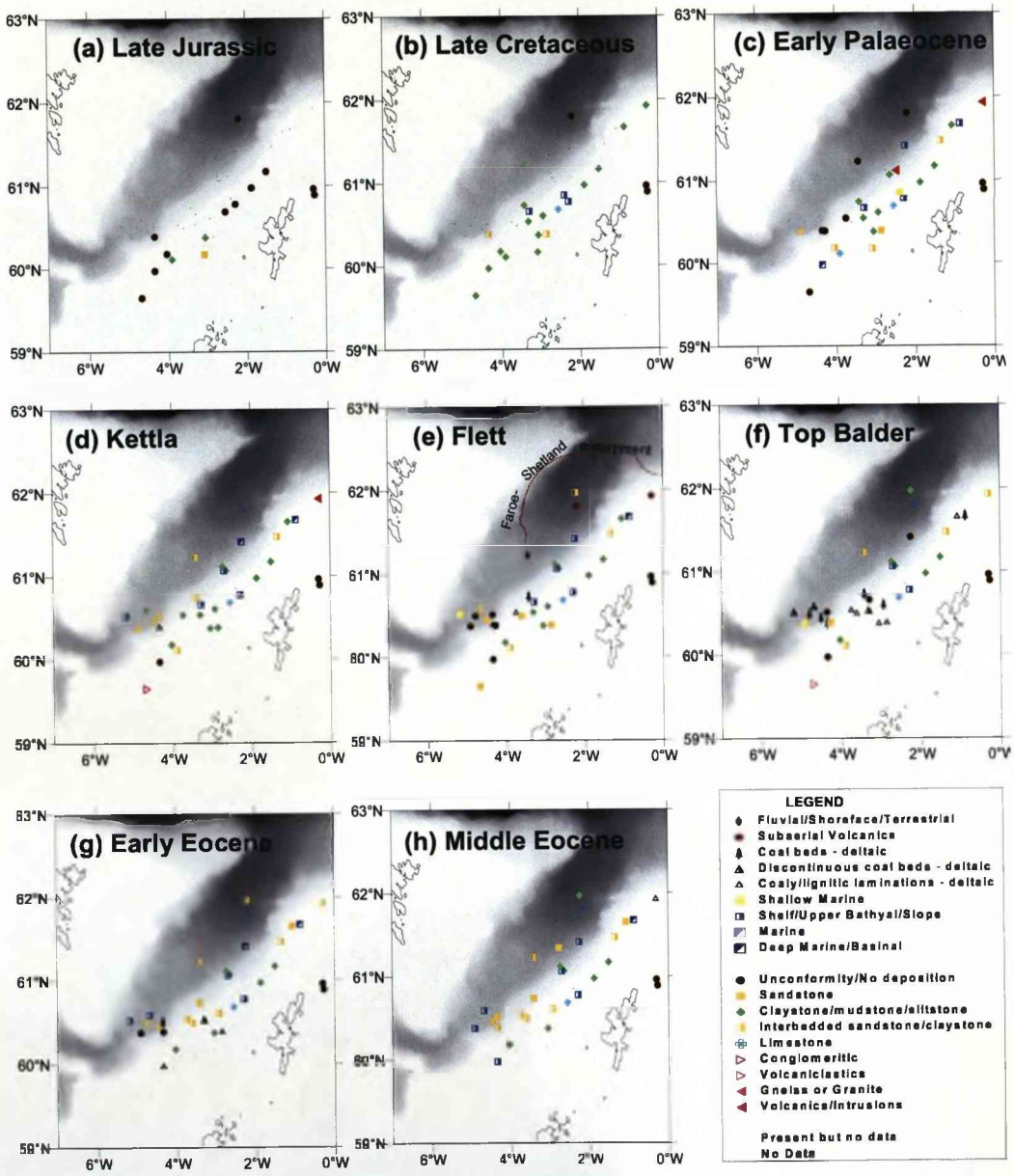

Figure 3.10: Series of well-log maps for key paleogeographic horizons in the FSB. Interpretative or descriptive symbols are plotted onto present day bathymetry. In the Late Jurassic (**a**) the basin was characterised by a series of subaerial fault block crests and marine basins, by Late Cretaceous times (**b**) the basin was fully marine. A number of minor unconformity surfaces formed in the Early Palaoecene (**c**), but by Kettla times (**d**) the basin had returned to deep marine. Uplift throughout the Palaeocene caused the basin to re-emerge; the tectonic uplift maxima occurred during Flett (**e**) times (Champion et al., 2008), indicated by an angular unconformity in the southern basin axis. The Faroe-Shetland escarpment represents a Flett-age palaeoshoreline. By Balder (**f**) times the south of the basin was relatively flat-lying and close to sea-level. Rapid subsidence of the basin occurred through the Eocene (**g-h**).

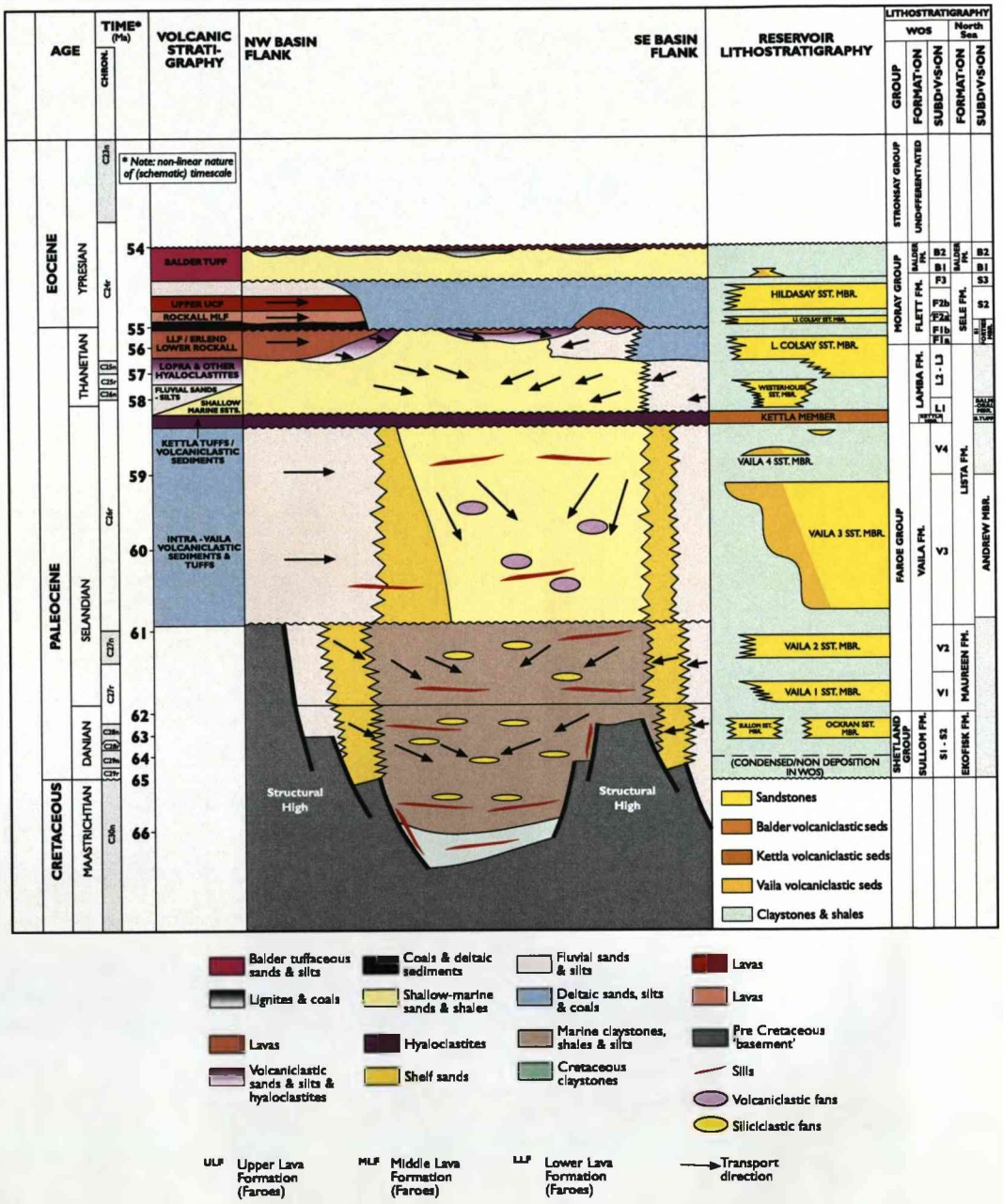

Figure 3.11: Volcanic- litho- and sequence stratigraphy for the Late Cretaceous to Early Eocene of the FSB area. Adapted from Gallagher and Dromgoole (2007).

the geological history of the basin.

3.5 Geological history of the basin

Palaeozoic and Mesozoic rifting

The oldest dated sediments in the basin are found in the Clair sub-basin (shown on profile F), which hosts an oil-bearing reservoir of aeolian and fluvial clastic sediments of Devonian age (Earle et al., 1989). Subsequent Permo-Triassic extension events created further continental clastic filled sub-basins as a series of half graben separated by NW-SE trending transfer faults (Booth et al., 1993). Extension continued through the early Jurassic, although a major mid-Jurassic unconformity masks details of this event (Booth et al., 1993). Rising relative sea-levels allowed organic-rich Kimmeridgian sediments to deposit in restricted marine sub-basins between subaerial ridges. The Kimmeridgian sediments provide a source for hydrocarbon plays in the FSB (Dean et al., 1999). Significant rifting occurred along the entire Atlantic margin in a zone which extends from the Vøring and Møre basins, through the FSB and the Rockall Trough at Late Jurassic to Early Cretaceous times (Haszeldine et al., 1987; Doré et al., 1999; Roberts et al., 1999). The Late Jurassic and mid-Cretaceous horizons in the FSB are cut by large faults which generally trend NE-SW (Figures 3.2, 3.7 and 3.8), representing a series of stretching events which probably continued throughout most of the Cretaceous (Dean et al., 1999; Doré et al., 1999; Hooper and Walker, 2002). Late Jurassic and Early Cretaceous rifting induced differential subsidence which created a dramatic fault block topography including subaerial Rona, Corona and Westray ridges (Dean et al., 1999) at this time. Post-rift thermal subsidence accompanied continued extension on the major faults (Turner and Scrutton, 1993; Dean et al., 1999) and the basin became deeper and wider throughout the Cretaceous period. This general deepening trend is apparent if the well-log maps of the Late Jurassic (Figure 3.10a) and the Late Cretaceous (Figure 3.10b) horizons are compared. Late Cretaceous sedimentation was dominated by marine shales and siltstones, with the absence of coarse clastics and is thought to indicate tectonic quiescence (Mitchell et al., 1993).

Early Palaeocene - NAIP uplift and clastic terriginous input

The first of two phases of North Atlantic Igneous Province (NAIP) volcanism (~62-59Ma; (Saunders et al., 1997) has been related to protracted uplift of the whole North Atlantic area (White and McKenzie, 1989), resulting in an influx into the basin of clastic terriginous material derived from both southeasterly (Shetland) and northwesterly (Greenland) sources (Knott et al., 1993; Mitchell et al., 1993; Ebdon et al., 1995; Lamers and Carmichael, 1999; Jolley and Widdowson, 2005). The Early Palaeocene Vaila Formation deepwater fan and channel sands comprise the major reservoir rocks of the Foinaven and Schiehallion oil fields in the Judd sub-basin (Cooper et al., 1999; Lamers and Carmichael, 1999; Leach et al., 1999). Sedimentation was accompanied by minor faulting and folding (e.g. see Figure 3.12a-d) and thin ashes from distant NAIP volcanism. On a number of the well-logs (Figure 3.9), particularly those on Mesozoic fault block crests, Late Cretaceous-Early Palaeocene unconformity surfaces are indicated. These unconformities may be erosional surfaces caused by footwall uplift related to continued extension on Mesozoic faults or caused by uplift related to the first phase of NAIP volcanism. There is no evidence in the well-logs that these unconformity surfaces were non-marine.

The Kettla Tuff, a regionally prominent seismic reflector, marks the end of the first phase of North Atlantic volcanism. Kettla-age sediments (see Figure 3.10d for well-log map) are thought to have been deposited in a deep-marine environment in the FSB (Lamers and Carmichael, 1999). The Kettla horizon marks a change in the basin's evolution, from aggradational to progradational marine sedimentation (Naylor et al., 1999), and sediment provenance shifted from Mesozoic to Carboniferous sources (Ebdon et al., 1995) at this time. Smallwood and Gill (2002) noted that the Kettla Tuff reflector is sparsely offset by faulting (see Figures 3.12a-d) stating that it 'appears to represent the end of rifting in the basin'.

Basalts and progradational sedimentation: basin infill and uplift

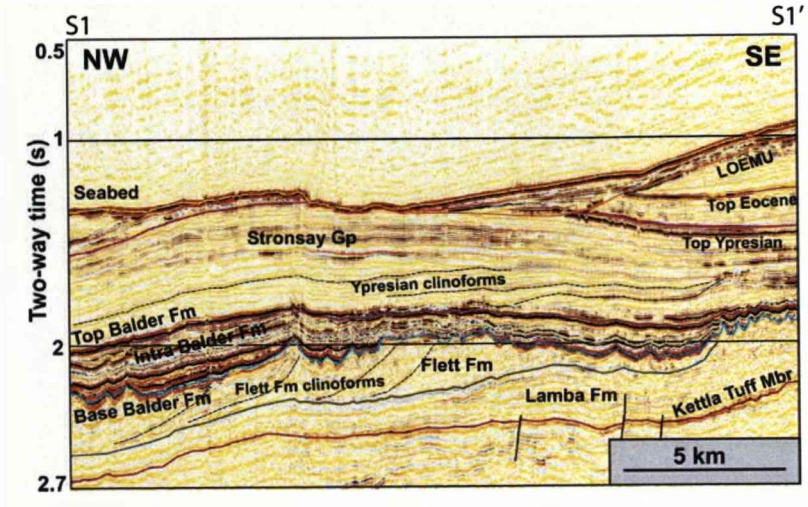

(a)

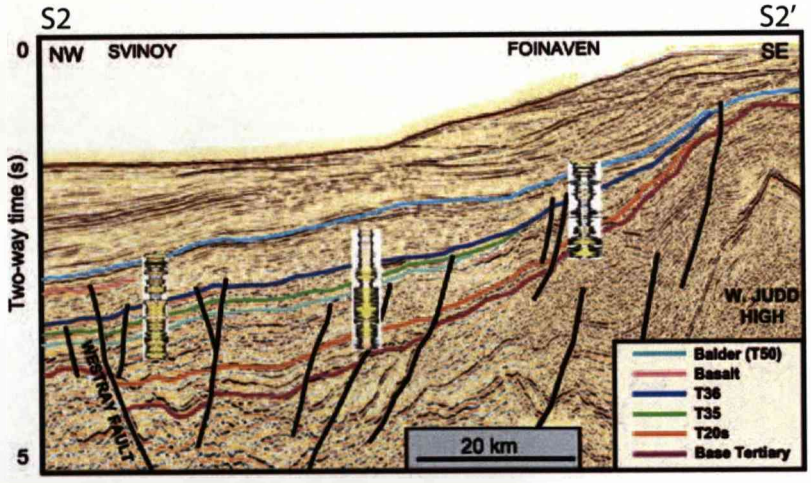

(b)

Figure 3.12: Seismic profiles through the Palaeocene section. (**a**) illustrates Palaeocene stratigraphy in the FSB (Smallwood and Gill, 2002). Relief on the Base Balder unconformity surface due to cut down from fluvial system. The unconformity was rapidly submerged as accommodation space for Balder and Ypresian sediments was created. (**b**) and (**c**) Interpreted profiles from (Smallwood and Kirk, 2005), showing that the extension accommodated by faulting decreases through the Palaeocene. Extension of the Base Tertiary horizon is estimated to be less than 10 % ; seismically observable offset of the Balder Formation is extremely rare and is estimated to be less than 1 %. Note also sills in the Cretaceous section in **c**. (**d**) Interpreted seismic profile from Gallagher and Dromgoole (2007) showing Top Basalt and sub-basalt layers. Note that Top Basalt and younger layers are only very sparsely offset. See Figure 3.2 for locations of profiles.

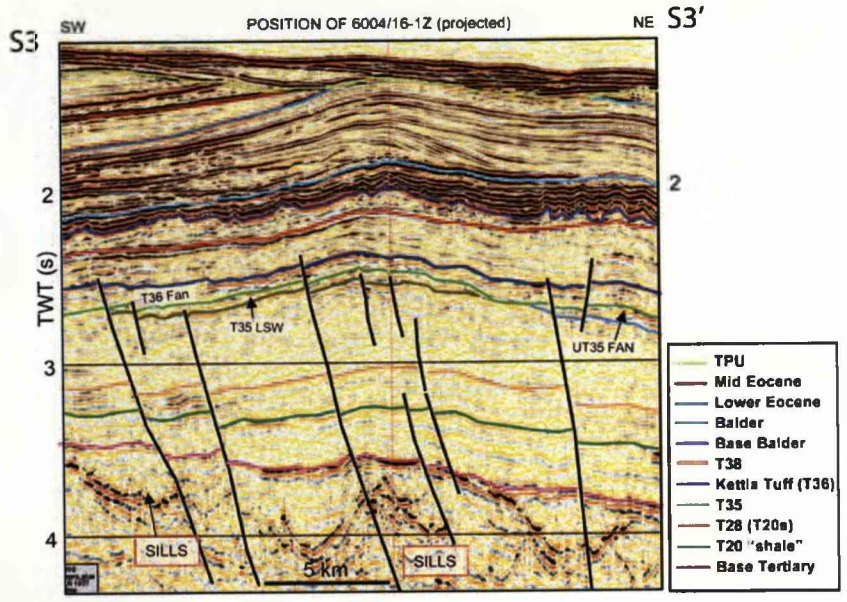

(c)

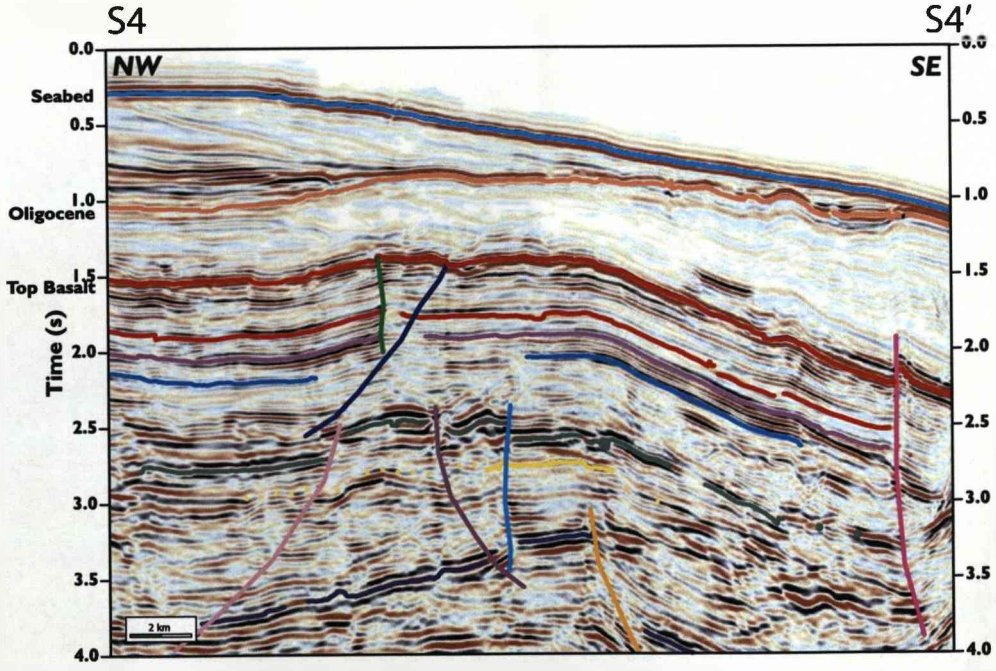

(d)

Figure 3.12: Caption on previous page.

The second phase of NAIP volcanism at 56-54Ma was associated with continental breakup and seafloor spreading initiation along the North Atlantic margins. Voluminous extrusive volcanism at the Faroes margin (Rasmussen and Noe-Nygaard, 1970; Waagstein, 1988) covered the western side of the FSB and basalt flows are interfingered with progradational Lamba and Flett Formation sediments in the basin. The Faroes Lava Group has only been sampled at outcrops on the Faroe Islands, in the deep drillhole (Lopra) on Suderøy (the southernmost of the Faroe Islands), and by a few exploration wells, and are geomagnetically dated between Chrons C26r and C24r (Riisager et al., 2002; Abrahamsen, 2006). The environment of eruption of the Lava Group has been deduced from these data points, reconstruction of seismic data and inferences from palaynological data. At the site of the Lopra drillhole, the thoeillitic, Lopra hyaloclastites are overlain by the Lower Basalt Formation which were erupted as sheet-like flows subaerially or into estuaries or marginal lagoons. Laterally discontinuous coals and reddened tops indicate the existence of minor swamps between flows (Ellis et al., 2002). At the top of the Lower Basalt Formation, a hiatus in volcanic activity is marked by drainage patterns in the unconformity surface and a 10-20m thick coal layer in the Faroe Islands (Naylor et al., 1999). Palynological data suggest that the Lopra hyaloclastites are contemporaneous with the Lamba Formation (Jolley and Widdowson, 2005), the first of two major progradational packages which record a sequence of increasing restriction (Mudge and Bujak, 2001). 500m-high clinoforms within the Lamba Formation (Smallwood and Gill 2002; Figure 3.12a) in the southern part of the basin indicate the minimum palaeobathymetry at the slope front during progradational infilling of the basin at this time.

The MORB-like Middle and Upper Lava Formations were erupted during Chron 24r (Riisager et al., 2002; Abrahamsen, 2006), and form the Seaward Dipping Reflectors (SDRs) on the Faroes Margin. On the Faroe Islands, lavas are interbedded with conglomeritic and terriginous material, the architecture of which was probably influenced by active transfer zones in the region (Rumph et al., 1993). Palynological analysis on Upper Lava Formation samples from the Faroe Islands suggests that there was less

than 300m of topographic relief in the region at this time, with some areas showing evidence of marine or estuarine influences (Ellis et al., 2002). If seismic profiles from the southern part of the basin are re-datumed to the top of the Upper Lava Series, progradational and sheet-like flows are reconstructed, suggesting that the palaeogeography was of subaerial low relief close to sea-level (Ellis et al., 2002). In the north of the basin, the Faroe-Shetland Escarpment (Figure 3.10e) represents the palaeocoastline where subaerial Middle Lava Series lavas prograded into relatively deep water as hyaloclastite breccia (Kiørboe, 1999; Naylor et al., 1999).

The Flett Formation, the second major progradational package, is contemporaneous with Middle and Upper Formation Lavas. Southwest of the Clair transfer zone (see Figure 3.2 for location), prograding deltas infilled much of the remaining bathymetry. Flett-age clinoforms suggest a minimum bathymetry of 300m at the slope front (Smallwood and Gill 2002; Figure 3.12a) in the southern part of the basin. The infilling of local depressions appears to have been contemporaneous with an unconformity in the south of the basin where Flett and Lamba Formations are absent (Naylor et al., 1999; Smallwood and Gill, 2002; Smallwood and Kirk, 2005; Champion et al., 2008). In Q204 (for location see Figure 3.2), a series of northwards-draining channels are imaged on the angular unconformity surface indicating topographic relief of at least 500m (Smallwood and Gill, 2002; Champion et al., 2008, Figure 3.13). Above the unconformity surface in Q204, the oldest Flett is characterised by delta top and coastal plain sediments, coal and high levels of recovered pollen and spores, which indicate subsidence and a return to sea-level. Champion et al. (2008) demonstrate that the Q204 area experienced tectonic uplift and subsequent subsidence at least 490m between Lamba and Top Balder times, peaking at Lower Flett times (Figure 3.14).

Seismic mapping and direct sampling of Upper Flett and Upper Lava Formation suggest that the palaeogeography of the FSB area at the time of deposition was close to sea-level, particularly in the southern part of the basin (see Figure 3.10e). However, there is evidence for an approximately northeasterly-directed palaeoslope: In the south is a subaerial unconformity surface, coastal plain and lagoonal sediments, local depressions

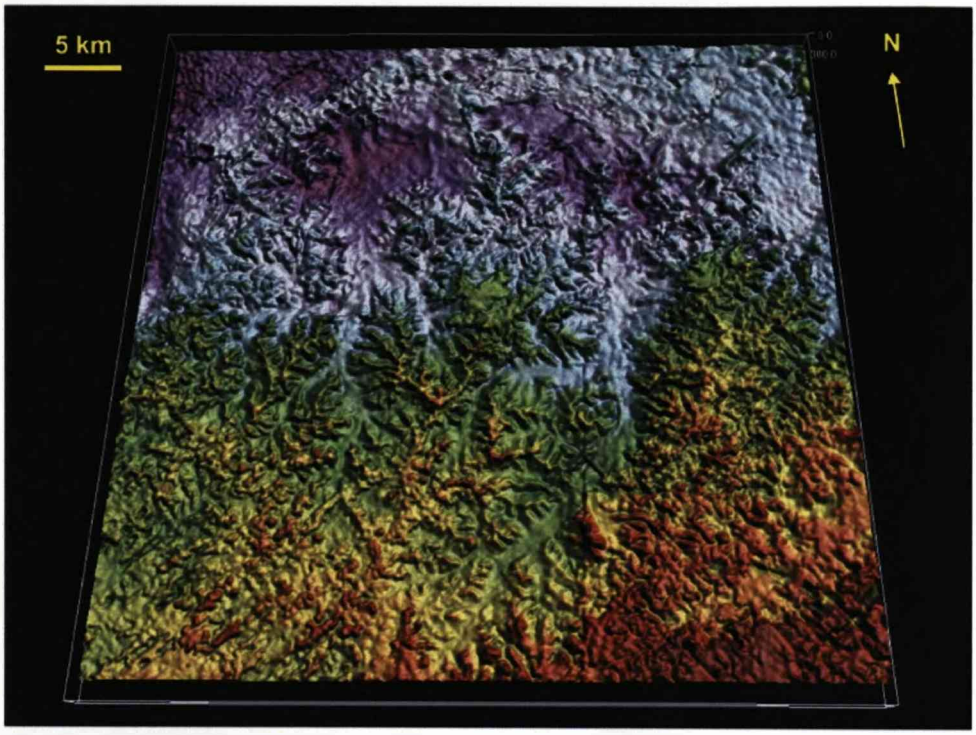

Figure 3.13: 3D view of Balder Formation isochore in Quad 204, showing the valley network incised on the Balder unconformity surface. Red (thin) to blue (thick) colours show Balder Formation thickness - range from 20-350m. From Smallwood and Gill (2002).

which were being infilled by prograding deltas, and lavas were erupted as sheet-like subaerial flows; towards the north the lava flows entered relatively deep water at the Faroe-Shetland Escarpment, although the well-logs show that fault blocks crests in the centre of the basin were subaerial at this time, possibly as small islands. The Middle and Upper Lava Series thin towards the southwest, also suggesting a northeasterly palaeoslope during emplacement (Ellis et al., 2002).

The Balder Tuff

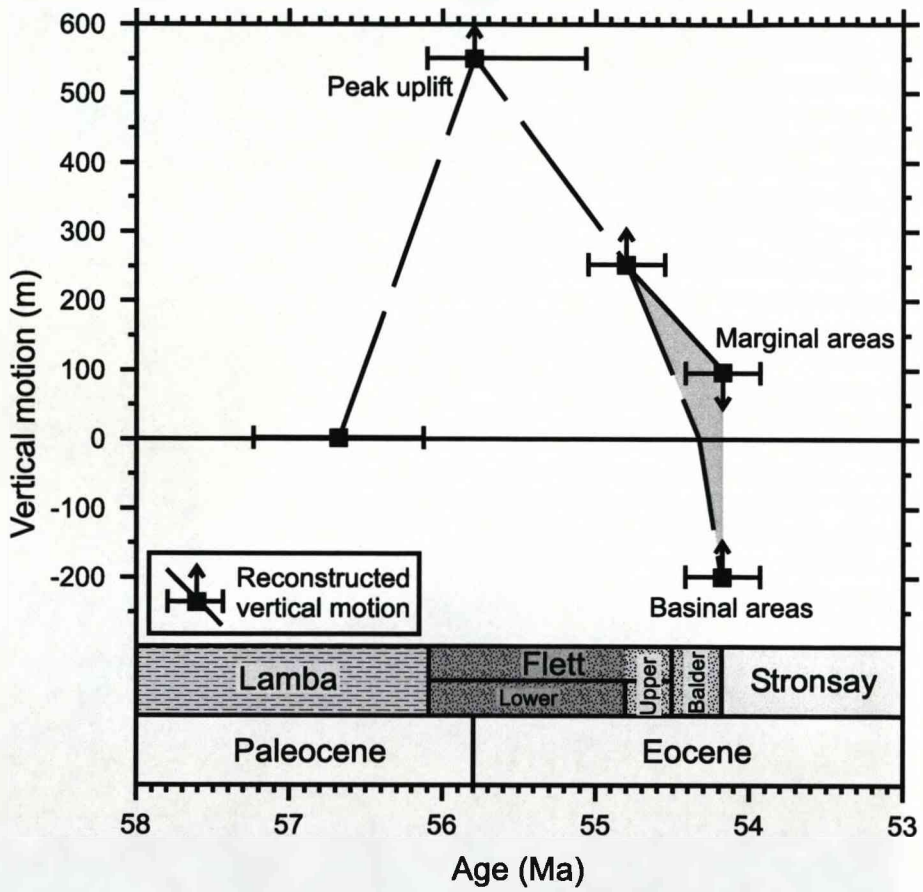

Figure 3.14: Relative vertical motion (equivalent to water-loaded tectonic subsidence) history of the Quad 204 area, from (Champion et al., 2008).

The Balder Tuff marks the last major pyroclastic event associated with the North Atlantic Igneous Province and the cessation of explosive volcanic activity (c.54Ma) associated with the onset of seafloor spreading at the Ægir Ridge at end Palaeocene times (Naylor et al., 1999). Concurrent infilling, volcanic addition and a number of uplift-erosion and subsidence cycles caused much of the basin to be low-lying or shallow marine by Top Balder (Ebdon et al., 1995; Lamers and Carmichael, 1999; Naylor et al., 1999; Mudge and Bujak, 2001; Smallwood and Gill, 2002, Figure 3.10f). Emergence is manifested in sediments by delta top sediments including coal beds or lignitic debris, fluvial deposits, and oxidised paleosols. Palynological evidence shows floral and faunal assemblages becoming increasingly restricted, particularly in the southwest of the basin, at upper Thanetian to lower Ypresian times (Mudge and Bujak, 2001). The flat, low-lying to paralic palaeogeography of the Top Balder horizon makes it a useful and important horizon which can be used to test models of the formation of the basin.

Palaeocene intrusive igneous activity in the FSB

A number of volcanic centres have been identified in the FSB. Most of the igneous activity is Late Palaeocene in age, suggesting that melting occurred beneath the FSB synchronous with continental breakup and the onset of seafloor spreading in the Atlantic. The Erlend complex (see Figure 3.2), a Palaeocene volcano of the same age as the Lower Formation Lavas, is onlapped by the Balder Formation (Gatliff et al., 1984; Jolley and Bell, 2002). Small Palaeocene eruptive centres and a sill complex (dated, where possible, c. 53-55Ma) have been imaged and sampled in wells in the FSB (Hitchen and Ritchie, 1993; Ritchie et al., 1999; Bell and Butcher, 2002; Trude et al., 2003). These sills and volcanic centres are therefore the same age as the Faroes Lava Series. No thick layers of underplate or highly intruded lower crust has been imaged underneath the basin, although it is possible that seismic imaging may fail to resolve a small thickness of volcanic addition.

Post-Atlantic-breakup subsidence

Following the onset on seafloor spreading at the Møre and Faroes margins, the Eocene saw a rapid return to marine conditions in the FSB (Lamers and Carmichael, 1999; Mudge and Bujak, 2001; Sorensen, 2003; Figures 3.10g-h). Coaly or lignitic layers persist into the earliest Eocene on the flanks of the basin, although clinoforms of height 250m (indicating minimum palaeobathymetry at the slope front) are found in the Stronstray group (Ypresian) in the southern axis of the basin (Smallwood and Gill, 2002). The Early to Middle Eocene sedimentary package is up to 1km thick (e.g. Figure 3.8), illustrating relatively rapid creation of accommodation space in the Eocene. Well-log maps (Figure 3.10g-h) show that deep marine conditions were quickly re-established across the basin, and deepwater conditions prevail to the present day.

The NE Atlantic margin has experienced a number of SE-directed compression episodes since the Early Eocene which have been attributed to ridge push forces and reorganisation of plate boundaries in the Atlantic (Boldreel and Andersen, 1998). This compression is responsible for the minor reverse faulting, (e.g. in the basalt close to the East Faroes High: Figures 3.2 and 3.7) and the growth of anticlines (Ritchie et al., 2003). The Lava Formations on the Faroe Islands, deposited below 300m (Ellis et al., 2005), now reach up to 882m, although the precise timing of their uplift is unclear. Sediment deposition in the basin continues to the present day, although it remains under-filled and has served as an important oceanographic gateway since the Oligocene (Davies et al., 2001).

3.6 Summary

- The Faroe-Shetland basin has experienced multiple rifting events since at least Devonian times. The large fault blocks which are well imaged on the Shetland side of the basin are predominantly a result of Late Jurassic - Early Cretaceous rifting in the basin.

- Regional uplift associated with activity within the British Tertiary Igneous Province caused a thick Palaeocene sequence of progradatonal and aggradational sediments

to be deposited in the basin. During the Late Palaeocene, syn-breakup basalts from the adjacent Faroes margin covered approximately half of the basin. By end Palaeocene times the southern part of the basin was subaerial-low lying marine, becoming increasingly marine further north. This palaeobathymetric constraint is very useful for calculating tectonic subsidence over a large area, and is used in subsequent analysis.

- Marine conditions rapidly returned to the basin in the Eocene, and prevail to the present day.

- Crustal thickness estimates for the FSB, determined from seismic and gravity analysis, show that the crust beneath the FSB has been thinned by up to a factor of three.

In the next chapter the magnitude of extension and thinning in the Palaeocene is quantified, and in Chapters 5 and 6 this information is compared to models of formation for the FSB.

Chapter 4

Stretching and subsidence in the Faroe-Shetland basin

4.1 Introduction

In this chapter, the upper crustal extension and tectonic subsidence history of the Faroe-Shetland basin is quantified. It is assumed that extension of the continental lithosphere is accommodated by brittle faulting in the upper crust, and more distributed strain in the lower crust and lithospheric mantle. The magnitude of upper crustal extension in the basin is quantified by evaluating fault heaves on seismic profiles. Faulting also indicates the timing of rift events, as faulting can only offset older horizons. Although the focus of this work is the Tertiary development of the FSB, previous rift events can influence the response of the lithosphere to tectonic events. Therefore the Mesozoic extension of the basin is evaluated, assuming that extension which occurred during discrete or protracted extensional events in the Late Jurassic and Cretaceous is equivalent to that indicated by offset across the top Jurassic horizon. For the Palaeocene section, extension is assessed by examining the magnitude of faulting at the Base Tertiary to Top Balder horizons.

The subsidence history of a rift basin gives important clues about the nature, timing and

magnitude of tectonic events, as vertical movements in the basin are the surface manifestation of the lithospheric and sub-lithospheric deformation processes. Water-loaded tectonic subsidence refers to the amount of water-loaded subsidence (or uplift) which occurs at a location due to tectonic processes (rather than due to sediment-loading or sea-level changes). In this chapter the post-Palaeocene water-loaded tectonic subsidence is calculated for each of the ten profiles presented in the previous chapter (Figures 3.7 and 3.8) using 2–D flexural backstripping. It is thought that much of the FSB lay close to sea-level at late-Palaeocene times, this palaeobathymetric constraint allows post-Palaeocene subsidence to be accurately determined for the basin. In addition, the one-dimensional subsidence history of the basin is examined for two pseudo-well locations where palaeobathymetric data are available.

The subsidence history of a basin can be compared with those predicted by models of basin formation models to assess the applicability of the models to the basin. A successful model should explain the subsidence history of the basin and be consistent with upper crustal extension estimates, crustal thinning estimates from seismic and gravity data, geological knowledge and the tectonic context of the basin. Commonly, the subsidence history of a basin is matched to the subsidence predicted by the model of basin formation by pure shear stretching of the continental lithosphere (McKenzie, 1978, Figure 2.4), a simple yet powerful model of basin formation. In chapter 5 I assess whether the FSB can be modelled as an intracontinental rift, where lithospheric extension occurs by pure shear deformation (McKenzie, 1978, Figure 2.4). Departures from the predictions made by the pure shear model of rifting may be attributable to a number of causes, including the effects of a mantle plume, underplating, unrecognised rift events, or indicate that lithospheric thinning is depth-dependent. These explanations and their applicability to the Tertiary development of the FSB are examined in chapters 5 and 6.

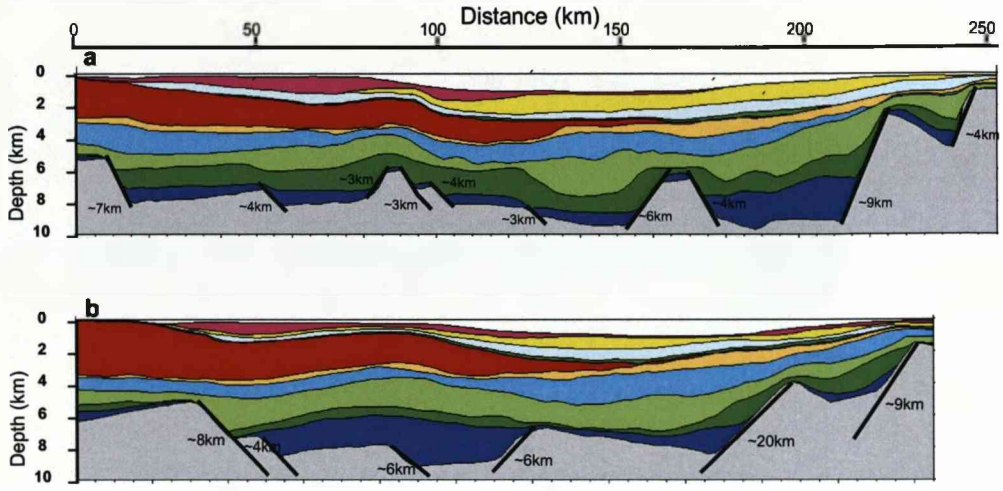

Figure 4.1: Late Jurassic fault heaves.(**a**) Profile A and (**b**) Profile E with interpreted faults on Late Jurassic horizon marked in black, annotated with fault heave measurement.

4.2 Upper crustal extension in the FSB

Upper crustal extension in the FSB is calculated by summing fault heaves (extension) which offset a particular horizon. Stretching factors (β) are calculated by:

$$\beta_{uppercrust} = \frac{length\ of\ profile}{length\ of\ profile\ -\ extension} \tag{4.1}$$

This determination of the stretching factor (β) of the upper crust is equivalent to the stretching factor calculated by equation 3.1. Estimating upper crustal extension is limited by the availability and quality of seismic data. The offset observed on a horizon using seismic data or interpretations is a minimum, and following Walsh et al. (1991), I assume that up to 40% more extension may be present below seismic resolution.

4.2.1 Mesozoic extension

Extensional offset of the interpreted Top Basement reflector on profiles A and E is 53 km and 45 km respectively (Figure 4.1). These determinations of extension correspond to average stretching factors (β) of 1.3 and 1.25 for the respective profiles. Extension estimates on the other profiles yield estimates of extension between 1.2 and 1.4. Seismic resolution of fault blocks underneath the thick basalt sequence is poor, although the spacing and size of the fault blocks underneath the basalt appears to be similar to those where seismic resolution is good in the West of Shetland region. I do not attempt to determine the distribution of Mesozoic extension across the profiles, due to the low seismic resolution underneath the basalt. Assuming that up to 40% more extension may be below seismic resolution following Walsh et al. (1991), gives upper limits of Mesozoic extension of β=1.5 and β=1.35 on profiles A and E respectively.

4.2.2 Palaeocene extension

Palaeocene sedimentary horizons in the basin are offset by much smaller faults than the Mesozoic horizons, and the amount of extension accommodated by faulting decreasing upwards through the Palaeocene section (Figures 3.12a-d). Total extension of the Base Tertiary horizon for the seismic interpretation in Figure 3.12b, is 4-5km, the profile is around 95km long, giving a stretching factor of 1.04 - 1.06. For the seismic profile in Figure 3.12c, extension of the interpreted Base Tertiary horizon is approximately 1.5km, the profile is around 24km long, giving a stretching factor of 1.07. For the purposes of comparing upper crustal extension to crustal and lithosphere stretching factors determined from wide angle seismic and subsidence analysis, upper crustal stretching factors are considered to be less than 10% ($\beta_{uppercrust}$ <1.1) on the Base Tertiary horizon.

Very few faults can be interpreted on the Top Balder horizon or in the basalt section (e.g. see Figures 3.12a-d). Smallwood and Gill (2002) present a map of the Balder Formation isochore in the Quad 204 area, showing details of a drainage network

(Figure 3.13); the level of detail resolved also suggests that this area has not been subsequently faulted. Additionally, on the Faroe Islands, extensional faulting of the Basalts is minimal (Richard Walker., pers. comm.). Post-top Palaoecene upper crustal stretching factors are considered to be less than 1% ($\beta_{uppercrust}$ <1.01) for the purposes of this study.

4.3 Calculation of 2–D profiles of water-loaded tectonic subsidence

Water-loaded tectonic subsidence can be quantified for a horizon by flexural backstripping and decompaction of overlying sediment packages. In this section, the 2–D flexural backstripping program *FlexDecomp* (Nadin and Kusznir, 1995; Roberts et al., 1998) was used to flexurally backstrip and decompact the 2–D depth converted regional profiles. The method assumes that the lithosphere responds to loading as a perfectly elastic plate.

4.3.1 Flexure of an elastic plate

The general equation which describes the deformation of an elastic plate on an inviscid substratum (the mantle) in response to a load is:

$$D\frac{d^4y}{dx^4} + (\rho_m - \rho_{infill})yg = 0 \tag{4.2}$$

(e.g. Watts, 2001), where x is the horizontal coordinate, y the vertical deflection, ρ_m and ρ_{infill} are the densities of the mantle and of the infill material respectively, g is gravitational acceleration and D is the flexural parameter. D is related to the elastic properties of the material Young's modulus (E), and Poisson's ratio (ν), and to the thickness of the elastic plate (Te) by the following equation:

$$D = \frac{E\ Te^3}{12(1-\nu^2)} \tag{4.3}$$

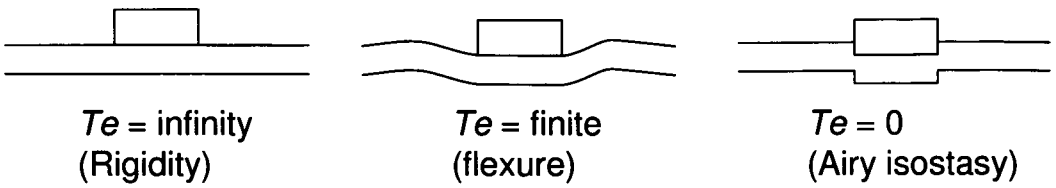

Figure 4.2: The response of an elastic plate to a load: dependence on effective elastic thickness, Te.

Many papers quote the flexural properties of the lithosphere in terms of the effective elastic thickness Te, which has units of length.

Equation 4.2 is a fourth order diferential equation which can be solved using the method of quadratics. The solution to equation 4.2 is of the form

$$y = e^{\lambda x}(A_c cos\lambda x + B_c sin\lambda x) + e^{-\lambda x}(C_c cos\lambda x + D_c sin\lambda x) \tag{4.4}$$

Where A_c, B_c, C_c and D_c are the four arbitary constants of integration and λ is a parameter that determines the amplitude and wavelength of the deformation and is given by (e.g Watts, 2001):

$$\lambda = [\frac{(\rho_m - \rho_{infill})g}{4D}]^{1/4} \tag{4.5}$$

If the plate is weak ($D \rightarrow 0$) then the response to loads is local and is equal to the Airy isostatic response, and if the plate becomes rigid ($D \rightarrow \infty$) then there is no response ($y \rightarrow 0$, which is the Bouguer response). If the effective elastic thickness (Te) is finite then the lithosphere will flex in response to the load (Figure 4.2).

The response of the lithosphere to a load depends on the width and amplitude of the load itself. The lithosphere effectively acts as a filter that suppresses the large amplitude, short wavelength deformation and passes the small-amplitude and long wavelength deformation. The degree to which the effects of the short wavelength loads are filtered is a function of the flexural parameter, or the effective elastic thickness of the plate.

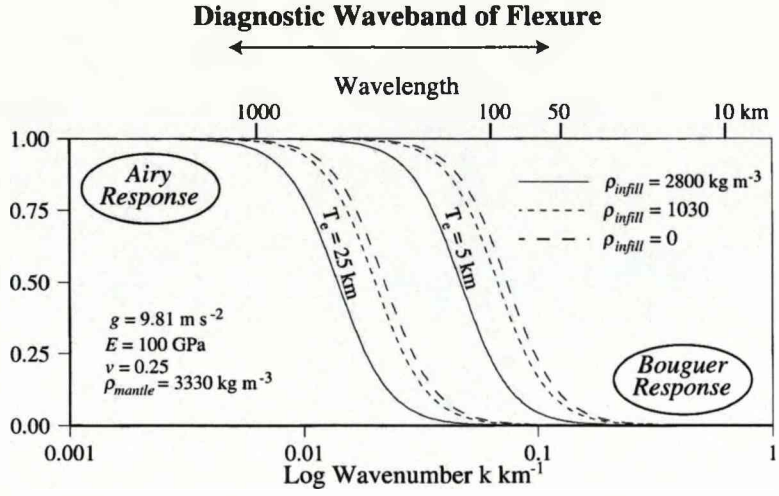

Figure 4.3: The flexural response function for a relatively weak (Te=5km) and a relatively strong (Te=25km) elastic plate as a function of the wavenumber of the load, for a range of infill densities. From Watts (2001).

4.3.2 Spatially-varying loads

The response of the lithosphere to spatially-varying loading (for example sedimentary basin fill) or unloading can be calculated using the following formulations and assumptions:

The response of an elastic plate to a periodic load is given by (e.g Watts, 2001):

$$D\frac{d^4y}{dx^4} + (\rho_m - \rho_{infill})yg = (\rho_c - \rho_w)ghcos(kx) \tag{4.6}$$

Where D is the flexural rigidity, y is the flexure, x is the horizontal distance, h is the amplitude of the load and k is the wavenumber of the load in the x direction.

The solution to equation 4.6 is periodic and of the form

$$y = \frac{(\rho_c - \rho_w)hcos(kx)}{(\rho_m - \rho_{infill})}[\frac{Dk^4}{(\rho_m - \rho_{infill})g} + 1]^{-1} \tag{4.7}$$

The flexural response parameter $\Phi_e(k)$ is a parameter which describes the modification

of the Airy response to produce flexure.

$$\Phi_e(k) = \frac{Output}{Input} \tag{4.8}$$

where

$$\Phi_e(k) = [\frac{Dk^4}{(\rho_m - \rho_{infill})g} + 1]^{-1} \tag{4.9}$$

(e.g Watts, 2001).

The dependence of $\Phi_e(k)$ on k for a range of infill densities is shown in Figure 4.3. Curves are shown for a relatively weak plate (Te = 5km) and for a relatively strong plate (Te = 25km). For long wavelength (low wavenumber) loads the plate behaves as a weak Airy-type structure, for short wavelength loads the plate appears rigid. The flexural response is of the lithosphere to loading and unloading is dependent on the wavelength of the load, and is calculated in the spectral domain using Fourier analysis by *FlexDecomp*.

4.3.3 Sediment compaction and decompaction

In order to account for compaction of a package of sediments, which occurs as a result of loading by younger sediments, the *FlexDecomp* package uses the following assumptions and relationships: At the time of deposition, sediments are composed of grains of density ρ_{grain} and have an initial porosity of ϕ_0. The bulk density of sediments at the surface (ρ_0) is therefore:

$$\rho_0 = (1 - \phi_0)\rho_{grain}. \tag{4.10}$$

Porosity ϕ_z decreases exponentially with depth (z) so that:

$$\phi_z = \phi_0 e^{-cz} \tag{4.11}$$

(Sclater and Christie, 1980), where c is the compaction constant. A sedimentary package will therefore compact during burial due to loading, and the bulk density of the sediment increases with burial depth (e.g. see table in Figure 3.8, which shows the average density of sedimentary packages in the FSB). The *FlexDecomp* package reverse-models the compaction process during calculation of water-loaded tectonic subsidence.

4.3.4 Flexural backstripping and decompaction using *FlexDecomp*

The *FlexDecomp* calculates the tectonic water-loaded subsidence as follows:

1. Overlying sedimentary packages are removed, and the flexural isostatic response to the unloading is calculated and applied to the remaining cross-section. If flexural backstripping is performed on short wavelength sedimentary packages, careful consideration must be given to the effective elastic thickness used during backstripping. Roberts et al. (1998) suggest using a small but finite (1-5km) effective elastic thickness, which avoids unrealistic internal deformation of fault blocks.

2. The underlying layers are decompacted according to the porosity-depth relationship suggested by Sclater and Christie (1980), calibrated with samples from wells. Density and decompaction parameters for the profiles across the FSB are displayed in Figure 3.8.

3. The change in water load associated with decompaction is calculated, and its isostatic response is applied to the profile. The effects of first order global sea-level variations (from Haq et al., 1987) are also considered.

4. Steps 1-3 are repeated for each horizon above the target horizon.

5. The palaeobathymetry of the target stratigraphic horizon is subtracted from the resulting bathymetric profile. The resulting profile represents water-loaded tectonic subsidence since deposition of the horizon.

The availability and accuracy of palaeobathymetry data is a major limiting factor when calculating tectonic subsidence. The backstripping technique can only be used

to calculate a tectonic water-loaded subsidence profile for a horizon when accurate palaeobathymetry data are available.

4.4 Post-Palaeocene water-loaded tectonic subsidence in the FSB

Palaeobathymetric evidence suggests that much of the basin was close to sea-level during deposition of the Balder Formation (Section 3.5). If the whole basin is assumed to have been at sea-level at Top Balder times, it is possible to calculate tectonic subsidence since Top Balder times over a large area. The assumption that the basin was at sea-level at Top Balder times is critical for the subsequent analysis performed in the following chapters, the relevant evidence regarding this assumption is briefly restated: In the southern part of the basin and on the Shetland Platform where well and seismic data are dense, it has been widely published that the basin was close to sea-level (with a low-lying, paralic or shallow marine palaeogeography) during deposition of the Balder Formation (Ebdon et al., 1995; Lamers and Carmichael, 1999; Naylor et al., 1999; Mudge and Bujak, 2001; Smallwood and Gill, 2002, Figure 3.10f). Estimates of tectonic subsidence in this area are considered to be accurate. On the Faroes Platform, there are no well data publicly available, however Ellis et al. (2002) suggest that the Upper Lava Series (which is around 0.1Myr older than the Top Balder horizon) were extruded across subaerial low relief which was close to sea-level. This palaeogeography is interpreted to extend across the axis of the basin. The Balder Formation was deposited on top of Upper Series Lavas, which were probably subsiding by this time. Additionally, it is likely that the present day aerial limits of the Balder Formation are close to the palaeoshoreline, as sediments deposited in water have a much higher preservation potential than those deposited subaerially.

There is also evidence for subaerial conditions at Upper Lava Formation/Flett Formation times in the northern part of the basin. The Faroe-Shetland escarpment of the Upper Basalt series is thought to represent a palaeoshoreline, and subaerial volcanics

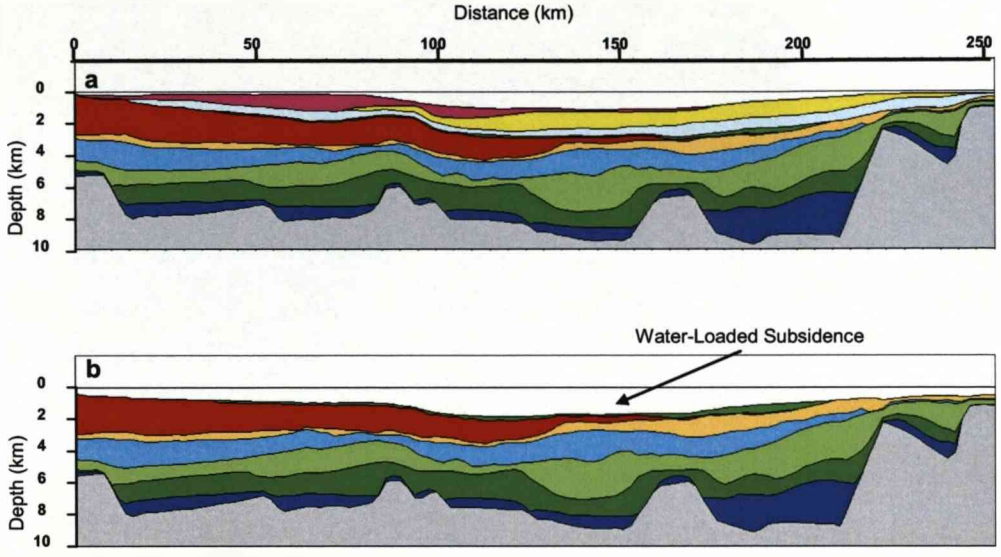

	Age of unit	(Ma)	Initial poros-ity (Φ_0)	Deco-mpac-tion const-ant (c) [km^{-1}]	Grain densi-ty (ρ_{grain}) [kgm^{-3}]	Densi-ty* (ρ_{sed}) [kgm^{-3}]	Seism-ic veloci-ty [ms^{-1}]
	(Water)	-	-	-	1000	1000	1490
	Top Oligocene - Seabed	0-25	60.2	0.46	2710	1120	2250
	Top M.Eocene –T. Oligocene	25-40	61.6	0.49	2710	1360	2250
	Top Balder-Top M.Eocene	40-54	59.5	0.45	2700	1720	2250
	Top Basalt to Top Balder	54-54.1	59.1	0.45	2700	1900	4500
	Basalt	54.1-58	1.0	0.01	2800	2770	3000
	Top Kettla - Base Basalt	58-59	58.1	0.43	2700	2030	3000
	T.Cretaceous - Top Kettla	59-65	57.4	0.41	2690	2230	3000
	T.Cenomanian –T. Cretaceous	65-99	60.2	0.47	2700	2530	3000
	Top Jurassic – T.Cenomanian	99-144	63.0	0.51	2720	2640	3500
	Top Basement to Top Jurassic	144-155	60.9	0.47	2710	2630	4500
	Basement	-	0.0	-	-	2850	-

Figure 4.4: Water-loaded tectonic subsidence. (**a**) Profile E (present day). (**b**) Profile E after flexural backstripping and decompaction to the Top Balder horizon assuming an effective elastic thickness (Te) of 2.5km. The Top Balder horizon was deposited close to sea-level (see text), so the resulting apparent bathymetry of the backstripped profile represents tectonic water-loaded subsidence since Top Balder deposition (also referred to as post-Palaeocene subsidence).

have been drilled in the axis of the basin on probable palaeohighs. In this area it may be more appropriate to calculate the Top Basalt-Present Day subsidence, as the area was marine by Balder times. However, the Balder Formation is less than 300m thick in this area, therefore the difference between Top Balder-Present and Top Basalt-Present Day tectonic subsidence is less than 140m assuming a water:sediment density ratio of 2.2. In some areas in the north of the basin, away from the (palaeohigh) fault block crests, marine conditions probably persisted throughout the Palaeocene. It is not possible to determine the post-Palaeocene subsidence without accurate palaeobathymetry data, and the Top-Balder-Present Day subsidence should be considered a maximum in areas where marine conditions persisted. The detailed analysis of stretching and thinning in the basin presented in this thesis is focused on the southern part of the basin where the basin is confidently assumed to have been close to sea-level at Top Balder Formation times. The Top Balder to Present Day water-loaded tectonic subsidence is also referred to as 'post-Palaeocene subsidence' in the following sections.

Figure 4.4a shows profile E, and 4.4b shows profile E flexurally backstripped and decompacted to the Top Balder horizon. The bathymetry of the backstripped profile represents the post-Palaeocene water-loaded tectonic subsidence. The post-Palaeocene water-loaded tectonic subsidence has been calculated for each of the profiles in Figure 3.8 using a range of effective elastic thicknesses (0km, 2.5km and 10km) during flexural backstripping and contoured to produce post-Palaeocene tectonic subsidence maps (Figures 4.5a-c). The post-Palaeocene sediment loads are of long wavelength compared with the likely flexural wavelength corresponding to the effective elastic thickness of the basin, and so post-Late Palaeocene water-loaded tectonic subsidence calculated using this method are relatively insensitive to the effective elastic thickness used during flexural backstripping.

Post-Palaeocene subsidence follows the shape of the present day basin bathymetry. In the southwest of the basin, post-Palaeocene subsidence is more than 1km above the Judd Basin (in Quad 204)- Westray Ridge area, increasing northwards along the axis to more than 2 km above the Corona Ridge close to 213/23-1, and 2.4km on the Corona

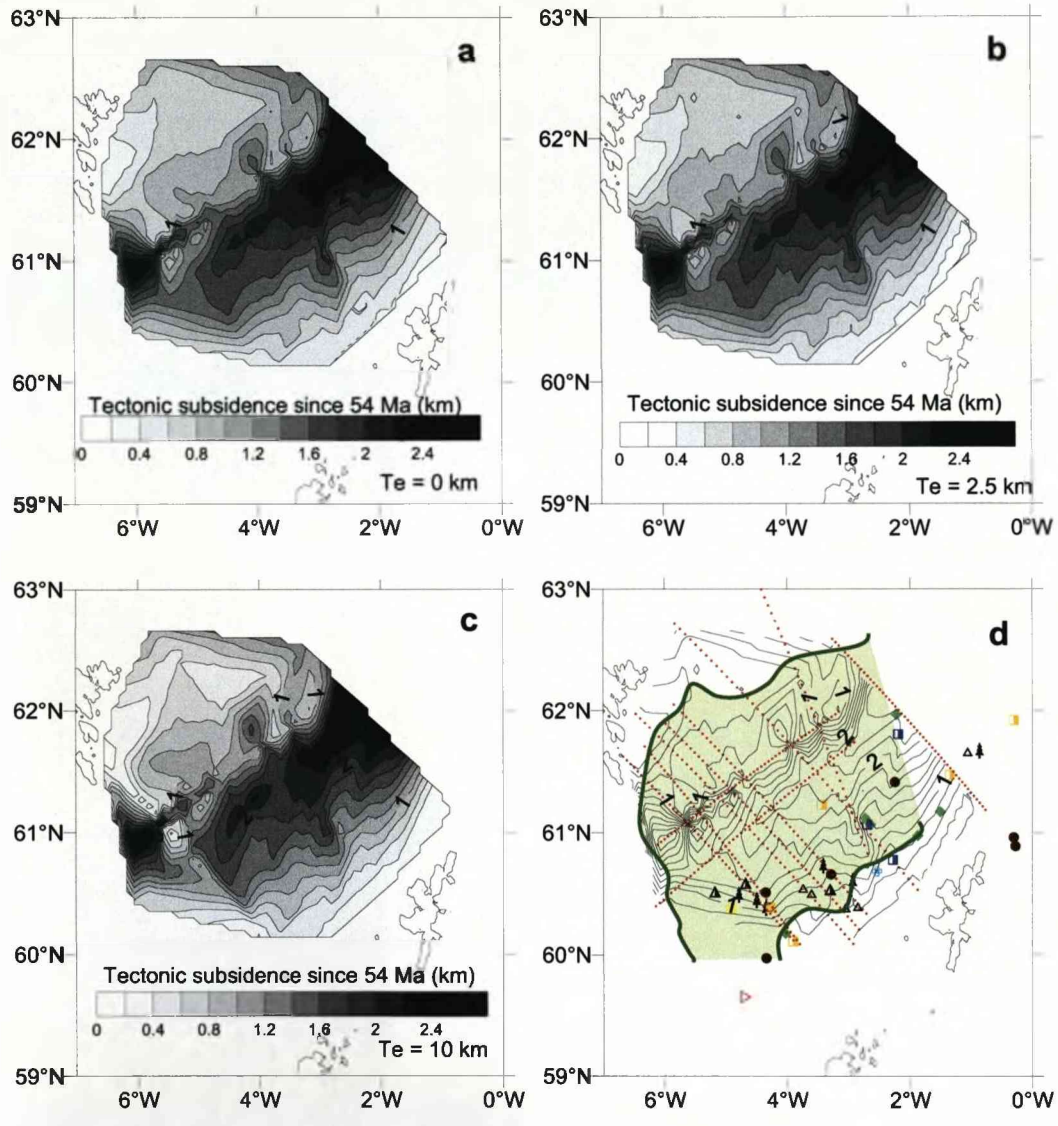

Figure 4.5: Post-Palaeocene subsidence maps calculated assuming effective elastic thickness (Te) of (**a**) 0km (local isostasy; (**b**) 2.5 km and (**c**) 10km. Subsidence profiles were calculated for each profile shown in Figure 3.8 and gridded using the triangular and linear interpolation algorithm in *Surfer*. The long wavelength of the post-Top Balder sediment packages compared to the likely effective elastic thickness (Te) means that estimates of Top Balder-Present day water-loaded tectonic subsidence are relatively insensitive to the value of effective elastic thickness used during flexural backstripping and decompaction. (**d**) map showing post-Palaeocene subsidence calculated using Te=2.5km, simplified Balder Formation well-log map, location of profiles and aerial extent of Balder Formation (in green; digitized from the Balder Formation isochore in Smallwood and Gill (2002)).

Ridge close to 214/9-1. On the basin flanks, where palaeobathymetric data exist that suggest the Top Balder Formation was close to sea-level and at the outer limits of the Balder Formation, around 500m of post-Palaeocene subsidence has occurred (see Figure 4.5d). The region around the FSB area is often considered to have experienced regional post-Atlantic breakup subsidence following, for example, removal of dynamic support from a mantle plume. This analysis shows that 500m is the upper limit of regional (i.e. single valued over the whole area) subsidence which can be 'removed' from the FSB area without violating palaeobathymetric constraints.

4.5 Water-loaded subsidence though time in the FSB

1–D subsidence curves can constrain the timing of tectonic events in the basin if palaeobathymetry data are available for multiple horizons. The method of determining the subsidence history of a stratigraphic column using 1–D Airy backstripping is well established (Steckler and Watts, 1978). However, the assumption of local isostasy (effective elastic thickness, Te=0) can give rise to significant errors if the location of the stratigraphic column is close enough to a fault block to be affected by basement topography or to the effects of effective elastic thickness of the lithosphere during loading and unloading (Sawyer, 1986; Roberts et al., 1998).

1–D subsidence curves for pseudo-well locations along a profile can be extracted during 2–D flexural backstripping of that profile. After flexurally backstripping and decompacting the sediments above the target horizon, the resulting bathymetry of the profile is recorded at the pseudo-well location, and plotted as a function of time. Where palaeobathymetry data are available, the curve is corrected; otherwise, assuming no erosion, the resulting curve represents the maximum tectonic subsidence since deposition of the horizon. A simplified example of how a 1–D subsidence profile can be constructed is shown in Figure 4.6.

1–D subsidence history curves were extracted during flexural backstripping and decompaction at two pseudo-well locations PW1 and PW2 close to and structurally aligned with wells which have some palaeobathymetric control (Figure 4.7a and 4.7d). The

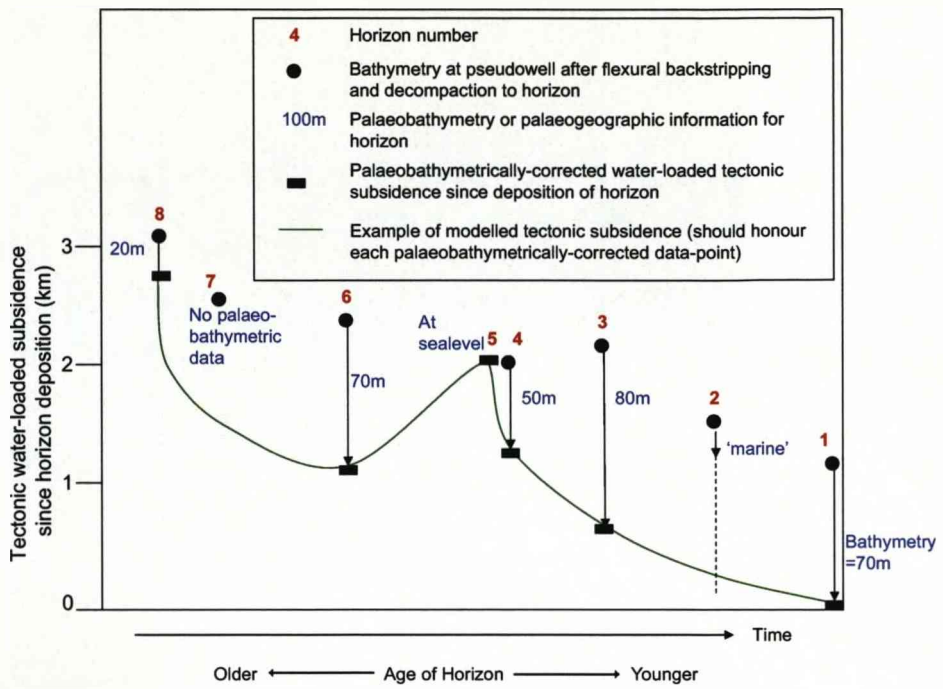

Figure 4.6: Schematic diagram to show method for correcting 1–D tectonic subsidence curves for palaeobathymetry.

pseudo-wells are on fault block crests which are thought to have been subaerial in the Late Jurassic (Dean et al., 1999), and close to sea-level at Late Palaeocene times. The 1–D water-loaded subsidence curves of pseudo-well locations illustrate a general trend of subsidence in the basin since the Jurassic. However, the number of data points and accurate palaeobathymetric data for each location are limited; therefore we do not have a detailed subsidence history with which to match to model subsidence histories. However, the Palaeocene sediments in the basin illustrate relative shallowing and deepening, which is suggestive of at least one transient uplift event. This is consistent with Champion et al. (2008), who by backstripping mapped seismic horizons, show that the Judd sub-basin (Q204; see Figure 3.2 for location) of the FSB experienced a transient uplift event of minimum magnitude 490m in the Late Palaeocene, peaking at Lower Flett times (Figure 3.14).

The water-loaded subsidence curves presented in Figure 4.7b and 4.7e are calculated assuming local isostasy; the method is equivalent to that in Steckler and Watts (1978).

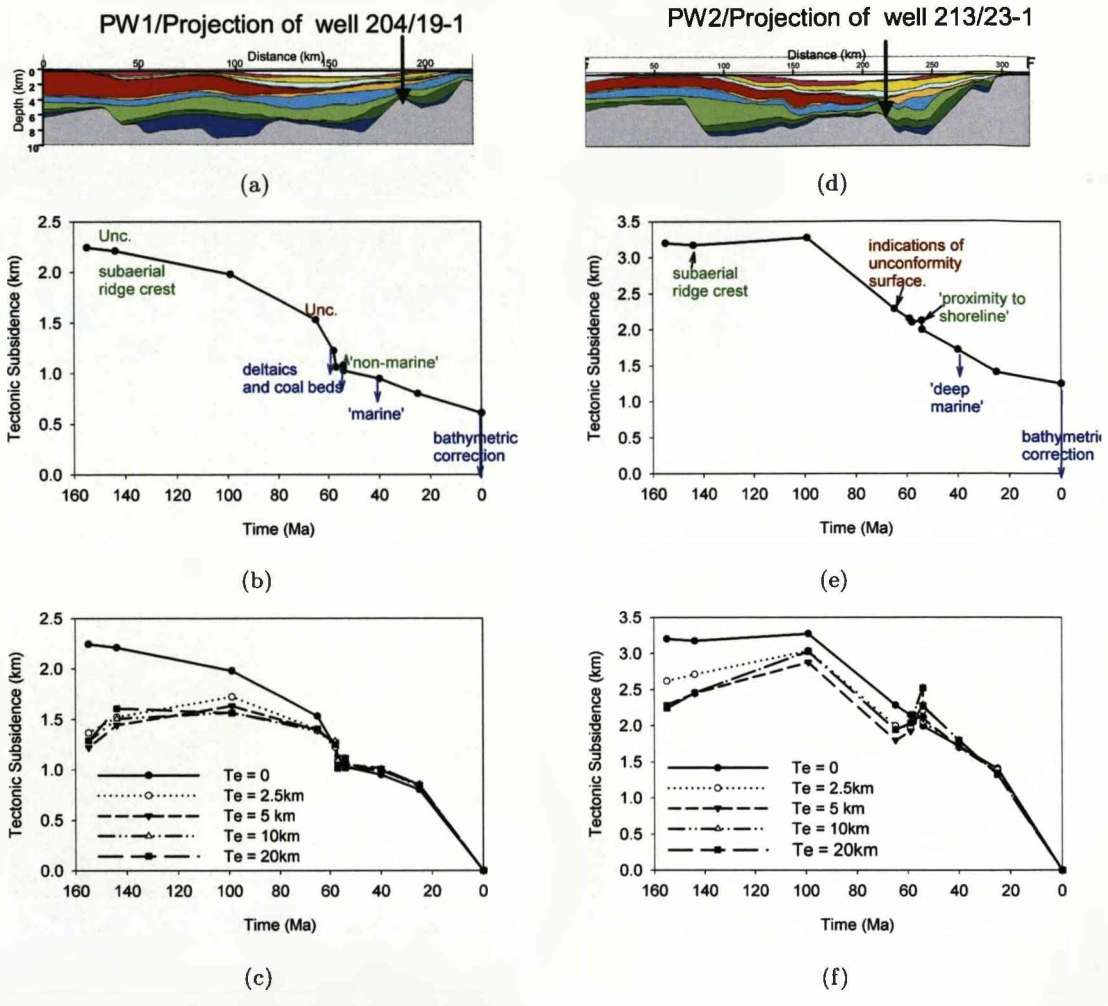

Figure 4.7: 1-D subsidence history of the FSB. (**a**) Location of PW1 on profile A (188km). (**b**) 1–D subsidence history for pseudo-well location PW1, calculated assuming local isostasy (Te=0). The dashed curve joins determinations of maximum tectonic subsidence between horizons and present day, assuming marine conditions. Annotations and arrows indicate palaeogeographic information at well 204/19-1, close to PW1. Where palaeobathymetric data indicate that the location was close to sea-level, model tectonic subsidence history should intersect the datapoint; where the location was marine, downwards arrows indicate that modelled subsidence should plot below the data point, where no information is available there are no constraints. 'Unc.' indicates unconformity. (**c**) Effect of Te on 1–D subsidence history for pseudo-well PW1 calculated by progressively backstripping profile A using *FlexDecomp*. The Te used during flexural backstripping can have a significant impact on the subsidence history when backstripping through short wavelength sedimentary package between large fault blocks. Note that these data are not palaeobathymetrically-corrected (except for the datapoint at t=0, where the bathymetry is known), so the apparent uplift around 100Myr is probably not real. Figures (**d-f**): as **a-c** but for PW2 (at 211km on profile F), palaeogeography data from well 213/23-1.

However, although the effective elastic thickness of rift basin locations is usually considered to be low, Te<10km (Barton and Wood, 1984; Karner and Watts, 1982), a small finite effective elastic thickness can have a significant effect on the resulting subsidence curve if the stratigraphic column or pseudo-well location lies close to basement topography and short wavelength sediment packages (Sawyer, 1986; Roberts et al., 1998, Figure 4.7c and 4.7f). 1–D subsidence curves are commonly matched to those predicted by the pure-shear basin formation model to derive the rifting history of a basin. However, the subsidence history of a basin may be affected by its flexural strength (Figure 4.7c and 4.7f). It is therefore important to consider the likely flexural strength of the lithosphere (if possible) during backstripping, as the best-fitting theoretical curve may be sensitive to the effective elastic thickness used during backstripping. I will briefly examine this in the next chapter.

4.6 Summary

- Stretching factors determined from summing extension of the upper crust (by brittle faulting) are between 1.2 and 1.4 for the Late Jurassic-Cretaceous phase of rifting in the basin.
- Early Palaeocene stretching factors are considered to be less than 1.1, determined by summing fault heaves on the Base Tertiary horizon.
- Very few faults are interpreted on the Top Balder horizon or in the basalt section. Post-top Palaoecene upper crustal stretching factors are considered to be less than 1.01.
- In order to calculate tectonic subsidence, accurate palaeobathymetry data are required. Much of the FSB is thought to have been close to sea-level at end Palaeocene times, enabling post-Palaeocene tectonic subsidence to be determined over a large area. Post-Palaeocene subsidence is ~500m on the basin flanks, ~1500m in the southwest axis of the basin, increasing north-eastwards to ~2400m over the Corona Ridge.

- One-dimensional subsidence histories may enable the timing of tectonic events to be constrained, however the subsidence of a basin is affected by its flexural strength, this should be considered when comparing backstripped subsidence histories to models.

Chapter 5

Is the Faroe-Shetland basin an intracontinental rift basin?

5.1 Introduction

In this chapter, I test the hypothesis that the development of the Faroe-Shetland basin (FSB) can be explained by the model of intracontinental rift basin formation by pure-shear extension and thinning of the lithosphere (McKenzie, 1978, Figure 2.4). In this model, basin formation occurs when the continental lithosphere is stretched by a factor of beta, β, before thermally equilibrating. Syn-rift subsidence or uplift, (also termed initial subsidence, Si) is the net result of crustal thinning, which causes subsidence, and thermal uplift caused by thinning the lithosphere and elevating the geothermal gradient. Post-rift subsidence (St) follows an exponential decay curve as the lithosphere cools by conduction and thermally contracts.

In order to assess the applicability of this model to the formation of the FSB, the apparent stretching factor implied by the magnitude of subsidence is compared to that implied by upper crustal extension due to faulting. If the timing and magnitude of stretching along a profile implied from faulting is equal to that implied by subsidence, then the basin may be considered a product of pure-shear stretching. The ability of the pure-shear model of basin formation to account for the basin's development is

considered in two parts: pre-Late Palaeocene and post-Palaeocene, although the focus is on the latter. To compliment the 2–D modelling, the 1–D subsidence history of the basin is also modelled using the pure-shear model.

Departures from the predictions made by the pure-shear model of rifting may be attributable to a number of causes, including the effects of a mantle plume, underplating, unrecognised rift events, or indicate that lithospheric thinning is depth-dependent. These explanations and their applicability to the Tertiary development of the FSB are examined in this chapter.

5.2 Analysis of post-Palaeocene water-loaded tectonic subsidence: apparent lithospheric stretching factors assuming pure-shear extension

If the FSB is considered to have formed by pure-shear extension of the lithosphere, then the magnitude of the rift event may be calculated from the post-Palaeocene subsidence, if a rift age is assumed, using the following equations from McKenzie (1978):

Initial subsidence (syn-rift subsidence) for a basin which has been extended by a factor of β, where β is the ratio between the initial and final thickness, is given by (McKenzie, 1978):

$$Si = \frac{a((\rho_m - \rho_c)\frac{c}{a}(1 - \frac{\alpha T_1 c}{2a}) - \frac{\alpha T_1 \rho_m}{2})(1 - \frac{1}{\beta})}{\rho_m(1 - \alpha T_1) - \rho_w} \tag{5.1}$$

where ρ_m is the density of the mantle at 0°C, ρ_c is the density of the crust at 0°C, ρ_w is the density of water, α is the coefficient of thermal expansion (considered to be the same for crust and mantle), a the initial lithospheric thickness, c the initial crustal thickness and T_1 is the mantle potential temperature.

Thermal subsidence is time dependent, exponentially decaying with time. The final depth of the basin (E_0) is given by (McKenzie, 1978):

$$E_0 = \frac{4a\rho_m\alpha T_1}{\pi^2(\rho_m - \rho_w)} \tag{5.2}$$

and the elevation above the final depth $e(t)$ by (McKenzie, 1978):

$$e(t) = E_0 r exp(-t/\tau) \tag{5.3}$$

where

$$r = \frac{\beta}{\pi} sin\frac{\pi}{\beta} \tag{5.4}$$

τ is the thermal time constant which determines the rate at which heat can diffuse from the system. It is given by (McKenzie, 1978):

$$\tau = \frac{a^2}{\pi^2 \kappa} \tag{5.5}$$

where κ is the thermal diffusivity of the mantle. In this chapter the thermal time constant is assumed to be 62.8Myr, after McKenzie (1978). The thermal diffusivity of the mantle is related to the thermal conductivity k by

$$\kappa = kT_1/a. \tag{5.6}$$

The thermal subsidence since extension is:

$$St = e(0) - e(t) \tag{5.7}$$

and the total syn- and post- rift subsidence:

$$Stotal = Si + St \tag{5.8}$$

The post-Palaeocene water-loaded tectonic subsidence in the FSB may be considered to be a product of either post-rift thermal subsidence (St) following a pre-end Palaeocene rift event, or syn-and post-rift subsidence (initial and thermal subsidence, $Si + St$) due to a post- Palaeocene rift event. Additionally, it is possible to account for regional subsidence effects; for example, during continental breakup at the proto-north Atlantic the region may have been uplifted due to the effects of a mantle plume (e.g. Nadin

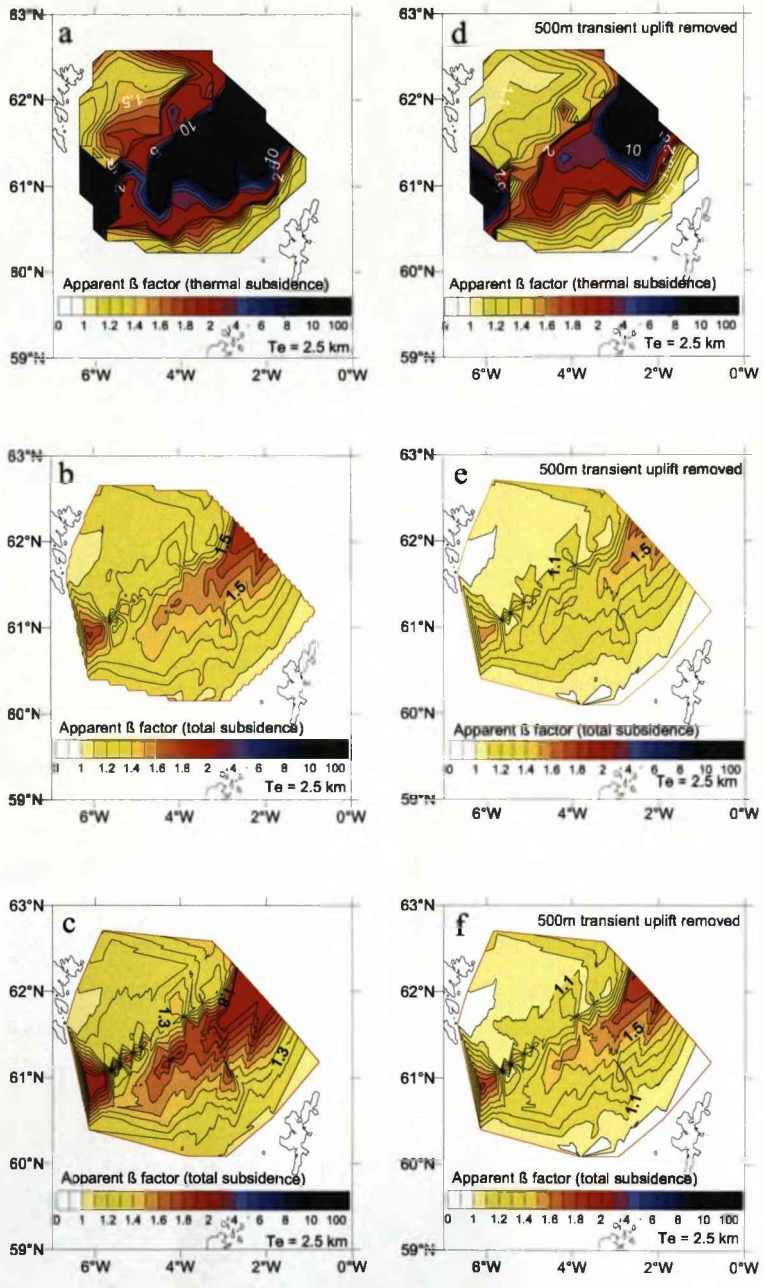

Figure 5.1: Apparent lithosphere stretching factor maps for the FSB, calculated assuming that post-Palaeocene subsidence calculated with Te=2.5km is due to: (**a**) post-rift thermal subsidence (St) following a pre-end Palaeocene stretching event; (**b**) Syn- and post-rift subsidence ($Si + St$) following a post-Palaeocene stretching event assuming crustal thickness prior to rifting of 35km; (**c**) Syn- and post-rift subsidence ($Si + St$) following a post-Palaeocene stretching event assuming crustal thickness prior to rifting of 30km. (**d-f**) as **a-c** but 500m post-Palaeocene subsidence is assumed to be caused by removal of transient support following breakup. Calculations made using equations in McKenzie (1978). Constants for equations: Mantle density: 3330kgm^{-3}; Crustal density: 2850kgm^{-3}; thermal time constant: 62.8Myr.

et al., 1997), and the region has subsequently subsided.

Apparent pre- and post-Late Palaeocene stretching factors required to account for the post-Palaeocene subsidence in the FSB are calculated using the above formulae and are shown in map form in Figures 5.1**a-c**. The apparent stretching factor β is calculated for each data point (approx 2km spacing) along each of the depth-converted profiles by iteratively solving equations 5.1 to 5.8, and assuming that rifting occurred at 54Ma. The exercise was repeated assuming that 500m of post-Palaeocene subsidence is caused by removal of regional dynamic support from the mantle (e.g. from the proto-Iceland plume) (Figure 5.1**d-f**).

5.3 Apparent stretching factor maps

In Figure 5.1a an apparent pre-Late Palaeocene stretching factor map for the FSB is shown. Apparent stretching factors were calculated assuming that stretching and thinning occurred at 54Ma (i.e. just prior to deposition of the Top Balder horizon), and that post-Palaeocene subsidence is a result of thermal subsidence (St) only. They represent minimum stretching factors, as earlier (e.g. Mesozoic) rift events would result in less post-Palaeocene subsidence. In the basin axis, the apparent pre-Late Palaeocene stretching factor is greater than 10 in the centre of the basin (Figure 5.1a). Even when 500m of the post-Palaeocene subsidence is removed due to 'regional' effects (i.e. post-plume subsidence), the apparent pre-Late Palaeocene stretching factor is greater than 2 in the centre of the basin (Figure 5.1d). This is much higher than the magnitude of extension illustrated by fault heaves in the Palaeocene section ($\beta_{uppercrust}$ <1.1). The apparent stretching factor maps in Figures 5.1a and 5.1d were calculated assuming stretching occurred at 54Ma; however, most of the faults in the Palaeocene section are close to the base Tertiary (65Ma). An older rift age would increase the apparent stretching factors and increase the discrepancy between upper crustal and whole lithosphere extension factors.

In Figures 5.1b-c and 5.1e-f, post-Palaeocene subsidence is modelled as both syn- and post- rift subsidence ($Si + St$) caused by a stretching event at 54Ma (i.e. at

or just after deposition of the Top Balder horizon). For an initial crustal thickness of 35km, the apparent stretching factor in the basin axis in the south of the basin is more than 1.4 (Figure 5.1b), or more than 1.2 (Figure 5.1c) if 500m of the post-Palaeocene subsidence is removed due to 'regional' effects (i.e. post-plume subsidence). The apparent stretching factor increases northwards along the axis. These apparent stretching factors are much greater than suggested by the very minor faulting of the upper Basalts, Balder and post-Palaeocene horizons ($\beta_{uppercrust}$ <1.01). Prior to the Late Palaeocene rifting, however, the crust was probably thinner than 35km, due in part to Mesozoic rifting. The apparent post-Palaeocene stretching factor increases as crustal thickness decreases (e.g. compare Figures 5.1**b** and **c**), thus making the discrepancy between stretching factors calculated from fault heaves and subsidence even greater. If the values of τ and $\Delta\rho$ ($\Delta\rho = \rho_m - \rho_c$) are given upper and lower bounds of 50-75Myr and 430-530kgm^{-3} respectively, and the crust is assumed to be 35km thick, the post-Palaeocene subsidence in the Quad 204 area (800-1200m) corresponds to apparent stretching factors in the area of between 1.14 and 1.37, which is still much greater than that determined from the summation of extension on Palaeocene and younger faults in the upper crust.

Minor post-Palaeocene upper crustal faulting in the FSB suggests that post-Palaeocene subsidence is a result of post-rift thermal subsidence only (St). The magnitude of post-Palaeocene subsidence in the basin suggests stretching factors much greater than those implied from fault heaves and the post-Palaeocene subsidence in the FSB therefore cannot be modelled as a consequence of pure-shear lithospheric thinning from a Palaeocene rift event.

5.4 Flexural backstripping and reverse thermal subsidence modelling of the FSB

In this section I assess whether the post-Palaeocene subsidence in the FSB can be explained by subsidence caused by multiple pure-shear extension events (i.e. subsidence

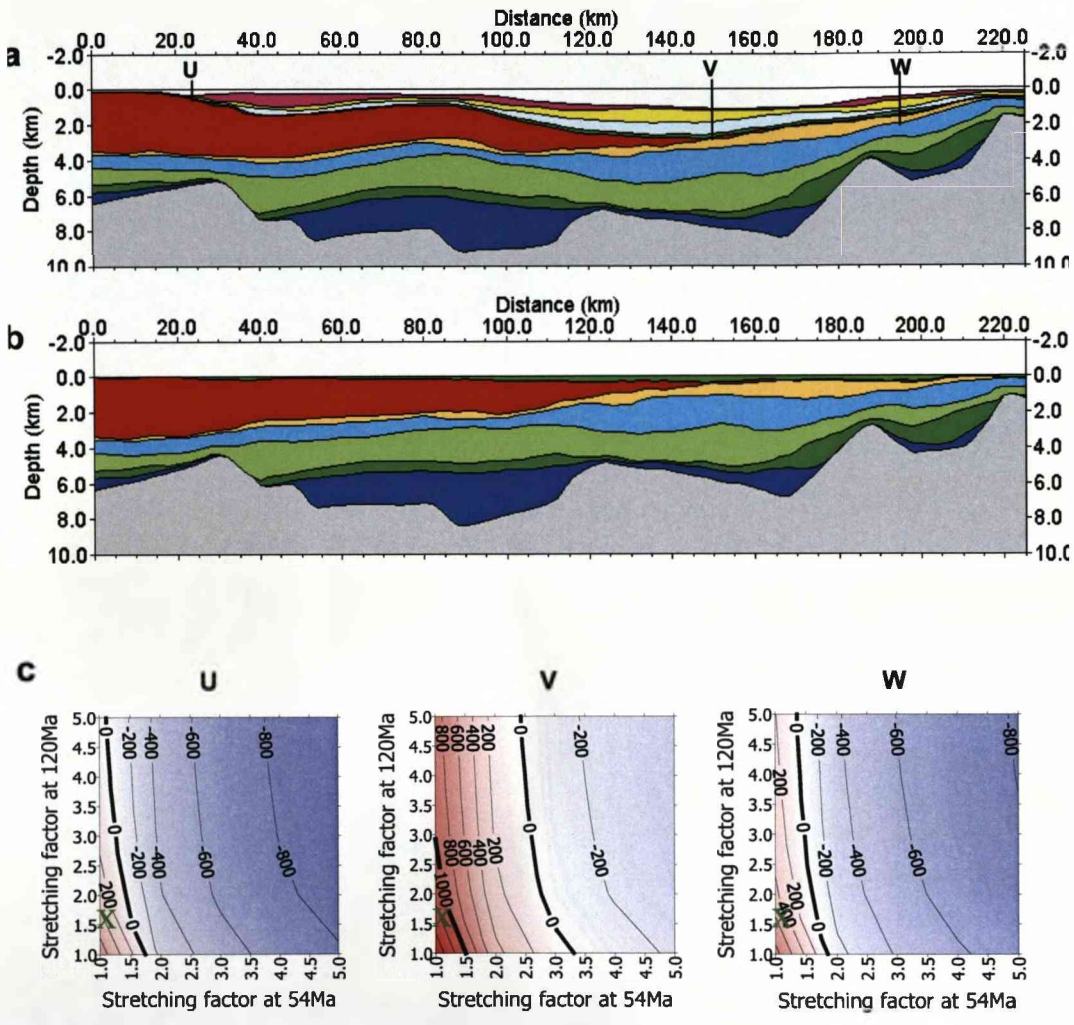

Figure 5.2: (**a**) Profile A and (**b**) profile A restored to presumed palaeobathymetry at Top Balder (sea-level). (**c**) Contour plots to illustrate the range of rifting histories which account for the post-Palaeocene subsidence of pseudo-well locations U, V and W. Contours show magnitude (in m) of post-Palaeocene subsidence required, in addition to post rift thermal subsidence from rifting events at 120Ma and 54Ma, to restore the Top Balder horizon to sea-level. 120Ma is chosen as median age for Mesozoic rifting. Calculated using *FlexDecomp*. Crosses indicate maximum stretching factors implied from fault heaves.

caused by Palaeocene rifting plus residual post-rift thermal subsidence from Mesozoic rifting), plus regional subsidence caused by other processes (for example the removal of thermal support from a mantle plume). The magnitude of the rift events and the subsidence caused by other processes required to account for the post-Palaeocene subsidence has multiple solutions, the likelihood of these solutions are considered in terms of the extension factors determined from fault heave analysis and other evidence.

The analysis was carried out by flexural backstripping and reverse thermal subsidence modelling of 2–D profiles; the method is similar to that described in Section 4.3. However, the method differs from that described in Section 4.3 in that, in addition to removing the loading effects of the sediments as described in step 1 of Section 4.3, post-rift thermal subsidence from (pure-shear) rift events or due to other processes is removed from the profile during backstripping. The reverse modelling generates an apparent uplift when subsidence is removed. The amount of post-rift thermal subsidence removed depends on the age and magnitude (β) of the rift event (Equations 5.2 to 5.3). Only post-rift subsidence from a rift event can be removed, so this technique cannot be used to backstrip through the syn-rift sequence. A successful model results in palaeobathymetric restoration of the target horizon which agrees with observations. The Top Balder and Top Basalt horizons in the FSB are only very sparsely faulted, indicating that no significant crustal extension has occurred since their deposition. It is therefore suitable to use flexural backstripping, decompaction and reverse thermal and plume-related subsidence modelling to attempt to restore the basin to sea-level at the Top Balder horizon. Post-Palaeocene tectonic water-loaded subsidence across profile A is 1.5km at pseudowell V, close to the centre of the basin. Assuming that this is due to post-rift thermal subsidence from a single Late-Palaeocene rifting event requires an extension event with a stretching factor of more than three ($\beta > 3$) in the centre of the basin, as shown in the previous section (Figure 5.1**a**). This magnitude of whole lithosphere thinning is incompatible with estimates of Palaeocene rifting from fault heave analysis (which suggests that stretching of less than a factor of 1.1 ($\beta < 1.1$) occurred in the upper crust during the Palaeocene).

However, a proportion of the Post-Palaeocene subsidence may be a result of residual post-rift thermal subsidence following an earlier rift event, or subsidence caused by another process such as regional subsidence. The magnitude of rift events and the excess subsidence required to account for the post-Palaeocene subsidence is calculated at pseudo-wells U, V and W which lie on profile A (Figure 5.2). Pseudo-well U is close to the westward limit of the Balder Formation, and V and W are located near wells which show evidence of having a palaeobathymetry close to sea-level at Top Balder times, therefore there is high confidence that post-Palaeocene subsidence values for those locations are correct.

For each of the pseudo-wells, the amount of extra subsidence required to restore the pseudo-well back to sea-level at the Top Balder horizon was calculated after removing post-rift thermal subsidence from both Mesozoic and Late Palaeocene rift events of variable magnitudes (Figure 5.2). An age of 120Ma was assumed for the Mesozoic rifting, corresponding to, or slightly younger than, the approximate age of maximum faulting suggested in the literature (Dean et al., 1999; Hooper and Walker, 2002). For example, at location V, the post-Palaeocene subsidence can be accounted for by thermal subsidence from a mid Cretaceous rift event of β=1.6, a Late Palaeocene rift event of β=1.1 plus the removal of transient uplift of 1200m. Assuming stretching factors from upper crustal extension are indicative of the magnitude of Jurassic-Cretaceous (β<1.6) and Palaeocene (β<1.1) pure-shear rifting events, the transient uplift which has been removed since the end of the Palaeocene required to restore the three locations back to sea-level is 400-700m at location U, 1200-1500m at location V, and 500-800m at location W. It is therefore not possible to restore the whole profile to sea-level by removing (single-valued) regional uplift. Removing 500m of transient (plume-related) uplift in addition to post-rift thermal subsidence palaeobathymetrically restores the flanks of the basin but does not restore the centre of the basin back to sea-level. Similarly, removing 1500m of transient uplift over-restores the flanks of the basin to at least 700m above sea-level; this is a significant over-restoration: well data indicate that the flanks were low-lying, and no evidence for significant Palaeocene erosion of the flanks is seen in

seismic data. This suggests that the centre of the FSB along profile A has subsided at least 500m more than can be explained by post-rift thermal subsidence and removal of transient plume uplift. The 'excess' subsidence discrepancy in the basin axis increases in magnitude towards the NE, to around 1600m on the Corona Ridge (e.g. at PW2 on Profile F, of 2400m post-Palaeocene subsidence, 800m may be accounted for by removing transient plume uplift and addition to post-rift thermal subsidence). Possible explanations for the excess post-Palaeocene subsidence in the basin axis are explored in Section 5.8.

5.5 The pre-Atlantic breakup subsidence history of the FSB

The seismically reflective basalts mean that the pre-Atlantic break-up history of the FSB is more difficult to study than the younger history of the basin. However, it is clear in the eastern part of the basin that the Late Jurassic horizon is cut by large faults (e.g. Figures 3.7 and 3.8), representing a stretching event which may have continued throughout most of the Cretaceous. Fault heave analysis of the Top Jurassic horizon of profiles A and E suggests that the total magnitude of Jurassic and Cretaceous rift events was between 1.25 and 1.5. Reverse thermal subsidence modelling during flexural backstripping and decompaction is used to test whether a Late Jurassic - Early Cretaceous pure-shear stretching can explain the pre-Top Balder subsidence history of the basin.

For profiles A and E, the pre-Late Palaeocene history of the basin is modelled using the *FlexDecomp* package, this is illustrated in Figure 5.3

1. Profiles A and E are backstripped and decompacted to the Top Balder horizon, and the profile is flattened. As the palaeobathymetry of the Balder horizon is known to be approximately at sea-level, this is a useful starting point for the modelling.

2. The layers are sequentially flexurally backstripped, decompacted and thermal

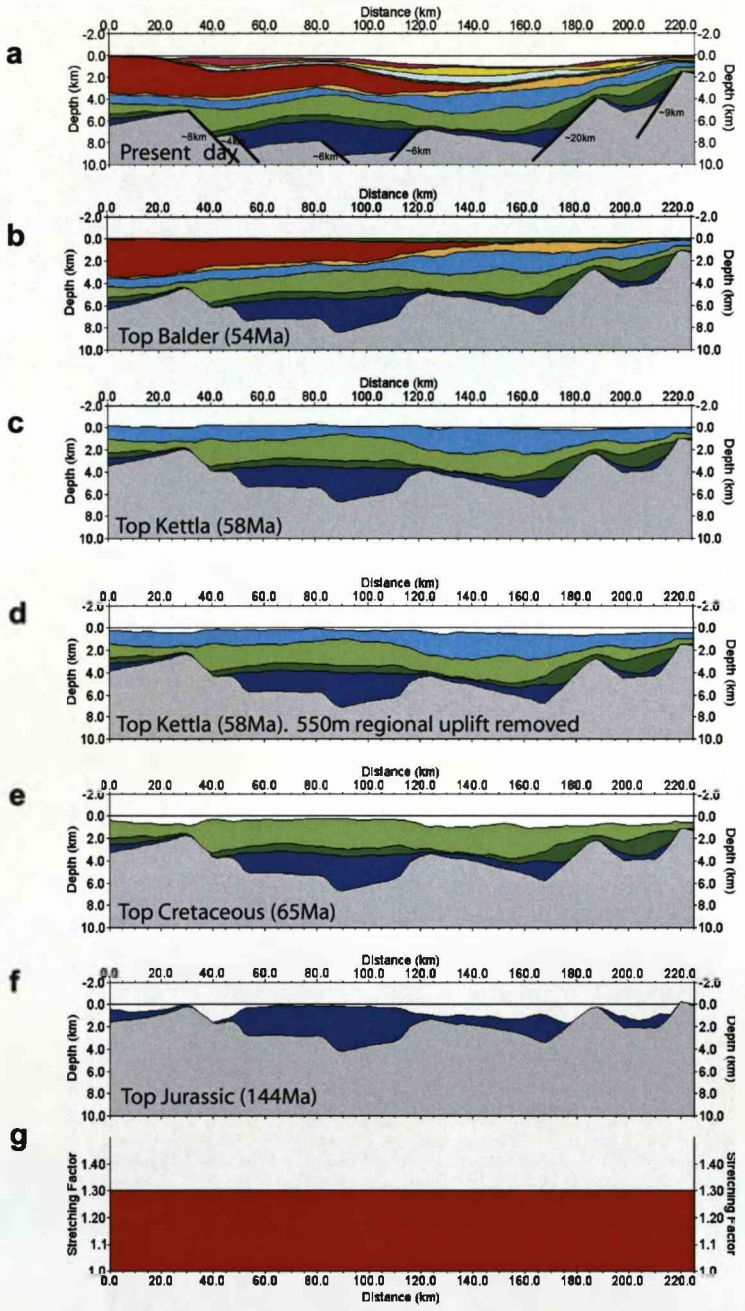

Figure 5.3: (**a**) Profile A (**b**) Profile A flattened at the Top Balder horizon. (**c**) after flexural backstripping, decompaction and reverse thermal subsidence modelling from a rift event (β=1.25 at 144Ma,(**g**) to the Top Kettla horizon. (**d**) A minimum of ~550m of uplift must be removed between Top Kettla and Top Balder to restore the Top Kettla horizon and the (**e**) Top Cretaceous horizons to marine paleogeography. (**f**) Late Jurassic subaerial fault block restoration can be achieved using this model. **g**)Magnitude of Late Jurassic rifting. (**h-n**) Next page - as **a-f**, but for profile E. Minimum uplift required on profile E is 450m. For layer properties see Figure 3.8.

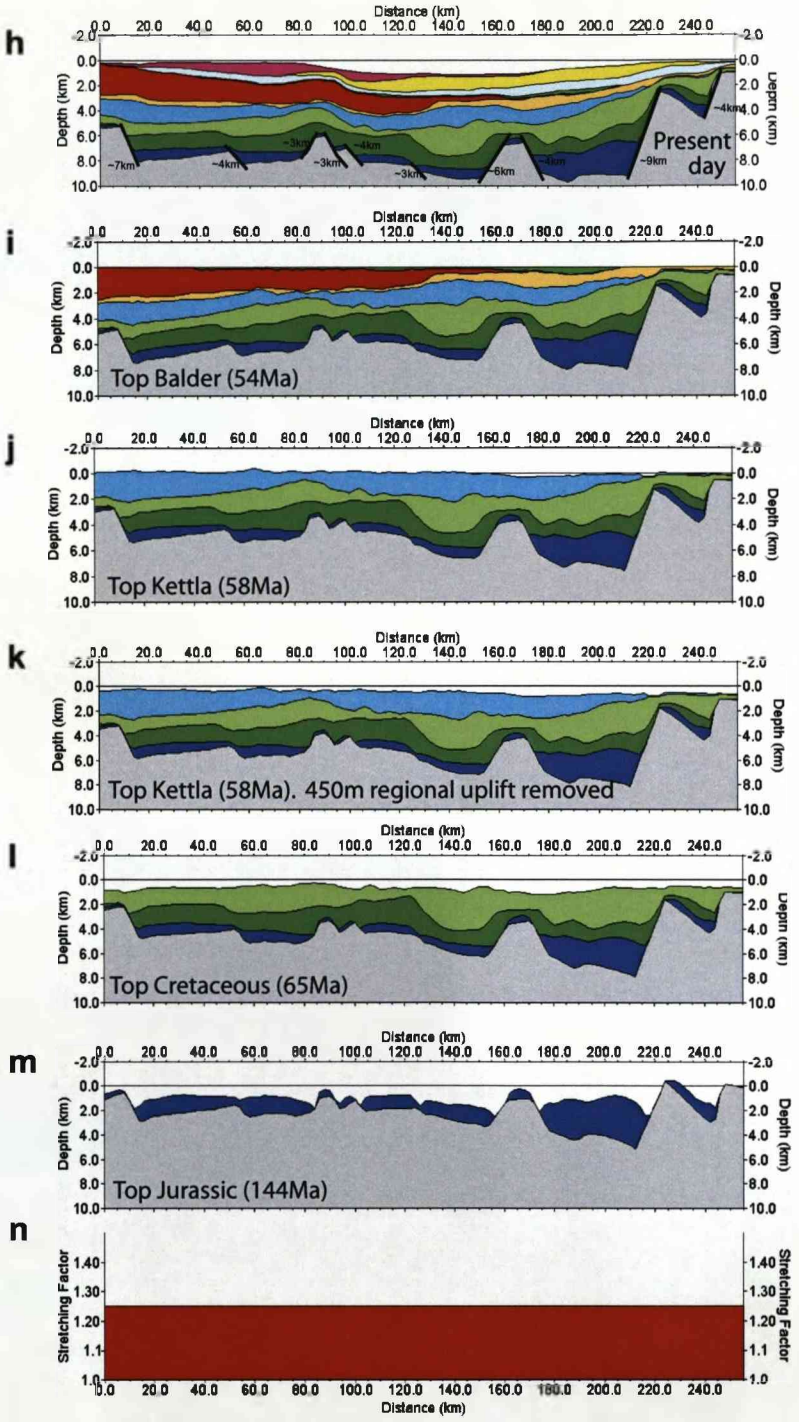

Figure 5.3: continued. See caption on previous page

subsidence from a basin-wide rifting event at 144Ma is reverse-modelled. The magnitude of the stretching event at 144Ma is assumed to be 1.3 for profile A and 1.25 for profile E, as determined from fault heaves in Chapter 4. When the layers above the Kettla tuff horizon are removed, shallow marine to emergent topography across the basin is predicted. There are no detailed palaeobathymetry data for the Kettla horizon, but the basin is thought to have been characterised by deep marine conditions during Kettla and lower Vaila deposition (Lamers and Carmichael, 1999).

3. Removing a minimum of 450-550m of transient uplift at this point in the back-stripping process produces an entirely marine profile across the basin. The precise timing of peak uplift cannot be determined here; however, the inference of an uplift event during the Late Palaeocene is consistent with previous work in the basin (e.g Smallwood and Gill, 2002; Champion et al., 2008) and other areas of the North Atlantic, which experienced Late Palaeocene uplift associated with volcanic breakup of the NE Atlantic, possibly in the presence of a mantle plume (e.g. White and McKenzie, 1989; Nadin et al., 1997).

4. Further backstripping through the Cretaceous produces sequential profiles with marine bathymetry until the top Jurassic, where presumed fault block crests are emergent, in agreement with the probable fault-top crest palaeogeography of the time.

The success of this simple model shows that the FSB's pre-Late Palaeocene history can be modelled using the pure-shear model of continental lithosphere extension and basin formation: Pure-shear extension was accommodated by faulting in the upper crust, and probably distributed pure-shear at deeper levels, in the Late Jurassic. The basin subsequently thermally subsided before eperiogenic uplift of at least 450m occurred during the Late Palaeocene. Mesozoic rifting was more protracted and complex than this single rift event model suggests, however the scarcity of detailed Mesozoic palaeobathymetric data precludes attempting a more detailed model of Mesozoic development

of the basin.

5.6 Modelling the 1–D Late Jurassic - Present Day subsidence history of the FSB

To compliment the 2–D subsidence history analysis, the subsidence history of pseudowell location PW2 is modelled using a 1–D numerical model of instantaneous pure-shear stretching events and transient uplift events. Models must honour the palaeobathymetrically-calibrated data points on a subsidence versus time plot - these were calculated in the previous chapter (and see Figure 4.6). The effect of effective elastic thickness used during backstripping of a stratigraphic column on the resulting 'best-fitting' geological history is also briefly illustrated. Because there are only three palaeobathymetrically-correct data points for pseudowell 2, the subsidence history can be honoured with many different rifting histories. However, other geologic and structural evidence may be used to assess the applicability of the model to the basin.

Modelling the FSB as a Mesozoic intracontinental rift basin

The FSB has previously been interpreted as a Mesozoic rift basin which underwent extension prior to the opening of the North Atlantic (Haszeldine et al., 1987; Mitchell et al., 1993; Hooper and Walker, 2002). The magnitude of the Late Jurassic-present day total subsidence and hence the stretching event required to satisfy that subsidence depends on the effective elastic thickness used during flexural backstripping and decompaction (Figure 5.4a). However, regardless of the effective elastic thickness used during backstripping, modelling the subsidence history of PW2 as post-rift subsidence from a single Late Jurassic rift event requires a Late Jurassic stretching factor of more than 2.8 (much greater than that implied from fault heaves) and transient uplift of more than 1700m in the Late Palaeocene (Figure 5.4b). Although several hundred meters of uplift probably occurred during the Palaeocene, the maximum regional post-Palaeocene subsidence, corresponding to the removal of transient uplift, which can be applied to

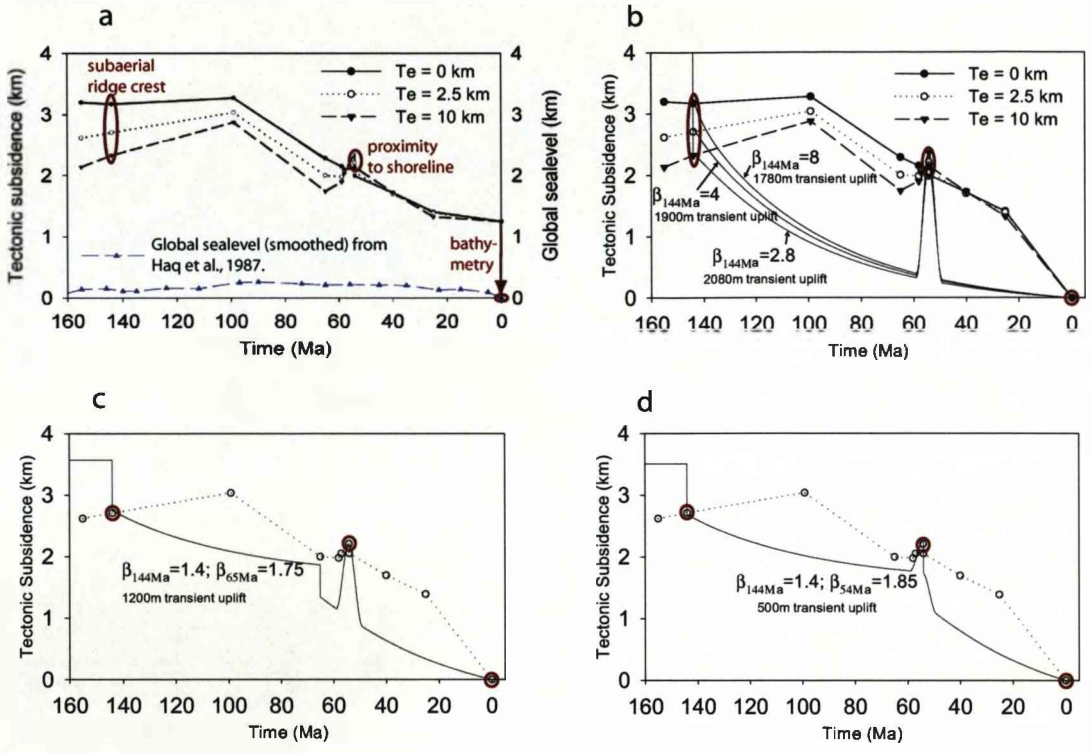

Figure 5.4: Forward modelling the 1–D subsidence history of the Faroe-Shetland basin. The subsidence history at PW2 is determined by flexural backstripping, and modelled assuming depth-uniform stretching. (**a**) Tectonic subsidence calculated using variable effective elastic thicknesses (Te) of 0km, 2.5km and 10km. Tectonic subsidence is corrected for first-order (smoothed) global sea-level variations (after Haq et al., 1987), which are also plotted. Palaeobathymetrically-corrected Late Jurassic and Top Flett (equivalent to Top Basalt) data-points are highlighted in red. Modelled tectonic subsidence should intersect the three palaeobathymetrically-corrected data-points. At all other times the basin is assumed to be marine and modeled tectonic water-loaded subsidence should plot below the calculated (maximum) tectonic subsidence data points. (**b**) Subsidence at PW2 is modeled as post-rift thermal subsidence from a single Late Jurassic rift event and a Late Palaeocene transient uplift event. Plot illustrates the effect that the presumed effective elastic thickness (Te) can have on the best-fitting theoretical model. (**c**) Subsidence at PW2 calculated using Te=2.5km modeled with two Mesozoic rift events and a Late Palaeocene transient uplift event. (**d**) Subsidence at PW2 calculated using Te=2.5km modeled with a Late Jurassic and Late Palaeocene rift events and a Late Palaeocene transient uplift event. Note that the apparent post-Palaeocene lithosphere thinning event in the FSB calculated using this method is higher than the value calculated for the same location in Figure 5.1f, because the effects of Mesozoic rifting were not included in the calculations used to produce Figure 5.1f.

the whole basin without violating palaeobathymetric constraints is 500m; therefore this model cannot explain the subsidence history of the basin.

To approximate protracted rifting, the basin can also be considered a product of Late Jurassic and Late Cretaceous rift events. However to satisfy the subsidence data, uplift of at least 1200m at the Late Palaeocene is required (Figure 5.4c), which again is much greater than the maximum value of 500m determined in the previous chapter. In agreement with the conclusions made in Section 5.2 and 5.4 using 2–D backstripped profiles, the Tertiary development of the basin cannot be explained if the basin is modelled as a Mesozoic rift basin.

Modelling the FSB as a Palaeocene intracontinental rift basin

Fault heave analysis and 2–D flexural backstripping suggested that the FSB experienced a Late-Jurassic -Early Cretaceous rifting event with a stretching factor between 1.25 and 1.5. The maximum regional subsidence which can be applied to the whole basin is 500m. Assuming an effective elastic thickness (Te) of 2.5km, Late-Jurassic-Late Palaeocene subsidence at PW2 can be modelled as post-rift thermal subsidence from a Jurassic rifting event, 500m of transient uplift peaking in the Late Palaeocene, and a post-top Palaeocene stretching event of β=1.85 (Figure 5.4d). However, post-Palaeocene upper crustal extension suggests than no post-Palaeocene rifting occurred, again illustrating that the apparent post-Palaeocene stretching factor of the basin is much greater than that implied by the sparse faults which offset the Late Palaeocene horizons.

5.7 Modelling the FSB as an intracontinental rift basin - summary

Both fault heave analysis and 1–D and 2–D analysis subsidence in the FSB suggest that the Late Jurassic to Late Palaeocene history of the basin can be successfully modelled by a Late Jurassic depth-uniform stretching event of magnitude between 1.25 and 1.3 and Palaeocene regional uplift of 450-550m. In contrast, the basin experienced large

amounts of post-Palaeocene water-loaded tectonic subsidence, which suggests that a significant rift event occurred in the Palaeocene, but only relatively minor Palaeocene or post-Paleocene upper crustal extension is observed. Post-Palaeocene subsidence in the FSB varies from ~500m on the flanks of the basin to 1400-2400m in the axis of the basin. These values imply a pre-Late Palaeocene stretching factor in the axis of the basin of at least β=2, or a post-Palaeocene stretching factors of at least β=1.2. However, Palaeocene faulting in the basin is minor (β<1.1), and post-Palaeocene faulting is minimal (β<1.01). The removal of regional transient thermal support (or other regional effect) since the Late Palaeocene may account for up to 500m of the post-Palaeocene subsidence, and residual post-rift thermal subsidence from Jurassic and Cretaceous rifting may also contribute to the post-Palaeocene subsidence. However, in the axis of the basin, the post-Palaeocene subsidence is at least 500m more than can be explained by pure-shear extension factors implied from upper crustal faults and removal of regional subsidence. This excess subsidence increases northwards to 1200-1600m on the Corona Ridge.

Seismic refraction and gravity modelling (see Section 3.3) show that crustal thickness is less than 11km in the basin axis, suggesting whole crustal stretching factors up to three. The timing of crustal thinning cannot be determined, but the magnitude is similar to that implied from the post-Palaeocene subsidence. More thinning is implied from crustal stretching factors than is suggested from summation of fault heaves on the top Jurassic and younger horizons (up to a factor of ~1.6). This suggests that a crustal thinning event which did not cause Jurassic or younger faulting has affected the basin, and may imply preferential removal of the lower crust.

If upper crustal stretching factors determined from faulting are assumed to be representative of whole lithosphere stretching, then there is a discrepancy between the observed subsidence, crustal thickness and extension accommodated by faulting in the upper crust. In the following section I will consider possible explanations for these discrepancies, and the implications for understanding the formation of the FSB.

5.8 Possible causes of anomalous subsidence in the Faroe-Shetland basin

5.8.1 Transient support by the Iceland plume

Transient uplift caused by elevated mantle potential temperatures or dynamic support from mantle upwelling has been inferred to explain subsidence history anomalies all over the North Atlantic close to the time of continental breakup and coincident with massive outpourings of basalt (Nadin and Kusznir, 1995; Nadin et al., 1997; Mackay et al., 2005; Champion et al., 2008) at the proto-Atlantic margin. Nadin et al. (1997) and Champion et al. (2008) calculate transient uplift at Late Palaeocene times in the FSB as 900m and >490m respectively. However, a single valued transient uplift event cannot restore the Late Palaeocene palaeobathymetry when the basin is reverse modelled. Transient uplift caused by a caused by a large mantle feature such as a plume would be expected to have a diameter of more than 2000 km (White and McKenzie, 1989). The anomalous post-Palaeocene subsidence in the FSB has a short wavelength which correlates with present day bathymetry, and does not decrease away from the inferred location of the Iceland plume at the end of the Palaeocene. Transient uplift also cannot explain thinning of the crust to <11km thickness. Thus dynamic plume support alone cannot explain the departure from thermal subsidence from Late Jurassic and Palaeocene rift events.

5.8.2 Underplating?

Igneous underplating beneath the Faroe Islands and FSB, related to continental break-up at end Palaeocene times has also been suggested as a mechanism for anomalous subsidence in the North Atlantic (Clift and Turner, 1998; Ceramicola et al., 2005; England et al., 2005). Igneous intrusion (underplating) of the lower crust can cause uplift due to thermal expansion which is transient; and crustal thickening by volcanic addition which is permanent. The amount of uplift U caused by the addition of a layer of x thickness and a density of ρ_x to the lithospheric column is given by the following

equation (adapted from Brodie and White (1994)):

$$U = (\frac{\rho_m - \rho_x}{\rho_m - \rho_{infill}})x \tag{5.9}$$

where ρ_m is the mantle density and ρ_{infill} the density of the infill material (air or water). The relaxation of plume-related regional uplift may have been partially offset by permanent uplift on the Faroese flank of the basin due to underplating, resulting in short wavelength post-break-up subsidence. The Faroese flank of the basin has subsided at least 500m less than the centre of the basin since deposition of the Top Balder horizon. Assuming a mantle density of 3330kgm^{-3}, underplate density of 3000kgm^{-3}, and water density of 1000kgm^{-3}, post-Palaeocene age underplate at least 3.5 km in thickness is required to account for this difference. Wide angle seismic imaging on the Faroese margin (Bohnhoff and Makris, 2004; Raum et al., 2005; Roberts, 2007) identified a few km of high velocity lower crust, which may be partly responsible for the uplift of the Faroe Islands. However, the high velocity lower crust does not underlie the basin. Furthermore, underplating is thought to occur synchronously with massive outpourings of basalt during continental breakup (Cox, 1993), so permanent uplift from crustal thickening is likely to have occurred prior to deposition of the Top Balder horizon (which represents the end of massive volcanism). Thus underplating is both too thin and probably too old to explain the short wavelength post-Palaeocene subsidence across the basin. Uunderplating also does not explain thinning of the crust to less than 11km.

5.8.3 Inversion and crustal thickening?

The North Atlantic margins have experienced a number of compression events since breakup (Boldreel and Andersen, 1993, 1998; Andersen et al., 2000). Crustal thickening due to compression on the Faroes block may explain the short wavelength post-Palaeocene subsidence across the FSB. Compression in the FSB area is manifested by minor faults and folds. Shortening in the Faroes area has not been quantified, although it is relatively minor. Compression on the Norwegian margin is estimated at 2-3%

(Vagnes et al., 1998), and is likely of a similar magnitude in the Faroes area. The Fugloy ridge is an anticlinal structure, although this is probably due to subsidence on each side of the ridge rather than due to shortening (Hurst et al., 2004). No major reverse faults have been identified which could have thickened the crust sufficiently to account for the relative uplift of the Faroes block, therefore it seems unlikely that compression of the Faroes block can account for the anomalous subsidence of the basin.

5.8.4 Unrecognised faulting?

The amount of lithospheric thinning indicated by the magnitude of post-Palaeocene subsidence (β_{lith}>2) is far greater than the amount of thinning indicated to have occurred in the upper crust by faulting (β_{crust}<1.01). For other basins and margins where depth-dependent stretching has been documented, Reston (2007) suggests that extension accommodated by faulting is underestimated due to poor seismic imaging, second generation faulting or sub-seismic resolution faulting. However, Davis and Kusznir (2004) use the fault scaling relationships of Walsh et al. (1991) to show that unrecognised faulting cannot explain observed discrepancies between apparent upper crustal and whole lithosphere stretching factors at the Goban Spur, Galicia bank, Vøring and South China sea margins. In the FSB, many (large) unrecognised faults would be required to account for the large amount of extension (more than 100%) implied by post-Palaeocene subsidence. However, there is a dense array of 2–D and 3–D seismic imaging within the FSB, and it is very difficult to imagine that significant faulting within and above the Palaeocene horizons has not been recognised. It is therefore considered very unlikely that unrecognised faulting can explain the descrepancy between upper crustal extension and thinning factors implied by post-Palaeocene subsidence in the FSB.

5.8.5 Phase changes?

Phase changes in the lithospheric mantle or lower crust could potentially thin the seismic and gravity-defined crust, and load the lithosphere to cause subsidence. The

addition of crustal material (i.e. by volcanic addition) however, generates uplift, not subsidence, unless underplating occurs in the eclogite stability field, which is unlikely (McKenzie, 1984). Crustal phase transformation from gabbro to eclogite or garnet granulites cause density to increase and would therefore cause subsidence, but these transformations are unlikely to occur at depths shallower than 50km, particularly if temperatures are high. Petrini et al. (2001) show that the consideration of metamorphic reactions reduces the syn-rift subsidence and increases the initial post-rift subsidence rate compared to the model of (McKenzie, 1978). However, the magnitude of these effects are insufficient to explain the large discrepancy between observed faulting and subsidence in the FSB.

5.8.6 Depth-dependent lithosphere stretching?

Depth-dependent lithosphere stretching, where upper crustal stretching, as indicated by extensional faulting, appears to be substantially less than stretching of the whole crust and mantle has previously been recognized at both volcanic and non-volcanic rifted margins, as well as ahead of propagating rift tips (Royden and Keen, 1980; Clift et al., 2001; Davis and Kusznir, 2004; Kusznir et al., 2004, 2005; Kusznir and Karner, 2007). Although a pure-shear model of intracontinental rifting can be applied to the pre-Atlantic history of the FSB, post-Palaeocene lithospheric extension in the FSB cannot be explained by a model of depth-uniform lithosphere thinning and extension by pure-shear. The high magnitude of subsidence and crustal thinning, but paucity of extensional faulting since the end of the Palaeocene may be explained if extension and thinning of the FSB is considered to be depth-dependent. The implications of this are discussed in the following chapter. A simple conceptual model of depth-dependent stretching is shown in Figure 5.5.

5.9 Summary

The applicability of the pure-shear model of continental lithosphere extension and basin formation (McKenzie, 1978) has been tested by comparing the amount of stretching

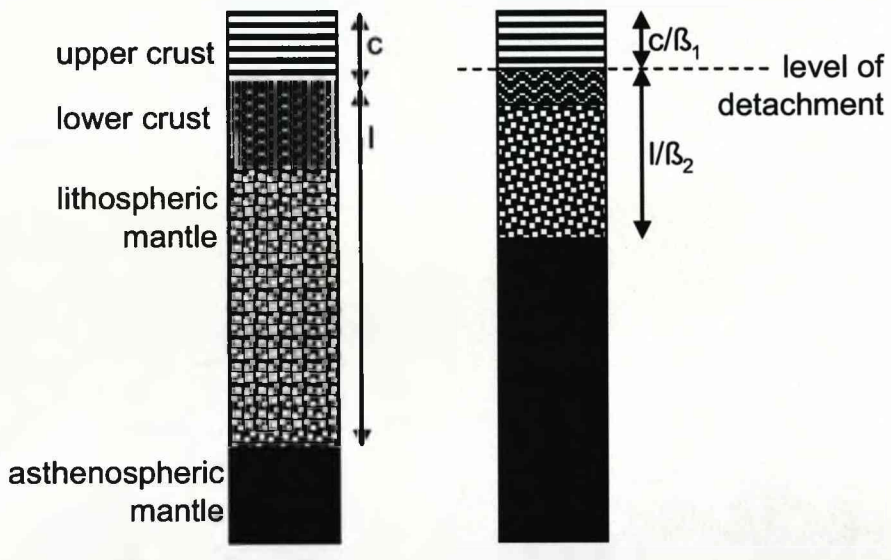

Figure 5.5: Schematic model of depth-dependent stretching for a 1–D lithosphere column. In this simple model of depth-dependent stretching, the upper lithosphere above a detachment surface stretches by a factor of β_1, whilst the lithosphere below the detachment is stretched by a factor of β_2. In the cartoon shown here the detachment surface is arbitrarily chosen to be in the mid-crust. In the Earth the distribution of stretching with depth may evolve with both depth and time.

and thinning implied for the upper crust (from fault heave analysis), the whole crust (from crustal thickness estimates), and the whole lithosphere (from subsidence analysis). The pure-shear model assumes that thinning is depth-uniform. Although the Late Jurassic to Late Palaeocene subsidence history of the FSB is consistent with lithosphere thinning by a pure-shear stretching mechanism, the post-Palaeocene subsidence cannot be explained by the pure-shear model. Palaeocene lithospheric stretching and thinning in the FSB appears to be depth-dependent; the lithospheric mantle and lower crust have been thinned more than the upper crust. In the next chapter I examine the implications of depth-dependent stretching on models of basin development, as well as discussing possible causative mechanisms and the implications for understanding basin formation and continental lithospheric breakup.

Chapter 6

Depth-dependent stretching in the Faroe-Shetland basin

6.1 Introduction

Lithospheric thinning in the Faroe-Shetland basin (FSB) is depth-dependent; more extension is implied by post-Palaeocene subsidence than can be explained by extensional faulting in the upper crust. The effects of depth-dependent stretching on subsidence, heatflow and melting are discussed in this chapter.

At Late Palaeocene times the FSB was coaxial with the incipient Møre margin (Figure 2.13), and is just inboard of the Faroes Margin, consequentially the basin may have been affected by the processes which caused lithospheric rupture on these margins. In this chapter an attempt to resolve the timing of depth-dependent stretching in the basin is made, and the likely cause of depth-dependent stretching in the FSB is discussed. At the end of this chapter a summary of the analysis of the FSB presented in chapters 3 to 6 is given.

6.2 Implications of a depth-dependent stretching model of basin formation for the FSB

Depth-dependent lithosphere stretching, where the lower crust and lithospheric mantle are preferentially thinned with respect to the upper crust, results in subsidence, heat-flow and melting which differ from that predicted by the McKenzie (1978) model of depth uniform lithosphere stretching (Royden and Keen, 1980; Kusznir et al., 2005). A simple 1D model of depth-dependent stretching was illustrated in Figure 5.5. Above a detachment level, the lithosphere is thinned by a factor of β_1, whilst below the detachment the lithosphere thins by a factor β_2. The difference between depth-uniform and depth-dependent stretching of the continental lithosphere has important consequences on the temperature evolution in depth and time. If lithospheric thinning and stretching is assumed to occur by pure-shear and thermal models of basin evolution are made based on stretching factors calculated using upper crustal extension estimates alone, significant under-prediction of subsidence, heat-flow, and hydrocarbon maturation can result (Kusznir et al., 2005).

To demonstrate the problems associated with making predictions based on apparent stretching factors, tectonic subsidence, heatflow and crustal thickness history predicted by a depth-dependent stretching model is compared with those predicted by depth uniform models (Figure 6.1**a-c**). Three models are considered. In all three of the models, an initial lithospheric stretching event of β=1.4 occurs at 144Ma, and is followed by an event at 54Ma. The 'events' considered are 1.) No extension (corresponding to β=1); 2.) Pure-shear thinning by a factor of 3 (β=3); 3.) Depth-dependent thinning, where the upper crust thins by a factor of 1 and the lower crust and lithospheric mantle thin by a factor of three (β_1=1, β_2=3). The depth-dependent model is calculated using the model of decoupled pure-shear of Royden and Keen (1980).

For the model where lithosphere thinning is depth-dependent (β_1=1, β_2=3), syn-breakup subsidence is reduced with respect to the depth-uniform, β=3, model. This is because crustal thinning in the depth-dependent model is reduced with respect to

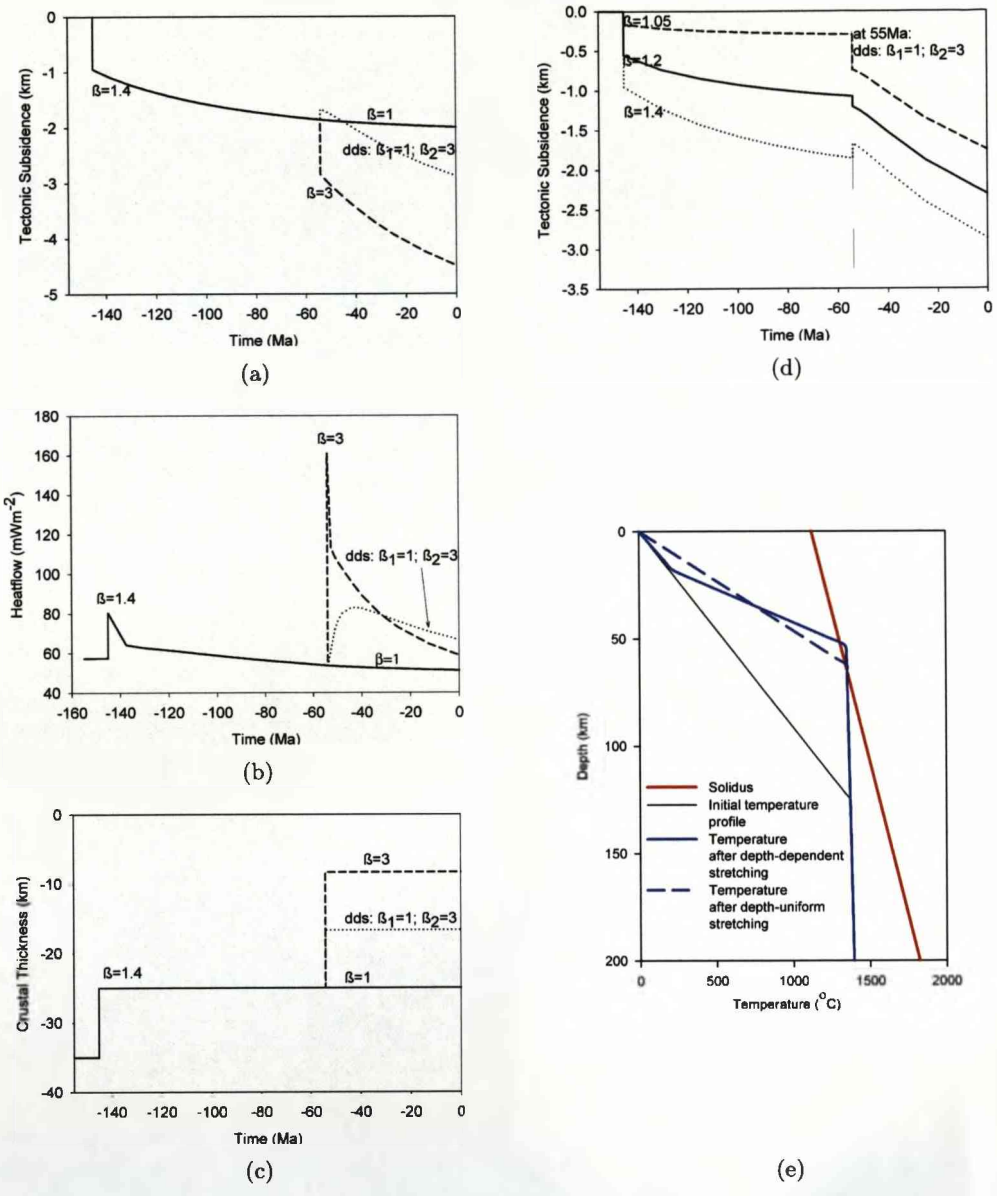

Figure 6.1: (**a-c**) Tectonic subsidence, heatflow and crustal thickness evolution predicted by depth-uniform and depth-dependent stretching models. Calculated assuming initial crustal thickness of 35km and decoupling is assumed to occur in the mid crust. (**d**) Sensitivity of syn-rift subsidence to magnitude of initial rift event and crustal thickness at time of depth-dependent stretching. (**e**) Temperature structure of depth-uniform and depth-dependent stretching scenarios with equivalent whole-lithosphere thinning, such that the integrated thermal perturbation at the end of the syn-rift for each scenario is the same. For the depth-dependent model, where the lithospheric mantle and lower crust are thinned preferentially compared to the upper crust, more melting is predicted than for the depth-uniform model.

the depth-uniform model. The magnitude of post-rift thermal subsidence is mainly dependent on the stretching factor of the lower lithospheric layer, and so thermal subsidence for the depth-uniform (β=3) model is similar to that for the depth-dependent (β_1=1, β_2=3) model. The depth-dependent stretching model predicts a later and lower heat-flow peak than the depth-uniform model, as the thermal perturbation takes time to conduct through the upper layer. Additionally, syn-breakup subsidence (or uplift) is sensitive to the magnitude of earlier stretching events (Figure 6.1**d**), and the level at which the detachment occurs.

In Figure 6.1**e** the temperature structure after depth-dependent stretching, where the lithospheric mantle and lower crust are preferentially thinned compared to the upper crust, is compared to that of depth-uniform stretching model. The integrated thermal anomaly of the two models (and therefore the total post-stretching thermal subsidence which will occur) is equal, yet the depth-dependent model predicts more melt than the depth-uniform stretching model.

These tests illustrate the potential problems which may be encountered if apparent stretching factors calculated for the upper crust, whole crust or whole lithosphere are assumed to represent the magnitude of depth-uniform thinning. For example, if thinning is assumed to be depth-uniform and heatflow is calculated by estimating the magnitude of thinning from fault heave analysis, but thinning was actually depth-dependent, then the heatflow history will be mis-predicted. Furthermore, the simple model of depth-dependent stretching presented above assumes instantaneous stretching and a discrete detachment surface which is arbitrarily chosen to be the middle of the crust. In reality depth-dependent stretching may be more accurately described as a function which varies with depth and time. For example, if depth-dependent stretching is considered to be a bottom-upwards process, the lithospheric mantle may be thinned prior to the lower crust, which would result in uplift (caused by thinning of the lithospheric mantle), then rapid subsidence (caused by lower crustal thinning) and then post-rift thermal subsidence. This type of syn-rift uplift may explain some of the Palaeocene uplift and subsequent subsidence in the FSB.

6.3 Timing of depth-dependent stretching in the FSB

At Late Palaeocene times, the FSB was close to the site of proto-Atlantic continental breakup and seafloor spreading initiation. Between mid-Norway and the Hatton margin, the oldest magnetic anomaly on the North Atlantic margin is Chron 24r (Muller et al., 1997) suggesting that the onset of seafloor spreading along this section of the margin occurred approximately synchronously in geologic time. The uplift maxima in the FSB coincides with voluminous volcanism on the Faroes margin and the emplacement of the Seaward Dipping Reflectors. Post-Palaeocene subsidence in the FSB therefore represents subsidence which occurred during or after seafloor spreading initiation in the Atlantic. But what is the timing of the depth-dependent stretching? Did it occur before, during or after seafloor spreading initiation on the NE Atlantic margin? Understanding the timing of depth-dependent stretching in the FSB has implications for understanding continental breakup processes. If depth-dependent stretching in the FSB occurred prior to Atlantic breakup, we may interpret the FSB as an abandoned site of breakup, where the locus of thinning and strain migrated (or jumped) from the FSB to the Faroes margin (Figure 6.2a). If the depth-dependent stretching occurred during or after Atlantic breakup, this may suggest that intense lithospheric thinning during continental breakup may sometimes occur simultaneously along more than one axis (Figure 6.2b). Preferential thinning of the lithospheric mantle and lower crust is unlikely to significantly post-date breakup, because maximum extensional stress and thermal energy will have occurred immediately around the time of continental rupture of the Atlantic.

Subsidence histories may be useful for constraining the mode of lithosphere thinning. For example, syn-rift uplift was predicted by the instantaneous depth-dependent stretching model in Figure 6.1a. If depth-dependent stretching is an upwards propagating lithospheric deformation process (i.e. the lithospheric mantle thins prior to the lower and upper crust), then uplift during lithospheric mantle thinning will occur. However, Palaeocene uplift in the FSB is not necessarily diagnostic of depth-dependent stretching, as regional Late Palaeocene uplift from a mantle plume around much of the

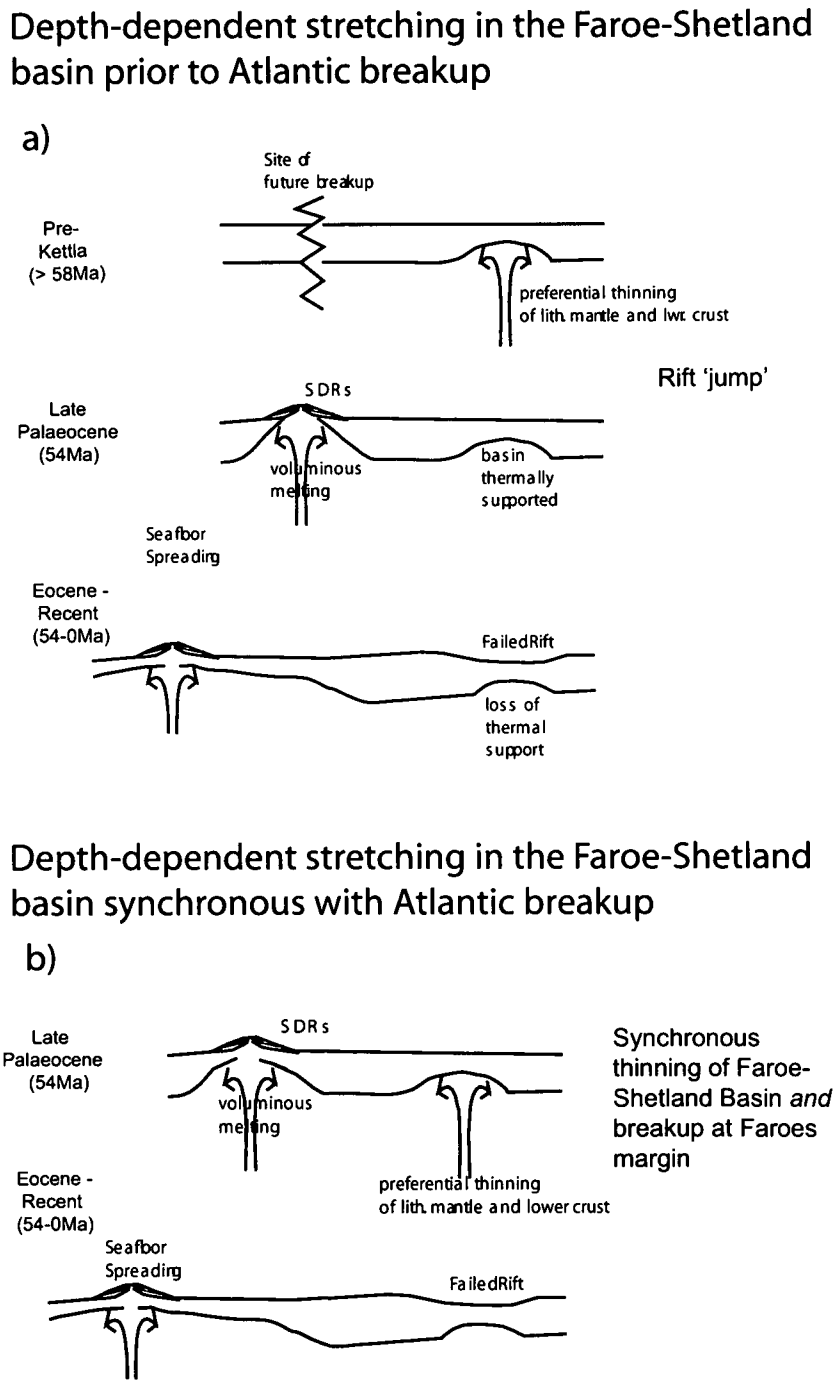

Figure 6.2: Timing of depth-dependent stretching in the Faroe-Shetland basin. Schematic illustration of (**a**) pre-Atlantic breakup and (**b**) syn-Atlantic breakup depth-dependent stretching in the FSB.

North Atlantic may obscure that caused by depth-dependent stretching. Similar problems separating the effects of syn-thinning and regional subsidence and uplift, and the effects of underplating have been encountered when reverse modelling the Norwegian margin (Roberts et al., 2009). If detailed subsidence histories were available all over the basin, then depth-dependent stretching may be manifested as uplift of the basin axis relative to the flanks due to preferential thinning of the lithospheric mantle in the axis. Plume-related regional uplift would be expected to affect the whole basin approximately equally and simultaneously. Similarly, fast rates of subsidence immediately before and after the Balder formation (Smallwood and Gill, 2002; Champion et al., 2008) may be suggestive of preferential lower crustal thinning at this time, but without more detailed subsidence data this signal cannot be distinguished from subsidence due to post-plume collapse.

Pre-Late Palaeocene or syn/post-Late Palaeocene depth-dependent stretching?

In the southern axis of the FSB, there has been at least 500m of post-Palaeocene subsidence which cannot be explained by the removal of dynamic support or by residual thermal subsidence from Mesozoic rifting. Further northeast, on the Corona Ridge, this value increases to over 1500m of 'excess' post-Palaeocene subsidence. In an attempt to resolve the question of timing of depth-dependent stretching in the FSB, I have modelled 1500m of excess post-Palaeocene subsidence and predicted melt thicknesses using three simple 1D models:

In the first model (Figure 6.3a), 1.5km of subsidence is modelled as the result of a pure-shear stretching event at 54Ma of magnitude β=1.6. In this model no melting is predicted. This model is incompatible with seismic images of post-Palaeocene upper crustal extension, which indicate that very little stretching has occurred.

In the second model (Figure 6.3b), lithosphere stretching is depth-dependent and instantaneous (54Ma). Excess post-Palaeocene subsidence is modelled as post-rift thermal subsidence following depth-dependent stretching. This would be the case for the

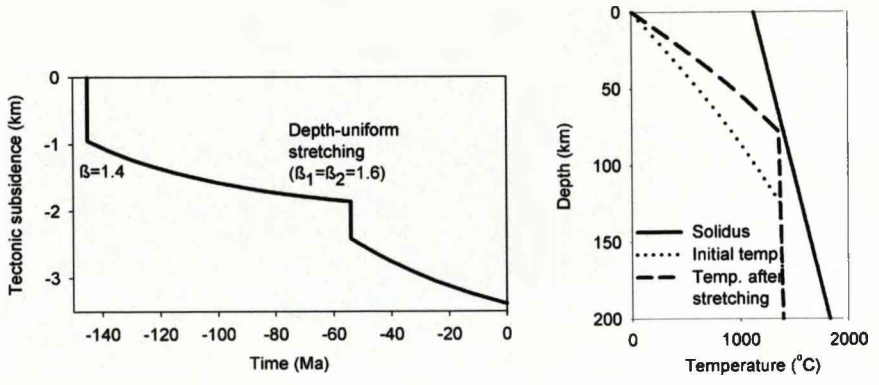

(a)

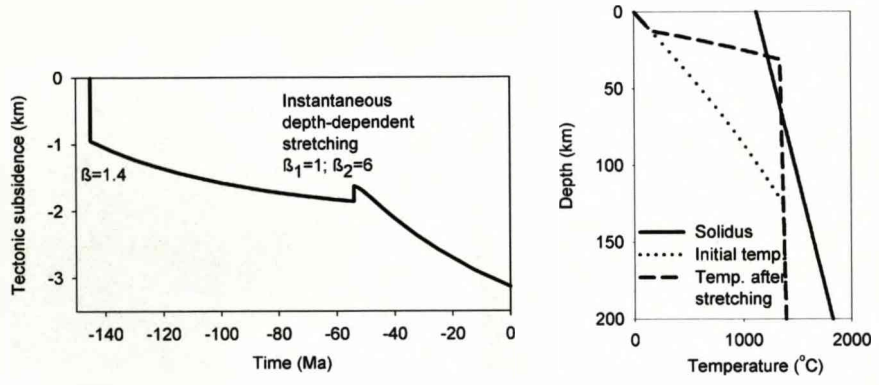

(b)

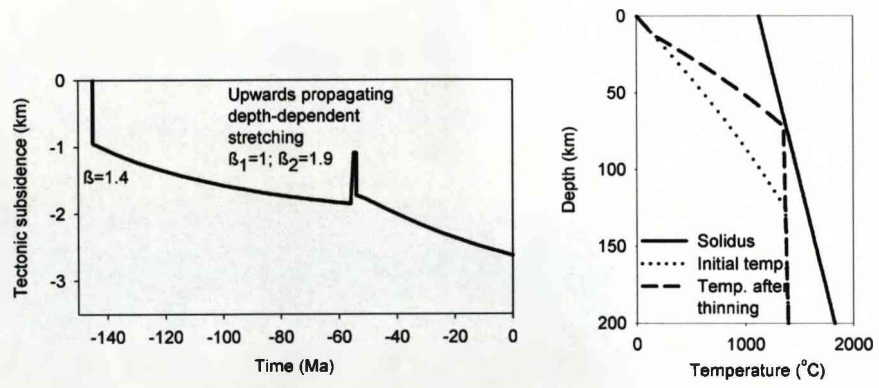

(c)

Figure 6.3: Models of depth-dependent stretching in the Faroe-Shetland basin. Subsidence history and temperature structure predicted by (**a**) Instantaneous depth-uniform, (**b**) instantaneous depth-dependent, and (**c**) upwards-propagating depth-dependent stretching models. Each model predicts 1.5km post-Palaeocene subsidence, but the upper crustal extension, temperature structure and predicted thickness of melt varies between the models.

FSB if depth-dependent stretching occurred prior to breakup of the Atlantic. Using this model, post-Palaeocene subsidence of 1.5km requires β_2=6. This magnitude of lower lithospheric thinning results in melting of the lithospheric mantle, and a melt thickness of 1.8km is predicted.

In the third model (Figure 6.3c), depth-dependent stretching is upwards propagating: the lithospheric mantle is thinned first, before the end of the Palaeocene, then the lower crust is thinned post-end Palaeocene. Upper crustal extension is again assumed to be negligible (β_1=1). Uplift caused by thinning the lithospheric mantle therefore precedes subsidence caused by lower crustal thinning. Excess post-Palaeocene subsidence is modelled as that which occurs between the maximum uplift (after lithospheric mantle thinning but before lower crustal thinning) and present day. This model corresponds to depth-dependent stretching occurring in the FSB at the same time as, or shortly after, Atlantic breakup. This model requires β_2=1.9, and no melting is predicted.

An important difference between the second and third models presented above is the thickness of melt predicted. The amount of melt predicted by the instantaneous depth-dependent stretching model is greater than that predicted by the upwards propagating depth-dependent stretching model. Whilst voluminous volcanism occurred on the Faroes margin at the end of the Palaeocene, resulting in the west of the basin being covered in thick extrusive basalts, only minor melting occurred underneath the FSB. Small Palaeocene eruptive centres and sills (see Section 3.5) show that some melting occurred under the FSB around the time of breakup, but large (km-scale) thicknesses of intrusives have not been imaged. It seems unlikely that more than 2km thicknesses of intrusives exists within or beneath the FSB.

Although it is not possible to discriminate between these two models' applicability to the FSB based on melting predictions alone, Late Palaeocene continental breakup of the proto-Atlantic is thought to have been accompanied by high mantle potential temperatures (White and McKenzie, 1989). Increasing the mantle potential temperature would increase predicted melt thickness for the models shown in Figure 6.3. Assuming that the asthenosphere beneath the FSB was undepleted, the low melt thicknesses are

more easily explained with the upwards propagating depth-dependent stretching model, implying that depth-dependent stretching in the FSB was occurring at the same time as continental breakup on the Faroes margin, and that part of the post-Palaeocene (post-Top Balder) subsidence is syn-thinning subsidence. Lower crustal thinning during Balder times also helps to explain fast rates of subsidence between the Flett and early Ypresian, and the rapid creation of accommodation space during the Balder and through the Eocene. Furthermore, the predominantly Late Palaeocene ages of the sills and volcanic centres in the FSB support a Late Palaeocene age for maximum (depth-dependent) thinning.

6.4 Failed continental breakup in the FSB

Ocean isochrons (e.g. Figure 3.5**a**) suggest that continental rupture occurred simultaneously between mid-Norway and Hatton Bank (Muller et al., 1997), around Chron 24. This implies that rifting either did not propagate along that section of the margin or propagated faster than can be resolved with current techniques. This work suggests that preferential lithosphere and lower crustal thinning in the FSB occurred synchronously with the emplacement of SDRs and the onset of seafloor spreading at the Faroes margin.

The FSB is coaxial with the Møre Basin to the north, inboard of the Møre continental margin. Much larger Mesozoic extension (up to a factor of two (Roberts et al., 2009)) occurred in the Møre basin than in the FSB, and the Møre basin is a wide zone of highly thinned continental crust (e.g. Figure 3.5**a**). The Møre basin has also experienced more post-Palaeocene subsidence than can be explained by upper crustal extension (Kusznir and Karner, 2007; Roberts et al., 2009), and so may also represent a site of preferential lithospheric mantle and lower crustal thinning which occurred during the latter stages of Atlantic breakup. However, more public-domain seismic and subsidence analysis would be required to compare the Møre basin to the FSB.

There are a number of conceptual explanations for the failure of continental lithospheric rupture in the FSB. One is a ridge-jump model, where thinning was localised within the

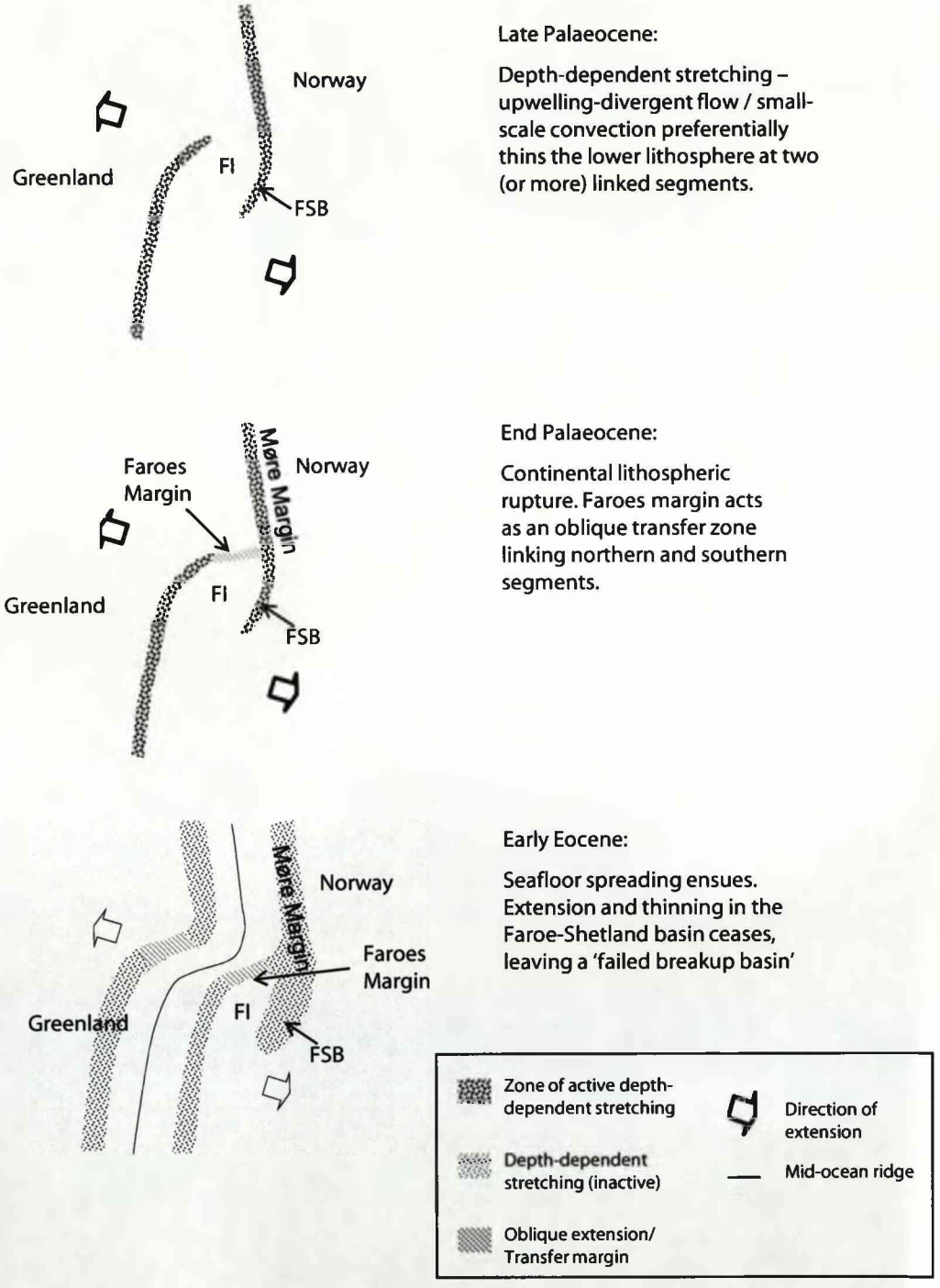

Figure 6.4: Formation of the FSB by linked propagation. FI denotes location of the Faroe Islands on the Faroes continental block.

FSB before jumping or migrating westwards to the location of breakup at the Faroes margin. However, since continental lithospheric thinning occurred synchronously beneath both the FSB and at the Faroes margin, the ridge-jump model is inappropriate. The development of the FSB with respect to opening of the Atlantic is consistent with a model of continental breakup by a linked propagation process (Figure 6.4). In the simplified conceptual model shown in Figure 6.4, during the Palaeocene, depth-dependent thinning was occurring along two offset, but overlapping zones prior to breakup: one along the FSB-Møre basins and one to the west of the Faroes continental block and towards the Hatton margin. Continental breakup subsequently occurred at the end of the Palaeocene to the west of the Faroes and at the Møre margin, with the Faroes margin acting as an oblique 'relay zone'. Active thinning and deformation in the FSB subsequently ceased, leaving a 'failed breakup basin'. The ultimate site of continental rupture may have been determined by the strength of the lithosphere; the pre-thinned lithosphere in the FSB is likely to have been stronger than unthinned lithosphere (e.g. England et al., 2005).

The phenomenon of linked propagation suggested for the formation of the FSB during continental breakup of the Atlantic margin is analogous to overlapping spreading centres at mid-ocean ridges (e.g. Macdonald and Fox, 1983), and to fault segmentation and relay zones in fault zones and rifts. Further observations in the surrounding margins and at other potential failed breakup basins and modelling may enable this hypothesis for the behaviour of the continental lithosphere during continental breakup to be tested.

Depth-dependent stretching models of continental lithosphere thinning can result in a space problem. In the 1–D models presented in this chapter, stretching of the upper and lower lithosphere is decoupled at a detachment level. However the mismatch between upper and lower lithospheric extension across this detachment level must be accommodated elsewhere. One explanation is that upper crustal extension was accommodated over a much wider area (1000's km wide) than extension in the lower lithosphere; however extension over such a large area (which would extend across much of northern Europe) in the Late Palaeocene has not been observed. An alternative explanation is

that the lower crust and lithospheric mantle are pushed outwards, effectively thickening these layers on the flanks of the basin, or moved out of the plane of section due to three-dimensional processes. However the mechanism by which this can occur is not clear. Preferential lithospheric thinning may occur during small-scale convection in the lithospheric mantle and lower crust (e.g. Huismans et al., 2001a). Two-dimensional models of lithospheric thinning are investigated in the remainder of this thesis, and are applied to the FSB in Chapter 10.

6.5 Summary

1. In the Faroe-Shetland basin, the magnitude of stretching implied by post-Palaeocene subsidence and by whole crustal thinning far exceeds that implied by upper crustal faulting. The magnitude of post-Palaeocene subsidence in the FSB suggests whole lithosphere stretching factors of more than 3 if the stretching is assumed to be Palaeocene or older, or at least 1.2 if the stretching is assumed to be younger than Palaeocene. Wide-angle seismic surveys and gravity inversion suggest that the crust is stretched by up to a factor of 3. However, determination of stretching factors derived from upper crustal faulting seen in the seismic profiles indicate far less extension than is inferred from the magnitude of subsidence.

2. Much of the Faroe-Shetland basin was close to sea-level at the end of the Palaeocene, and so post-Palaeocene water-loaded tectonic subsidence can be determined over large areas. Post-Palaeocene water-loaded tectonic subsidence is ~500m on the basin flanks, in the southwest axis of the basin post-Palaeocene subsidence is ~1500m, increasing north-eastwards to ~2400m over the Corona Ridge. A maximum of ~500m of post-Palaeocene subsidence can be accounted for by regional subsidence following transient uplift caused by a mantle anomaly such as a plume. Therefore the short wavelength post-Palaeocene subsidence cannot be accounted for by regional baselevel changes associated with the proto-Iceland plume, as suggested by Nadin et al. (1997) and Champion et al. (2008). Compression and

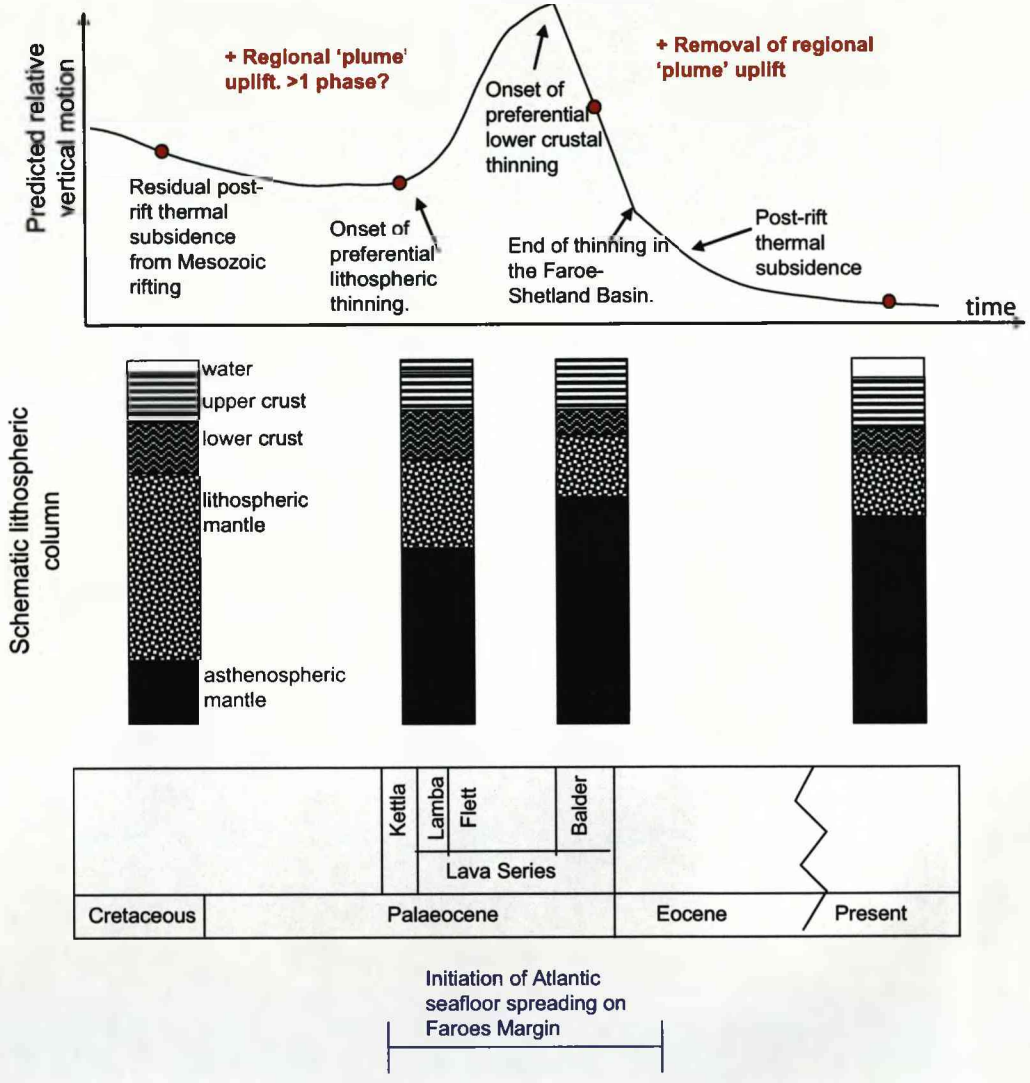

Figure 6.5: Preferred schematic model for lithosphere thinning in the Faroe-Shetland basin

underplating have been suggested as causes of anomalous subsidence in the basin, however neither the thickness of underplating nor the extent of compression required to account for the subsidence anomaly are supported by seismic evidence. Furthermore, transient plume uplift, underplating and compression theories for the anomalous subsidence also fail to explain the thin crust beneath the axis of the FSB.

3. Fault heave analysis and 1–D and 2–D analysis subsidence in the FSB show that the Late Jurassic-Late Palaeocene tectonic evolution of the basin can be successfully modelled by a Late Jurassic depth-uniform stretching event of magnitude 1.25 to 1.5, and Palaeocene regional uplift of ~500m. This demonstrates the applicability of a pure-shear model of rifting for the Mesozoic history of the basin.

4. Palaeocene and Post-Palaeocene lithospheric extension in the FSB appears to be depth-dependent. The precise timing of depth-dependent stretching is difficult to constrain, particularly as transient regional uplift and subsidence may have obscured the signal in the subsidence history. However, Palaeocene uplift and rapid Late Palaeocene to early Eocene subsidence suggest that depth-dependent stretching in the FSB probably occurred at the same time as continental lithospheric rupture on the Møre and Faroes Margins. The model of simultaneous lithospheric thinning in the FSB and at the proto-Atlantic margin is also supported by the ages of sills in the basin. Additionally, it is difficult to explain the magnitude of post-Palaeocene subsidence as post-depth-dependent stretching thermal subsidence without invoking a significant thickness of melting in the basin, which is not observed. I conclude that depth-dependent stretching in the FSB probably occurred during the Late Palaeocene, synchronous with breakup and early seafloor spreading (Figure 6.5).

5. The development of the FSB with respect to opening of the Atlantic is consistent with a model of continental breakup by a linked propagation process, where thinning was occurring at two offset but overlapping segments, before breakup

occurred, leaving a failed breakup basin (the FSB). It is unclear why lithospheric thinning in the FSB was abandoned and strain localised at the Faroes margin. It is possible that the lithosphere in the FSB had been strengthened by previous rift events.

6. The mode of lithospheric deformation responsible for depth-dependent stretching is also not well understood, and it is this question which serves as the motivation for the further investigation of the processes which occur during continental lithospheric thinning and breakup. This is done using both kinematic and dynamic modelling approaches in the following chapters. The kinematic model is applied to the FSB in Chapter 10.

Chapter 7

Kinematic forward models of continental lithosphere thinning: pure-shear versus upwelling-divergent flow

7.1 Introduction

The lithosphere (the Earth's upper rigid layer) accommodates extension by thinning and stretching at continental rift basins. If extension continues, the lithosphere ruptures, leaving two rifted continental margins either side of a new ocean basin. The mechanism by which continents are thinned and eventually rupture is debated, and number of conceptual models have been proposed for the formation of rifted margins (see Chapter 2 for a discussion).

The continental lithosphere is commonly thought to accommodate extension by approximately pure-shear thinning, in which case the distribution of stretching is uniform with depth. The pure-shear model (McKenzie, 1978, and Figure 2.3) and its derivatives have been successful in modelling many intracontinental rift basins (e.g. the Gulf of Suez (Steckler et al., 1988), the Kenya Rift and the North Sea, (Kusznir et al.,

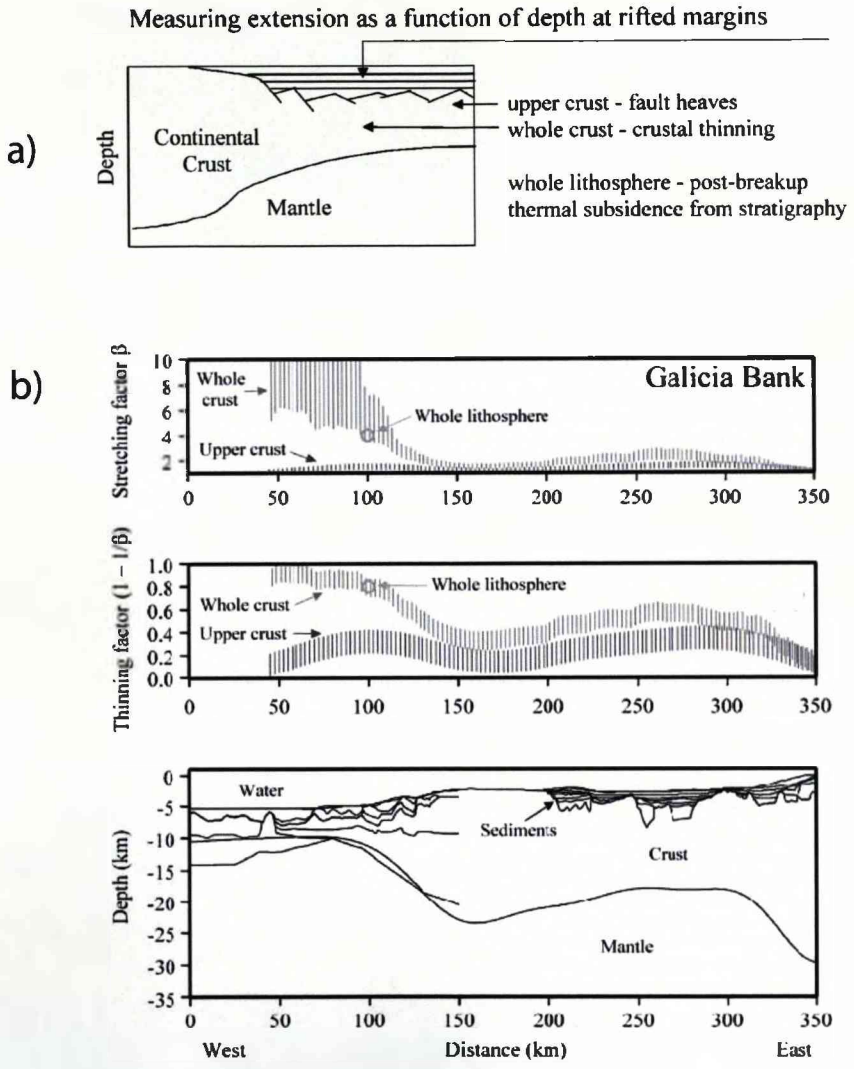

Figure 7.1: Depth-dependent stretching at rifted continental margins. (a) Schematic diagram illustrating the three methods which can be used to estimate extension/thinning. (from Kusznir and Karner, 2007). (b) Example of depth-dependent stretching at a rifted margin: Stretching and thinning factors determined across the Galicia margin and Galicia Interior basin, and crustal section across the margin. Modified from Davis and Kusznir (2004).

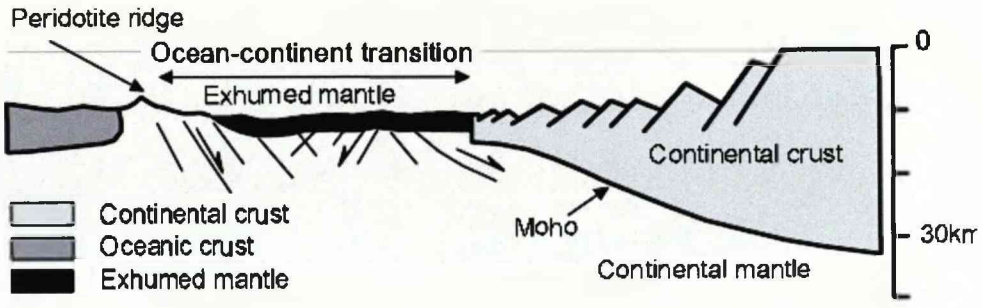

Figure 7.2: Mantle exhumation at rifted continental margins. Interpreted line drawing of the Iberian rifted margin. Modified from Pickup et al. (1996).

1995), the Jeanne d'Arc Basin (Kusznir et al., 1991) and the Rio Grande rift (Wilson et al., 2005)). However, numerous continental rifted margins exhibit depth-dependent stretching, where the lithosphere has apparently been thinned much more than the upper crust (e.g. the eastern Canada margin (Royden and Keen, 1980); the Vøring margin (Roberts et al., 1997); the northwest Australian margin (Driscoll and Karner, 1998); the South China Sea (Clift et al., 2001); Goban Spur and the Galicia margin (Davis and Kusznir, 2004, Figure 7.1); the Newfoundland and Iberian margins (Kusznir and Karner, 2007)). Depth-dependent stretching has been observed at volcanic and non-volcanic margins, including conjugate margin pairs. A number of basins which are, or which may have been, propagating rift tips of incipient oceanic spreading centers also exhibit depth-dependent stretching (e.g. the Nam Con Som basin (Clift et al., 2001), the Woodlark basin (Kusznir and Karner, 2007), the Faroe-Shetland basin (Chapters 3-6 of this thesis)), suggesting that depth-dependent stretching may occur prior to continental breakup, and is not a result of early seafloor spreading.

At some non-volcanic margins (including conjugate pairs) a wide zone (up to 170km wide) of transitional crust separates the unequivocal oceanic crust from the unequivocal continental crust (e.g. Boillot et al., 1987, 1989; Pickup et al., 1996; Dean et al., 2000). This transitional crust appears to be composed of serpentinised continental peridotite,

and the continental lithosphere appears to have been pulled out seaward from underneath the continent during the onset of seafloor spreading (e.g. the Iberian margin: Figure 7.2), which is difficult to explain with the pure-shear model. In addition, apparently anomalously high or low volumes of volcanic addition observed at continnetal rifted margins may be difficult to explain with the pure-shear model, unless large temperature or compositional heterogeneities are invoked (e.g. White and McKenzie, 1989; Minshull et al., 2001; Pérez-Gussinyé et al., 2006).

Whilst some of the observations which do not fit the predictions made by the pure-shear model can be ascribed to the influence of temperature or compositional variations in the continental lithosphere and mantle, or transient effects of mantle plumes (e.g. White and McKenzie, 1989; White and Latin, 1993; Reston and Morgan, 2004; Champion et al., 2008), other workers have proposed alternative models of rifted margin formation (Figure 2.3). Wernicke (1985) suggested that lithospheric breakup may occur by simple-shear (see Figure 2.3), resulting in a 'upper plate' and a 'lower plate'. However, Driscoll and Karner (1998) found that pairs of conjugate margins both appeared to be 'upper plate' margins (where lithosphere thinning exceeds upper crustal thinning). Royden and Keen (1980) proposed a simple model of depth-dependent stretching where the lithospheric mantle was stretched more than the crust (Figure 2.3). Although this model is able to explain observations and make valuable prediction about the implications of depth-dependent stretching, the model does not balance total extension with depth and results in a space problem.

Dynamic models have demonstrated the influence of initial conditions and heterogeneities in the style and symmetry of continental breakup. A number of dynamic models predict deformation by depth-dependent or decoupled pure-shear, where the distribution of extension varies in depth and with time (e.g. Rowley and Sahagian, 1986; ter Voorde et al., 1998; Huismans and Beaumont, 2008), depending on the initial rheological and temperature structure of the lithosphere. In some models small-scale convection is induced in the lower lithosphere, enhancing depth-dependent stretching

(e.g. Keen, 1985; Buck, 1986; Huismans et al., 2001a). Whilst dynamic models are valuable for understanding the forces responsible for the processes which cause continental lithospheric thinning and breakup, it is not always easy to use them for predictive purposes. Kinematic models, models in which the deformation field can be defined by a set of equations and model parameters, are useful for understanding the response of a system to processes that are poorly constrained by geophysical or field data, and can be used to invert observational data and investigate case histories.

Davis and Kusznir (2004) suggest that upwelling-divergent flow (UDF) may be used to describe the dominant process active during lithosphere thinning leading to continental breakup. The upwelling-divergent flow field is described analytically using the cornerflow solution (Batchelor, 1967), maintains a balance of total extensional strain (i.e. conserves volume), and is variable in its form (Figure 2.3e). Upwelling-divergent flow of the mantle occurs at mid-ocean ridges, and the analytical UDF solution of Batchelor (1967) and its derivatives have previously been used to describe mid-ocean ridge processes (e.g. Reid and Jackson, 1981; Spiegelman and McKenzie, 1987; Braun et al., 2000). The UDF model of continental lithospheric thinning therefore evolves into a simple model of seafloor spreading. Kusznir et al. (2005) showed the ability of the UDF model to explain depth-dependent stretching and the overall lithospheric scale structure of volcanic and non-volcanic margins by varying the form of the upwelling diverging flowfield. The form of the UDF flowfield is defined by the ratio of the axial upwelling velocity to the half spreading velocity (V_z^0/V_x^0). Low flow-velocity ratios result in a margin architecture which resembles a non-volcanic margin, whilst high velocity ratios imply that buoyant flow is important ('active' rifting) and results in margin geometry which resembles volcanic margins. Kusznir et al. (2005), Healy and Kusznir (2007) and Kusznir and Karner (2007) have successfully applied the model to a number of case histories by matching observed bathymetry and gravity profiles to those predicted by the model.

In this chapter the pure-shear and UDF models of lithospheric thinning leading to rited

margin formation are presented and compared. In Section 7.2, the method of calculating the temperature field, subsidence and heat-flow histories and finite deformation is described. Section 7.3 describes the pure-shear model, and the sensitivity of the model to the width of the pure-shear region, mantle potential temperature and crustal thickness. Section 7.4 describes the upwelling-divergent flow model, and the sensitivity of the resulting margin geometry, heat-flow and subsidence to the velocity ratio and to time-dependence of the flow is discussed. The predictions made by the pure-shear and upwelling-divergent flow models are compared, and in Section 7.5 the implications for applying the models to real rift basins and margins are discussed. In Chapter 8 the models are further developed to calculate melt production, which provides further constraints with which to compare model predictions to real rift basins and rifted margins. Observational constraints from the Iberian margin and from the Faroe-Shetland basin are used in Chapters 9 and 10 respectively to try to determine the relative roles of pure-shear and upwelling-divergent flow during their formation.

7.2 Method

The velocity fields of the two end-member lithospheric deformation mechanisms, pure-shear and upwelling-divergent flow are defined by a set of equations. In each case, the velocity field was applied to an initially thermally equilibrated continental lithospheric mantle. The evolving temperature field and the location of the Moho were used to calculate top basement heat-flow and subsidence histories. Finite deformation tensors were used to calculate finite strain. An example of the way in which the resulting temperature field, velocity field, finite deformation and resulting margin structure are presented in this chapter is given in Figure 7.3. A list of parameters and values of constants used in this and the following chapter is given in table 7.1.

7.2.1 Temperature calculation

The temperature field was calculated using the finite difference method at nodes on a Cartesian grid 600km wide and 125km deep with nodes spaced 5km apart. The initial

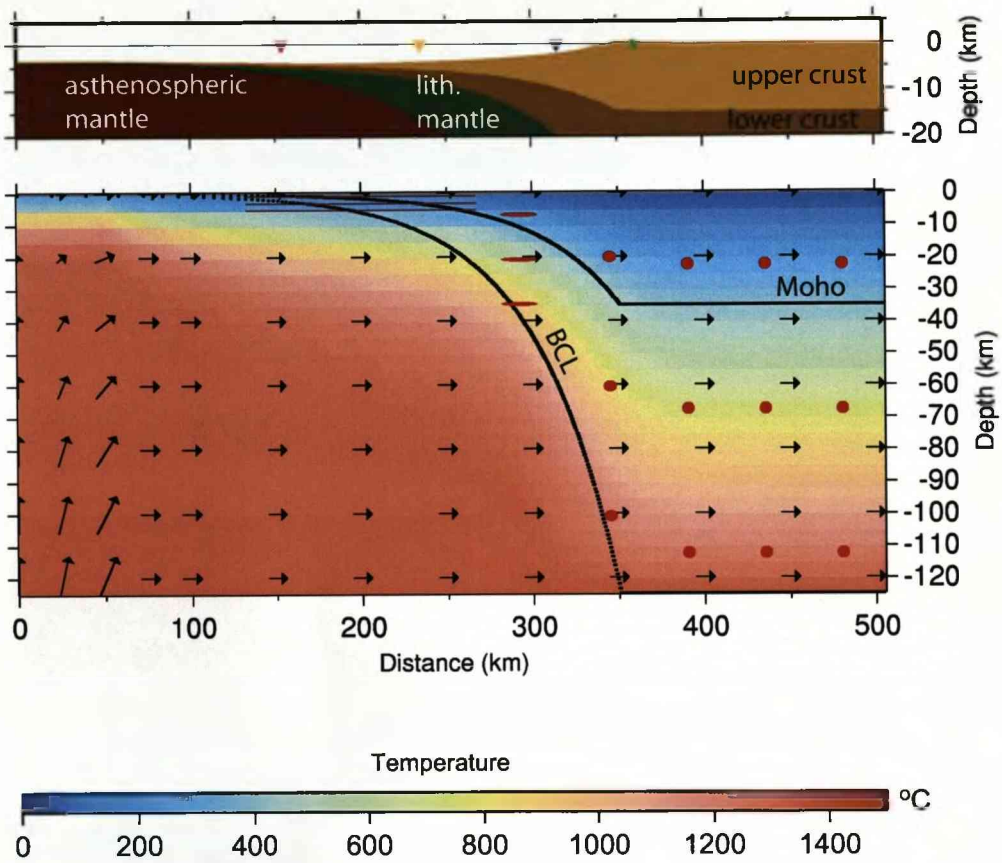

Figure 7.3: Example of model results output. Many of the results of the model output in this and the next chapter are presented in this format. The main panel shows the temperature field, calculated using the finite-difference advection-diffusion equation and displayed on a Eulerian grid. Temperature scale is the same for all similar plots in this chapter. The positions of the initially-horizontal Moho and base of the continental lithosphere (BCL) are calculated using the advection equation. The black arrows show the velocity vectors within the model space-at the right hand side of the model the velocity field is equal to the half-extension rate V_x^0. Finite deformation ellipses are plotted in red, these illustrate the finite deformation since t=0. The upper panel shows the structure of the upper 20km of the model, after isostatic corrections for crustal thinning, the thermal perturbation and water-loading (air-loading if net uplift is predicted).

Variable	Meaning	value	units
A, B, C, D	Constants in the velocity equation	-	kmMyr^{-1}
c_t	Initial crustal thickness	35*	km
$E_{1/2}$	Half-extension (margin extension)	-	km
f	Melt fraction	-	-
g	Gravitational acceleration	9.81	$\mathrm{m}^2\mathrm{s}^{-1}$
h	adiabatic gradient	0.3	$^o\mathrm{Ckm}^{-1}$
k	Thermal conductivity	3.15	$\mathrm{Wm}^{-1}{}^o\mathrm{C}^{-1}$
a	Initial lithosphere thickness; plate thickness	125*	km
P	Pressure	-	Pa
R	Rate of melt production (plane of section)	-	$\mathrm{km}^2\mathrm{Myr}^{-1}$
T_0	Mantle potential temperature	1333*	^{o}C
$T(x,z)$	Temperature at x,z	-	^{o}C
t	time	-	Myr
V_x^0	Characteristic horizontal velocity for upwelling-divergent flow	-	kmMyr^{-1}
V_z^0	Characteristic vertical velocity for upwelling-divergent flow	-	kmMyr^{-1}
V_{up}	Upwards propagation velocity of upwelling-divergent flowfield	-	kmMyr^{-1}
$\mathbf{V}_{(x,z)}$	Local velocity vector at x, z	-	kmMyr^{-1}
$W_{1/2}$	Halfwidth of upwelling zone	-	km
X_{mw}	Width of melting zone	-	km
x	Horizontal coordinate	-	km
z	Vertical coordinate	-	km
α	Thermal expansion coefficient	3.28×10^{-5}	$^o\ \mathrm{C}^{-1}$
β	Stretching factor	-	-
γ	Thinning factor	-	-
κ	Thermal diffusivity of the mantle	8×10^{-7}	$\mathrm{m}^2\mathrm{s}^{-1}$
ρ	Density	-	kgm^{-3}
ρ_c	Reference crustal density	2850	kgm^{-3}
ρ_m	Reference mantle density	3330	kgm^{-3}
ρ_v	Reference volcanic addition density	2850	kgm^{-3}
ρ_w	Density of water	1000	kgm^{-3}

*unless stated

Table 7.1: Table of constants and physical parameters used in this and the following chapter.

temperature structure of the continental lithosphere was assumed to be in thermal equilibrium so that

$$T_{(t=0)} = T_0 \frac{z}{a} \tag{7.1}$$

where $T_{(t=0)}$ is the initial temperature field at time zero (t=0), T_0 is the mantle potential temperature (1333^{o}C unless stated) and a the lithosphere thickness and z is depth. 125km was used as a nominal lithospheric thickness, unless stated. The evolving temperature field was calculated using the advection-diffusion equation:

$$\frac{\partial T(x,z)}{\partial t} = \kappa \nabla^2 T(x,z) - \mathbf{V}_{(x,z)} \cdot (\nabla T(x,z) + h) \tag{7.2}$$

where x and z are horizontal and vertical coordinates respectively, $T(x,z)$ is temperature at (x,z); κ is the thermal diffusivity of the mantle ($8 \times 10^{-7} m^2 s^{-1}$),$\mathbf{V}_{(x,z)}$ is the velocity vector at (x,z) and h the adiabatic gradient (0.3^{o}C/km). The characteristic diffusion time of the system is therefore 62Myr (McKenzie, 1978). The time-step always satisfied the Courant condition (see e.g. Press et al., 1992). Radiogenic heat productivity in the continental crust is ignored.

7.2.2 Material advection and calculation of subsidence and heat-flow history

The Moho and the base of the continental lithosphere (BCL) are assumed to be initially horizontal. A nominal crustal thickness of 35km was assumed unless otherwise stated, and the Moho assumed to be a density and compositional boundary. The continental lithosphere was assumed to be initially 125km thick. Material is advected during lithospheric deformation. The resulting temperature and lithosphere structure predicted by the model was used to calculate locally isostatically compensated topography and bathymetry.

Density (ρ) is temperature-dependent:

$$\rho = \rho_m (1 - \alpha T) \tag{7.3}$$

or

$$\rho = \rho_c(1 - \alpha T) \tag{7.4}$$

The reference crustal density (ρ_c) is assumed to be 2850kgm^{-3}, reference mantle density (ρ_m) 3330kgm^{-3}, and α is the coefficient of thermal expansion (3.28×10^{-5} ^{o}C^{-1}). To calculate the isostatic response of the lithosphere in the model, the total load at each time-step was calculated at each surface node for its corresponding lithospheric column:

$$Load_{total}(x,t) = \sum_{z=0}^{z=a} \rho g \Delta z \tag{7.5}$$

where g is gravitational acceleration. The lithospheric load was compared to the load for a reference column ($Load_{ref}$, a column of thermally-equilibrated continental lithosphere at t=0). The total mass deficiency or excess ($\Delta Load$) is the sum of mass deficiencies or excesses caused by thermal expansion and crustal thinning and is:

$$\Delta Load = Load_{ref} - Load_{total}(x,t) \tag{7.6}$$

Mass excesses (negative $\Delta Load$) were compensated with water loading (using $\rho_{infill} = \rho_{water}$=1000kgm^{-3}), mass deficiencies (positive $\Delta Load$) by air-loading ($\rho_{infill} = 0$). In this chapter the subsidence is calculated assuming local isostasy so that:

$$Subsidence(x,t) = \frac{\Delta Load}{g\rho_{infill}} \tag{7.7}$$

Surface heat-flow, Q, is related to the vertical temperature gradient at the surface,

$$Q = -k\partial T/\partial z \tag{7.8}$$

where k is thermal conductivity, which was assumed to be constant (3.15Wm^{-1} ^{o}C^{-1}). Heat-flow was calculated at each surface node using a second order finite difference approximation. In the Earth, the continental crust contains radioactive elements which significantly contribute to surface heat-flow. As radioactivity is not considered in this

model, the heat-flow values predicted by the models are useful for comparing the magnitude of heat-flow from the lithospheric mantle predicted by different models, but should not be considered as an estimate which can be compared with data. The subsidence and heat-flow history was calculated for up to 6 pseudo-well locations across the profile. This was done by calculating the horizontal coordinate of the pseudo-well location at each time-step and interpolating between subsidence and heat-flow values calculated for adjacent nodes.

7.2.3 Calculation of finite deformation

The finite strain ellipse describes the shape of an initially circular (undeformed) object which has experienced deformation (Figure 7.4). Olivine and other mineral lattice preferred orientations have been related to finite strain in field and laboratory studies (e.g. Nicolas and Poirier, 1976). Flow-induced mineral alignment can contribute towards seismic anisotropy (e.g. McKenzie, 1979; Ribe, 1992; Blackman et al., 2002), therefore anisotropy at mid-ocean ridges and subduction zones can be used to infer finite deformation and consequently to constrain the flowfields operating in the mantle (e.g. Blackman et al., 1996; Fischer et al., 2000; Fouch et al., 2000). If breakup-related finite strain in the lithosphere can be quantified, and can be separated from inherited strain, it may be used to provide insights into the processes occurring during continental breakup.

In this thesis finite strain ellipses for deformation which occurs during lithospheric thinning and breakup are presented. Strain begins to accumulate at t=0, so the finite strain ellipses presented illustrate strain caused by lithospheric deformation during the breakup process. The finite strain ellipse is described by the finite deformation tensor, $\mathbf{F}$, which can be calculated for a parcel of material moving along a streamline. The time rate of change of deformation in a flowfield is:

$$\frac{\partial \mathbf{F}}{\partial t} = \mathbf{LF} \tag{7.9}$$

where $\mathbf{L}$ is the velocity gradient tensor:

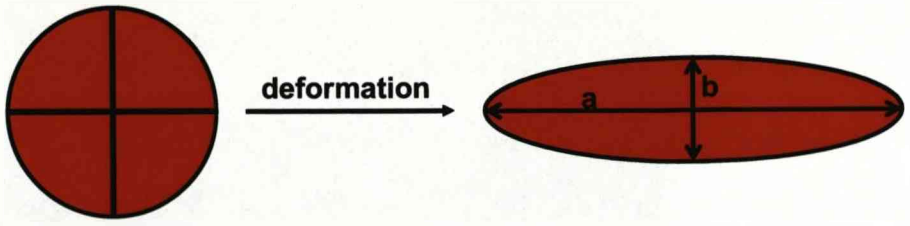

Figure 7.4: Schematic diagram of deformation of the finite strain ellipse. The finite strain ellipse describes the shape of an initially circular (undeformed) object which has experienced deformation. In this example the ellipse has experienced pure-shear strain.

$$\mathbf{L} = \begin{pmatrix} \frac{\partial V_x(x,z)}{\partial x} & \frac{\partial V_x(x,z)}{\partial z} \\ \frac{\partial V_z(x,z)}{\partial x} & \frac{\partial V_z(x,z)}{\partial z} \end{pmatrix} \tag{7.10}$$

$V_x(x,z)$ and $V_z(x,z)$ are the horizontal and vertical components of the velocity field respectively at x and z.

The finite deformation gradient tensor is multiplied by its transpose $\mathbf{F^T}$, to give the matrix $\mathbf{V^2}$. The positive square roots of the eigenvalues of $\mathbf{V^2}$ are the lengths of the major and minor axes of the finite strain ellipse. The corresponding eigenvectors of $\mathbf{V^2}$ are the orientations of the major and minor axes of the finite strain ellipse, and are found using a Jacobi transformation (Press et al., 1992).

The magnitude of strain , f, is quantified as the logarithm of the ratio of the length of major axis a to the length of the minor axis, b .

$$f = log_{10}(a/b) \tag{7.11}$$

The magnitude and orientation of strain calculated using the above method can be checked using the following equations from McKenzie (1979):

If $\mathbf{F}$ is a 2 X 2 matrix:

$$\mathbf{F} = \begin{pmatrix} \mathbf{F_{11}} & \mathbf{F_{12}} \\ \mathbf{F_{21}} & \mathbf{F_{22}} \end{pmatrix} \tag{7.12}$$

then:

$$\Gamma = \frac{(\mathbf{F_{11}} + \mathbf{F_{12}} + \mathbf{F_{11}} + \mathbf{F_{12}})}{2} \tag{7.13}$$

and

$$a/b = \Gamma + (\Gamma^2 - 1)^{\frac{1}{2}} \tag{7.14}$$

The orientation, θ, of the ellipse satisfies:

$$\tan 2\theta = \frac{2(\mathbf{F_{11}}^2\mathbf{F_{12}}^2 + \mathbf{F_{21}}^2\mathbf{F_{22}}^2)}{\mathbf{F_{11}}^2 - \mathbf{F_{12}}^2 + \mathbf{F_{21}}^2 - \mathbf{F_{22}}^2} \tag{7.15}$$

7.3 Pure-shear deformation

The pure-shear model of lithospheric thinning assumes that the continental lithosphere is stretched by a factor of beta (β) before thermally equilibrating (McKenzie, 1978, Figure 2.3, Figure 2.4). β is the ratio between initial and current thickness of a layer. Extension is distributed uniformly with depth.

7.3.1 Velocity field

In this section the response of the lithosphere to finite-duration pure-shear lithosphere thinning is calculated. Finite-duration pure-shear lithosphere thinning can be modelled using a 1–D velocity field:

$$V_z(z) \propto z \tag{7.16}$$

where $V_z(z)$ is the vertical (upwards) velocity at (z) where z is depth (Jarvis and McKenzie, 1980). To extend this 1–D solution into 2–D, pure-shear deformation was be considered to occur within a fixed half-width ($W_{1/2}$) axial zone in the lithosphere (Figure 7.5). The rate of thinning depends on the horizontal half-extension rate (V_x^0) and the width of the upwelling region: a wide zone of pure-shear leads to slow thinning of the lithosphere, a narrow zone of pure-shear results in fast thinning.

In the axial upwelling region the pure-shear deformation velocity field is:

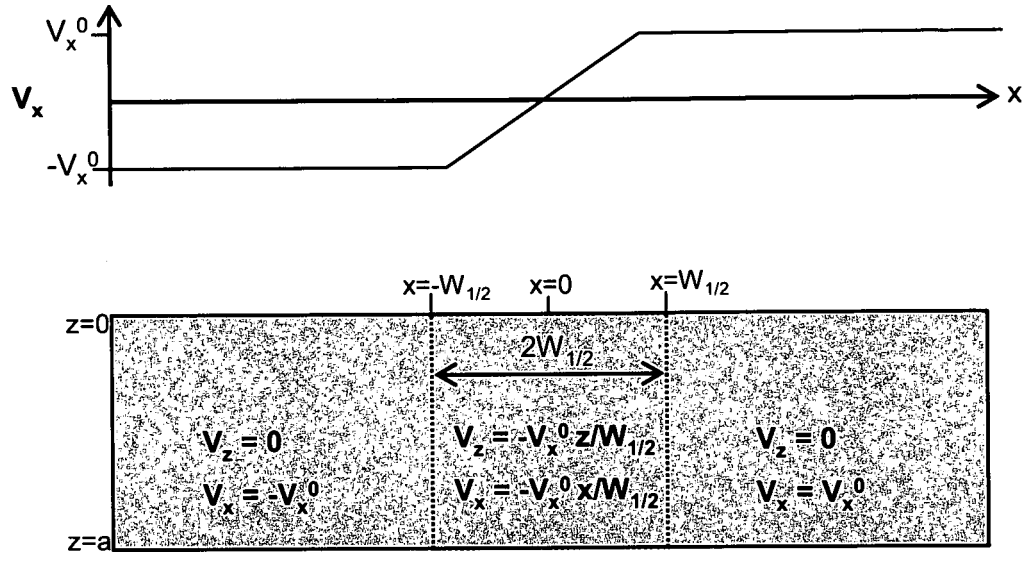

Figure 7.5: The 2–D pure-shear velocity field.

$$V_x(x,z) = V_x^0 \frac{x}{W_{1/2}} \text{ ; and } V_z(x,z) = -V_x^0 \frac{z}{W_{1/2}} \tag{7.17}$$

where $V_x(x,z)$ is the horizontal velocity component and $V_z(x,z)$ the vertical velocity component and x and z are the horizontal and vertical coordinates respectively.

Outside of the upwelling region material is simply translated so that:

$$V_x(x,z) = V_x^0 \text{ ; and } V_z(x,z) = 0 \tag{7.18}$$

The velocity field stays fixed with respect to the coordinate reference frame.

Half extension (i.e. margin extension), $E_{1/2}$, is a product of V_x^0 , the half extension rate and the duration of rifting t:

$$E_{1/2} = V_x^0 t. \tag{7.19}$$

The maximum stretching factor, β_{max} occurs within in the axial zone:

$$\beta_{max} = e^{(\frac{E_{1/2}}{W_{1/2}})} \tag{7.20}$$

Thinning factor, γ, is defined as

$$\gamma = 1 - \frac{1}{\beta} \tag{7.21}$$

In many numerical models, 'breakup', or rupture of the lithosphere is defined as the point at which the model reaches a critical stretching factor β_{crit} or critical thinning factor γ_{crit}. The critical thinning factor can be considered the thinning factor after which the continental crust is thin enough so that crustal rupture occurs. The critical stretching factor used in the literature varies: Pérez-Gussinyé et al. (2006) considered a stretching factor of three enough for breakup, whilst Minshull et al. (2001) required stretching by a factor of 50 before they considered breakup to have occurred. As $\gamma = 1 - 1/\beta$, the published critical stretching factors correspond to a range of critical thinning factors (γ_{crit}) of 0.67 to 0.98.

7.3.2 Example of pure-shear model development

An example of model evolution for extension velocity (V_x^0) of 20 mm/yr and an upwelling half-width ($W_{1/2}$) of 50 km is shown in Figure 7.6. The velocity field stays fixed in the reference frame of the axis, therefore material may advect out of the region of upwelling into the region of translation. This results in a tapered margin structure, between the unthinned continent and the region of maximum thinning. The temperature field evolves until it reaches a steady state in the coordinate reference frame, reflecting a balance between heat advection and conduction. In the frame of reference of the margin, subsidence occurs and heat-flow increases whilst a pseudo-well location on the surface of the model is within the upwelling zone. As a pseudo-well leaves the axial region, subsidence and heat-flow are controlled by cooling, decaying exponentially with time. In the hinterland (continentwards of thinned lithosphere), lateral conduction of heat into the continent causes thermal uplift and an increase in heat-flow. These are

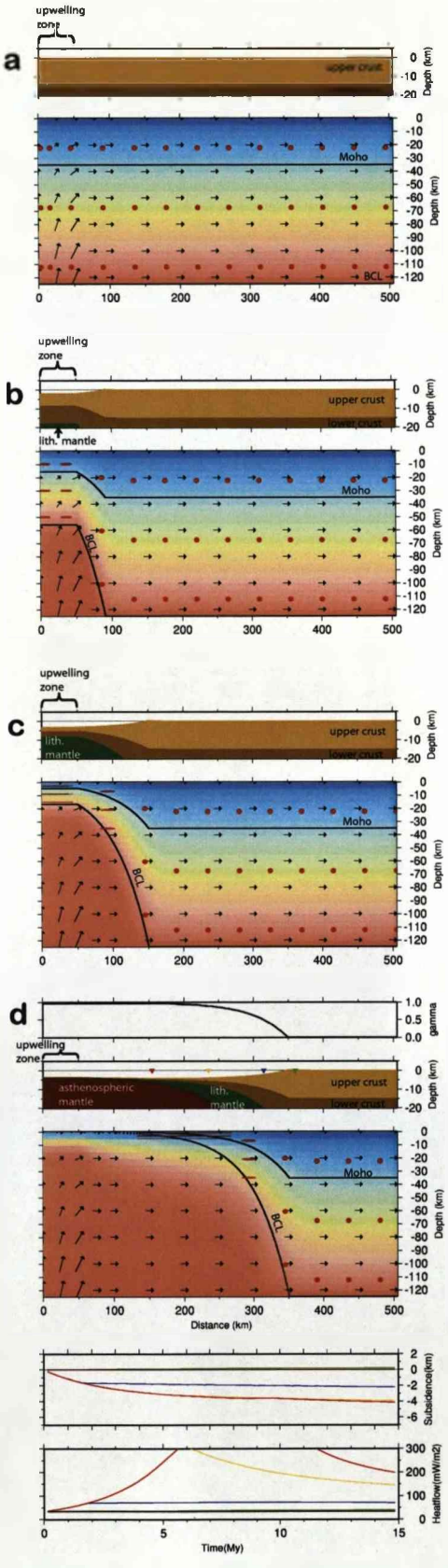

Figure 7.6: Model evolution of continental lithosphere thinning due to a finite width ($W_{1/2}$=50 km) pure-shear flow-field. Model is extending at V_x^0=20 mm/yr. Four snapshots in time at (**a**) t=0, with velocity vectors showing deformation field which is non time-dependent; (**b**) t=2 Myr, when the lithosphere in the axial region has thinned by a factor of β=2.23; (**c**) t=5 Myr; (**d**) the model after 15 Myr. In each case the main panel shows a Eulerian plot of temperature, the position of the Moho and base of the continental lithosphere (BCL), and red ellipses indicate direction and magnitude of strain since t=0; the upper panel shows the upper 20 km of the model, corrected for isostatic effects of thermal expansion, crustal thinning and water or air loading. In **d**: Upper panel shows thinning factors (gamma, γ) across the margin for the upper crust, the whole crust and the whole lithosphere are also shown. Lower panel shows subsidence and heat-flow history of pseudowell locations (shown as triangles in **d** on the margin; the colour of the subsidence or heat-flow history corresponds to colour of triangle).

transient effects which decay over tens of Myr. The magnitude of finite deformation is equal to the local magnitude of stretching (β) (therefore $f = \log_{10}\beta^2$), with the long axis in the direction of extension.

7.3.3 Benchmarking

The subsidence and heat-flow history of the axial region calculated by the 2–D pure-shear finite difference model is benchmarked against the 1–D analytical solutions for instantaneous pure-shear thinning McKenzie (1978). The temperature field, subsidence and heat-flow history calculated using my finite difference code for a pseudowell location in the rift axis after rapid duration (2Myr) lithospheric thinning by a factor of two is shown in Figure 7.7. The temperature and heat-flow history calculated using analytical solutions for heat-flow and subsidence following instantaneous thinning from McKenzie (1978) are plotted for comparison. After 2Myr, the results are very similar, showing the ability of the finite difference method to calculate subsidence and heat-flow histories accurately.

7.3.4 Model sensitivity to upwelling width

For a constant half-extension rate (V_x^0) the upwelling half-width ($W_{1/2}$), determines the maximum upwelling velocity, and therefore the rate of thinning (i.e. the rate of change of β with time) in the axial region. Increasing the model half-width causes a decrease in thinning rate and so conductive cooling has a bigger effect on syn-thinning subsidence and heat-flow. As the half-width increases, the rate of syn-rift subsidence decreases and the maximum heat-flow value reached is lower (Jarvis and McKenzie, 1980, Figure 7.8). In the hinterland lateral temperature gradients, and therefore the magnitude of heat-flow and thermal uplift, increase with decreasing half-width. Hinterland uplift can be up to a few hundred meters in magnitude.

The upwelling half-width also affects the final margin width, with a narrow half-width resulting in a narrow margin, and vice versa. For example, if the width of the margin is nominally defined as the width between unthinned lithosphere and lithosphere where

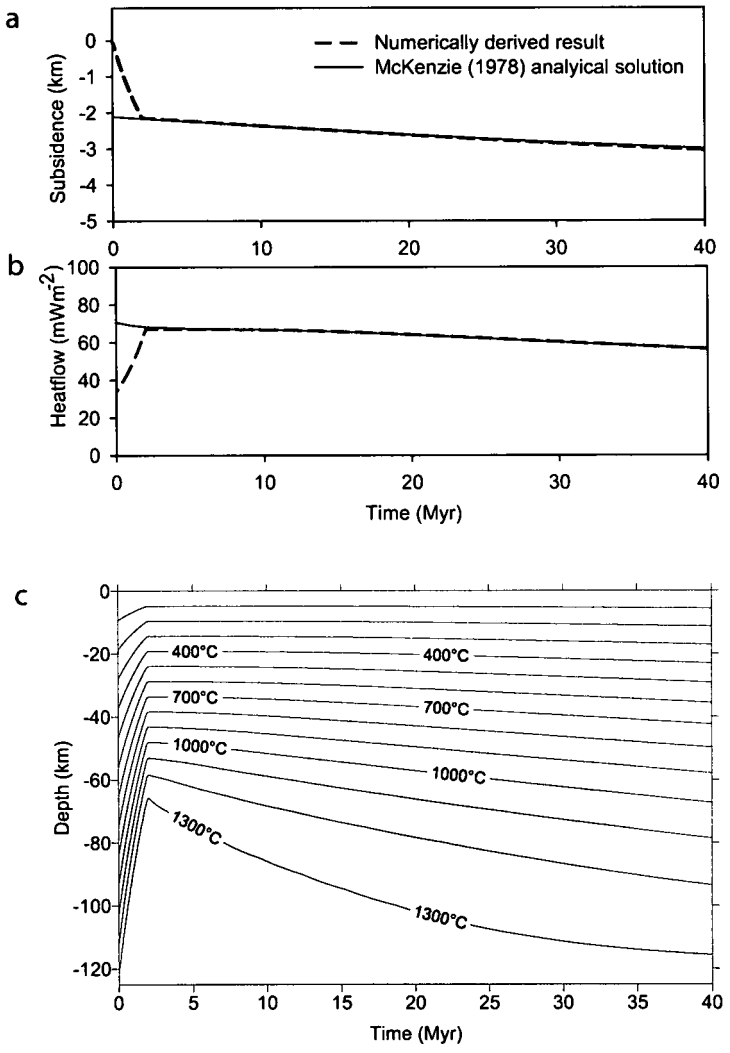

Figure 7.7: Comparison of subsidence and heat flow history calculations for lithosphere thinning by a factor of 2 in 2Myr using my finite difference program to those predictions made by analytical solutions in McKenzie (1978). The finite difference model was run at a grid-node spacing of 5km and time-step of 10000 yrs. The axial half-zone was made wide (200km) to reduce lateral cooling effects. Temperature structure of an axial lithospheric column through time also shown. Note that some of the values of constants are used for this calculation (from McKenzie, 1978) are different to those used in the rest of this chapter.

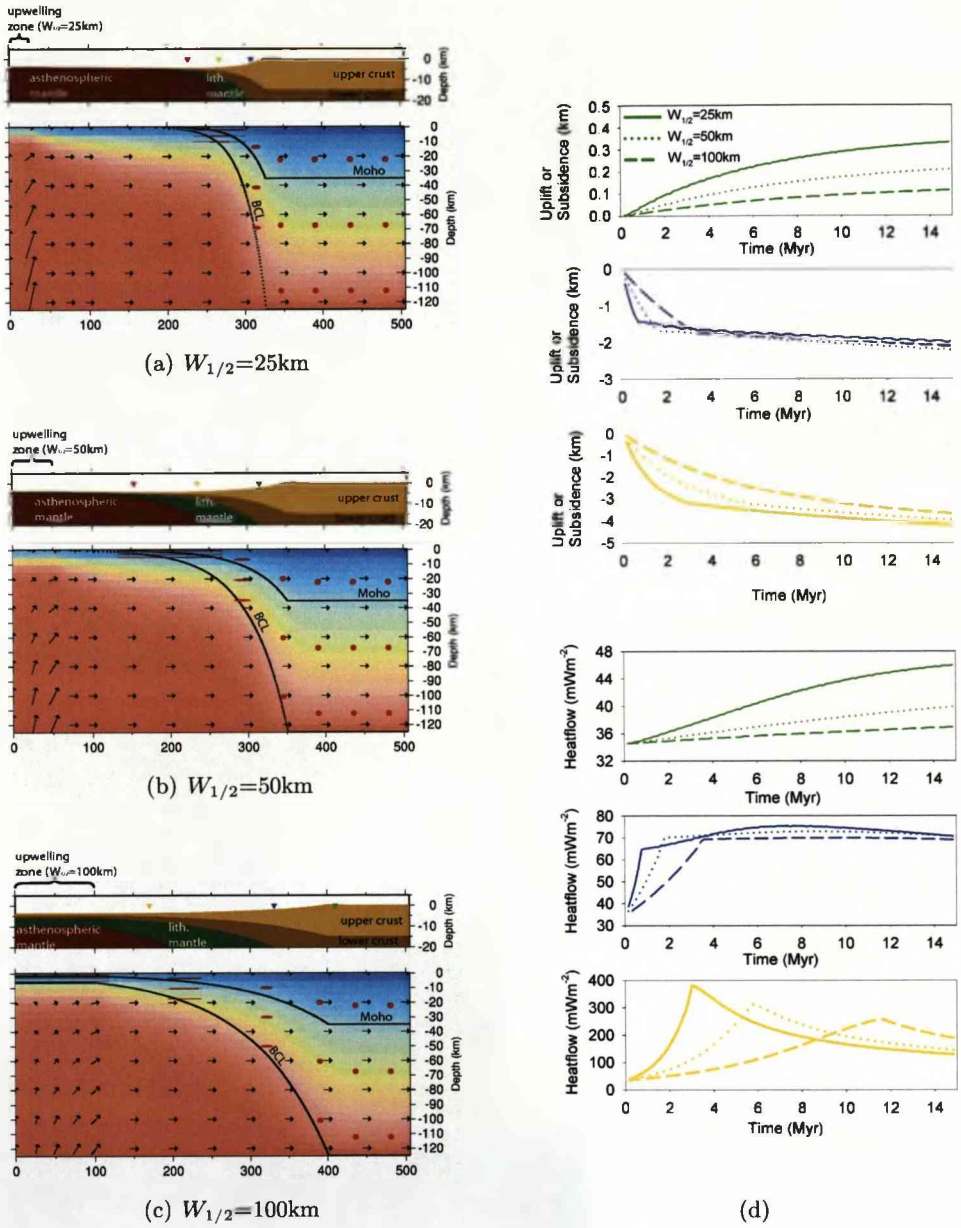

Figure 7.8: Sensitivity of the 2–D pure-shear model to the upwelling half-width. Models are shown after 300 km of horizontal half-extension at a half-extension rate of 20mm/yr for half-widths of (**a**) 25km, (**b**) 50 km and (**c**) 100 km. Blue triangles indicate where β=2, yellow triangles where β=10, red triangles where β=50, green triangles are 10km inboard of thinned lithosphere. (**d**) Subsidence and heat-flow histories for pseudowell locations. Plot line colour corresponds to colour of triangle plotted at pseudowell location. For each plot the solid line is for the model where $W_{1/2}$=25km, the dotted line for the model where $W_{1/2}$=50km and the dashed line for the model where $W_{1/2}$=100km.

the stretching factor is ten (β= 10, γ=0.9), the width of margin predicted by the model with a 25km-wide half-width axial upwelling region is 58km wide, whilst the width of margin predicted by the model with a 100km-wide half-width axial upwelling region is 230km wide.

7.3.5 Sensitivity of subsidence and heat-flow to pure-shear extension rate

The final lithospheric geometry (the distribution of extension) predicted by the pure-shear model is independent of spreading rate. However, the thinning rate, and therefore the subsidence and heat-flow history of a margin, is dependent on the half-extension rate (e.g. Jarvis and McKenzie, 1980). During lithosphere thinning, syn-rift subsidence is faster for faster extension rates (Figure 7.9). However, the effect of spreading rate on total (syn- + post-rift) subsidence decreases with time. The heat-flow maximum peaks earlier and to a higher value when extension rates are faster.

Ten kilometres inboard of the thinned lithosphere (the green triangle in Figure 7.9), the maximum uplift and maximum heat-flow, caused by lateral conduction of heat towards the continent, increases as spreading rate decreases. Surface heat-flow and thermal uplift and subsidence in a 2–D model is dependent on both vertical and lateral heat conduction, and in this example it is the lateral heat conduction which exerts the greater control on heat-flow and thermal uplift: at slower extension rates, the pseudo-well on the margin flank spends a longer time close to the (hot) rift axis, therefore allowing more heat to conduct into the continent.

7.3.6 Sensitivity of subsidence and heat-flow to mantle potential temperature and crustal thickness

The final lithospheric geometry predicted by the pure-shear model is independent of mantle potential temperature (T_0) and crustal thickness. However, increasing the mantle potential temperature increases the geothermal gradient, therefore heat-flow and the thermal components of uplift and subsidence are affected by the mantle potential

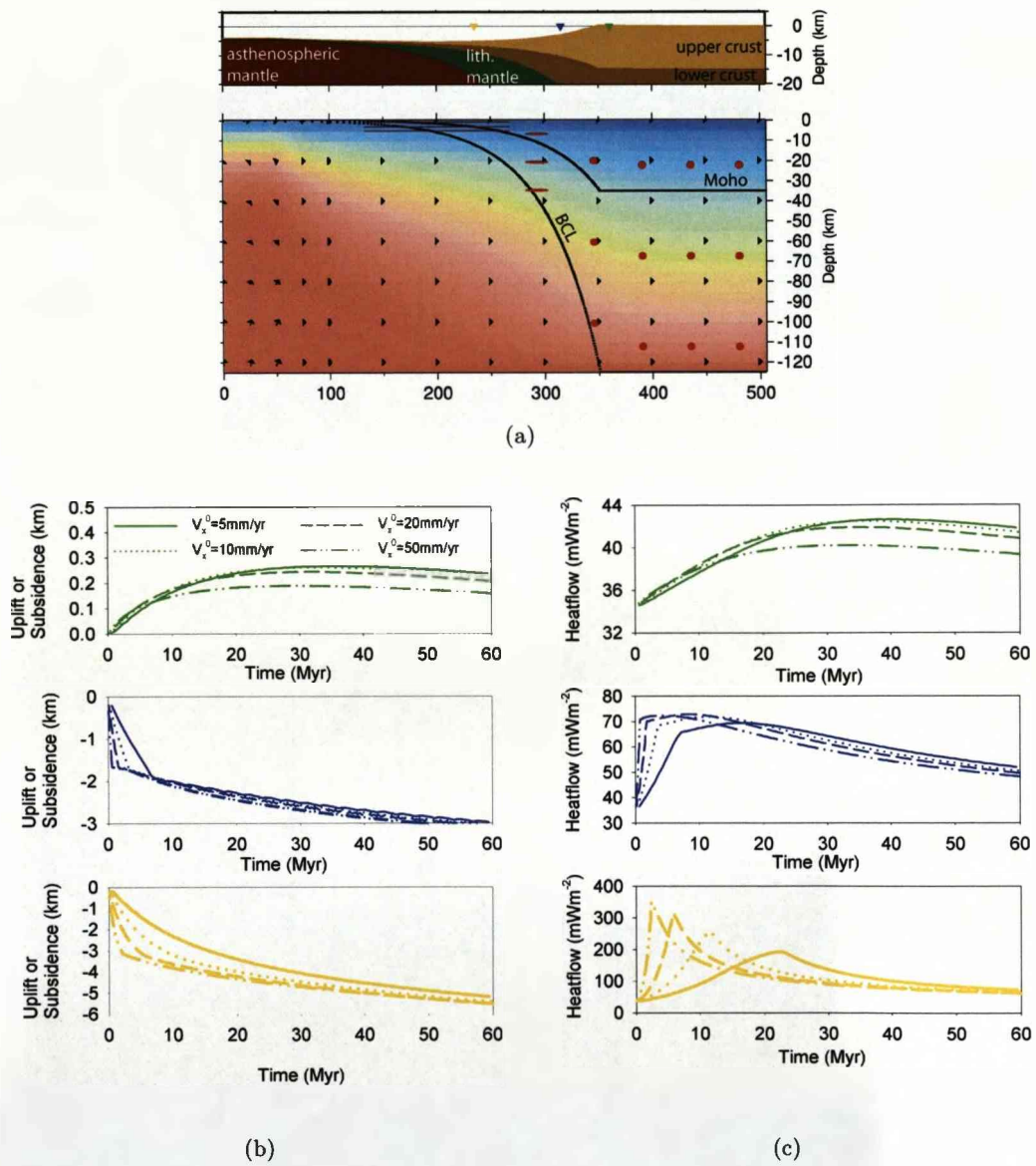

Figure 7.9: Sensitivity of the 2–D pure-shear model to extension rate. (**a**) Example of margin structure showing locations of pseudowells. (**b**) Subsidence and (**c**) heat-flow history for pseudowell locations where β=2 (blue triangle), β=10 (yellow triangle) and for a location 10km continentwards of thinned lithosphere (green triangle). Plot line colour corresponds to colour of triangle plotted at pseudowell location in **a**. In each plot the solid line shows results from the model run with V_x^0=5mm/yr, the dotted line for the model run with V_x^0=10mm/yr, the dashed line for the model run with V_x^0=20mm/yr, and the dot-dashed line for the model run with V_x^0=50mm/yr.

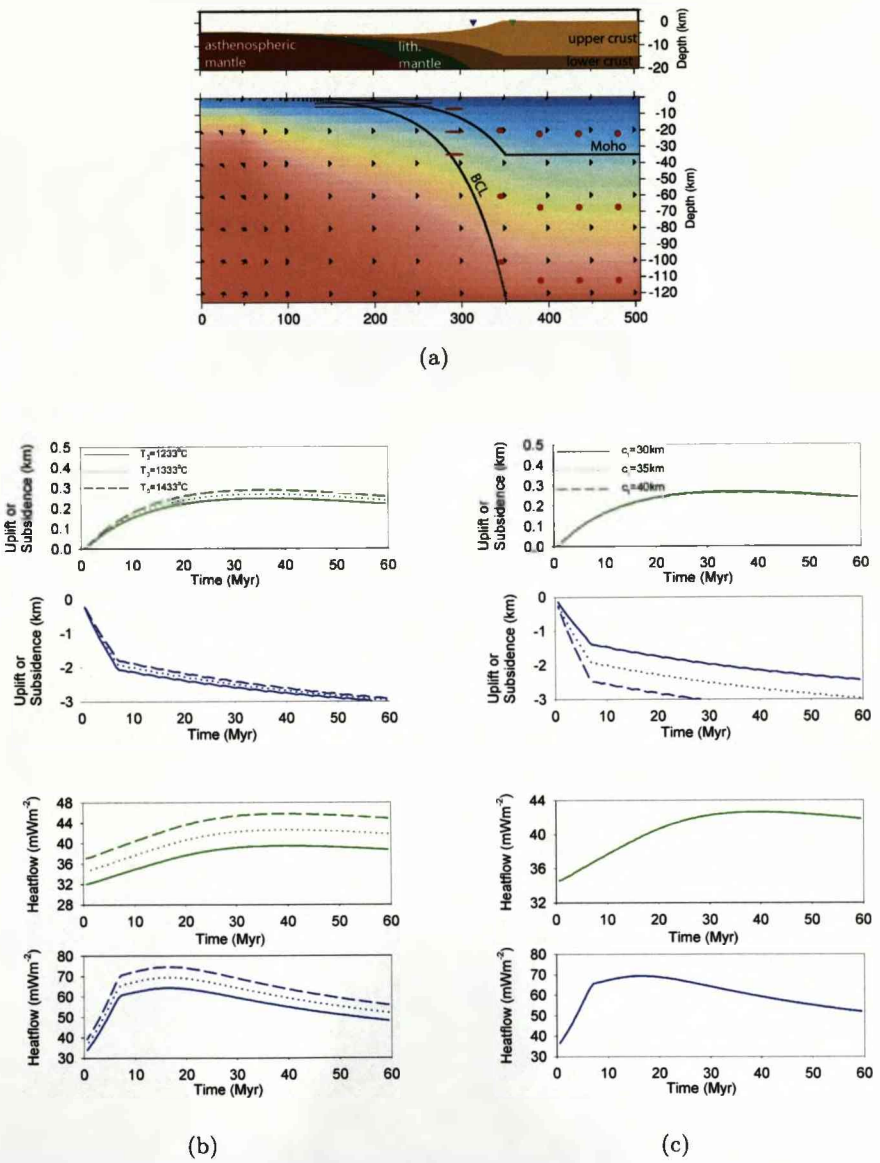

Figure 7.10: Sensitivity of the 2–D pure-shear model to mantle potential temperature and crustal thickness. (**a**) Example of margin structure showing locations of pseudowells where β=2 (blue triangle) and for a location 10km continentwards of thinned lithosphere (green triangle). (**b**) Subsidence and heat-flow history for pseudowell locations for variable mantle potential temperature (T_0). Plot line colour corresponds to colour of triangle plotted at pseudowell locations. In each plot the solid line shows results from the model run with T_0=1233^{o}C, the dotted line for the model run with T_0=1333^{o}C, the dashed line for the model run with T_0=1433^{o}C. (**c**) Subsidence and heat-flow history for pseudo-well locations for variable initial crustal thickness (c_t). In each plot the solid line shows results from the model run with initial crustal thickness of 30km, the dotted line for the model run with initial crustal thickness of 35km, the dashed line for the model run with initial crustal thickness of 40km. Pseudo-well locations indicated in **a**.

temperature (McKenzie, 1978, Figure 7.10). As the mantle potential temperature is increased, a decrease in syn-rift subsidence is predicted. Subsequent post-rift subsidence is faster, and the effect of mantle potential temperature on total subsidence decreases with time. The initial geothermal gradient increases with mantle potential temperature, thus an increase in mantle potential temperature results in correspondingly higher heat-flow peaks. An increase in mantle potential temperature also increases the rate of heat conduction into the continent, resulting in an increase in hinterland uplift and heat-flow. These results are consistent with the predictions made by McKenzie (1978). The thermal component of subsidence is unaffected by crustal thickness. However, syn-rift subsidence is highly dependent on crustal thickness (McKenzie, 1978). In the example shown in Figure 7.10, for β=2, syn-rift subsidence varies from 1.3km when the initial crustal thickness is 30km to 2.5km when the initial crustal thickness is 40km. The model predicts that crustal thickness has no effect on surface heat-flow. However, this model does not include radiogenic heating; in the Earth radioactive elements are concentrated in the upper crust and contributes up to ~40 % to heat-flow (Roy et al., 1968; Vitorello and Pollack, 1980), and should be considered when comparing model predictions to data.

7.3.7 Summary of variables affecting predictions made by the pure-shear model

In this chapter, pure-shear thinning is modelled in 2–D, so that the effects of lateral conductive heat-flow are accounted for in the calculations. As a result of extension, lithospheric stretching and thinning are assumed to occur within a fixed half-width axial zone in the lithosphere. The width of this axial zone determines the width of the resulting margin geometry. The uplift and subsidence history of a pseudowell on the margin depends primarily on the local stretching factor, although lateral heat conduction may also have an effect. In the kinematic model presented here, extension rate, mantle potential temperature and crustal thickness do not affect the margin geometry or the general pattern of subsidence and heat-flow history, but these variables do affect

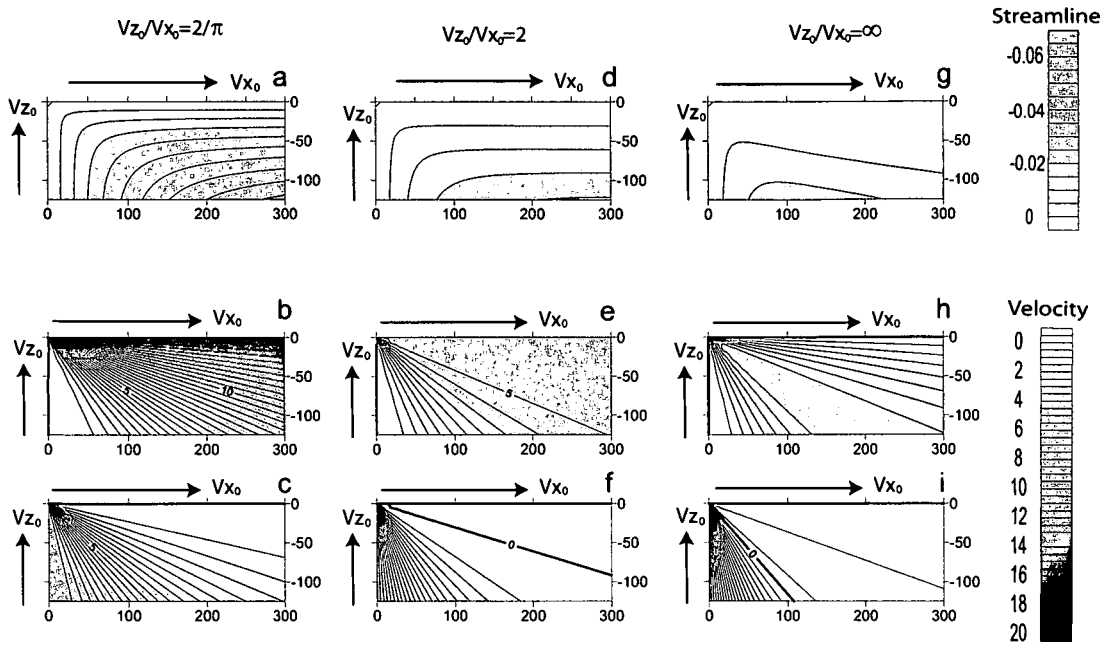

Figure 7.11: Upwelling-divergent flow: streamlines (streamfunction value in arbitrary units) and velocity field (arbitrary units). (**a**) streamlines, (**b**)horizontal velocity and (**c**) vertical velocity when $V_z^0/V_x^0=2/\pi$. (**d**) streamlines, (**e**)horizontal velocity and (**f**) vertical velocity when $V_z^0/V_x^0=2$. (**g**) streamlines, (**h**) horizontal velocity and (**i**) vertical velocity when $V_z^0/V_x^0=\infty$. V_z^0 is the same in each example.

the rate and magnitude of uplift and subsidence, and heat-flow.

7.4 Upwelling-divergent flow as a lithosphere thinning mechanism.

In this section deformation of the lithosphere during continental thinning leading to breakup is modelled using an upwelling-divergent flowfield (UDF) - the analytical cornerflow solution of Batchelor (1967). The velocity field is defined by a constant half-spreading rate at the surface, (V_x^0), and a constant axial upwelling rate, (V_z^0). The velocity field is (Turcotte and Schubert, 2002):

$$V_x(x,z) = -B - D\tan^{-1}(\frac{z}{x}) + (Cx + Dz)(\frac{-x}{x^2+z^2}) \tag{7.22}$$

and

$$V_z(x,z) = A + C\tan^{-1}(\frac{z}{x}) + (Cx + Dz)(\frac{-z}{x^2+z^2}) \tag{7.23}$$

where:

$A = 0$

$B = \frac{2\pi V_z^0 - \pi^2 V_x^0}{(\pi^2-4)}$

$C = \frac{4V_x^0 - 2\pi V_z^0}{(\pi^2-4)}$

$D = \frac{2\pi V_x^0 - 4V_z^0}{(\pi^2-4)}$

The surface horizontal velocity (V_x^0) and axial vertical velocity (V_z^0) can be varied, and the velocity ratio (V_z^0/V_x^0) of the flowfield determines the form of the flowfield. Figure 7.11 illustrates streamlines and horizontal and vertical components of velocity for the cornerflow solution at velocity ratios of $2/\pi$, 2 and ∞. A steady-state upwelling-divergent flow with velocity ratio of $2/\pi$ corresponds to that of a passively upwelling isoviscous material (PhippsMorgan, 1987). Dynamic models incorporating temperature- and strainrate-dependent rheology predict velocity ratios close to one beneath steady-state mid-ocean ridges, although the ratio appears to be higher (up to 5) if spreading rates are slow (Buck and Su, 1989; Shen and Forsyth, 1992; Braun et al., 2000). Using dynamic models, (Nielsen and Hopper, 2002, 2004) show that the ratio of axial upwelling to half spreading rate velocity may be as high as 15 during the formation of volcanic rifted margins. Davis and Kusznir (2004) suggest that upwelling-divergent flow (UDF) may be used to describe the dominant process active during lithosphere thinning leading to continental breakup. Predictions made by the UDF model are

compared to those made by the pure-shear model in the following sections.

In this section the margin geometry, subsidence and heat-flow predictions predicted by the UDF model are described. In this section UDF is assumed to act instantaneously within the whole continental lithosphere and asthenosphere (static model). The sensitivity of the model to the velocity ratio (V_z^0/V_z^0) is examined. These results are then compared to the predictions made by a model where the velocity field propagates upwards from the base of the lithosphere to the surface.

7.4.1 Model sensitivity to the axial upwelling to extension velocity ratio

Figure 7.12 illustrates examples of rifted margin development calculated by imposing a velocity field with V_x^0=20 mm/yr and V_z^0/V_x^0 ratios of 1, 2 and 5 onto an initially layered lithosphere. Subsidence and heat-flow histories for a number of locations, and plots of thinning factor versus distance across the model profile are also shown.

For models run with an axial upwelling to half spreading rate velocity ratio (V_z^0/V_x^0) of one during margin formation and early seafloor spreading, the velocity field causes the progressive exhumation of deeper lithospheric layers and a 125km wide zone of exhumed crust and continental mantle is predicted. At low velocity ratios, lateral heat conduction is low and the oldest continental mantle is exhumed at around 4000-5000m

Figure 7.12 *(following page)*: Time evolution of models of continental lithospheric thinning leading to breakup caused by an upwelling-divergent flowfield with variable V_z^0/V_x^0 ratios. V_x^0 =20mm/yr in all models. **a-c**) Model evolution where V_z^0/V_x^0=1. **d-f**) Model evolution where V_z^0/V_x^0=2. **g-i**) Model evolution where V_z^0/V_x^0=5. In each case the main panel shows a Eulerian plot of temperature, the position of the Moho and base of the continental lithosphere (BCL), and red ellipses indicate direction and magnitude of strain since t=0; the upper panel shows the upper 20 km of the model, corrected for isostatic effects of thermal expansion, crustal thinning and water loading. In **c**,**f** and **i** thinning factors (gamma) across the margin for the upper crust, the whole crust and the whole lithosphere are shown, and lower panels shows subsidence and heat-flow history of pseudowell locations (triangles) on the margin, colour of subsidence or heat-flow history corresponding to colour of triangle.

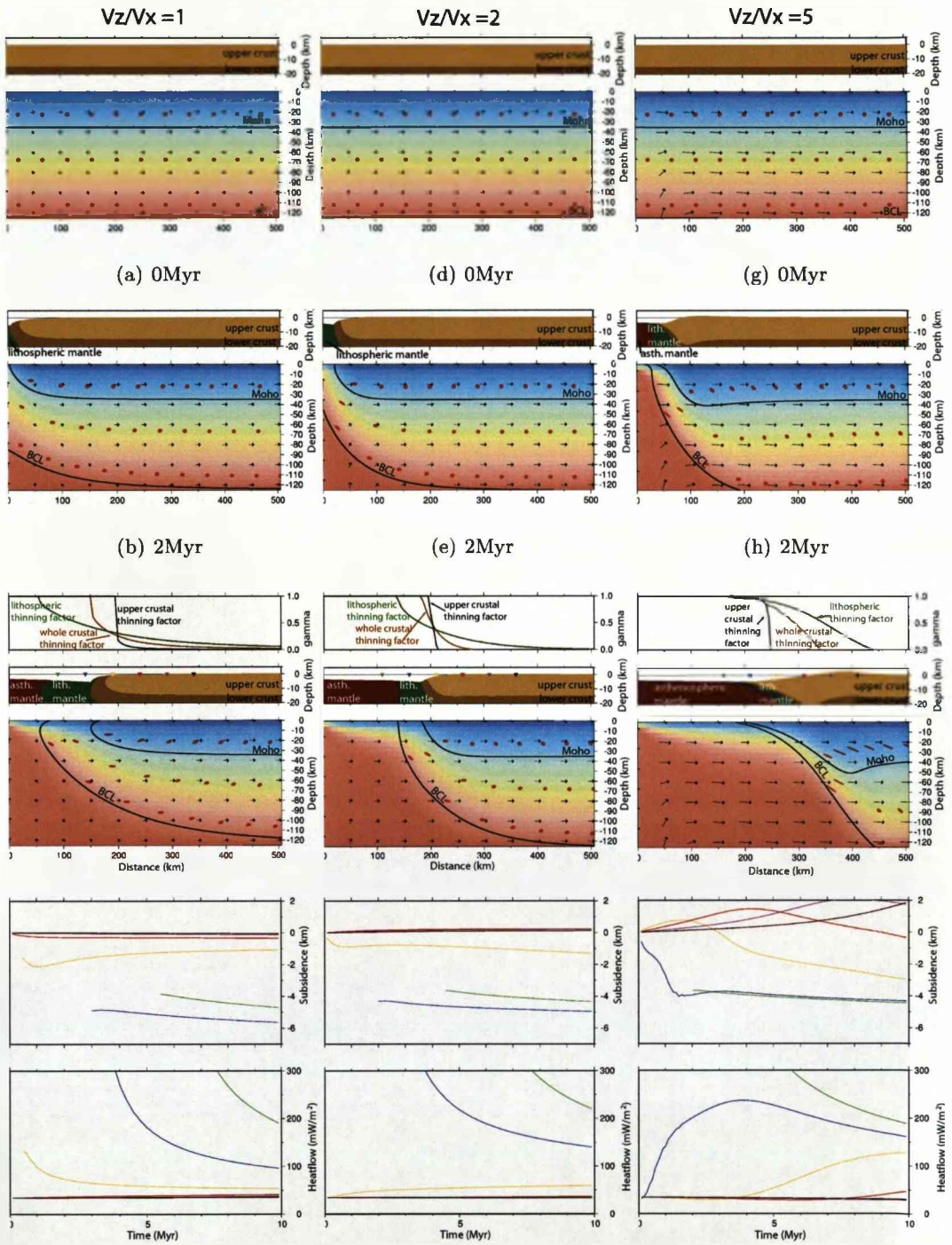

(a) 0Myr (d) 0Myr (g) 0Myr

(b) 2Myr (e) 2Myr (h) 2Myr

(c) 10Myr (f) 10Myr (i) 10Myr

water depth - much deeper than the bathymetry of the ridge axis at steady-state. Post-exhumation, the thermal subsidence of the exhumed mantle is relatively minor. The low lateral heat-flow also means that very little thermal uplift occurs in the continental hinterland.

Kusznir et al. (2005) suggest that the margin geometry predicted by a low velocity ratio UDF model resembles margins where wide zones of exhumed continental lithospheric mantle are exhumed (e.g. Iberia, Newfoundland and in the ancient Tethyan margins now exposed in the Alps). This type of structure is not predicted by the pure-shear model. For the same half-extension velocity (equivalent to half-spreading rate), the syn-breakup thermal perturbation at the margin and in the hinterland for a low velocity ratio UDF model is less than that for a pure-shear model. Consequentially, the magnitude of post breakup thermal subsidence at a non-volcanic margin predicted by the UDF model (to time $= \infty$) is less than the magnitude of that predicted by the pure-shear model.

For models run with high axial upwelling to half spreading rate velocity ratios during margin formation and early seafloor spreading, a sharp ocean-continent transition (i.e. the distance between the most oceanwards upper crust and the asthenospheric mantle) is predicted with little mantle exhumation. Depth-dependent stretching, where the lithospheric mantle is thinned to a greater extent than the upper crust, is predicted for a region 100s km wide. Material is pushed outwards from the axis (the proto-ocean ridge) underneath the continent. The balance of extensional strain is maintained by a small amount of crustal and lithospheric thickening in the continental margin hinterland, with the isostatic effect of uplifting the continental margin. The width and magnitude of this uplift increases with the syn-breakup velocity ratio; for a velocity ratio of 5, uplift of up to 2km occurs over a width of around 300km. Crustal and lithosphere thickening maxima move toward the continent as deformation continues, although the rate of deformation diminishes with distance from the axis. The downwards deflection of isotherms by the downwards component of the velocity field during deformation causes continued uplift as the lithosphere thermally equilibrates.

Kusznir et al. (2005) suggest that the narrow margin and hinterland uplift predicted by the high velocity ratio upwelling-divergent flow model make it broadly applicable to volcanic margins. The hinterland uplift predicted by the high velocity ratio UDF model is permanent, continues for tens of Myr and may be of the order of 0.5 -1.0 km in magnitude and 250-500 km in wavelength; it is much larger than the transient hinterland uplift which is predicted by the pure-shear model. Many volcanic margins exhibit km-scale hinterland uplift, including the Norwegian-Greenland and Brazil-southern African conjugate pairs (see Chapter 2). The uplift predicted by the model has been studied in more detail by Greenhalgh and Kusznir (2008).

The magnitude of finite strain is greatest where the velocity ratio is high, due to increased velocity gradients. At high velocity ratios, high finite strain pervades further continentwards into the margin than for low velocity ratios. At all velocity ratios the UDF model, unlike the pure-shear model, predicts maximum elongation occurs at an oblique angle to the surface.

7.4.2 Upwards-propagating upwelling-divergent flowfield.

The models described in the previous section were calculated assuming that an upwelling-divergent flowfield instantaneously began acting within a uniform thickness, layered, thermally equilibrated lithosphere. Kusznir and Karner (2007) suggest that a more realistic flow pattern during rifted margin formation may be a UDF which propagates upwards from (at least) the base of the continental lithosphere towards the surface.

Figure 7.13 *(following page)*: Time evolution of models of continental lithospheric thinning leading to breakup caused by an upwards-propagating upwelling-divergent flowfield. (**a-c**) the flowfield propagates upwards with velocity V_{up} equal to the characteristic upwelling velocity, V_z^0, V_z^0/V_x^0=1 and V_x^0=20mm/yr. (**d-f**) the flowfield propagates upwards at $V_{up} = V_z^0$=20mm/yr, where (V_z^0/V_x^0=20). When the flowfield reaches the surface it becomes static (remains fixed with respect to the coordinate reference frame) with V_x^0=10mm/yr and V_z^0/V_x^0=2. (**g-i**) the flowfield propagates upwards at $V_{up} = Vz$=20mm/yr, where (V_z^0/V_x^0=20). When the flowfield reaches the mid-crust it pauses for 10Myr (V_x^0=10mm/yr and V_z^0/V_x^0=2), before propagating to the surface (V_x^0=10mm/yr and V_z^0/V_x^0=2). For explanation of plots see caption for Figure 7.12.

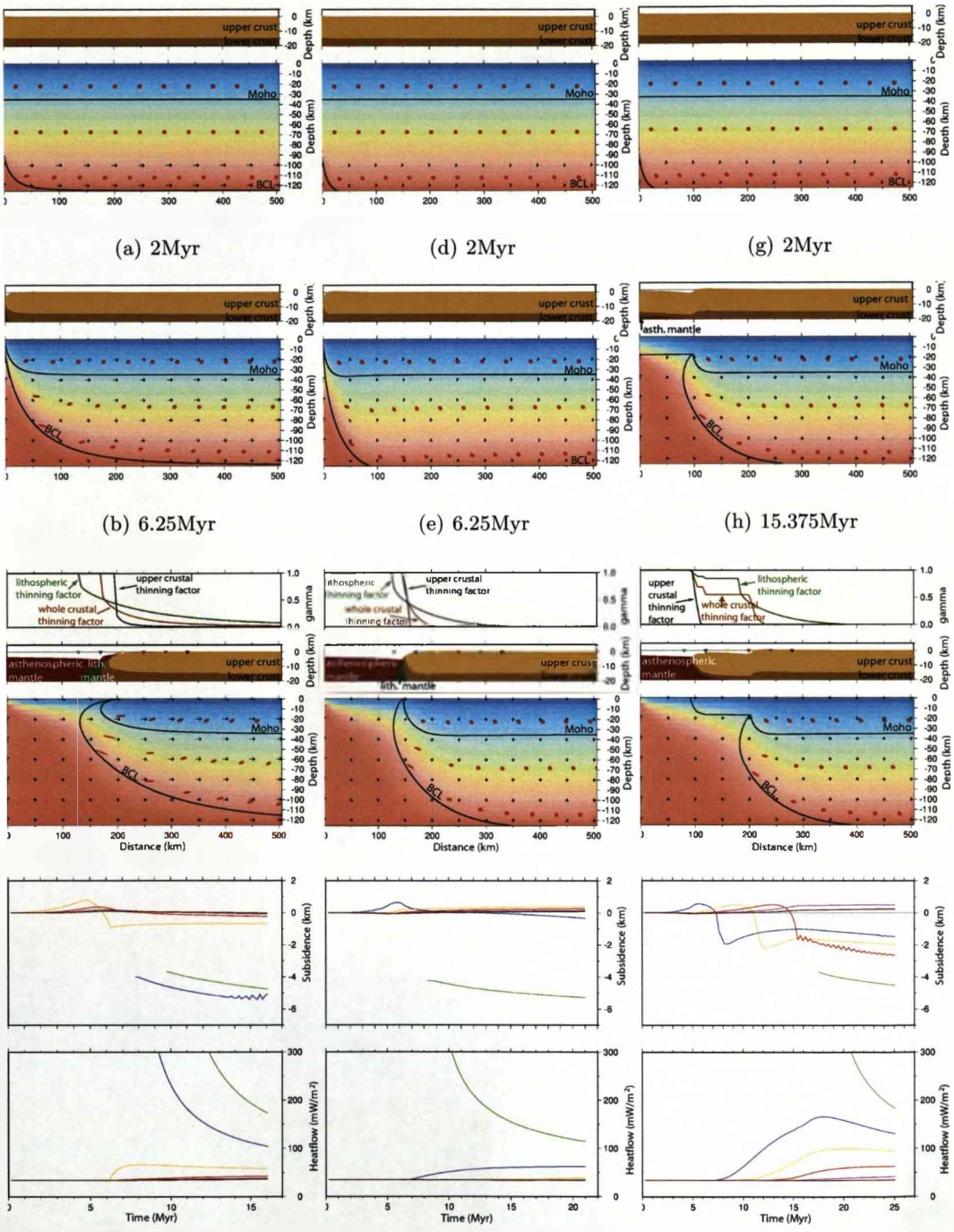

(a) 2Myr (d) 2Myr (g) 2Myr

(b) 6.25Myr (e) 6.25Myr (h) 15.375Myr

(c) 16.25Myr (f) 21.25Myr (i) 25.375Myr

The upwards propagating flow pattern may be understood most easily for propagating rift tips (e.g. Woodlark basin, Papua New Guinea), where lateral heat conduction and resultant thermal and melt buoyancy may cause thermal weakening and induce preferential thinning of the lithosphere prior to and ahead of upper crustal rupture. Figure 7.13 illustrates examples of rifted margin development where the flowfield propagates upwards from the base of the lithosphere. In Figures 7.13a-c the flowfield propagates upwards with velocity V_{up} equal to the characteristic upwelling velocity, V_z^0, V_z^0/V_x^0=1 and V_x^0=20mm/yr. When the flowfield reaches the surface and continental lithospheric rupture occurs, the flowfield becomes static (i.e. it remains fixed with respect to the coordinate reference frame). In comparison to the model where the UDF operates throughout the entire lithosphere at all times (i.e. that shown in Figure 7.12a-c), the model of upwards propagation of the flowfield produces a much narrower ocean-continent transition (the zone between unthinned crust and asthenospheric mantle) with much less lower crustal or lithospheric mantle exhumation. As the flowfield propagates upwards, the lithospheric mantle is thinned prior to any thinning of the crust, resulting in axial uplift. As the flowfield thins the lower crust, rapid subsidence occurs in the centre of the basin.

For the upwards-propagating flowfield described above, total extension is not conserved with respect to depth: the upwards propagation of the flowfield causes the layers to become horizontally offset through time. This offset is reduced when V_x^0 during upwards propagation is decreased. An example of the evolution of an upwards propagating UDF model with a low V_x^0 during the upwards propagation phase is shown in Figures 7.13d-f. The resulting margin is narrower, and hinterland uplift is greater than than for the previous model (compare to Figures 7.13a-c).

Kusznir and Karner (2007) show that wide zones of thinned crust between the upper crust and lithosphere may be explained by an upwelling-divergent flow pattern which propagates upwards from the base of the lithosphere, pausing at mid-crustal levels before reaching the surface. An example of this type of evolution is shown in Figure 7.13g-i. The model predicts a margin with a stepped bathymetry across a wide zone

where the lower crust and lithospheric mantle have been preferentially thinned, and thinned crust lies directly on top of asthenospheric mantle. Kusznir and Karner (2007) suggest that at some margins the upwards propagating flowfield is able to penetrate and thin the lithospsheric mantle and weak lower crust but does not act within the upper crust due to lithospheric rheology or plate kinematic constraints. They propose this type of model to explain observations of depth-dependent stretching on the Galician margin (see Figure 7.1) and in the Galicia Interior basin (GIB), suggesting that upwelling-divergent flow operated for a time in the lithospheric mantle and lower crust beneath the GIB before migrating westwards where rupture occurred. This type of flowfield is broadly similar to models of lithosphere thinning (e.g. Huismans and Beaumont, 2008) where small-scale convection occurs in the lower lithosphere whilst the upper lithosphere (which is partially or fully decoupled from the lower layer) deforms by distributed (brittle) extension models. It is also similar to that envisaged at ultra-slow spreading ridges, where upwelling-divergent flow operates beneath a (brittle) cool lithospheric lid which is on the order of 10km thick (e.g. Cannat, 1996). Kusznir and Karner (2007) suggest this type of model for the formation of wide zones of thinned crust which are observed at a number of rifted margins (e.g. the Galicia Interior basin, Exmouth Plateau, central South Atlantic salt basin). The upwards propagating upwelling-divergent flow model is able to explain preferentially thinned lower crust (compared to the upper crust) which cannot be explained by the pure-shear model of thinning. The upwards propagating UDF model predicts that pseudo-wells on the thinned crust crust exhibit uplift (as the lower lithosphere is thinned) prior to two phases of subsidence: rapid syn-thinning subsidence followed by post thinning subsidence controlled by the (offset) seafloor spreading. This subsidence history is more complex than is predicted by pure-shear deformation which thins the crust by an equivalent amount.

7.5 Discussion

Rifted continental margins record the transient stage of continental extension between initial continental rifting and seafloor spreading. Intra-continental rift basins can often

be successfully modelled as a consequence of pure-shear extension, or with a modified pure-shear extension model. However observation of depth-dependent stretching at rifted continental margins have caused the applicability of the pure-shear model to continental breakup and rifted margin formation to be questioned. Kusznir et al. (2005) suggested that upwelling-divergent flow, a deformation process similar to that which occurs at mid-ocean ridges, plays an role in the formation of rifted margins, and can explain both depth-dependent stretching and the presence of exhumed continental mantle at non-volcanic margins.

Models of rift basins and rifted margin formation by pure-shear and upwelling-divergent flow predict margin geometry, finite deformation and subsidence and heat-flow histories which differ in a number of important ways:

Margin architecture and depth-dependent stretching

The pure-shear model never reaches infinite thinning, although breakup can be assumed to occur at a critical thinning factor (γ_{crit}) of between 0.7 and 0.98. In contrast the UDF model predicts complete thinning of the crust and lithospheric mantle after finite amounts of extension.

The pure-shear model can predict both narrow and wide margins if the zone of upwelling in the rift axis is varied, although the pure-shear model always predicts depth-uniform stretching. The UDF model predicts a wide range of margin geometries which always exhibit depth-dependent stretching. The UDF model is symmetric about the rift axis and predicts that the sense of depth-dependent stretching will be the same on conjugate margins.

Finite Deformation

The direction and magnitude of finite deformation predicted by the two models differs very simply: the pure-shear model predicts syn-rift deformation in a single direction parallel to the extension direction. The maximum syn-breakup deformation predicted by the UDF model is smaller in magnitude than for the pure-shear model and the angle

of maximum strain is variable with depth and time. For the UDF model, the magnitude of finite strain increases with the velocity ratio (V_z^0/V_x^0).

Subsidence, uplift and heat-flow

The pure-shear model of lithospheric thinning predicts a two stage subsidence history: syn-rift subsidence is caused by the net result of crustal thinning and the thermal effects of lithospheric thinning, post-rift subsidence is caused by thermal equilibration. The pure-shear model predicts heat-flow which increases as the lithosphere is thinned, before exponentially decaying. The rate and magnitude of uplift, subsidence and heat-flow are affected by the thinning rate, crustal thickness and mantle potential temperature, this is true for both pure-shear and UDF models. However when considered as fixed variables inherent to the rift system during continental lithospheric thinning and breakup, these variables do not affect the overall pattern of subsidence and heat-flow evolution.
The subsidence and uplift and heat-flow histories predicted by the UDF models of continental lithosphere thinning and rifted margin formation are more varied and complex than those predicted by the pure-shear model. The subsidence and heat-flow predictions are dependent on the ratio of axial upwelling to half spreading rate, and whether the flowfield is static or propagates upwards. The UDF model may be able to explain subsidence histories which appear to be anomalous when compared to those predicted by a pure-shear model. If UDF plays a significant role in the formation of rift basins and rifted margins, the subsidence history of a pseudowell location on a margin cannot be inferred from crustal thickness, or from upper crustal extension. As a corollary, if UDF is an important process during rifted margin formation then the subsidence history cannot be simply used to infer crustal thickness or thinning factors.

Implications

The end-member pure-shear model of rifted continental margin formation implies that asthenospheric convection does not play an important role until the lithosphere is highly thinned and seaflorr spreading begins. In contrast, the end-member UDF model of

margin formation implies that the onset of asthenospheric convection occurs in the continental lithosphere soon after the onset of extension in the continental lithosphere. The comparison of observations to model predictions is best done on a case-specific basis. Available bathymetry, subsidence history, heat-flow, margin architecture and other data may indicate the mode of deformation and allow margin formation models to be assessed and subseqently re-tested if new data become available.

The models presented here are intended to represent kinematic end-member models which address the lithosphere-scale deformation and thermal evolution during lithospheric thinning and continental breakup. The continental lithosphere is here modelled as a continuous and homogeneous material. Therefore even if, on a lithospheric scale, the flowfields are broadly congruent to those which act during the breakup process, it should be considered that the real lithosphere does not accommodate strain continuously. In particular, the upper crust deforms by brittle deformation, on discrete fault surfaces; the likely deformation mechanism should be considered when comparing observations to the predictions made by the models.

Further, case-specific, comparisons of observational data with the predictions made by each of the models will enable continued assessment of the applicability of the rifted margin formation models. In the next chapter I calculate and compare the volcanic addition predicted by the pure-shear and UDF models, and consider various explanations for anomalous melting at rifted margins. The predictions of volcanic addition made by the models provide further constraints with which to compare against observational data. Observational constraints from the Iberian margin and Faroe-Shetland basin are compared to predictions made by the pure-shear and upwelling-divergent flow models in Chapters 9 and 10 respectively in order to asses the relative role that each of these processes played in their formation.

Chapter 8

Melting during continental lithospheric thinning: pure-shear versus upwelling-divergent flow

8.1 Introduction and aims

Rifted continental margins exhibit large variations in magmatic activity. Non-volcanic, or magma-poor, margins may display a broad ocean-continent transition, up to 170km wide, of exhumed continental mantle separating oceanic crust from thinned continental crust (e.g. Boillot et al., 1987; Lemoine et al., 1987; Boillot et al., 1989; Pickup et al., 1996; Dean et al., 2000; Beslier et al., 2004; Sibuet et al., 2007), whilst voluminous intrusive and extrusive volcanism of the order of 1000 km^3 per km along strike (e.g. Eldholm and Grue, 1994) may accompany breakup at volcanic margins (see Chapter 2 and Figure 2.8). This contrasts with volcanism at mid-ocean ridges, where the volcanic crustal thickness is consistently around 7 km, except at ultraslow spreading rates (less than 20mm/yr full rate) or in the presence of a mantle plume (White et al., 1992, 2001; Dick et al., 2003).

The cause of the variability of volcanism during rifted margin formation is debated: If the lithosphere is assumed to thin and eventually rupture by a pure-shear mechanism

(the model of McKenzie, 1978), the range in thickness of volcanic addition at rifted margins can be explained by mantle potential temperature and compositional heterogeneities and variations in spreading rate (e.g. White and McKenzie, 1989; Bown and White, 1995; Minshull et al., 2001; Reston and Morgan, 2004). However, other authors question the applicability of the pure-shear model to rifted margin formation. For example, a number of authors invoke 'active' upwelling (small-scale convection in the lithosphere prior to breakup or enhanced upwelling during early seafloor spreading) as the process responsible for voluminous volcanism at some margins (e.g. Mutter, 1985; van Wijk et al., 2001; Korenaga et al., 2002).

A major aim of this thesis is to investigate the processes that occur during continental lithospheric thinning, in particular to investigate the role of upwelling-divergent flow (UDF) during continental lithosphere thinning and margin formation. The kinematic model of continental rifted margin formation by upwelling-divergent flow was proposed by Davis and Kusznir (2004) to explain observations of depth-dependent stretching and mantle exhumation at rifted margins. The model was described and compared to the pure-shear model in the previous chapter. The form of the UDF is defined by the ratio of the axial upwelling velocity to half spreading rate; a model with a high velocity ratio is proposed for a volcanic margin, and a model with a low velocity ratio is proposed for a non-volcanic margin (Kusznir et al., 2005, and see Chapter 7). However, the melt production predictions of this model (a key constraint to consider when comparing model predictions to data) have not been tested. This is done in this chapter.

Three key questions are addressed in this chapter:

1. What factors may be responsible for the variation in melt thickness observed at rifted margins?

2. What is the timing and distribution of volcanic addition predicted by the upwelling-divergent flow model of continental lithosphere thinning leading to breakup and seafloor spreading? How do the predictions differ from those made by the pure-shear model of thinning?

3. How might observations of volcanic addition at rifted margins enable the processes responsible for lithosphere thinning be determined?

In Section 8.2 the method of melt calculation is described. The physical constants and melt parameterisation algorithm is tested by checking that oceanic crustal thicknesses predicted by the model during steady-state seafloor spreading are realistic. This is achieved in Section 8.2.3 by modelling seafloor spreading using the UDF model, and comparing predictions of melt thickness with observations and predictions made by dynamic models.

Melt production during continental thinning and rifted margin formation is then modelled. The melt predictions made by the pure-shear model are described in Section 8.3. The sensitivity of melt production to extension rate, mantle potential temperature, lithospheric thickness, water content, composition and migration behaviour is assessed, and the ability of each of these variables to explain anomalous melt thicknesses at volcanic and non-volcanic margins is discussed. Predictions of melt production made by the UDF model of continental lithospheric thinning and seafloor spreading initiation are presented in Section 8.4. The sensitivity of melt production to the ratio of axial upwelling to half spreading velocities is shown, and the effect that an upwards-propagating upwelling-divergent flowfield may have on melt production during basin and margin formation is also investigated. The predictions made by the UDF model are compared with those made by the pure-shear model.

In addition to calculating crustal thicknesses, the conditions (pressure, temperature and degree of partial melting) in the melting region are calculated for each model. I do not attempt to model the geochemistry of the melt in this thesis; however the conditions of melting may be used to predict testable geochemical and seismic velocity trends that may provide additional constraints on the nature of heterogeneities and processes which occur during rifted margin formation.

The various explanations for anomalous melt production during rifted margin formation are discussed in Section 8.5, and suggestions are made on how these may be tested. The ability of the pure-shear and upwelling-divergent flow models to honor observational

constraints at the non-volcanic Iberian margin is assessed in the following chapter.

8.2 Formulation of melt production calculations and modelling

The pure-shear and upwelling-divergent flow (UDF) models of continental lithosphere thinning were described in detail in the previous chapter. The pure-shear model assumes that lithosphere stretching occurs within a finite width zone and extension is uniform with depth. The upwelling-divergent flow model utilizes the analytical corner-flow solution of Batchelor (1967) to describe the formation of rifted continental margins. The UDF velocity field is defined by a constant half-spreading rate (V_x^0) at the top of the flowfield, and a constant axial upwelling rate (V_z^0). An initially uniform geotherm is assumed and the temperature field and margin geometry are calculated using the finite difference method. The models presented in this chapter are calculated in the same way as in the previous chapter; however, where the pressure-temperature conditions in the model cross the solidus, melting is predicted. The degree of partial melting is calculated using published peridotite melt parameterisations (Klein and Langmuir, 1987; McKenzie and Bickle, 1988; Katz et al., 2003) and melt is assumed to migrate quickly to the surface where it forms a volcanic layer. An example of the way in which the resulting temperature field, velocity field, finite deformation, resulting margin structure and volcanic addition properties are presented in this chapter is given in Figure 8.1. A list of parameters and values of constants used in this and the previous chapter was given in table 7.1.

8.2.1 Melt fraction as a function of temperature and pressure

Melting occurs when the temperature of the upwelling solid exceeds the solidus temperature at a given pressure. For an aggregate material such as peridotite, partial melting occurs so that the fraction of material which has melted, f, increases as temperature

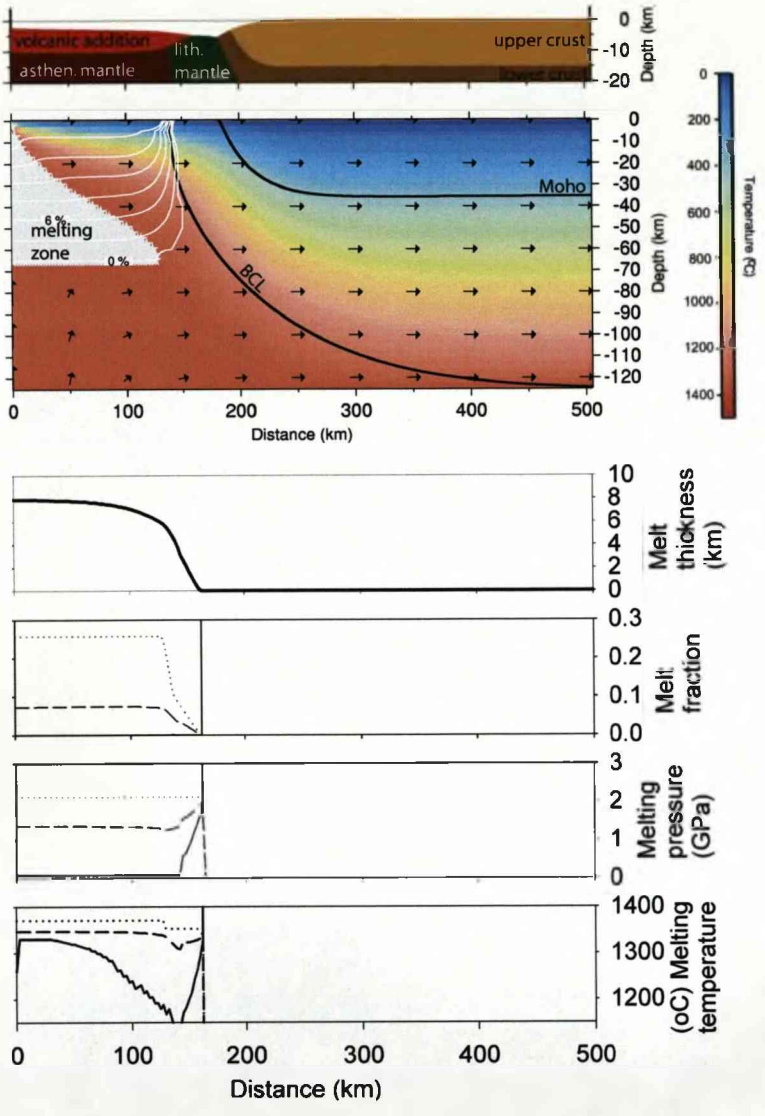

Figure 8.1: Example of model results output. Many of the results of the model output in this chapter are presented in this format. The main panel shows the temperature field, calculated using the finite-difference advection-diffusion equation and displayed on a Eulerian grid. Temperature scale is the same for all plots in this chapter. The positions of the initially horizontal Moho and base of the continental lithosphere (BCL) are calculated using the advection equation. The black arrows show the velocity vectors within the model space. The zone of melting is denoted by the grey area and depletion contours are plotted in white. The upper panel shows the structure of the upper 20km of the model, after isostatic corrections for crustal thinning, the thermal perturbation volcanic addition loading and water-loading (air-loading if net uplift is predicted). The lower panels show the thickness of volcanic addition and the minimum, weighted mean and maximum values of melt fraction, melting pressure and melting temperature from which the volcanic addition was sourced, as a function of distance across the model profile.

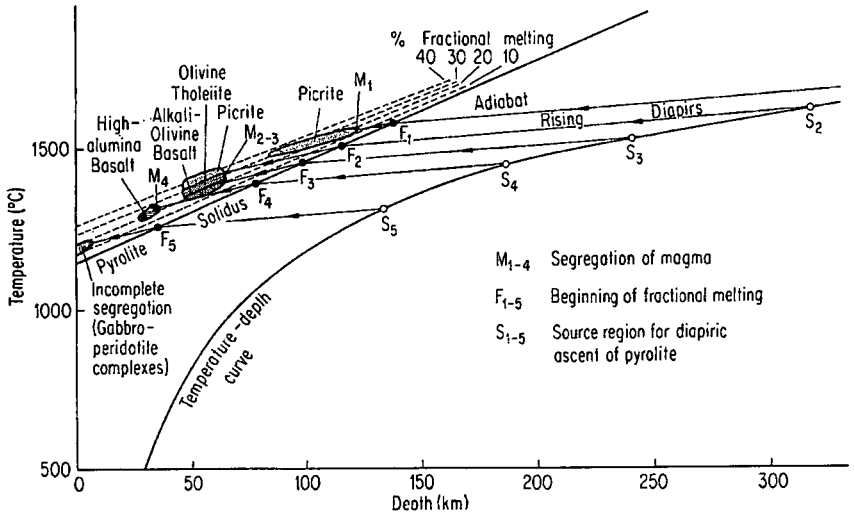

Figure 8.2: Diagram of the mantle pyrolite solidus and implications for magma geochemistry. From Green and Ringwood (1967).

increases or pressure decreases (e.g. Figure 8.2). Although melting is principally a function of pressure and temperature, the mantle is heterogeneous and the solidus and consequently the degree of partial melting (f) is affected by volatile content (particularly water content) and other compositional heterogeneities. A number of parameterisations of the partial melting of peridotite have been derived using extensive geochemical databases and thermodynamic calculations. A comparison of three parameterisations (Klein and Langmuir, 1987; McKenzie and Bickle, 1988; Katz et al., 2003) is shown in Figure 8.3. Unless stated I use the melt parameterisation of Katz et al. (2003) as the algorithm allows water and clinopyroxene (cpx) content to be specified. Unless stated cpx content is assumed to be 13% (Workman and Hart, 2005) and the mantle dry (a water content of zero).

8.2.2 Calculating melt production

If conditions in the model space exceed the solidus of peridotite, melting is predicted. Melt fraction (f) is calculated at each time-step for each node in the model as a function of temperature and pressure, clinopyroxene (cpx) content and water content. Pressure,

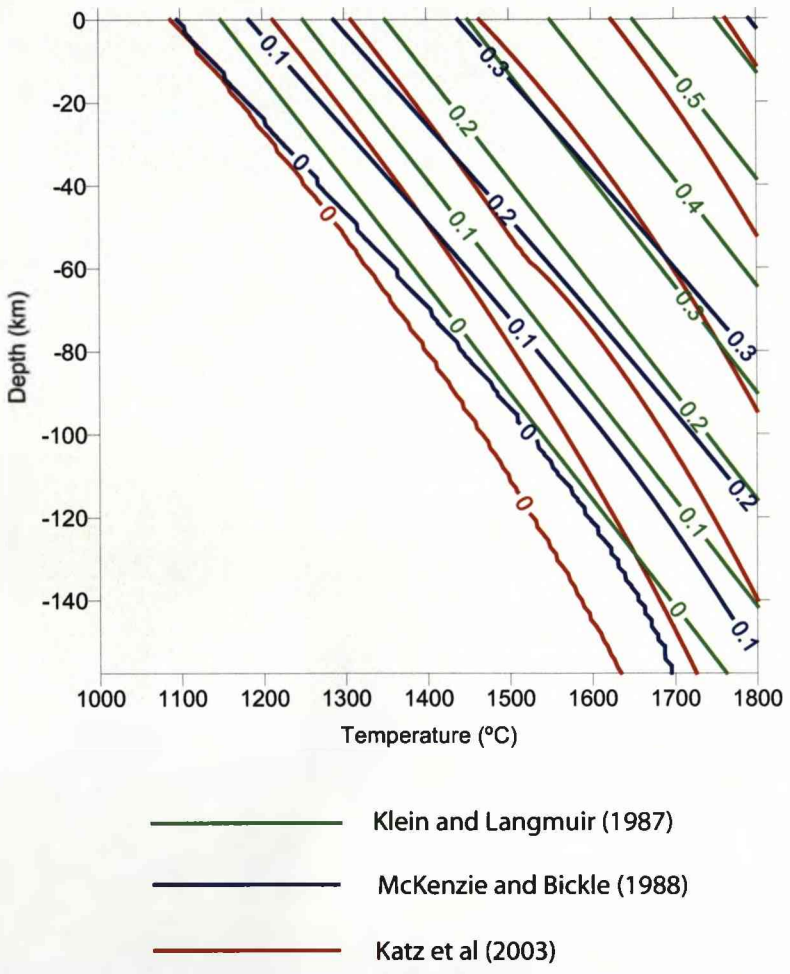

Figure 8.3: Melt fraction as a function of pressure and temperature, calculated by using three parameterisations (Klein and Langmuir, 1987; McKenzie and Bickle, 1988; Katz et al., 2003). The parameterisations of Klein and Langmuir (1987) and McKenzie and Bickle (1988) were calculated using the published equations, that of Katz et al. (2003) was calculated using FORTRAN code made freely available by the authors.

P is assumed to be a function of depth, z in the Eulerian model so that

$$P(z) = \rho_m g z \tag{8.1}$$

where ρ_m is mantle density and g is gravitational acceleration. When conditions at a node exceed the solidus the temperature at that node is corrected for latent heat in accordance with the parameterisation used. The rate of melt production R_t at time t is the sum of melt production in the melting zone and depends on the incremental increase in f so that:

$$R_t = \frac{\rho_m}{\rho_v} \int_{z=a}^{z=0} \int_{x=0}^{x=X_\infty} \frac{df}{dt} dx dz \text{ when } \frac{\partial f}{\partial t} > 0. \tag{8.2}$$

where a is the thickness of the lithosphere, x and z are the horizontal and vertical coordinates respectively, and ρ_v is the density of the volcanic addition. The minimum, weighted mean and maximum values of pressure (P), temperature ($T(x,z)$), and melt fraction (f) in the region of melt (when $\frac{\partial f}{\partial t} > 0$) are also recorded as a function of time. A parcel of mantle material becomes more depleted as it advects through the melting zone. Depletion (d) is the maximum degree of partial melting (f) experienced by a parcel of mantle, and is determined at the end of the model run by tracking the x and z coordinates backwards through time. At each time-step $T(x,z)$ and $P(z)$ are found by bilinearly interpolating between nodal values to find the maximum degree of partial melting experienced by that parcel of material.

It has been shown that melt quickly forms migration pathways at low melt fractions (McKenzie, 1989). If melt migration is assumed to be perfectly efficient, the thickness of the volcanic layer at the surface can be easily calculated. The method of calculating thickness of volcanic addition however, is different for the pure-shear and UDF models. For the pure-shear model, melt is assumed to migrate to the surface and is evenly distributed across the upwelling half-width ($W_{1/2}$), subsequently migrating laterally at

$\mathbf{V}_{(x,0)}$ so that the thickness of melt in the axial region at time t is:

$$thickness(t) = \frac{1}{\beta W_{1/2}} \int_0^t R_{t'} \beta_{t'} dt' \tag{8.3}$$

(adapted from Bown and White, 1995) where t' is a dummy time variable.

For the UDF model melt is assumed to migrate instantaneously to the axis (similar to mid-ocean ridges), after which time it moves horizontally with a velocity V_x^0 and the thickness of melt produced at time t is:

$$thickness(t) = \frac{R_t}{V_x^0} \tag{8.4}$$

The minimum, mean and maximum values of pressure ($P(z)$), temperature ($T(x,z)$), and degree of partial melting (f) within the melt zone were calculated as a function of time, and subsequently these properties were calculated for the volcanic addition as a function of horizontal distance along the surface of the model. The bathymetry or topography of the model is calculated assuming local isostasy, assuming that the density of the volcanic addition is ρ_v.

8.2.3 Testing the model: Melt thickness predicted by upwelling-divergent flow at mid-ocean ridges

Above full-spreading rates of around 20mm/yr, and away from fracture zones, oceanic crust is consistently 7.1 ± 0.8km thick, apart from where hotspots or other 'anomalies' affect melt production (White et al., 1992; Dick et al., 2003). Below 20mm/yr, the thickness of the seismic crust reduces dramatically, and in some cases appears to be absent (e.g. Klein, 2003; Dick et al., 2003, and see Figure 8.4). The relationship between crustal thickness and spreading rate can be used to test numerical models of spreading and volcanic crust production at mid-ocean ridges. A simple model of mantle flow at mid-ocean ridges is the model of upwelling-divergent flow. Reid and Jackson (1981) and Morgan et al. (1987), used the cornerflow solution of Batchelor (1967) to model the upwelling-divergent flow at mid-ocean ridges. They calculated melt thickness at

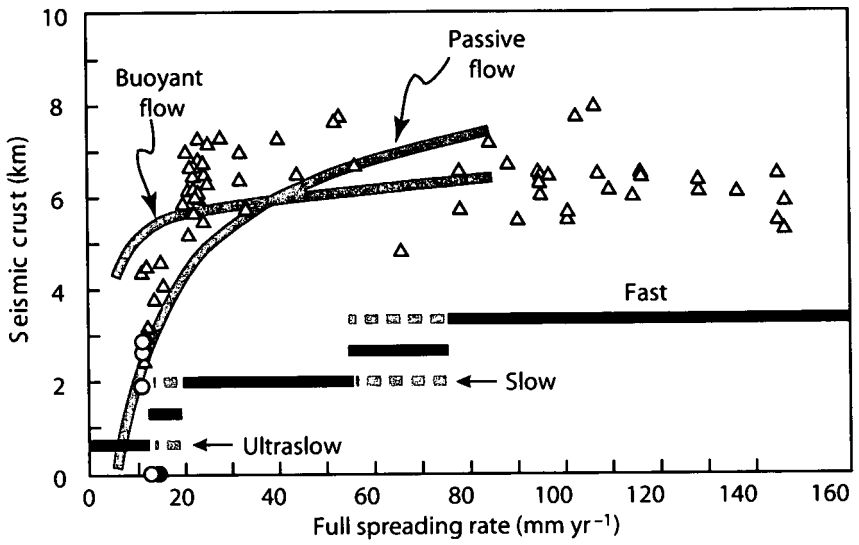

Figure 8.4: Observed (seismic) oceanic crustal thickness as a function of full spreading rate (triangles). Mid-ocean ridges are classified into 'Ultraslow', 'Slow' and 'Fast' based on spreading rate. Solid lines show predicted oceanic crustal thickness from models. 'Passive flow' relationship from model of Morgan et al. (1987), 'buoyant flow' relationship from Sotin and Parmentier (1989). Figure from Dick et al. (2003).

mid-ocean ridges assuming a constant velocity ratio (V_z^0/V_x^0) of $2/\pi$, the velocity ratio for passive flow (PhippsMorgan, 1987), at all spreading rates (see curve in Figure 8.4 labelled 'passive'). However, the constant velocity ratio UDF model for mantle flow at mid-ocean ridges under-predicts the crustal thickness at low spreading rates. The velocity ratio increases if temperature-dependent viscosity is assumed and if buoyancy forces are included in the model (e.g. Sotin and Parmentier, 1989; Shen and Forsyth, 1992; Braun et al., 2000; Tymms, 2006). This is because there is a positive feedback between viscosity and buoyancy beneath the axis of a mid-ocean ridge, causing a narrow region of (fast) upwelling to form; the increase in the velocity ratio is greatest at slow spreading rates. Predictions made by dynamic models which include temperature-dependent viscosity better match the observed relationship between crustal thickness and spreading rate (see example labelled 'active' in Figure 8.4).

To test that the physical constants of the model and melt parameterisation used in this chapter are realistic, and to demonstrate the use of kinematic models for constraining

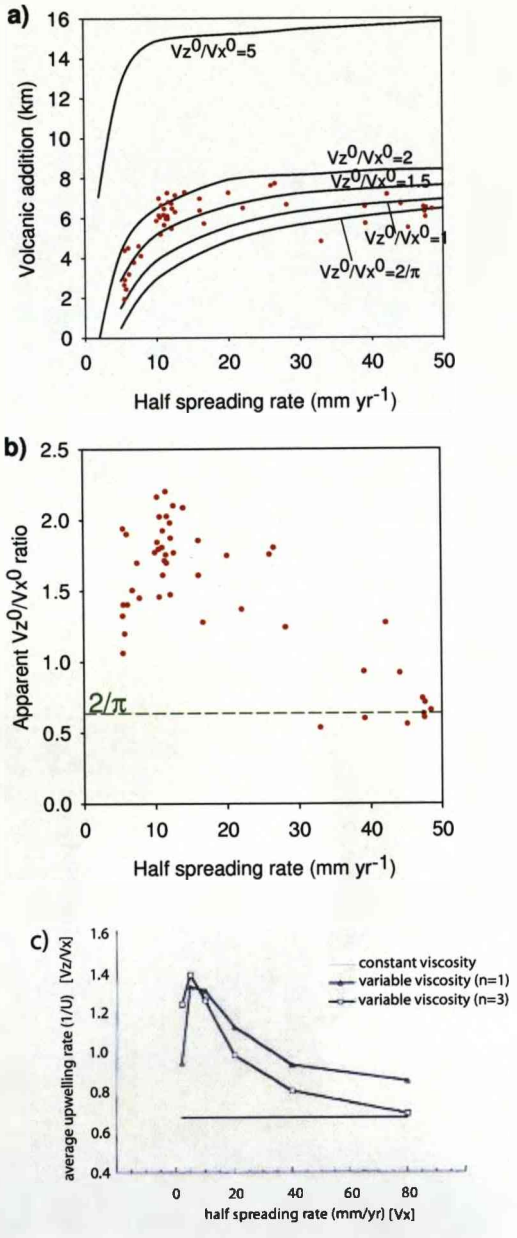

Figure 8.5: Apparent velocity ratio during seafloor spreading. (**a**) Steady-state volcanic addition predicted by upwelling-divergent flow model with various V_z^0/V_x^0 ratios, calculated using parameterisation of Katz et al. (2003) and assuming mantle potential temperature of 1333°C. Red dots indicate seismic oceanic crustal thickness versus half-spreading rate, datapoints are from Dick et al. (2003). (**b**)Apparent V_x^0/V_z^0 ratio during seafloor spreading. Data points have been inverted using model predictions shown in **a**. (**c**) Average upwelling to half-spreading velocity ratio ($\sim V_z^0/V_x^0$) as a function of half-spreading rate, calculated using a dynamic model of mid-ocean ridge flow, for a constant viscosity model, a linear temperature-dependent viscosity model (n=1) and a non-linear temperature-dependent viscosity model (n=3) (Modified from Shen and Forsyth, 1992). Note similarity of trends in **b** and **c**.

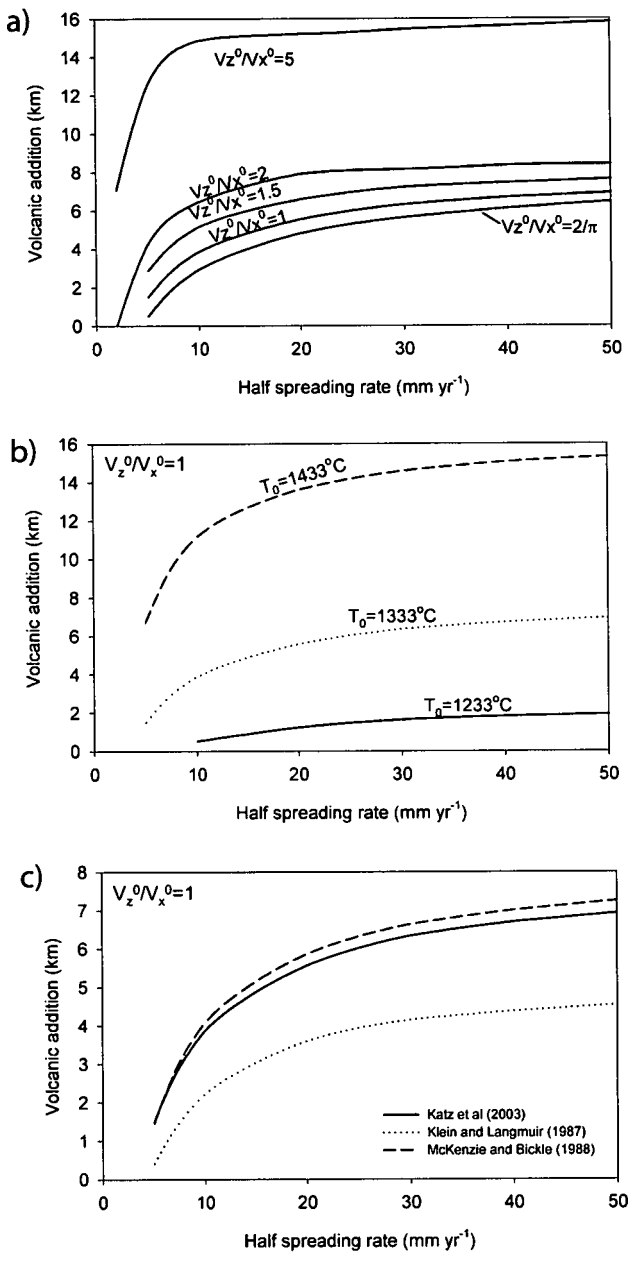

Figure 8.6: Steady-state volcanic addition predicted by the upwelling-divergent flow model. (**a**) Steady-state volcanic addition predicted by upwelling-divergent flow model with various V_z^0/V_x^0 ratios. Calculated using parameterisation of Katz et al. (2003) and assuming mantle potential temperature, T_0=1333°C. (**b**) Steady-state volcanic addition predicted by upwelling-divergent flow model with various mantle potential temperatures (T_0). Calculated using parameterisation of Katz et al. (2003) and V_z^0/V_x^0=1. (**c**) Steady-state volcanic addition predicted by upwelling-divergent flow model using various melt parameterisations. Calculated assuming T_0=1333°C and V_z^0/V_x^0=1.

patterns of mantle flow, the UDF model is used to demonstrate the apparent increase in axial upwelling to extensional velocity ratio at slow spreading rate mid-ocean ridges:

1. The steady-state melt thickness predicted by the analytical UDF model was calculated for velocity ratios of $2/\pi$, 1, 1.5, 2 and 5 assuming a mantle potential temperature of 1333 ^{o}C (Figure 8.5a).

2. Seismic crustal thickness measurements from mid-ocean ridges (from Dick et al., 2003) were then inverted for an apparent velocity ratio.

The results show an overall decrease in apparent velocity ratio as spreading rate increases (Figure 8.5b). At low spreading rates the apparent velocity ratio is around 2, decreasing towards $2/\pi$ as the spreading rate increases, showing similarity to predictions made by forward modelling of mantle flow using temperature and strain-rate viscosities (e.g. Shen and Forsyth, 1992, Figure 8.5c).

Figure 8.6b shows the dependence of steady state crustal thickness predicted by a UDF model with a velocity ratio of 1 on mantle potential temperature (T_0), demonstrating the effect that T_0 can have on oceanic crust thickness. Figure 8.6c also shows the steady state crustal thickness predicted by a UDF model with V_z^0/V_x^0 ratio of 1 using various melt parameterisations. The plot illustrates the importance of using a single parameterisation to make meaningful comparisons between models. However, it is noted that the Katz et al. (2003) and McKenzie and Bickle (1988) parameterisations make similar steady-state volcanic thickness predictions.

8.3 Melt generation during continental lithosphere thinning: Pure-shear

McKenzie and Bickle (1988) predicted that melting may occur during thinning of the lithosphere, and illustrated the dependence of the thickness and composition on mantle potential temperature. Bown and White (1995) extended the model to show the effect of finite thinning rate on the volume of melt predicted.

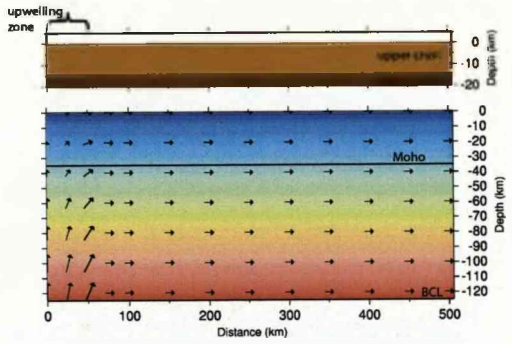

(a) 0Myr

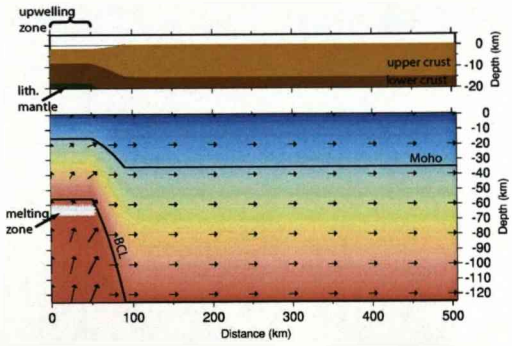

(b) 2Myr

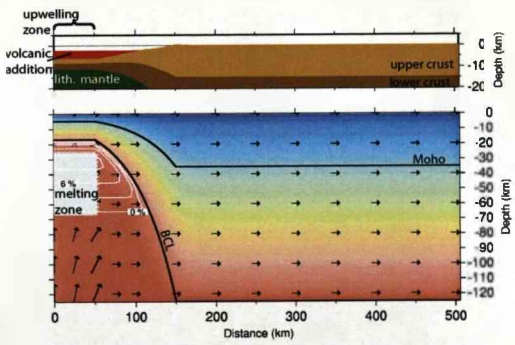

(c) 5Myr

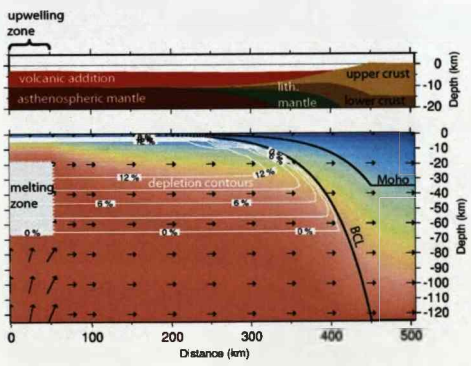

(d) 20Myr

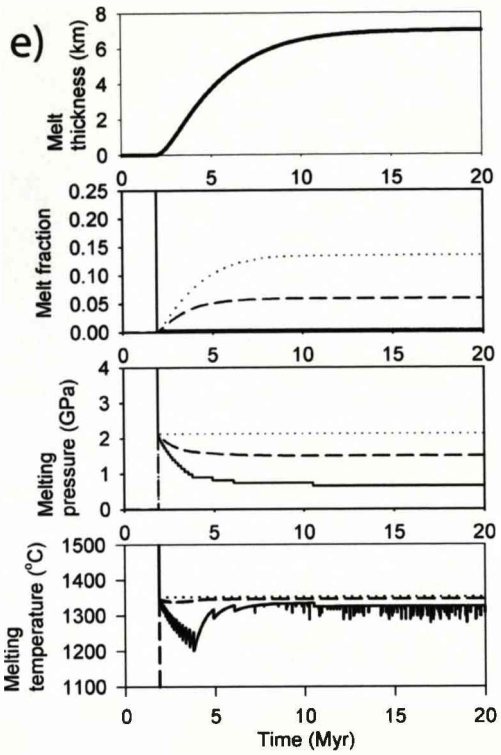

Figure 8.7: Model evolution of continental lithosphere thinning due to a finite width ($W_{1/2}$=50 km) pure-shear flowfield with half-extension rate (V_x^0) of 20 mm/yr. Velocity field is non-time-dependent in the axial reference frame. Four snapshots in time at (**a**) Time (t)=0; (**b**) t=2 Myr, shortly after melting begins, when the lithosphere has been stretched by a maximum factor (β_{max}) of 2.23; (**c**) t=5Myr (β_{max}=7.34); (**d**) t=20Myr (β_{max}=2980). In each case the lower panel shows a Eulerian plot of temperature, the zone of melting (grey), depletion (white contours), velocity vectors (black arrows) and the position of the Moho and base of the continental lithosphere (BCL); the upper panel shows the upper 20 km of the model, corrected for isostatic effects of thermal expansion, crustal thinning and volcanic and water loading. (**e**) Thickness of volcanic addition and minimum, mean and maximum values of pressure, temperature and melt fraction in the melting zone plotted as a function of time.

In this section melt production is calculated for a 2–D version of the pure-shear model (described in Chapter 7). The sensitivity of melt thickness to half-extension rate, the width of the upwelling zone, mantle potential temperature, thermal lithosphere thickness, composition and melt behaviour is tested. The ability of each of these variables to explain the variation in volcanic thicknesses at rifted continental margins is then assessed.

Figure 8.7 shows the temporal evolution of an initially thermally equilibrated model during pure-shear deformation. The model is extending at a half-extension rate of 20mm/yr, the pure-shear upwelling half-width ($W_{1/2}$) is 50km, and the mantle potential temperature is 1333°C. The temperature and pressure conditions in the model cross the solidus at a depth of 65km after 1.9Myr, when the axial stretching factor (β_{max}) is 2.14 and half-extension ($E_{1/2}$) 39km. Melt is therefore predicted to occur everywhere across the resulting basin or margin where the stretching factor (β) exceeds 2.14. The melting rate increases with time before reaching a steady-state. The steady-state thickness of volcanic addition of ~7km is reached after 10-15Myr. The melting region increases in size through time and the temperature, pressure and degree of partial melting in the melting region evolve to reflect this. The average degree of partial melt increases with time - the earliest melt would therefore be expected to have a high concentration of incompatible elements. The maximum pressure in the melt zone (2.3GPa, 65km) does not change through the model evolution, although the minimum and mean pressure of melt production decrease. The range of melting temperatures initially increases to around 200 °C before reducing to a range of around 50°C. Note that the jagged appearance of the minimum temperature plots may be artifacts of the numerical model: the minimum temperature in the melting zone may be influenced by single model-data points outside of the axial upwelling region where conductive heating causes pressure-temperature conditions to exceed the solidus, particularly in the early stages of the model. The mean temperature of melt decreases by a few tens of degrees after the onset of melting, but quickly reaches a constant value slightly above the mantle potential temperature. In this example the melt thickness reaches a steady state thickness after

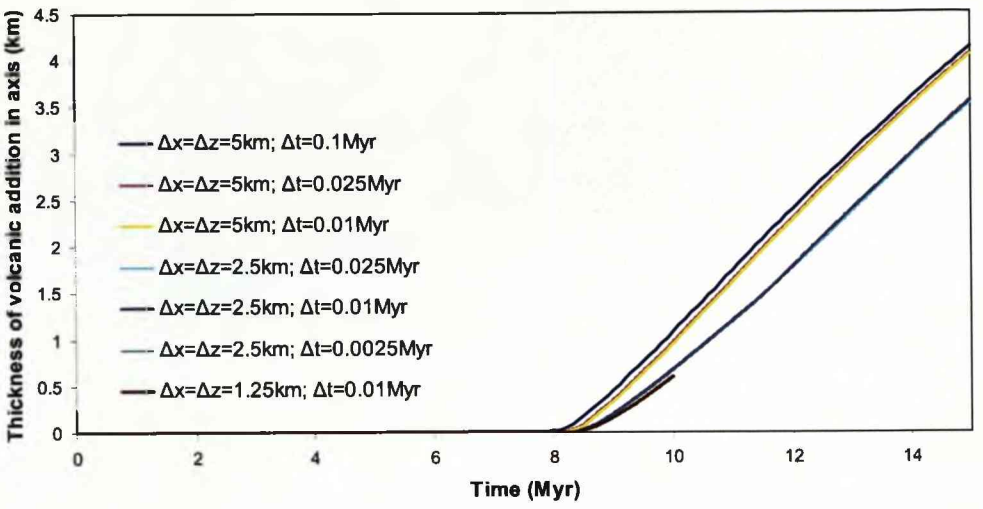

Figure 8.8: Melt production sensitivity to model resolution. Axial melt production for a model extending at 21.5mm/yr with a axial upwelling zone 200km wide. After 15Myr the stretching factor is 5. Mantle potential temperature 1400^o C. Δx, Δz and Δt denote the horizontal, vertical node spacing and time-step respectively.

around 20Myr; the conditions of melting are close to their steady state values much sooner, after around 5Myr.

8.3.1 Model resolution

Figure 8.8 shows the axial melt thickness predicted for a model of pure-shear thinning calculated using various nodal spacing and time-steps. The number of gridnodes and time-steps was limited by the FORTRAN compiler used. Melt production is sensitive to grid node spacings, but relatively insensitive to the time-step, as long as the Courant condition is satisfied. In the remainder of this chapter a grid node spacing of 2.5km and time-step <5000yr, which always satisfies the Courant condition, is used. The grid node spacing used was chosen in order to balance the need for high model resolution with constraints on computing time.

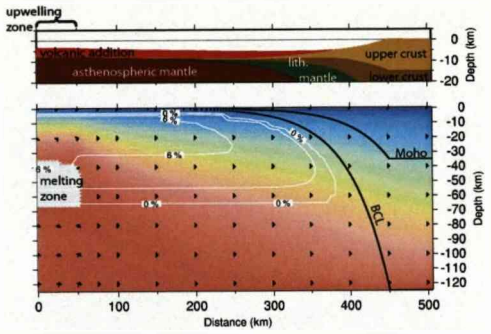

(a) V_x^0=5mm/yr, after 80Myr

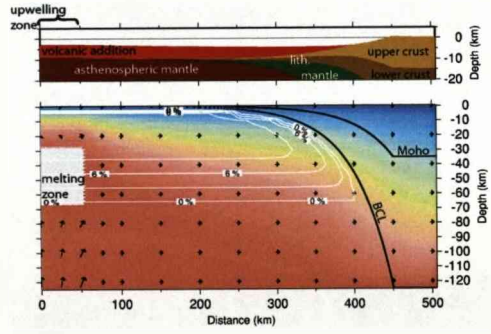

(b) V_x^0=10mm/yr, after 40Myr

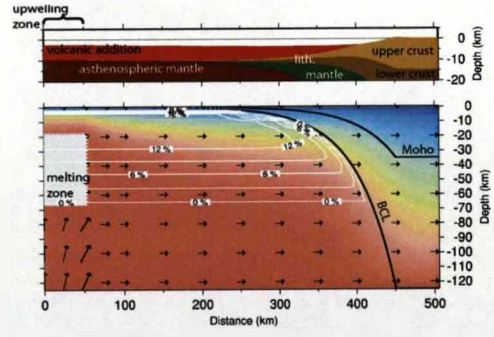

(c) V_x^0=20mm/yr, after 20Myr

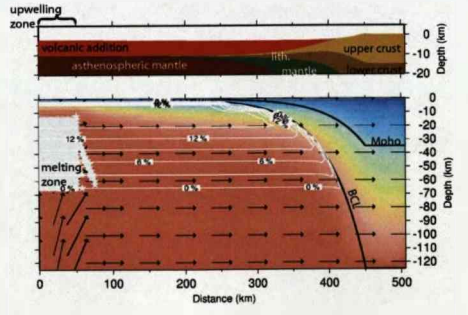

(d) V_x^0=50mm/yr, after 8Myr

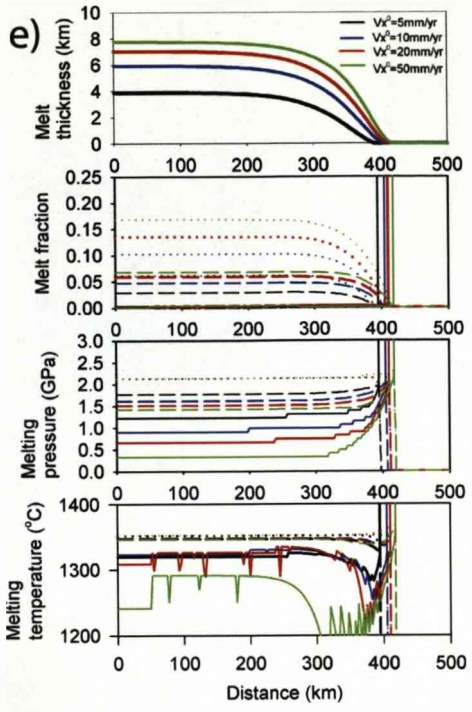

Figure 8.9: Sensitivity of volcanic addition to pure-shear half-extension rate. (**a-d**) show models with upwelling half-width ($W_{1/2}$) of 50km, after 400km half-extension at various half-extension rates (V_x^0) as indicated. In each case the lower panel shows a Eulerian plot of temperature, the zone of melting (grey), depletion (white contours), velocity vectors (black arrows) and the position of the Moho and base of the continental lithosphere (BCL); the upper panel shows the upper 20 km of the model, corrected for isostatic effects of thermal expansion, crustal thinning and volcanic and water loading. (**e**) Predicted melt thickness as function of distance along the profile, lower panels show minimum, mean and maximum melt fraction, melting pressure and melting temperature of melt also as a function of distance. Black lines correspond to V_x^0=5mm/yr; Blue lines to V_x^0=10mm/yr; Red lines to V_x^0=20mm/yr; Green lines to V_x^0=50mm/yr. Note that oscillations in the minimum temperature plots are due to single model-data points and are artifacts of the node spacing in the numerical model.

8.3.2 Sensitivity of volcanic addition to pure-shear half-extension rate

The final lithospheric geometry predicted by the pure-shear model is independent of the half-extension velocity. However, conductive cooling at slow rates of extension can retard the onset of melting during thinning (Bown and White, 1995). Figure 8.9 shows that as spreading rate increases, the stretching factor at which melt initiates decreases and the thickness of the volcanic addition increases. For the example shown, melting is predicted to initiate after the axis of the model has been thinned by a factor of 1.9 when the half-spreading rate is 50mm/yr; when the half-spreading rate is 5mm/yr, the lithosphere is thinned by a factor of 3.0 before melting begins. When the model was run with a half-spreading rate of 2mm/yr, no melt was predicted. Additionally, when compared to predictions made by models run at slower extension rates, models with faster rates predict melting at: a higher mean and maximum melt fraction; a lower mean melting pressure; a larger range of melting pressures; an initially larger range of melting temperatures; although similar mean melting temperatures.

At a normal mantle potential temperature (1333^{o}C), and using the melt parameterisation of Katz et al. (2003), the pure-shear model cannot predict melt thicknesses greater than 8km (the thickness of melt predicted by adaibatic upwelling). However, the pure-shear model can explain very low and even absent melt thicknesses if the spreading rate is very slow.

8.3.3 Sensitivity of volcanic addition to pure-shear upwelling half-width

The stretching factor at which melting initiates during pure-shear thinning depends on the thinning rate (Bown and White, 1995). For the 2–D pure-shear kinematic model presented here, the thinning rate depends on the half-extension rate and the width of the upwelling region (Equation 7.17). In 2–D, the width of the upwelling region also affects the influence of lateral heat conduction on melt production. Slow rates of upwelling over a wide zone have been suggested as a possible reason for low melt volumes observed at magma-poor margins (e.g. Whitmarsh and Miles, 1995).

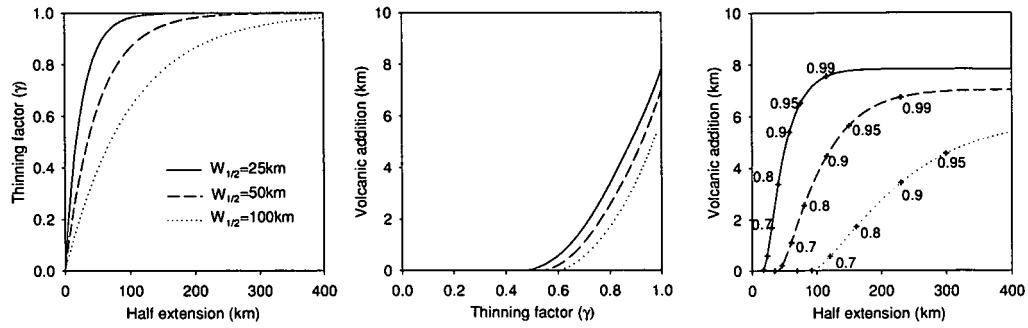

Figure 8.10: Sensitivity of volcanic addition to pure-shear upwelling half-width. Cross-plots of volcanic addition, thinning factor (gamma) and half-extension predicted by the 2–D pure-shear model run at a half-extension rate of 20 mm/yr and upwelling half-widths of 25km (solid lines), 50km (dashed lines) and 100 km (dotted lines). Thinning factor (γ) is related to stretching factor (β): γ = 1-1/β.

Cross-plots of melt thickness, thinning factor (γ) and half-extension predicted by the pure-shear model with axial half-widths of 25, 50 and 100 km, and half-extension rate of 20mm/yr, are shown in Figure 8.10. Melting initiates at a thinning factor of 0.5 (stretching factor (β)=2, half-extension = 17km) when the upwelling half-width is 25km. When the upwelling width is increased to 100 km, melting initiates at a thinning factor of 0.6 (stretching factor (β)=2.5; half-extension = 90km).

If the zone of upwelling is wide, and the thinning rate is slow, then conductive cooling can suppress melting during thinning. Mantle exhumation is predicted if melting is suppressed until after the critical thinning factor has been exceeded. This is possible if the critical thinning factor is low, the extension rate is slow and the zone of upwelling is very wide. A very narrow upwelling half-width cannot explain very thick volcanic addition: instantaneous thinning of the lithosphere to a thinning factor of 1 (β=∞) at normal mantle potential temperatures cannot predict melt thicknesses greater that 8km (the thickness of melt predicted by adaibatic upwelling).

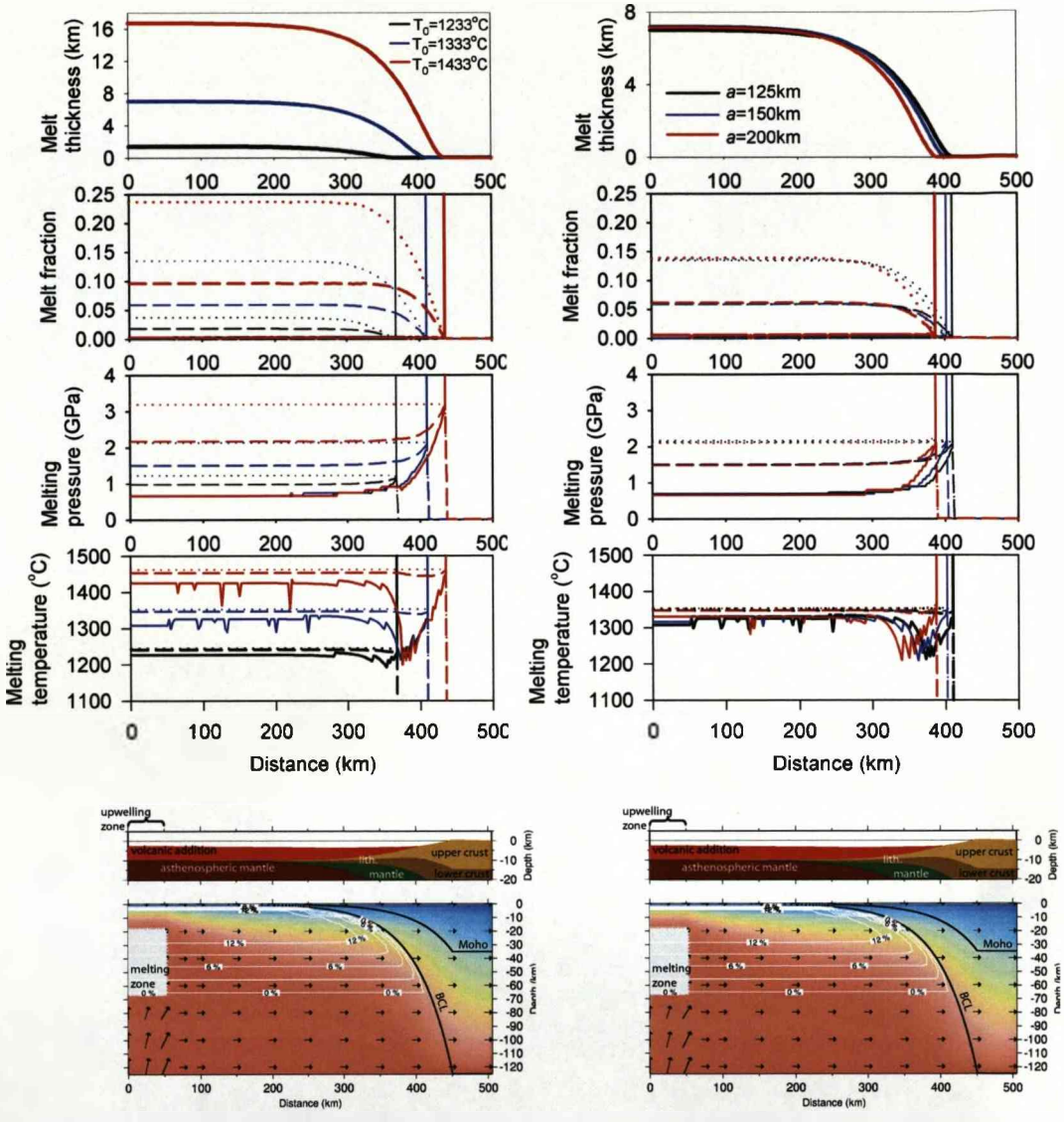

Figure 8.11: Sensitivity of melting to mantle potential temperature (T_0) and lithosphere thickness (a). (**Left**): Melt thickness, minimum, mean and maximum melt fraction, melting pressure and melting temperature of melt predicted as function of distance along the profile for mantle potential temperatures of 1233°C (black lines), 1333°C (blue lines) and 1433°C (red lines). Lower panels show plot of temperature, melting zone and depletion, and corresponding upper lithospheric structure for model run with T_0=1333°C. (**Right**): Melt thickness, minimum, mean and maximum melt fraction, melting pressure and melting temperature of melt predicted as function of distance along the profile for initial continental lithospheric thicknesses of 125km (black lines), 150km (blue lines) and 200km (red lines). Lower panels show plot of temperature, melting zone and depletion, and corresponding upper lithospheric structure for model run with a=125km.

8.3.4 Sensitivity of volcanic addition to mantle potential temperature

Mantle potential temperature heterogeneities have long been thought to be responsible for the voluminous volcanism that can accompany continental breakup (White and McKenzie, 1989). Volcanic margins are often associated in both time and space with large igneous provinces thought to be caused by mantle hotspots, for example the North Atlantic, the south Atlantic, the western India - Seychelles conjugates and the southern Red Sea (White and McKenzie, 1989). A cool geotherm caused by a lower-than-average mantle potential temperature may also explain the absence of volcanism at the non-volcanic margins of the Atlantic (e.g. Minshull et al., 2001; Reston and Morgan, 2004; Pérez-Gussinyé et al., 2006).

Increasing the mantle potential temperature for the pure-shear model causes melting to initiate earlier (after less extension), and increases the thickness of melt produced during lithospheric thinning. For the model shown in Figure 8.7 the mantle potential temperature was 1333°C, melting initiated when β= 2.14 and reached a steady state thickness of 7.0km. Increasing the mantle potential temperature by 100 °C (to 1433°C) causes melt to initiate at β= 1.33, reaching a steady state thickness of 16.7km. Decreasing the mantle potential temperature by 100°C (to 1233°C) causes melt to initiate at β= 5.03, reaching a steady state thickness of 1.4km. At higher mantle potential temperatures the pressure and temperature conditions of the model overstep the solidus to higher degrees of partial melt over a wider range of pressures and at higher temperatures than for models with lower mantle potential temperatures. Consequently, when compared to models run with lower mantle potential temperatures, models run with higher mantle potential temperatures predict melt which has: a higher mean and maximum melt fraction; a higher mean melting pressure; a wider range of melting pressures; and higher minimum, mean and maximum melting temperatures (Figure 8.11).

The observed variation in the thickness of volcanic addition at rifted margins (zero to around 15km) can be explained by mantle potential temperature heterogeneities with a range of a few hundred degrees Celsius.

8.3.5 Sensitivity of volcanic addition to initial continental lithosphere thickness

The temperature structure of the continents is affected by tectonic setting and geological history, and the continental lithosphere has a highly variable, if poorly defined, thickness (e.g Artemieva, 2006). In the models presented in this chapter, the continental geotherm is assumed to be initially linear, with a surface temperature of 0°C and a temperature at the base of the continental lithosphere of 1333°C. As discussed in Section 7.3.6, radiogenic heating is not included in these models. When compared to the example shown in Figure 8.7, increasing the lithospheric thermal thickness from 125km to 200km delays the onset of melting by 1.1Myr, to 3Myr after the onset of thinning. This means that for a thicker lithosphere melting begins after more extension (Figure 8.11). The thickness of the lithosphere has little effect on the steady-state thickness or the pressure, temperature and melt fraction in the melting zone. Although lithosphere thickness variations cannot explain volcanic addition at margins thicker than 7-8km, variations in the thickness of the thermal lithosphere may explain some of the variation in the amount of horizontal extension and thinning which occurs prior to the onset of melting at rifted continental margins.

8.3.6 Sensitivity of volcanic addition to mantle source composition

It has been suggested that the distribution of mantle compositional heterogeneities, rather than temperature heterogeneities, may be partly responsible for the distribution of volcanic addition on the Earth's surface (e.g. Asimow et al., 2004; Anderson, 2006). The melt parameterisation of Katz et al. (2003) allows the composition of the mantle source to be specified, in terms of clinopyroxene (cpx) and water content. These parameters are discussed here separately. The parameterisation assumes that cpx content does not affect the solidus, and so does not affect the timing of the onset of melting; however the cpx content affects the degree of partial melting. For the median model chosen in this chapter (Figure 8.7: mantle potential temperature 1333°C, half-extension

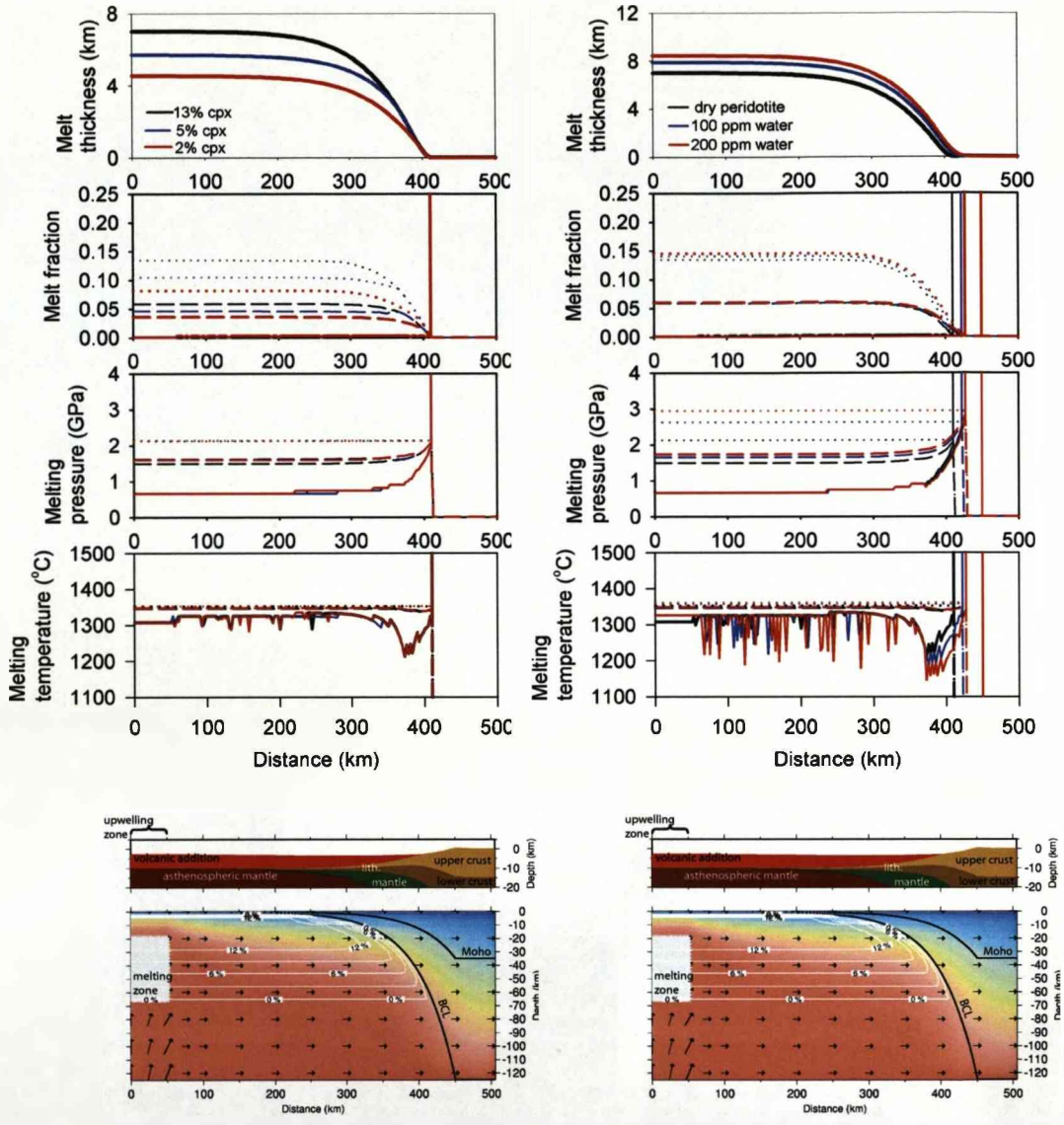

Figure 8.12: Sensitivity of melt to mantle source composition and water content. (**Left**): Melt thickness, minimum, mean and maximum melt fraction, melting pressure and melting temperature of melt predicted as function of distance along the profile for clinopyroxene (cpx) content of 13% (black lines), 5% (blue lines) and 2% (red lines). Lowest panel shows plot of temperature, melting zone and depletion, and corresponding upper lithospheric structure for model run with cpx content of 13 %. (**Right**): Melt thickness, minimum, mean and maximum melt fraction, melting pressure and melting temperature of melt predicted as function of distance along the profile for dry peridotite (black lines), water content of 100ppm (blue lines) and 200ppm (red lines). Lowest panel shows plot of temperature, melting zone and depletion, and corresponding upper lithospheric structure for model where dry peridotite is assumed.

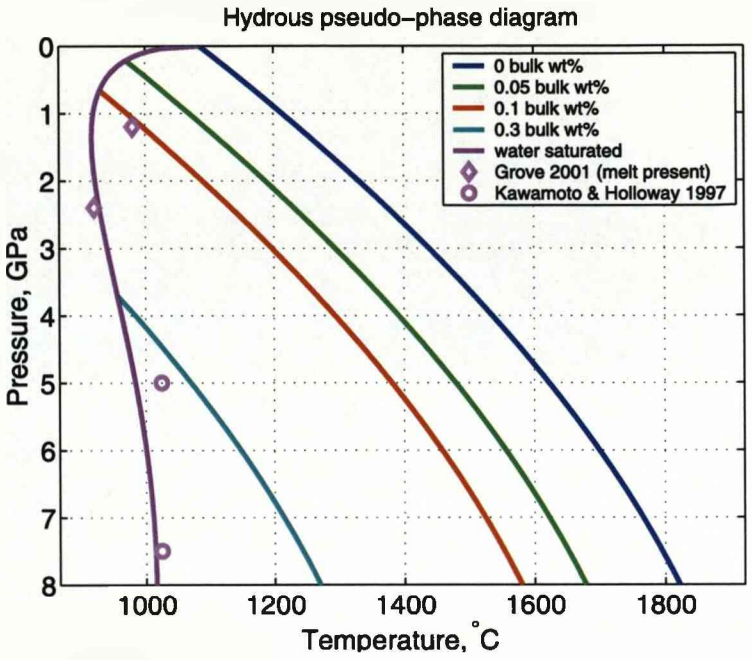

Figure 8.13: Effect of water on the peridotite solidus, from Katz et al. (2003).

rate 20mm/yr, upwelling half-width 50km), the cpx content does not affect the thickness or composition of melt for cpx-content above ~13%. However when cpx content is reduced below 13%, lower melt thickness and a lower mean and maximum melt fraction are predicted (Figure 8.12). The predicted melting pressure and temperatures are relatively unaffected by the cpx content. Assuming a range of mantle cpx content from 2% to 13%, at a half-extension rate of 20mm/yr, a range in maximum thickness of volcanic addition from 4km to 7km is predicted; therefore variations in cpx content alone cannot explain the range in volcanic thickness at rifted continental margins. However, the mantle may contain other minerals which are not included in this parameterisation (e.g. from recycled crust, Anderson, 2006) which may considerably affect the solidus and melt productivity of the mantle, as well as the resulting melt geochemistry.

8.3.7 Sensitivity of volcanic addition to mantle water content

Water in the mantle can significantly reduce the solidus temperature (Hirth and Kohlstedt, 1996, Figure 8.13). This allows melting to occur deeper in the mantle. Wet melting (melting in pressure-temperature space between the wet and dry solidii) may be responsible for a 'garnet signature' (indicating melting below the garnet-spinel phase transition at 60-90km depth) in some MORBs (Salters and Hart, 1989; Beattie, 1993). Thus water content may influence the onset and thickness of melt at rifted margins. The melt parameterisation of Katz et al. (2003) allows the water content of the mantle source to be specified. Workman and Hart (2005) calculate that average present-day mantle contains water with concentrations in the range of 70-160ppm, although the water capacity of the mantle increases with depth to up to 2000ppm at around 100km (Hirschmann et al., 2005; Hauri et al., 2006). When compared to the example shown in Figure 8.7, increasing the water content from zero to 200ppm causes melting to initiate after lithosphere stretching by a factor of 1.5 (compared to a stretching factor of 2.14 for dry mantle), the maximum melting pressure increases from 2.3 GPa to 2.9 GPa, and the maximum thickness increases from 7.0 km to 8.4 km (Figure 8.12). Unless water contents are exceptionally high (more than few hundred ppm), wet melting only accounts for an increase in the degree of partial melting of a few percent, so the contribution of wet melting to total melt thickness is relatively small. The continental lithospheric mantle composition and water content is difficult to constrain accurately. If compositional heterogeneities are in a range similar to those in the asthenospheric mantle (i.e. similar to the source for MORB) then compositional heterogeneities do not explain the large variation in thickness of volcanic addition observed at rifted margins. However, it is possible that continental lithospheric and sub-continental mantle may be more heterogeneous that the bulk mantle, due to the influence of earlier tectonic events, continental accretionary processes and the lithosphere's relatively long-lived nature. Compositional and water content heterogeneities may explain the range of volcanic addition thickness in the absence of temperature anomalies, although a signature may be expected in the resulting volcanics.

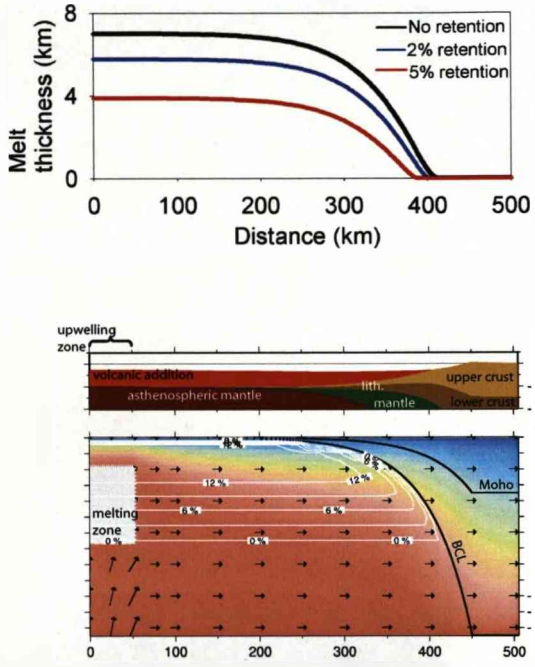

Figure 8.14: Sensitivity of predicted thickness of volcanic addition to melt migration behaviour. Upper panel shows melt thickness predicted as function of distance along the profile for models where all of the melt migrates to the axial zone (black line), the first 2% of melt produced is retained (blue line) and the first 5% of melt produced is retained (red line). Lower panel shows plot of temperature, melting zone and depletion, and corresponding upper lithospheric structure for model run assuming perfectly efficient migration. Conditions in the melting zone are not presented as this would require assumptions to be made about the composition of the retained melt.

8.3.8 Sensitivity of volcanic addition to migration efficiency

In the models described so far, all melt produced is assumed to migrate instantaneously to the axial region. Migration of melt to the surface is believed to occur rapidly at small melt fractions beneath mid-ocean ridges (Ahern and Turcotte, 1979). However, at rifted margins a migration pathway may not be readily available for the first melt produced, or the Moho may behave as a density filter, or melt may re-freeze as it ascends into cooler rock. These effects can reduce the amount of volcanics observed at the surface. Conductive cooling at ultra-slow spreading ridges means that oceanic crust may comprise gabbroic plutons rather than mafic extrusives, due to incomplete extraction (Cannat, 1996; Lizarralde et al., 2004). Incomplete melt migration may therefore explain the thin oceanic crust at ultra-slow spreading centres, and of thin or absent volcanic addition at rifted margins. Peridotite infiltrated with frozen melt has been observed on the Iberian and Newfoundland margins and at the exhumed continental mantle of the ancient Tethyan margin exposed in the Alps (Muntener et al., 2004; Chazot et al., 2005; Muntener and Manatschal, 2006). Figure 8.14 illustrates volcanic thickness predictions for incomplete melt migration. I assume that the first percentage of partial melt is retained, so the onset of melting is delayed and the resulting thickness of melt is reduced. Melt retention may partially explain thin or absent extrusive volcanics (and therefore mantle exhumation) at some rifted margins.

8.3.9 Summary of factors affecting melt production during pure-shear thinning of the lithosphere

A number of factors have been shown to influence both the timing of onset of melting and the thickness of melt produced during continental lithospheric thinning: mantle potential temperature, thinning rate, spreading rate, lithosphere thickness, mantle composition, mantle water content and melt migration. Factors which bring forward the onset of melting and increase the thickness of melt produced are:

1. Faster spreading rates

2. Increased mantle potential temperature
3. Thinner lithosphere
4. High clinopyroxene content of the mantle / other compositional heterogeneity
5. High mantle water content

Assuming that the thinning of the lithosphere at rifted margins occurs by pure-shear, only increased mantle potential temperature (by 100-200^{o}C) can easily explain very thick (up to 20km) volcanic addition.

Factors which retard the onset of melting and decrease the thickness of melt produced are:

1. Slower extension rates
2. Lower mantle potential temperature
3. Thicker lithosphere
4. Lower clinopyroxene content / other compositional heterogeneity
5. Melt retention (or re-freezing) in the mantle

Slow extension rates, low mantle potential temperature or melt retention can explain very thin (or absent) volcanism during pure-shear thinning of the continental lithosphere.

Possible factors which may have significantly influenced melt production during margin formation can be tested where observations are available. For example the extension rate and rift duration may be inferred from geological data and magnetic anomalies, lithosphere thickness may be inferred from that on the adjacent continent, and temperature and compositional heterogeneities may manifest their presence in the melt, or exhumed mantle, geochemistry.

This section has shown that a number of intrinsic properties of the mantle (water content, composition, potential temperature) and the kinematics of rifting (extension rate, lithosphere thickness) can influence melt production. However, in this section,

the assumption has been made that the lithosphere thins by pure-shear. In the previous chapters it has been shown that lithospheric thinning does not always occur by pure-shear, and upwelling-divergent flow has been suggested as a possible deformation process during thinning and margin formation. In the remainder of this chapter the implications of upwelling-divergent flow (UDF) during continental lithosphere thinning and margin formation on melt production are investigated. The timing and distribution of volcanic addition predicted by the UDF model, and the observations which may allow the various explanations for anomalous melting to be distinguished, are then discussed.

8.4 Melt generation during continental lithosphere thinning: upwelling-divergent flow

In this section the melt predicted by models of continental lithospheric thinning leading to breakup by upwelling-divergent flow is presented. Melt production is calculated in the same way as for the pure-shear model of continental lithospheric thinning, however, for the upwelling-divergent flow model melt is assumed to migrate to the axis of the model (rather than the axial zone), as described in Section 8.2.2. The effect of varying the velocity ratio, and the effect of an upwards-propagating upwelling-divergent flow, on melt production is tested.

Figure 8.15 *(following page)*: Time evolution of models of continental lithospheric thinning leading to breakup caused by an upwelling-divergent flowfield with variable V_z^0/V_x^0 ratios. V_x^0 =20mm/yr in all models. (**a-d**) Model evolution where V_z^0/V_x^0=1. (**e-h**) Model evolution where V_z^0/V_x^0=2. (**i-l**) Model evolution where V_z^0/V_x^0=5. In each case the main panel shows a Eulerian plot of temperature, the position of the Moho and base of the continental lithosphere (BCL); the upper panel shows the upper 20 km of the model, corrected for isostatic effects of thermal expansion, crustal thinning, volcanic addition and water loading. In **d**,**h** and **l** the minimum, mean and maximum melt fraction, melting temperature and melting pressure are also shown as a function of distance along the respective margins. Note different scale for melt thickness plots.

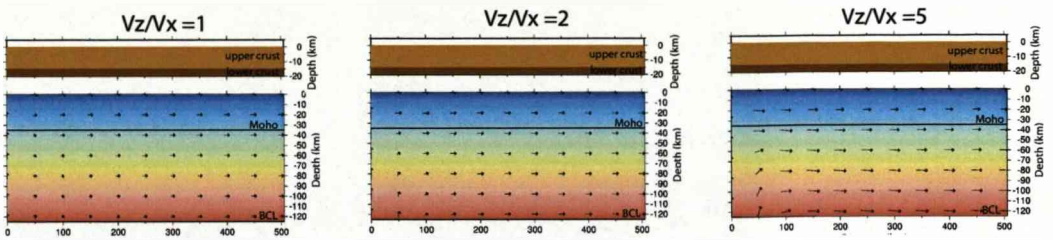

(a) V_z^0/V_x^0=1, t=0Myr (e) V_z^0/V_x^0=2, t=0Myr (i) V_z^0/V_x^0=5, t=0Myr

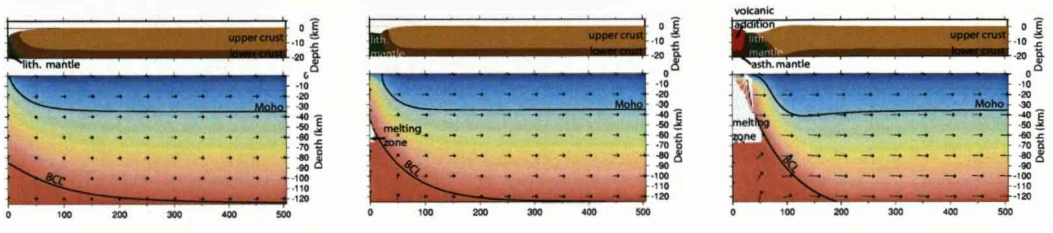

(b) V_z^0/V_x^0=1, t=2Myr (f) V_z^0/V_x^0=2, t=2Myr (j) V_z^0/V_x^0=5, t=2Myr

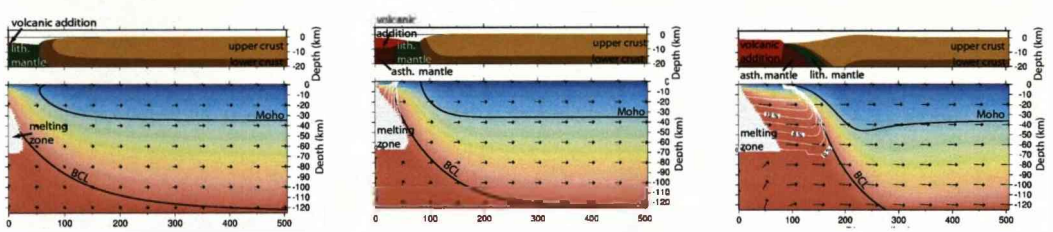

(c) V_z^0/V_x^0=1, t=5Myr (g) V_z^0/V_x^0=2, t=5Myr (k) V_z^0/V_x^0=5, t=5Myr

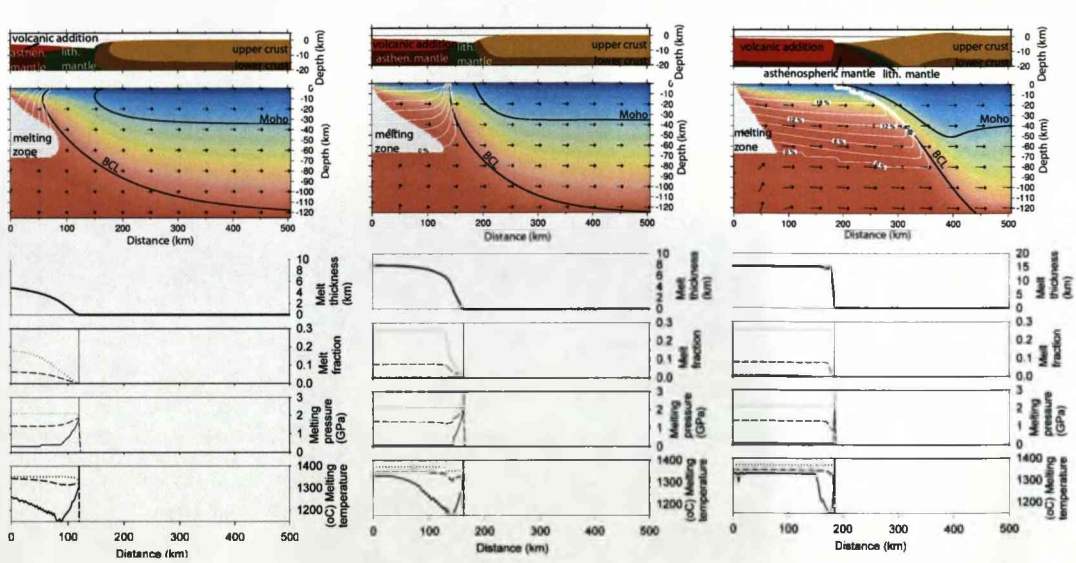

(d) V_z^0/V_x^0=1, t=10Myr (h) V_z^0/V_x^0=2, t=10Myr (l) V_z^0/V_x^0=5, t=10Myr

8.4.1 Sensitivity of volcanic addition to the axial upwelling to half spreading rate velocity ratio

The UDF model assumes that lithosphere deformation occurs due to an upwelling-divergent flowfield which acts in the continental lithosphere and asthenosphere during continental lithosphere thinning leading to breakup. The flowfield is defined by an axial upwelling velocity V_z^0 and a half spreading rate V_x^0.

Figure 8.15 illustrates examples of rifted margin development calculated by imposing a velocity field with a half spreading rate of 20 mm/yr and velocity ratios (V_z^0/V_x^0) of 1, 2 and 5 onto an initially horizontally layered lithosphere with a constant geotherm. At a velocity ratio of 1, melting initiates after 3.9 Myr, after 79 km of crust and lithospheric mantle have been exhumed. Assuming a crustal thickness of 35km this leaves a zone of exhumed continental mantle (ZECM) 44km wide. At higher velocity ratios, the onset of melting occurs after less horizontal extension and the width of the exhumed lower crust and lithospheric mantle is reduced. In the axial reference frame, a model run with a high velocity ratio reaches a steady-state (in terms of the thickness and melting properties of volcanic addition) faster than a model run with a low velocity ratio. The steady state thickness of volcanic addition increases with velocity ratio (this was discussed in Section 8.2.3). The minimum, mean and maximum values of pressure, temperature and degree of partial melting in the melting zone show a time-dependence similar to that described for the pure-shear model. The pressure, temperature and degree of partial melt produced at steady state is relatively unaffected by the velocity ratio; the increase in ratio affects only the flux of melt through the melting region and not the conditions of melting.

8.4.2 Sensitivity of volcanic addition to half spreading rate

The final lithospheric structure predicted by the upwelling-divergent flow model is independent of half-spreading rate. However, the timing of the onset of melting and the thickness of melt is dependent on the half-spreading rate. At slower half-spreading

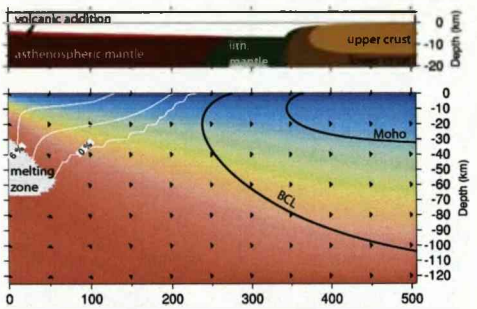

(a) V_x^0=5mm/yr; 80Myr

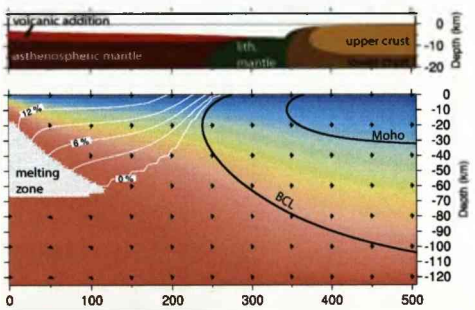

(b) V_x^0=10mm/yr; 40Myr

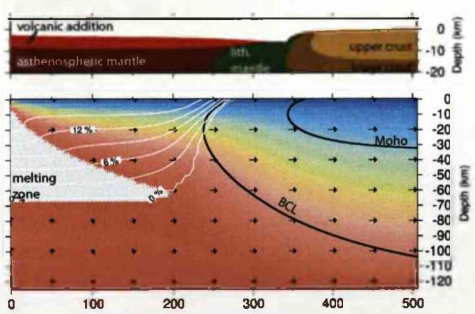

(c) V_x^0=20mm/yr; 20Myr

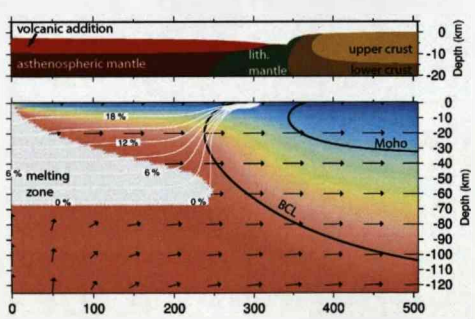

(d) V_x^0=50mm/yr; 8Myr

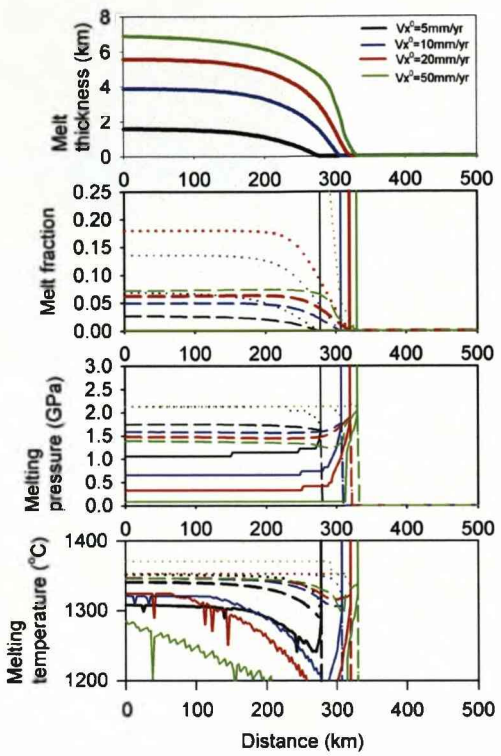

(e)

Figure 8.16: Sensitivity of volcanic addition to UDF spreading rate. (**a-d**) show models run with an axial upwelling to half spreading rate velocity ratio (V_z^0/V_x^0) of 1 after 400km half-extension. Half-spreading rates (V_x^0) as indicated. (**e**) The upper panel shows melt thickness predicted as function of horizontal distance from axis; lower panels show minimum, mean and maximum melt fraction, melting pressure and melting temperature of melt also as a function of distance from axis. Black lines correspond to V_x^0=5mm/yr; Blue lines to V_x^0=10mm/yr; Red lines to V_x^0=20mm/yr; Green lines to V_x^0=50mm/yr.

rates, more heat is conducted during upwelling than at faster half-spreading rates; consequently melting initiates after less extension and the width of the ZECM decreases with increasing half-spreading rate. Figure 8.16 shows the resulting temperature field, the zone of melting and depletion predicted by the UDF model run with velocity ratio of 2 at half-spreading rates of 5, 10, 20 and 50mm/yr after 400km half-extension. At 5mm/yr the width of the exhumed crust and mantle is 122km (therefore assuming a 35km thick crust, 87km of exhumed continental mantle is predicted), at 50mm/yr the width of the exhumed crust and mantle is reduced to 69km (therefore assuming a 35km thick crust, 34km of exhumed continental mantle is predicted). The temperature, pressure and degree of partial melting in the melting zone shows a similar dependence on rate as discussed for the pure-shear model (Section 8.3.2).

In the previous chapter it was proposed that an upwards-propagating UDF may be a more realistic flow pattern, in some cases, for continental lithosphere thinning and rifted margin formation. Figure 8.17 illustrates examples of rifted margin development where the flowfield propagates upwards from the base of the lithosphere to the surface. When the flowfield reaches the surface it becomes static (remains steady in the coordinate reference frame). In Figures 8.17a-c a UDF flowfield with a velocity ratio (V_z^0/V_x^0) of 1 propagates upwards at a velocity (V_{up}) 20mm/yr, equal to the characteristic upwelling velocity, V_z^0; therefore the flowfield takes 6.25Myr to reach the surface. In this model no exhumed mantle is predicted - melting initiates at 6.03Myr, and 0.1km^3 of melt is produced per km along strike before the flowfield has reached the surface. When the velocity ratio of the upwards-propagating upwelling-divergent flow is increased, the region of intense upwelling is narrower than for the previous example and lateral conductive cooling suppresses melting of the upwelling material until after the flowfield has reached the surface (Figures 8.17d-f), resulting in a prediction of a narrow (26km in the example shown) zone of exhumed asthenospheric mantle.

If the upwelling-divergent flow propagates upwards, but pauses to act only in the lower

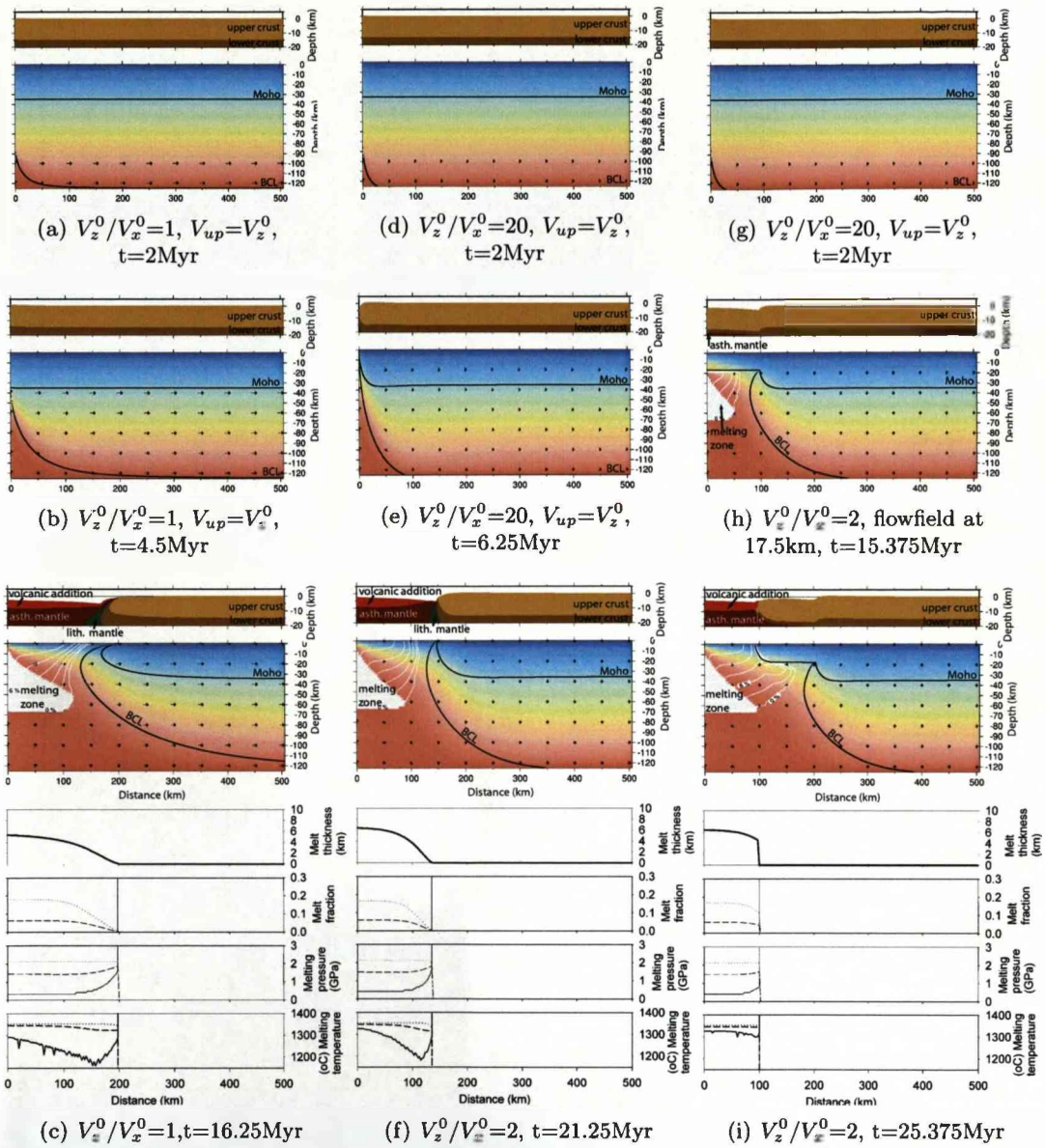

(a) V_z^0/V_x^0=1, V_{up}=V_z^0, t=2Myr

(d) V_z^0/V_x^0=20, V_{up}=V_z^0, t=2Myr

(g) V_z^0/V_x^0=20, V_{up}=V_z^0, t=2Myr

(b) V_z^0/V_x^0=1, V_{up}=V_z^0, t=4.5Myr

(e) V_z^0/V_x^0=20, V_{up}=V_z^0, t=6.25Myr

(h) V_z^0/V_x^0=2, flowfield at 17.5km, t=15.375Myr

(c) V_z^0/V_x^0=1,t=16.25Myr

(f) V_z^0/V_x^0=2, t=21.25Myr

(i) V_z^0/V_x^0=2, t=25.375Myr

Figure 8.17: Models of continental breakup caused by an upwards-propagating upwelling-divergent flowfield. (**a-c**) the flowfield propagates upwards with a velocity (V_{up}) of 20mm/yr, equal to the upwelling velocity, V_z^0. The flowfield becomes static when it reaches the surface. Velocity ratio (V_z^0/V_x^0) is one throughout model evolution. (**d-f**) the flowfield propagates upwards at V_{up} = V_z^0=20mm/yr, V_z^0/V_x^0=20. When the flowfield reaches the surface it becomes static with V_x^0=10mm/yr and V_z^0/V_x^0=2. (**g-i**) the flowfield propagates upwards at V_{up} = V_z^0=20mm/yr, where (V_z^0/V_x^0=20). When the flowfield reaches the mid-crust it pauses for 10Myr (V_x^0=10mm/yr and V_z^0/V_x^0=2), before propagating to the surface (V_x^0=10mm/yr and V_z^0/V_x^0=2). For explanation of plots see caption for Figure 8.15.

lithosphere, melting may occur prior to surface rupture. Figures 8.17g-i show the predictions of melting made by a model of rifted margin development where an upwelling-divergent flowfield propagates upwards from the base of the lithosphere, pausing in the mid-crust (17.5km) for 10 Myr before rupturing the upper crust and operating at the surface. In this example melting begins after 7.55 Myr, and 152km^3 of volcanic addition per km along strike is predicted before the flowfield ruptures the surface.
The upwards-propagating model of continental lithosphere thinning by UDF predicts a continental margin structure which differs from a static model of UDF (where the flowfield acts instantaneously throughout the whole continental lithosphere, and is fixed in the axial reference frame) in the continental lithosphere, as discussed in the previous chapter. The upwards-propagating UDF model also predicts that the onset of melting occurs after less surface horizontal extension than the static model of UDF, or that melting occurs prior to surface rupture. The upwards-propagating UDF model may help to explain voluminous volcanism prior to rupture at some volcanic margins.

8.5 Discussion

Rifted margins record the extension and rupture processes which occur in the continental lithosphere prior to the onset of seafloor spreading. Their formation is often considered a product of pure-shear extension and thinning. However, numerous continental rifted margins exhibit depth-dependent stretching, where the lithosphere has apparently been thinned much more than the upper crust (e.g. the eastern Canada margin (Royden and Keen, 1980); the northwest Australian margin (Driscoll and Karner, 1998); Goban Spur, the Vøring margin and Galicia margin (Davis and Kusznir, 2004)). At some non-volcanic margins (including conjugate pairs) a wide zone (up to 170km wide) of continental lithospheric mantle separates the unequivocal oceanic crust from the unequivocal oceanic crust (e.g. the Iberian margin; Pickup et al. (1996); Dean et al. (2000)). These observations have caused the validity of the pure-shear model to be questioned. If the lithosphere does not thin by a broadly pure-shear mechanism, there are implications for the production of melt, and for the geochemistry of the

volcanic addition at rifted margins.

The thickness of volcanic addition at rifted continental margins varies widely. Voluminous volcanic intrusive and extrusive rocks are observed at some rifted margins. These volcanics are usually synchronous with or associated with the breakup process. At some non-volcanic, or magma-poor, rifted continental margins, wide zones of mantle may be exhumed in the absence of volcanism. If the lithosphere is assumed to thin and rupture by pure-shear thinning, either temperature or compositional heterogeneities must be invoked to explain voluminous volcanism. At non-volcanic margins, temperature or compositional heterogeneities, very slow extension or incomplete melt migration may explain the absence of volcanism.

Davis and Kusznir (2004) suggested that upwelling-divergent flow, (a flow pattern similar to that which occurs underneath mid-ocean ridges) may play an important role in the formation of rifted margins, and the model has been used to explain observations of depth-dependent stretching, bathymetric and gravity profiles at a number of rifted margins. The thickness of melt predicted by the UDF model during rifted margin formation is highly dependent on the velocity ratio - the ratio of axial upwelling to half-spreading velocity. UDF models with low velocity ratios predict wide zones of exhumed mantle prior to the onset of melting. Models which include UDF flow with high velocity ratios, or UDF which occurs preferentially in the lower lithosphere prior to lithospheric rupture predict thick volcanic addition. No temperature or composition heterogeneities are required to explain either absent or very thick volcanism during continental breakup. These results support (but do not prove) the assertion made by Kusznir et al. (2005) that models of lithospheric thinning caused by a UDF with low and high velocity ratios are able to explain observations at some non-volcanic and volcanic margins respectively. Upwards-propagating UDF models predict the onset of melting after less surface horizontal extension than static model of UDF; the upwards-propagating UDF mode of deformation may be applicable to volcanic margins where voluminous volcanism occurred prior to lithospheric rupture.

The geochemistry (and consequentially the seismic velocity) of the volcanic addition

may help to determine which factors are responsible for anomalous melt production at rifted margins. For example, high mantle potential temperature and high velocity ratio upwelling diverging flow can explain thick volcanic addition at rifted margins, but predict different conditions in the melting zone. However, detecting small changes in seismic velocity or geochemistry requires very accurate and precise measurements, and results are debated. Both high temperature mantle and enhanced upwelling during very early seafloor spreading have been proposed as explanations for thick early oceanic crust in the North Atlantic (Korenaga et al., 2002; White et al., 2008). It is likely that high temperatures and high velocity upwelling-divergent flow during continental breakup are genetically linked, and that thick volcanics at a rifted margin is a product of both. As Nielsen and Hopper (2004) demonstrated using a dynamic model of continental breakup and seafloor spreading, a sub-lithospheric high temperature reservoir may induce high velocity ratio upwelling during continental thinning, leading to the production of thick volcanic crust.

The models presented in this and the previous chapter are kinematic end-members of the continental breakup process, and demonstrate theoretical implications of pure-shear and UDF models of continental breakup. Pure-shear and upwelling-divergent flow models make contrasting predictions about the overall geometry, finite deformation and heat-flow and subsidence history of rifted continental margins. The pure-shear model of lithosphere thinning predicts that extension in the lithosphere is constant with depth, and crustal extension, crustal thickness, subsidence and heat-flow history are consequentially related in a simple manner. The UDF model of continental margin formation predicts depth-dependent stretching at rifted margins, therefore the predicted relationships between crustal thickness, subsidence, heat-flow and melt production for the UDF model are more complex than for the pure-shear model. The margin geometry depends on the velocity ratio of the upwelling-divergent flow: high velocity ratios predict narrow margins, wide zones where the stretching of the upper crust is significantly less than that of the lower crust, permanent hinterland uplift and thick melt close to the continental crust at the margin. Low ratio flow models predict exhumation of a

wide zone of lower crust and continental mantle between the unthinned continental crust and the early oceanic crust. To a first-order, the general characteristics predicted by high and low velocity ratio (V_z^0/V_x^0) UDF models correlate well with volcanic and non-volcanic margins respectively.

Where observationally derived kinematic constraints are available (e.g. duration of continental thinning or breakup, early seafloor spreading rate, the distribution of extension), they can be used as input variables and other observations (volcanic thickness and geochemistry, finite deformation, subsidence and heat-flow) can be compared to predictions made by the pure-shear and upwelling-divergent flow models. Predictions made by combined pure-shear and upwelling-divergent flow models can also be compared to evaluate the relative role that the two deformation fields play. A good fit between observations and model predictions suggests that the model flowfield is a good approximation to the pattern of flow responsible for continental breakup. Where datasets are incomplete, the models make predictions which are testable when new data become available.

In the next chapter, observational constraints are used to compare the ability of the pure-shear and upwelling flow models of continental breakup to explain the formation of the Iberian margin. In chapter 10, pure-shear and UDF models are used to constrain the mode of deformation which occurred in the FSB in the Palaeocene.

Chapter 9

Melt initiation and mantle exhumation at the Iberian rifted margin: comparison of pure-shear and upwelling-divergent flow models of continental breakup.

Preface

This chapter has been peer-reviewed and published (in 2009) by *Comptes Rendus Geoscience* for a Special Issue entitled 'Ocean-Continent Transition', edited by Gwenn Péron-Pinvidic, Philippe Huchon and Gianreto Manatschal.

Melt initiation and mantle exhumation at the Iberian rifted margin: comparison of pure-shear and upwelling-divergent flow models of continental breakup.

Rosie Fletcher[1], Nick Kusznir[1], Mike Cheadle[2]

1. Department of Earth and Ocean Science, University of Liverpool, Liverpool, L69 3GP, UK

2. Department of Geology and Geophysics, University of Wyoming, Laramie, Wyoming, USA

Corresponding Author: Rosie Fletcher, Department of Earth and Ocean Science, University of Liverpool, Liverpool, L69 3GP, UK. +441517945160. rjf@liv.ac.uk

Abstract

Observations of a wide (up to 170 km) zone of exhumed continental mantle on the Iberian non-volcanic rifted margin have questioned our understanding of the processes involved in continental breakup and seafloor spreading initiation. Models of continental lithosphere thinning by pure-shear predict melt generation before continental breakup, and thus do not predict the exhumation of mantle. Whilst the paucity of volcanism during breakup on the Iberian Margin may be explained by invoking a cooler or depleted mantle, or by poor melt extraction, other lithosphere scale processes may play an important role during continental breakup. We compare melt production predicted by pure-shear models of continental lithosphere thinning to that predicted by an upwelling-divergent flow model, using kinematic constraints appropriate to the Iberian margin. The upwelling-divergent flow model predicts exhumation of a more than 50 km-wide zone of continental mantle prior to melt initiation, and we suggest that this mode of lithosphere deformation may play an important role in the formation of rifted margins.

Keywords: Continental margins, rifting, continental breakup, melting, exhumed mantle, lithosphere thinning

9.1 Introduction

A wide transitional zone of exhumed serpentinised continental mantle, isolated continental fault blocks and thin oceanic crust is observed between unequivocal continental and oceanic crust at some non-volcanic rifted continental margins. Such transition zones are termed zones of exhumed continental mantle (ZECM) and have been documented at the Iberian-Newfoundland and Greenland-Labrador conjugate margins and the remnants of the margins of the Liguria-Piemonte ocean now exposed in the Alps (e.g. Boillot et al., 1987, 1989; Chian et al., 1995; Pickup et al., 1996; Manatschal and Bernoulli, 1999; Whitmarsh et al., 2001a). The exhumation of mantle implies that thinning and rupture of continental crust occurred in the absence of significant volcanic addition, which is difficult to explain if continental breakup occurs by pure-shear stretching and thinning. The Iberian margin is well studied in terms of structure and kinematics, and we use it in this paper as a type-locality to test models of continental breakup which include melt generation by decompression melting.

Pure-shear thinning of continental lithosphere, first quantified by McKenzie (1978), is widely thought to be the process responsible for intracontinental basin formation. The pure-shear model predicts that the magnitude of stretching and thinning, accommodated by both brittle faulting and ductile processes, is uniform with depth. The pure-shear model has also been used to explain continental breakup and rifted margin formation (Bown and White, 1995; Minshull et al., 2001), although it predicts far more melt than is observed or is suggested by the seismic velocity structure at the Iberian margin (Minshull et al., 2001; Reston and Morgan, 2004). The lack of volcanism may be explained by an anomalously cool mantle prior to breakup (Minshull et al., 2001; Reston and Morgan, 2004; Pérez-Gussinyé et al., 2006), a depleted mantle source (Pérez-Gussinyé et al., 2006) or initially slow extension or distributed thinning (Whitmarsh and Miles, 1995; Harry and Bowling, 1999). However, observations of depth-dependent lithospheric stretching, exhumation of lower continental crust and continental mantle, and apparently anomalous volcanism at non-volcanic and volcanic rifted margins, including conjugate pairs, (e.g Royden and Keen, 1980; Chenet et al.,

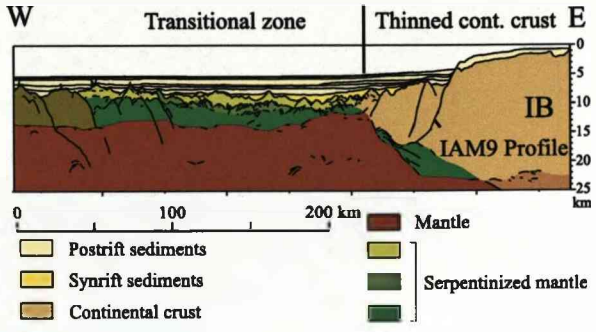

Figure 9.1: Line drawing and interpretation along the IAM-9 seismic section across the Iberian margin. Along this section the transition zone between continental and oceanic crust is around 170 km wide. Adapted from Sibuet et al. (2007).

1982; Davis and Kusznir, 2004; Kusznir et al., 2004) suggest that lithosphere-scale deformation processes other than pure-shear may play an important role during continental breakup. Upwelling-divergent flow (UDF), a mode of deformation similar to that envisaged for mid-ocean ridges (e.g. Reid and Jackson, 1981; Braun et al., 2000), is a possible lithospheric thinning mechanism which may operate as continental breakup evolves into seafloor spreading (Kusznir et al., 2005; Kusznir and Karner, 2007). The UDF model implies that thermal buoyancy forces drive lithospheric and asthenospheric convection in the continental lithosphere soon after the onset of extension in the continental lithosphere.

In this paper we investigate melt production predicted by a pure-shear model and a UDF model of continental lithosphere thinning leading to seafloor spreading initiation and compare the results to published observations at the Iberian margin. The two models are considered kinematic end-members of the continental breakup lithosphere deformation process; it is probable that the process by which the lithosphere actually deforms is a combination of both. We aim to examine the large scale thermal evolution and consequent first order melt generation predicted by these two models of lithosphere thinning. The continental lithosphere is represented as a continuous homogeneous medium and we do not attempt to model surface features such as faulting.

Seismic surveys across the Iberian margin show a transition zone up to 170 km-wide (Chian et al., 1999; Dean et al., 2000) between thinned continental and oceanic crust,

exposing serpentinised peridotite at the seafloor. Figure 9.1 shows an interpreted line drawing of the IAM-9 seismic refraction profile, where the transition zone is at its widest. Magnetic anomalies in the transition zone are weak and may originate from the emplacement of minor magmatic intrusions (Whitmarsh and Miles, 1995) or by the serpentinisation of peridotite (Sibuet et al., 2007) during progressive exhumation. Petrologic work suggests that the exhumed mantle is subcontinental in origin, and has a complex history of enrichment and depletion (Chazot et al., 2005; Muntener and Manatschal, 2006). Exhumed mantle is present on the Iberian margin and its conjugate, the Newfoundland margin, for around 300 km along strike, varying in width from 50 km to 170 km (Sibuet et al., 2007). The seismic velocity structure in the transition zone differs from the structure in adjacent oceanic and thinned continental crust and Moho reflections are weak or absent, indicating the presence of exhumed mantle with decreasing mantle serpentenisation with depth (Whitmarsh et al., 2001a). The seismic velocity structure and the low amplitude of magnetic anomalies in the basement suggests that either no volcanic addition or only minor volcanic addition (probably present as gabbroic intrusions rather than as surface volcanic addition) is present within the ZECM (Whitmarsh et al., 2001b; Minshull et al., 2001).

A series of Ocean Drilling Project (ODP) wells, drilled along a profile 40 km north of the IAM-9 profile provide constraints on the timing of margin formation. Shallow water Tithonian (~149 Ma) sediments recovered from the tops of continental fault blocks (Whitmarsh et al., 2001a) are thought to be pre-rift sediments deposited in a platform environment of a few hundred meters water depth. Isostatic considerations suggest that the crust was around 28–30 km thick at this time (Pérez-Gussinyé et al., 2006), although reconstruction of seismic sections imply that the crust may have been only 10 km thick (Manatschal, 2004). Plagioclase in gabbros from the lowermost crust exposed at the seafloor on a detachment fault at the landward edge of the transition zone has an Ar-Ar age (indicating the rock cooling below c.150 °C) of 136.4 ± 0.3 Ma (Féraud et al., 1996). This implies that significant thinning of the continental crust had occurred by this time. Within the ZECM, depleted subcontinental mantle has been cored without

encountering any mafic rocks with a syn-rift intrusion age (Whitmarsh et al., 2001b). Along the IAM-9 profile, magnetic anomaly analysis (Whitmarsh and Miles, 1995; Dean et al., 2000; Russell and Whitmarsh, 2003; Sibuet et al., 2007) demonstrates the progressive exhumation of mantle oceanwards, which may have begun as early as the early Berriasian, around 142 Ma (Sibuet et al., 2007). The exhumation of mantle requires that the continental crust is significantly thinned, and probably present only as small discrete allochthons between exposures of exhumed continental mantle. Subsequent exhumation of more than 100 km of continental mantle widened the ZECM at a half-spreading rate of between 6 and 13 mm/yr (Sibuet et al., 2007). Tucholke et al. (2007) suggest that the rising asthenosphere breached the continental lithosphere at latest Aptian-earliest Albian times (112 Ma) and normal seafloor spreading ensued. However the onset of localised seafloor spreading in the area is complex and the exact timing remains uncertain (Jagoutz et al., 2007; Tucholke et al., 2007; Peron-Pinvidic et al., 2007b).

Considering the lithological and age constraints from the ODP wells to the north of the section and following Dean et al. (2000) and Minshull et al. (2001), we have placed the following quantitative limits on the kinematics and characteristics of the Iberian margin along IAM-9: 1) the continental crust was significantly thinned, so that continental mantle could be exhumed, in less than 15 Myr (from the Tithonian until exhumation of the lowermost crust); 2) crustal stretching factors (β_{crust}) of more than 10 are required for mantle exhumation to occur (i.e. continental crust less than 3 km thick if the initial crustal thickness was 30 km); 3) the half-extension (or half-spreading) rate during the formation of the ZECM was 10 mm/yr; 4) volcanic addition in the transition zone is less than 2 km thick (Minshull et al., 2001); 5) extension across the Iberian margin, prior to the formation of oceanic crust (i.e. continental extension plus the width of the ZECM), is 150–200 km.

We model continental breakup using pure-shear and UDF models with half-spreading rates of 10mm/yr and compare predictions made by the models to observations on the Iberian margin. The effects of a slower extension rate on the predictions of volcanic

thickness made by the model are investigated, as there are uncertainties related to the timing of margin formation. The influence of a variable continental geotherm and melt extraction efficiency on model predictions are also presented.

9.2 Lithosphere thinning by pure-shear

Pure-shear thinning of the lithosphere can be defined as a 1–D velocity field $V_z(z)$, where $V_z(z)$ is the vertical (upwards) velocity and z is depth (Jarvis and McKenzie, 1980). To extend this definition into 2–D, we define a deformation field where pure-shear occurs within a fixed half-width, $W_{1/2}$, axial zone in the lithosphere. A wide zone of pure-shear leads to slow thinning of the lithosphere, whereas a narrow zone of pure-shear results in very fast thinning. We assume rifting is symmetrical. In the axial upwelling region the pure-shear deformation velocity field is:

$$V_x(x,z) = V_x^0 \frac{x}{W_{1/2}} \tag{9.1}$$

$$V_z(x,z) = -V_x^0 \frac{z}{W_{1/2}} \tag{9.2}$$

Outside of the upwelling region material is simply translated so that:

$$V_x(x,z) = V_x^0 \tag{9.3}$$

$$V_z(x,z) = 0 \tag{9.4}$$

Figure 9.2 *(following page)*: (**a–d**) Model evolution of continental lithosphere thinning and seafloor spreading initiation due to a finite width ($W_{1/2}$=50 km) pure-shear flow-field extending at a half-rate (V_x^0) of 10 mm/yr. Four snapshots in time at (**a**) t=0, with velocity vectors showing deformation field which is non time-dependent; (**b**) t=5 Myr, shortly after melt initiation; (**c**) t= 10 Myr and; (**d**) t= 20 Myr. (**e–h**) Model evolution of continental lithosphere thinning and seafloor spreading initiation due to an upwelling-divergent flow-field with $V_x^0 = V_z^0$=10 mm/yr. Four snapshots in time at (**e**) t=0, with velocity vectors showing deformation field which is non time-dependent; (**f**) t=5 Myr; (**g**) t=10 Myr, shortly after melt initiation and; (**h**) t= 20 Myr. For explanation of plots see caption for Figure 7.3.

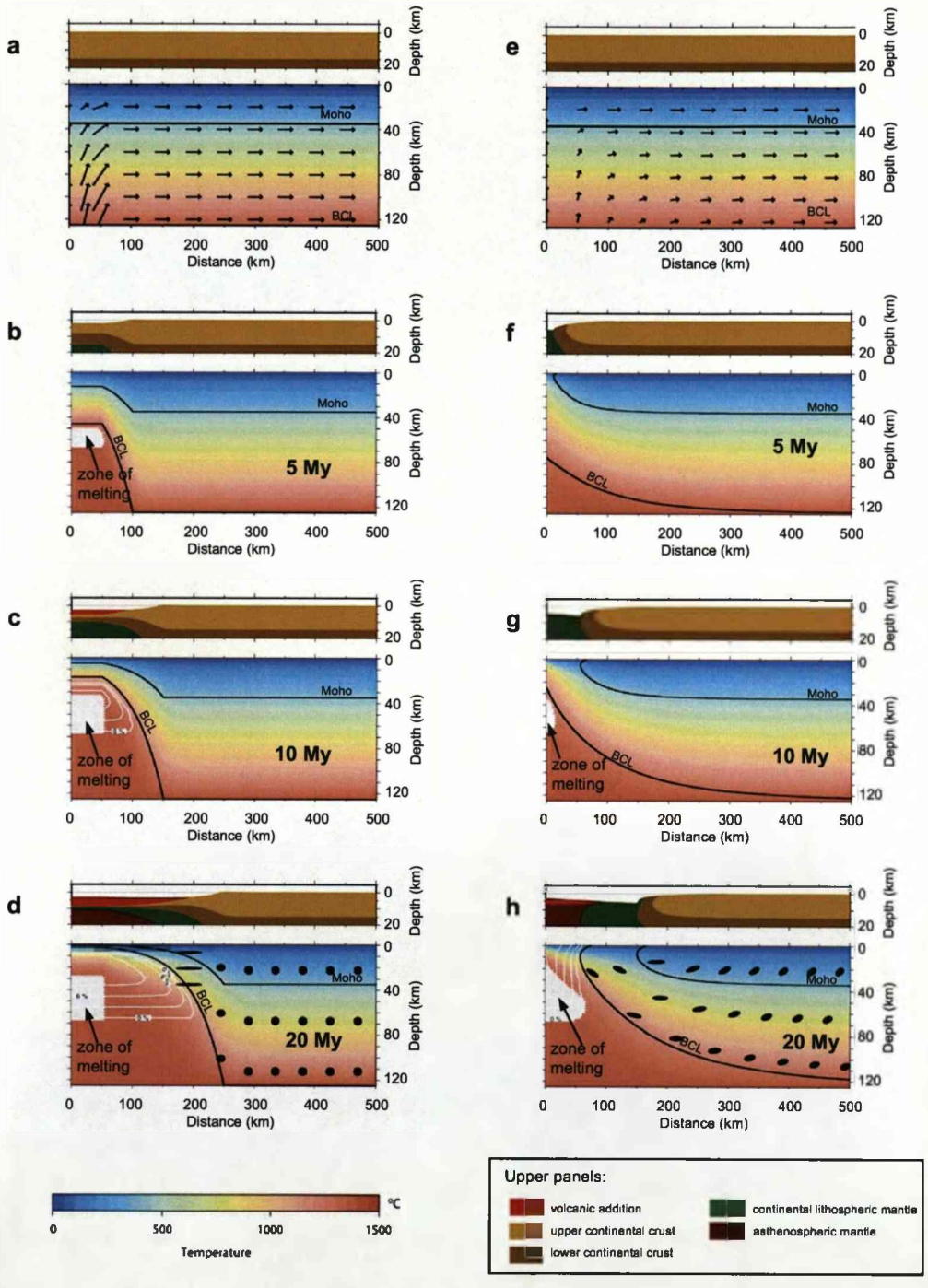
a
b
c
d
e
f
g
h
Moho
BCL
zone of melting
5 My
10 My
20 My
Depth (km)
Distance (km)
0
20
40
80
120
100
200
300
400
500
Temperature
°C
0
500
1000
1500
Upper panels:
volcanic addition
upper continental crust
lower continental crust
continental lithospheric mantle
asthenospheric mantle

$V_x(x,z)$ and $V_z(x,z)$ are the horizontal and upwelling velocities respectively at x and z, the horizontal and vertical coordinates respectively. V_x^0 is the half-extension rate. $V_x(x,z)$ and $V_z(x,z)$ are symmetric about x=0. Half-extension (i.e. extension on one margin), E, is a product of V_x^0 and the duration of rifting t, such that $E = V_x^0 t$. The stretching factor, β, is the ratio between initial and current thickness of a layer such as the crust (McKenzie, 1978), and the thinning factor, $\gamma = 1 - 1/\beta$. The initial temperature structure of the continental lithosphere is assumed to be in thermal equilibrium so that the initial temperature is:

$$T(x,z)_{(t=0)} = T_0 \frac{z}{a} \tag{9.5}$$

where T_0 is the mantle potential temperature (1333 ^{o}C) and a the lithosphere thickness (assumed to be 125 km). Radiogenic heat productivity is ignored. We model the thermal evolution of the lithosphere using the advection-diffusion equation:

$$\frac{\partial T}{\partial t} = \kappa \nabla^2 T - \mathbf{V} \cdot (\nabla T + h) \tag{9.6}$$

using the finite difference method, where T is temperature, κ is the thermal diffusivity of the mantle (0.8 X 10^{-6}m^{2}s^{-1}), $\mathbf{V}$ is the velocity vector and h is the adiabatic gradient (assumed to be 0.3 ^{o}C /km). The temperature structure evolves in response to the imposed pure-shear flow-field, reflecting a balance between heat advection and conduction.

The temperature field is used to calculate melt production. If conditions in the model space exceed the solidus of dry peridotite, melting is predicted. We calculate the melt fraction, f, at each node in the model grid as a function of temperature and pressure at each time step using the parameterisation of Katz et al. (2003). The rate of melt production at time t (R_t) depends on the incremental increase in f so that:

$$R_t = \frac{\rho_m}{\rho_v} \int_{-\infty}^{0} \int_{0}^{+\infty} \frac{\partial f}{\partial t} dx dz \text{ when } \frac{\partial f}{\partial t} > 0 \tag{9.7}$$

Volcanic addition is assumed to have a lower density than the mantle source: ρ_m (3330 kgm^{-3}) and ρ_v (2850 kgm^{-3}) are the mantle and volcanic addition densities, respectively. A parcel of mantle material becomes more depleted as it advects though the melting region. Depletion, d, is the maximum f experienced by a parcel of mantle. If melt migration is assumed to be instantaneous and perfectly efficient, the thickness of the layer of volcanic addition can be calculated. For the pure-shear model, melt is assumed to migrate to the surface and is evenly distributed across the upwelling half-width ($W_{1/2}$), subsequently migrating laterally at $\mathbf{V}(x,0)$; the thickness of melt in the axial region at time t (H_t) can be calculated:

$$H_t = \frac{1}{\beta W_{1/2}} \int_0^t R_{t'} \beta_{t'} dt' \tag{9.8}$$

following Bown and White (1995), where t' is a dummy time variable.

Continental lithosphere material is advected according to the deformation field, and the distribution of depletion is tracked through time. Subsidence or uplift caused by density changes due to thermal effects, crustal thinning or thickening and volcanic addition are calculated assuming local isostasy and water-loading. Figures 9.2a–d show the temporal evolution of continental breakup by pure-shear, where V_x^0=10 mm/yr and $W_{1/2}$=50 km. These parameters result in a stretching factor (β) close to 50 after 20 Myr, corresponding to the critical β used to define breakup by Minshull et al. (2001) in their application of the pure-shear melting model (Bown and White, 1995) to the Iberian margin. In the example shown in Figures 9.2a–d, melting initiates at 4.6 Myr, after 46 km of half-extension, when the stretching factor in the axial region (where $0 < x < W_{1/2}$) is 2.5. The thickness of volcanic addition increases as the lithosphere continues to thin: when the stretching factor reaches 10, a 3.4 km thick layer of volcanic addition is predicted in the axial region, and after 20 Myr (when the axial stretching factor is 50) the thickness of the volcanic addition is 5.4 km. Crust or lithosphere undergoing pure-shear requires infinite extension to reach zero thickness, but rupture of continental crust (a prerequisite for mantle exhumation) may be considered to occur at a critical crustal thinning factor γ_{crit}, which we assume equals 0.9 ($\beta = 10$).

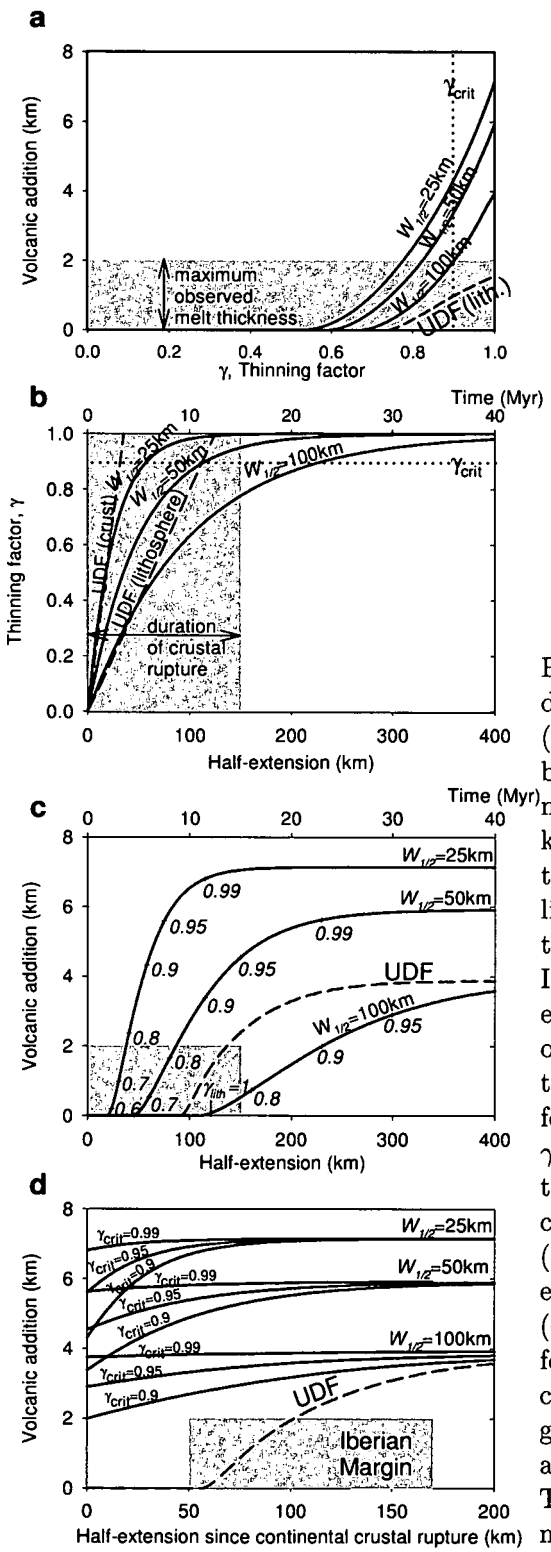

Figure 9.3: (**a-c**) Cross-plots of volcanic addition, thinning factor and half-extension (i.e. extension on one margin) predicted by the 2–D pure-shear model run at 10 mm/yr and upwelling half-widths of 25 km, 50 km and 100 km (solid lines) and the upwelling-divergent flow model (dashed lines). Note depth-dependent stretching in the UDF model means that $\gamma_{lith} \neq \gamma_{crust}$. In both cases all parameters are the same except the deformation field. Estimates of observed melt thickness (<2 km) and duration of complete crustal rupture (<15 Myr) for the Iberian margin are plotted in grey. γ_{crit} is the assumed critical thinning factor after which mantle exhumation can occur. In **c** 'γ_{lith}=1' refers to UDF model. (**d**) Volcanic addition plotted against half-extension since continental crustal rupture (γ_{crit} for the pure-shear model, γ_{crust} =1 for the UDF model). The grey box indicates width of ZECM on the Iberian margin. Pure-shear model results are solid lines and the UDF model results are dashed lines. The UDF model predicts exhumation of mantle prior to melt production.

Cross-plots of melt thickness, thinning factor and half-extension predicted by the pure-shear model with axial half-widths of 25, 50 and 100 km are shown in Figure 9.3. More volcanic crust is predicted by the pure-shear model at crustal rupture ($\gamma = 0.9$) than is observed at the Iberian margin (< 2 km thickness), unless the upwelling zone $W_{1/2}$ is wider than ~100 km (Figure 9.3a). However, if the upwelling zone is very wide, the pure-shear model predicts thinning rates that are too slow to rupture the continental crust within the time available (15 Myr) on the Iberian margin (Figure 9.3b). With a mantle potential temperature of 1333 °C, it is not possible to rupture the crust by pure-shear ($\gamma > 0.9$) in less than 15 Myr without producing more than 2 km of volcanic addition (Figure 9.3c).

Figure 9.4a illustrates the effects of varying the half-spreading rate, the mantle potential temperature, lithosphere thickness, melt migration efficiency and the upwelling half-width on the thickness of melt predicted by the pure-shear model.

Decreasing the half-extension velocity by a factor of two to 5 mm/yr (equivalent to increasing the duration of continental thinning by a factor of two) causes the onset of melting to occur later due to the effects of conductive cooling. For a model run with the same parameters as that shown in Figure 9.2a–d, but at a half-extension rate of 5mm/yr, melting initiates after 55 km of half-extension (when $\beta = 3$). When the stretching factor reaches 10 (after 23 Myr), a 1.9 km thick layer of volcanic addition is predicted in the axial zone. The thickness of volcanic addition increases to more than 2 km just 1 Myr later, and so based on our criteria may predict up to 5 km width of 'exhumed mantle', far less than that observed on the Iberian margin. Substantially lower half-extension rates are required to generate the observed width of exhumed mantle, which would require a much longer duration and earlier onset of continental lithosphere thinning.

Decreasing the mantle potential temperature by 100 °C delays the onset of melting until a thinning factor of 0.88 has been reached, and the thickness of volcanic addition remains below 2 km for the duration of the model. Similarly, if melt migration is inefficient or does not migrate to the surface, or if the asthenospheric mantle (it is

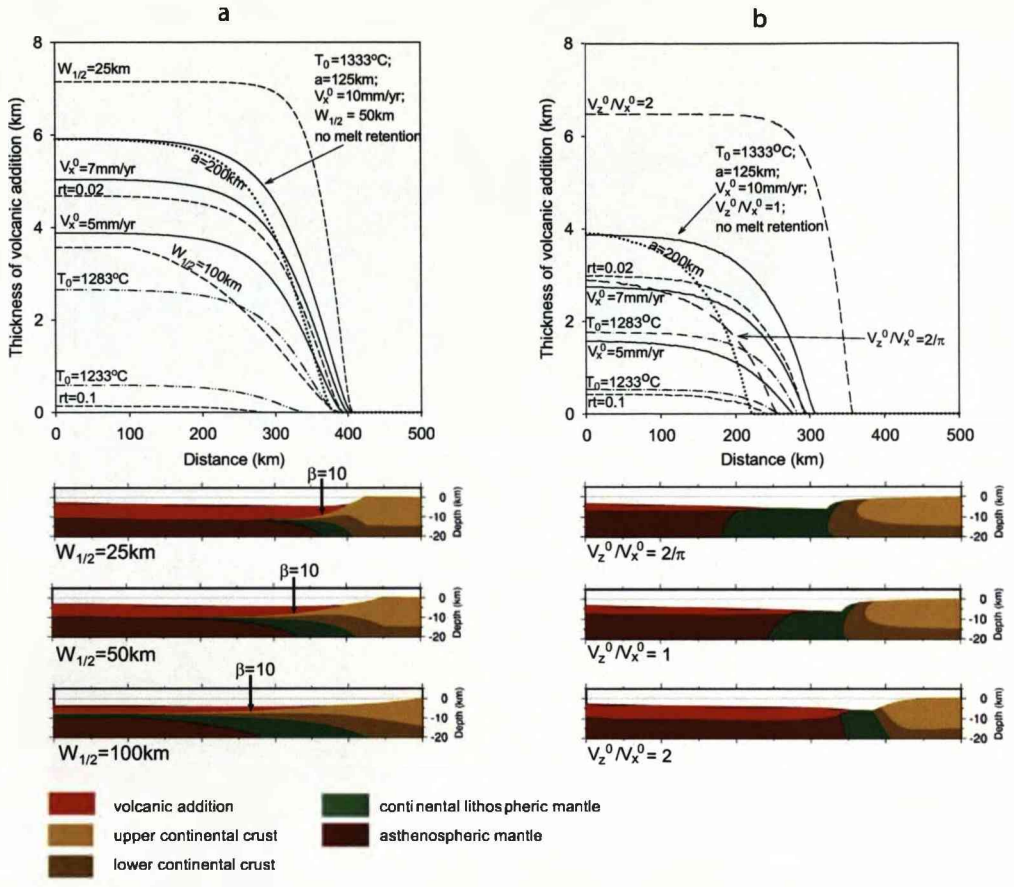

Figure 9.4: Thickness of volcanic addition versus horizontal distance plotted for various model parameters for (**a**) pure-shear and (**b**) upwelling-divergent flow models. In **a**, the median pure-shear model assumes a half-extension velocity of 10 mm/yr, initial lithospheric thickness (a) of 125 km, a mantle potential temperature (T_o) of 1333 ^{o}C, an upwelling half-width ($W_{1/2}$) of 50 km and perfectly efficient melt extraction. The other curves show results for models run with variable parameters as indicated, otherwise all model parameters are the same as in the median model. The upwelling half-width is the only variable which affects the upper structure and margin geometry (lower panels) predicted by the pure-shear model, the other variables affect only the predicted melt thickness. In **b** the median UDF model assumes a half-extension velocity of 10 mm/yr, initial lithospheric thickness (a) of 125 km, a mantle potential temperature (T_o) of 1333 ^{o}C, a velocity ratio of 1 and perfectly efficient melt extraction. The other curves show results for models run with variable parameters as indicated, otherwise all parameters are the same as in the median model. The velocity ratio is the only variable which affects the upper structure and margin geometry (lower panels) predicted by the UDF model, the other variables affect only the predicted melt thickness. For both sets of results rt indicates the degree of melt retention. The first fraction (rt) of melt is assumed to remain in the matrix and volcanic addition occurs only after f exceeds rt. rt may also be considered a proxy for the degree of depletion of the continental mantle.

predominantly the asthenospheric mantle which partially melts) is highly depleted, the onset of melting is delayed and the thickness of volcanic addition is severely reduced. These results support previous conclusions that the formation of a wide ZECM on the Iberian margin may only be explained by pure-shear lithospheric thinning in the presence of a cool asthenosphere or a much depleted mantle during breakup (Minshull et al., 2001; Reston and Morgan, 2004; Pérez-Gussinyé et al., 2006).

9.3 Lithosphere thinning by upwelling-divergent flow

We use a cornerflow solution (Batchelor, 1967) to describe the upwelling-divergent flow (UDF) deformation field during continental break-up. The solution and its derivatives have previously been used to describe mid-ocean ridge processes (e.g. Reid and Jackson, 1981; Braun et al., 2000). The velocity field is defined by a half-spreading rate at the surface, V_x^0, and an axial upwelling rate, V_z^0:

$$V_x(x,z) = -B - D\tan^{-1}(\frac{z}{x}) + (Cx + Dz)(\frac{-x}{x^2+z^2}) \tag{9.9}$$

$$V_z(x,z) = A + C\tan^{-1}(\frac{z}{x}) + (Cx + Dz)(\frac{-z}{x^2+z^2}) \tag{9.10}$$

where:

$$A = 0,\ B = \frac{2\pi V_z^0 - \pi^2 V_x^0}{(\pi^2-4)},\ C = \frac{4V_x^0 - 2\pi V_z^0}{(\pi^2-4)},\ D = \frac{2\pi V_x^0 - 4V_z^0}{(\pi^2-4)}$$

In order to calibrate the model against mid-ocean ridge crustal thickness data, we calculated steady state volcanic addition (oceanic crustal thickness) for a range of velocities, V_z^0/V_x^0 ratios and mantle potential temperatures (Figure 9.5). For V_z^0/V_x^0=1 and T_0=1333^{o}C, steady state volcanic addition is predicted to be 5–7 km when the half-spreading rate is above 20 mm/yr. At half-spreading rates less than 20 mm/yr, a higher V_z^0/V_x^0 ratio or higher mantle potential temperature fits the oceanic crustal data better. The UDF model presented here is concerned with the transient period of continental break-up prior to steady state seafloor spreading, the dynamics of which

are poorly understood. For passive isoviscous divergent flow, $V_z^0/V_x^0=2/\pi$ (PhippsMorgan, 1987); although a higher V_z^0/V_x^0 ratio is probably a more suitable approximation when temperature and stress-dependent viscosity are considered (e.g. Shen and Forsyth, 1992). For this reason, we assume that $V_z^0/V_x^0=1$ during rifted margin formation.

The temperature structure, melt generation and subsidence are calculated in the same way as described for the pure-shear model. All melt is assumed to migrate to the surface at the divergence axis so that:

$$Hc_t = \frac{R_t}{V_x^0} \tag{9.11}$$

where Hc_t is the thickness of the volcanic layer produced at the axis at time t. The surface volcanic layer subsequently moves laterally away from the axis at V_x^0.

Figures 9.2e–h show the temporal evolution of a model of continental break-up due to UDF with $V_x^0=V_z^0=10$ mm/yr. As the model evolves, the flow-field causes the thinning and rupture of the upper crust and progressive exhumation of deeper lithosphere layers. At a time of 9.8 Myr, after a 98 km-wide section of continental crust and mantle has been exhumed, the first melt is produced as the temperature-pressure conditions in the model cross the dry peridotite solidus at a depth of around 55 km under the axis. As the model thermally evolves, the zone of melting becomes wider and the thickness of volcanic addition increases, until approximately 30 Myr, when the amount of melt produced reaches a steady state (Figure 9.3c). Assuming an initial crustal thickness of 35 km, the UDF model predicts rupture of the continental crust after just 35 km of half-extension, before rupture of the continental lithosphere (Figure 9.3b). The UDF model predicts that mantle exhumation begins after much less upper lithosphere extension than the pure-shear models. Predicted volcanic addition as a function of lithosphere thinning is also much less for the UDF model than the pure-shear model (Figure 9.3a). The UDF model predicts that melt generation commences after 98 km of horizontal lithosphere half-extension (Figure 9.3c), several Myr after rupture of the continental crust, and (assuming an initial crustal thickness of 35 km) 63 km of continental mantle is exhumed prior to the initiation of melting (Figure 9.3d). At a lithosphere thinning

factor of 1 (after 125 km of half-extension) the UDF models predicts approximately 1 km of volcanic addition, which is within the range observed for the Iberian margin. Figure 9.4b illustrates the effects of varying the the mantle potential temperature, lithosphere thickness, half-spreading rate, melt migration efficiency and the velocity ratio (V_z^0/V_x^0) on the thickness of melt predicted by the UDF model. The amount of extension prior to the onset of melting, and consequentially the width of the ZECM predicted by the UDF model is more sensitive to the above factors than the pure-shear model. A wide zone of exhumed mantle is favoured when continental lithosphere thinning and rupture occurs with a low mantle potential temperature, initially thick continental lithosphere, slow extension rates, poor melt migration efficiency or high levels of depletion or with a low velocity ratio.

The mode of deformation which occurs during rifted margin formation is a complex function of the initial temperature and compositional structure of the (heterogeneous) lithosphere and the extension rate (e.g. Dunbar and Sawyer, 1989; Bassi, 1991; Harry and Bowling, 1999). For the UDF model, a higher velocity ratio flow predicts a narrower margin structure and a narrower zone of exhumed mantle than if the velocity ratio is low (Figure 9.4b), and may be more appropriate for volcanic margins (Kusznir et al., 2005). High velocity ratio flow may be more likely to occur if the lower lithosphere is initially, weak, hot or pre-thinned (Nielsen and Hopper, 2004).

9.4 Discussion

A zone of exhumed continental mantle, up to 170 km wide, between the continental and oceanic crust, is observed at the Iberian continental margin. No syn-breakup volcanic addition has been directly observed in the ZECM, and seismic data indicate that a thickness of less than 2 km of magmatic origin is present. We show that the pure-shear model of continental thinning predicts more than 2 km of volcanic addition when the continental crustal ruptures ($\beta > 10$) in less than 15 Myr. There are a number of possible explanations for the paucity of extrusive or shallow intrusive volcanism. If continental lithosphere thinning by pure-shear occurred over a much longer period of

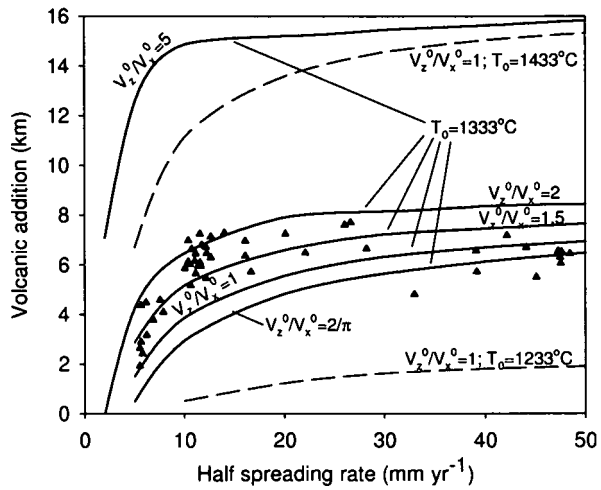

Figure 9.5: Crustal thickness predicted by the UDF model at steady state, showing the sensitivity of the model to mantle potential temperature and V_z^0/V_x^0 ratio. Unless stated, the steady state crustal thickness is calculated with V_z^0/V_x^0=1 and T_0=1333°C. Solid triangles indicate seismically defined oceanic crustal thicknesses at mid-ocean ridges (Data-points from White et al., 2001).

time, conductive cooling may suppress the onset of melting. However, the thinning and extension rates required to explain the formation of a wide (many tens of km or more) zone of exhumed mantle are much slower than those thought to have been active during the formation of the Iberian margin and would require a much earlier onset in order to rupture the continental crust by ~ 136Ma. It is possible that melting during formation of the Iberian Margin was inhibited due to low mantle potential temperatures (~100 °C lower) (Minshull et al., 2001; Reston and Morgan, 2004) or the presence of depleted (> 10% depletion) (Pérez-Gussinyé et al., 2006) asthenospheric mantle beneath the Iberian-Newfoundland rift during the breakup process. Another possible explanation is that, early in the breakup process, melt migration to the surface was hindered by freezing or impermeability some distance ahead of the solidus (recorded as the first depletion contour). On the Tethyan non-volcanic rifted margin in the Alps and on the Galician margin (~ 100 km north of IAM-9), exhumed mantle shows evidence of syn-break-up infiltration by asthenospheric melt (Muntener et al., 2004; Chazot et al., 2005), showing that complete melt extraction does not always occur in the early stages of rifting and seafloor spreading at non-volcanic rifted margins. It is possible that some

melt is distributed throughout the lithosphere under the transition zone, although it is unlikely to be able to account for a very wide zone of exhumed mantle as melt quickly forms migration pathways at low melt fractions (McKenzie, 1989).

Another possibility, which we have focused on, is that pure-shear is not the dominant mechanism of continental lithosphere thinning leading to breakup and seafloor spreading initiation. Figure 9.3d shows volcanic addition as a function of half-extension since crustal rupture ($\gamma = \gamma_{crit}$ for the pure-shear model and where crustal thickness is zero (γ_{crust}=1) for the UDF model) predicted by the two models for a half-spreading rate thought to be applicable to the Iberian margin (10 mm/yr). For both pure-shear and UDF models, melting is delayed in the transient stages of continental breakup due to the upwelling of initially cool lithospheric material and slow spreading rates. Continental lithosphere breakup due to UDF predicts the exhumation of more than 50 km of continental mantle prior to the initiation of melting. The UDF model predicts mantle exhumation because it thins the continental crust more rapidly than the lithosphere and as a consequence the crust ruptures before melt generation begins. In contrast, the pure-shear model thins the crust and lithosphere at the same rate. The ability of the UDF model to predict a wide ZECM prior to the onset of melting and volcanic addition suggests that UDF may play a role in the formation of non-volcanic rifted margins. The pure-shear and UDF models of lithosphere thinning are intended to represent end-member models, however, it is probable that UDF operates together with pure-shear deformation. A pure-shear contribution to lithosphere thinning is clearly indicated by faulting in the upper brittle layer ($\sim$ 10 km) of the continental crust prior to breakup.

The UDF model presented here predicts a 63 km-wide zone of exhumed continental mantle whereas the ZECM of the Iberian margin is up to 170 km wide. So whilst the UDF model can partially explain the exhumation of mantle prior to melt initiation at non-volcanic rifted margins, compositional and temperature heterogeneities in the mantle may also play an important role in retarding the onset of melting during breakup, and could also be responsible for lateral variability of volcanism observed at

rifted margins.

To further assess the possible contribution of UDF deformation to lithosphere thinning leading to continental breakup, other predictions made by the models can be examined. The overall margin structure predicted by the UDF model differs from that predicted by the pure-shear model. The UDF model predicts progressive exhumation of wide zones of the lower continental crust and mantle, whilst the pure-shear model predicts that much narrower zones of lower continental crust and mantle would be exhumed, even if melting did not occur. On the Iberian margin, lower crustal material was found at the seafloor on the landward side of the transition zone by drilling (Whitmarsh et al., 2000, 2001a), although the continental crust at the seafloor does not typically exhibit the high seismic velocities expected of the lower crust. The transition zone peridotites from the ocean floor have a heterogeneous but depleted subcontinental origin, an observation which may support the UDF model.

The two models differ in their predictions of strain and rotation, the distribution of depletion (Figure 9.2), and the pressure-temperature history of the exposed mantle. However, measuring these differences may be difficult due to inherited strain, compositional heterogeneities and overprinting of signals during serpentinisation. Continued sampling of the Iberian and other non-volcanic rifted margins may enable further discrimination between the two models and place constraints on their relative importance.

9.5 Summary

A wide zone of exhumed continental mantle (ZECM) at the Iberian rifted continental margin is difficult to explain if pure-shear is assumed to be the dominant mechanism of continental lithosphere thinning leading to crustal rupture and breakup. Factors such as a cooler mantle, inherited depleted mantle and inefficient melt migration can explain why extrusive volcanism is not observed within the ZECM. However, it is also possible that other lithosphere deformation processes play an important role during continental breakup. Upwelling-divergent flow (UDF), the flow-field envisaged at mid-ocean ridges, predicts exhumation of the lower crust and subcontinental mantle during continental

break-up and seafloor spreading initiation, consistent with observations on the Iberian Margin. We therefore propose that upwelling-divergent flow may play an important role during non-volcanic rifted margin formation.

Acknowledgements

The authors acknowledge constructive reviews by Garry Karner and two anonymous reviewers for their comments which significantly improved this paper. RJF thanks NERC for a Research Studentship. We also acknowledge the MM2 (Margin Modelling Phase 2) partners (BP, ConocoPhillips, StatoilHydro, Shell, Petrobras, TOTAL, BG, BHP-Billiton). The GMT software of P. Wessel and W. H. F. Smith was used to construct several figures.

Chapter 10

Forward modelling depth-dependent stretching in the Faroe-Shetland basin

10.1 Introduction

The aim of this chapter is to use models of depth-uniform and depth-dependent lithosphere stretching to determine the mode of thinning in the Faroe-Shetland basin (NE Atlantic margin) during the Late Palaeocene. The Faroe-Shetland Basin has experienced several episodes of rifting since the Palaeozoic (Dean et al., 1999; Roberts et al., 1999, and see Chapter 3 for discussion). The analysis presented in Chapters 5 and 6 suggests that the basin experienced depth-dependent stretching at the end of the Palaeocene. Since the end of the Palaeocene, the axis of the basin has experienced water-loaded tectonic subsidence of up to 2.4km (Turner and Scrutton, 1993; Nadin et al., 1997; Ceramicola et al., 2005, this study). This magnitude of post-Palaeocene subsidence in the basin suggests that a Late-Palaeocene rift event occurred, but very little tectonostratigaphic evidence for rifting (i.e. faulting) is observed in the upper crust (Turner and Scrutton, 1993; Ceramicola et al., 2005, Chapters 3-6 and Figure 10.1). At

Late Palaeocene times the lithospheric mantle and lower crust appear to have been preferentially thinned with respect to the upper crust, approximately synchronously with lithospheric rupture and the initiation of seafloor spreading at the Møre and Faroes Margins (see Figure 10.1 for location map).

Depth-dependent stretching, where the lithospheric mantle and whole crust are thinned much more than is implied by upper crustal extension, has been observed at numerous volcanic and non-volcanic margins and propagating rift tips (e.g Royden and Keen, 1980; Roberts et al., 1997; Driscoll and Karner, 1998; Davis, 1999; Clift et al., 2001; Davis and Kusznir, 2004; Kusznir and Karner, 2007). However, the cause and mechanism of depth-dependent stretching and thinning is not well understood. One possible explanation is that lithospheric extension can occur by decoupled pure-shear: the upper crust may extend over a much broader area than the lower crust and lithospheric mantle (Huismans and Beaumont, 2008). This mode of deformation is implicit in 1D models of depth-dependent stretching (Royden and Keen, 1980). It has also been widely suggested that induced small-scale convection in the lower lithosphere may preferentially thin and remove the lithosphere and lower crust (e.g. Keen, 1985; Huismans et al., 2001a).

The mechanism of crustal and lithospheric thinning in basins and at rifted margins controls variations in the temperature evolution and resulting geometry of the basin or margin, as well as subsidence, heatflow, extensional faulting, finite deformation and melt production. The subsidence and heatflow history of rift basins and margins is particularly important for understanding the development of petroleum systems, and the use of incorrect assumptions regarding the mode of deformation to make predictions about the heatflow or subsidence history of a basin or margin may yield erroneous results (Kusznir et al., 2005).

In this chapter six kinematically described modes of continental lithospheric thinning are considered as candidate mechanisms for the Late Palaeocene thinning event in the Faroe-Shetland basin. For each model the total horizontal extension is the same, but the mode of deformation is different. The basin geometry, subsidence and heatflow

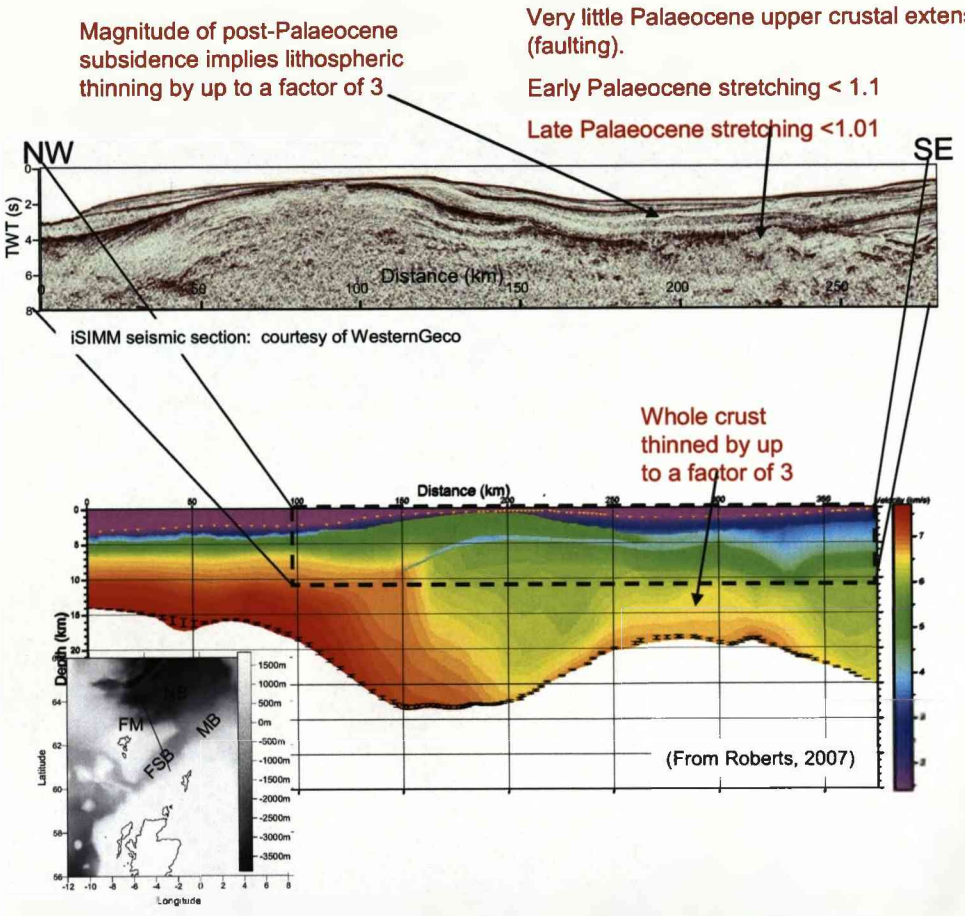

Layer	Apparent stretching since Late Jurassic	Apparent Palaeocene stretching	Apparent post-Palaeocene stretching
Upper crust	$\beta < 1.6$	$\beta < 1.1$	$\beta < 1.01$
Whole crust	$\beta \approx 3$	?	?
Whole lithosphere	?	$\beta > 3$	$\beta > 1.2$

Figure 10.1: Seismic reflection and refraction profiles across the Faroe-Shetland basin. On inset map, FSB is the Faroe-Shetland basin, MB is the Møre basin, FM is the Faroes margin and NB is the Norwegian basin (oceanic crust). The table lists apparent stretching factors (β) in the FSB for the upper crust (determined by summing fault heaves, the whole crust (determined from crustal thickness estimates) and the whole lithosphere (determined from subsidence analysis), since late Jurassic times, since the early Palaeocene, and post-Palaeocene.

history, finite deformation and melt production predicted by each model is compared to those made by the other models, and to observations in the FSB where these are available. The model predictions demonstrate the implications of various modes of deformation and lithosphere thinning, and an attempt is made to determine the mode of deformation which best explains the observations in the FSB.

10.2 Method

Forward kinematic models are useful for investigating the effects of processes which may be responsible for basin formation. A successful forward model of a basin should honour the available observational constraints in that basin, as well as making predictions about parts of the system which have not yet been, or cannot be, observed. It is usually possible to honour available geological and geophysical constraints using a range of models and model parameters, particularly if limited data are available, and further complexity and ambiguity may arise if the basin has been or is influenced by factors such as dynamic topography from a subduction zone, regional uplift or global sea-level changes. However, predictions made by models can be tested as subsequent data become available and considered in terms of the regional understanding and tectonic implications.

In this chapter, modes of deformation are described kinematically; the mechanism by which deformation occurs is defined by a flowfield. Flow-fields are calculated analytically, and are made up of components of pure-shear thinning and upwelling divergent flow (UDF). Six modes of deformation are considered as possible mechanisms by which depth-dependent stretching may have occurred in the FSB. A schematic diagram of each of the lithosphere thinning mechanisms is shown in Figure 10.2.

10.2.1 Modes of lithosphere thinning

The following modes of deformation for the FSB are examined:

M1 Whole lithospheric stretching and thinning by pure-shear.

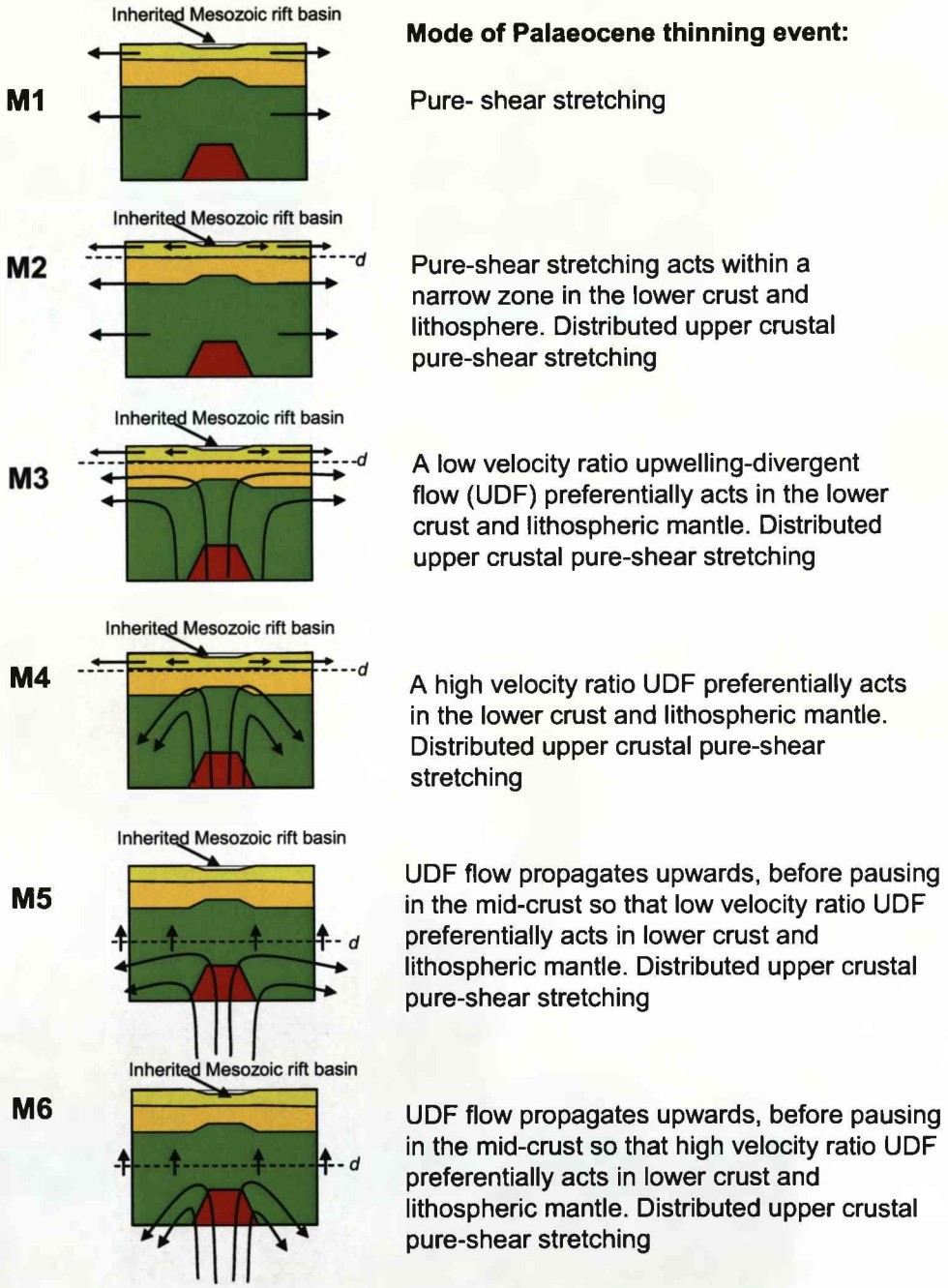

Figure 10.2: Schematic diagrams showing the modes of deformation investigated in this chapter. In models M2-M6 the flow is decoupled so that above the decoupling depth (d) extension is accommodated by distributed pure-shear thinning. Below the decoupling depth deformation may occur by either pure-shear or by upwelling-divergent flow. In M5 and M6 the upwards propagating flow has a horizontal velocity of zero until flow reaches the mid-crust. In all models the total horizontal extension is constant with depth.

M2 Decoupled pure-shear stretching, with focused stretching and thinning of the lower crust and lithosphere (over a half-width of 25km), distributed extension (over a half-width of 50km) in the upper crust.

M3 A low velocity ratio (V_z^0/V_x^0=1) upwelling-divergent flow which acts only in the lower crust and lithospheric mantle. Distributed pure-shear extension (over a half-width of 50km) in the upper crust.

M4 A high velocity ratio (V_z^0/V_x^0=2) upwelling-divergent flow which acts only in the lower crust and lithospheric mantle. Distributed pure-shear extension (over a half-width of 50km) in the upper crust.

M5 An upwards-propagating upwelling-divergent flow ($V_{up} = V_z^0$, V_x^0=0 during upwards propagation), which pauses in the mid-crust, acting with a low velocity ratio (V_z^0/V_x^0=1) only in the lower crust and lithospheric mantle. Distributed pure-shear extension (over a half-width of 50km) in the upper crust.

M6 An upwards-propagating upwelling-divergent flow ($V_{up} = V_z^0$, V_x^0=0 during upwards propagation). The flowfield pauses in the mid-crust, acting with a high velocity ratio (V_z^0/V_x^0=2) only in the lower crust and lithospheric mantle. Distributed pure-shear extension (over a half-width of 50km) in the upper crust.

Each of the modes of deformation are considered to be proxies for various processes by which lithospheric thinning may occur. The models of continental lithospheric thinning by pure-shear (M1), or decoupled pure-shear (M2) imply that convective flow is not induced during basin formation. The static upwelling divergent flow (UDF) models (M3 and M4) imply that convection in the lithospheric mantle and lower crust is induced after a small amount of lithospheric stretching, the vigor of such convection can be quantified by the ratio of axial upwelling to the maximum horizontal velocity. Above a decoupling depth the upper crust deforms by distributed pure-shear extension. The decoupling depth may be considered to represent the brittle-ductile transition, and the decoupled flow is analogous to that which may occur at very slow oceanic spreading

centres (e.g. Cannat, 1996). The upwards-propagating UDF models (M5 and M6) imply that thinning is initiated by upwelling divergent flow, or small-scale convection, in the lower lithosphere after a small amount of horizontal extension, which may be due to thermal or melt buoyancy. The upwelling divergent flow propagates upwards to the mid-crust where it operates below a brittle-ductile decoupling depth.

For all of the models, the lithosphere thinning mechanism is assumed to act in the FSB during the Late Palaeocene, being responsible for depth-dependent stretching and the resulting 'anomalous' post-Palaeocene subsidence in the basin. The deformation is assumed to act for a short time before ceasing, and the lithosphere cools until present day. Possible explanations for the cessation of thinning and stretching are considered in Section 10.4.

10.2.2 Model constraints

Subsidence

The FSB has experienced anomalously large amounts of post-Palaeocene water-loaded tectonic subsidence (referred to as post-Palaeocene subsidence). This post-Palaeocene subsidence is well constrained over large areas of the basin where palaeobathymetric evidence suggests that the basin was low-lying and close to sea level at this time (see Chapters 3 and 4 for discussion and for method of calculating post-Palaeocene water-loaded tectonic subsidence). The calculated post-Palaeocene subsidence is insensitive to the effective elastic thickness assumed during backstripping, as post-Palaeocene sediment packages have a relatively long-wavelength in comparison to the likely flexural wavelength corresponding to the effective elastic thickness of the basin.

The subsidence analysis presented in Chapter 4 shows that post-Palaeocene subsidence is ~500m on the basin flanks. In the southwest axis of the basin post-Palaeocene subsidence is ~1500m, increasing north-eastwards to more than 2km where the basin opens out into the Norwegian basin. Post-Palaeocene water-loaded tectonic subsidence profiles for eight dip lines are shown in Figure 10.3. Around 500m of post-Palaeocene subsidence can be accounted for by regional subsidence following Palaeocene transient

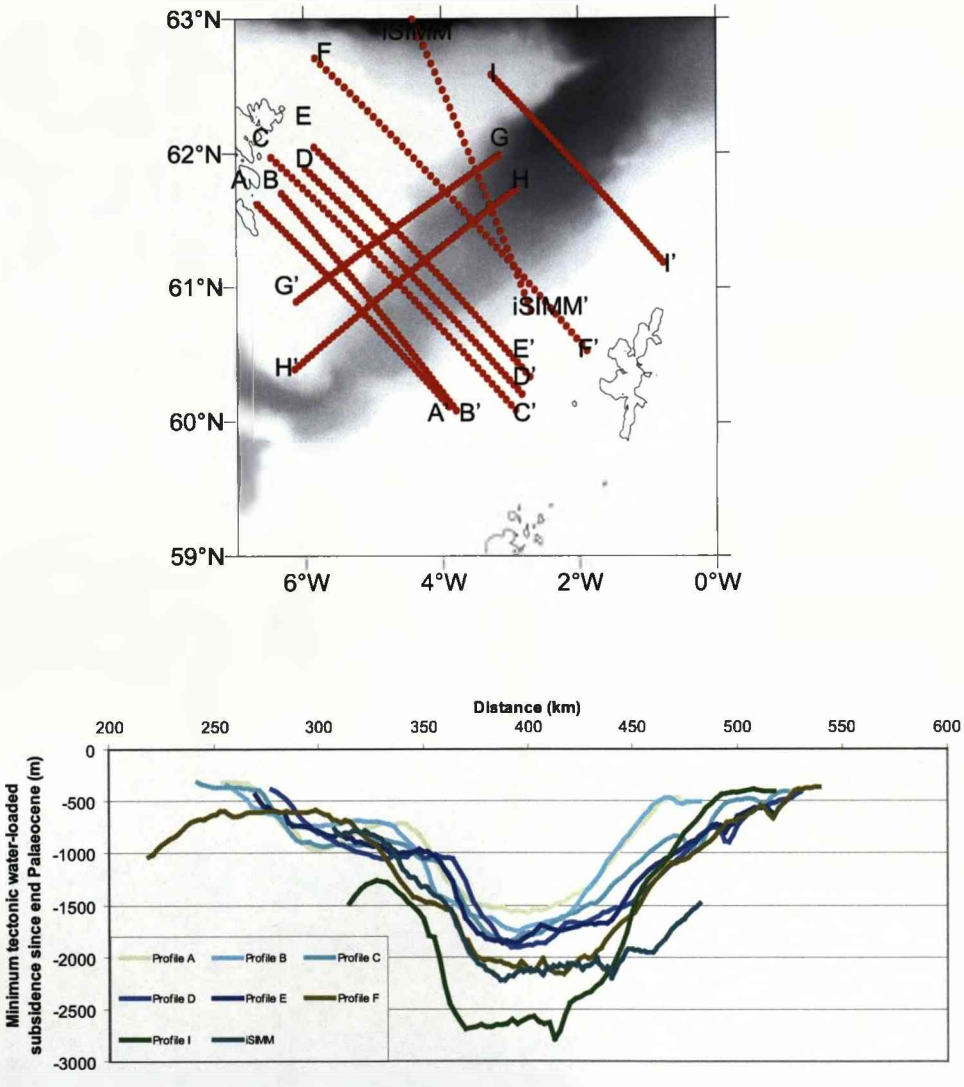

Figure 10.3: Post-Palaeocene water-loaded tectonic subsidence in the FSB for eight dip profiles, calculated by flexural backstripping assuming an effective elastic thickness (Te) of 2.5km to the Top Balder horizon, which was close to sealevel at Late Palaeocene times (see Chapter 4 for calculation method). Up to 500m of this subsidence may be attributed to regional subsidence since Late Palaeocene times, possibly due to the decay of thermal support from a mantle plume. Profiles are located on bathymetric map. For seismic and depth-converted sections, from which these profiles were derived, see Figures 3.7 and 3.8. For method of calculation see Section 4.3.

uplift, which may have been associated with a mantle thermal anomaly or plume. The remainder of the post-Palaeocene subsidence therefore is assumed to represent the minimum amount of subsidence which was caused by the Late Palaeocene lithosphere thinning event (modelled here). This is the target subsidence which a successful forward model should explain.

Palaeocene extension

Although the magnitude of post-Palaeocene subsidence in the basin suggests that a Late-Palaeocene rift event occurred, very little tectonostratigaphic evidence for rifting (i.e. faulting) is observed in the upper crust in Palaeocene or younger horizons (Turner and Scrutton, 1993; Smallwood and Gill, 2002; Ceramicola et al., 2005, and see Chapter 4). Analysis of fault heaves on the base Tertiary horizon suggest that the upper stretching factor since the end of the Cretaceous is less than 1.1. Very few faults are seen on the late Paleocene horizons, the post-Palaeocene upper crustal stretching factor is estimated to be less than 1.01 (Chapter 4).

For each of the models presented in this chapter, 25km of upper crustal extension was assumed to have accompanied the post-Palaeocene deformation responsible for the anomalous subsidence, corresponding to an average Palaeocene stretching factor of 1.1 over a region 250km wide. This amount of extension is at the upper limit of observed Palaeocene upper crustal extension; however, if extensional strain is to be conserved in the models a small amount of upper crustal extension is required in order to create accommodation space and to preferentially thin the lithospheric mantle.

Timing

Thinning of the lithospheric mantle and lower crust beneath the FSB occurred in the Late Palaeocene, approximately synchronously with lithospheric rupture and the onset of seafloor spreading at the Faroes and Møre margins. The detailed relative timing of formation of the basin is not yet well constrained. Additionally the duration of the Palaeocene thinning event in the FSB is poorly constrained, although volcanism associated with continental lithospheric rupture on the Faroes margin occurred within

approximately 2-4Myr (Waagstein, 1995, 1988; Hitchen and Ritchie, 1993; Trude et al., 2003) and fast subsidence rates in the Faroe-Shetland basin between the time of the Flett Formation to the early Eocene also suggests that crustal thinning was a rapid process.

For each model the extensional deformation in the upper crust is assumed to occur over a period of 1.25Myr, at a half-extension rate of 10mm/yr (total horizontal extension is 25km). The low temporal resolution of observational data precludes an attempt to distinguish between models of different rates. The duration of thinning affects the rate of uplift and subsidence, and volume of melt predicted, although the final basin structure and total tectonic subsidence are relatively insensitive to the duration of thinning.

Mesozoic rifting history

It was shown in Chapter 5 that the pre-end Palaeocene history of the basin can be satisfied by a pure-shear stretching event of maximum magnitude 1.25-1.4. The basin's early history affects the response of the lithosphere to subsequent rifting and thinning events and therefore a protracted (20Myr duration) Mesozoic pure-shear rift event is included in each model.

10.2.3 Model set up

The models shown in this chapter are calculated in a similar way to that described in Chapters 7-9: A deformation velocity field is defined, and the advection of material and the evolution of the temperature field is calculated using the finite difference method. In this chapter, the flowfield is assumed to be decoupled; the upper crust deforms by distributed pure-shear extension whilst the lower lithosphere deforms by either pure-shear (which may occur over a different width than the upper crust) or upwelling-divergent flow. The equations for pure-shear and upwelling-divergent flow, which are defined fixed in Eulerian space, are given in Chapter 7. Most of the flowfields used in this chapter have components of both pure-shear and upwelling-divergent flow and consequently the flowfields above and below the decoupling depth are summed. The

decoupling depth is assumed to be 12.5km for all models, approximately equivalent to the middle of the crust prior to the Palaeocene thinning event and approximately equivalent to the brittle-ductile transition. The total horizontal extension above and below the depth of decoupling is constant, so that the total horizontal extension of each model is balanced.

The six models evolve as follows:

1. Each model starts with an initial crustal thickness of 35km and a thermally equilibrated lithosphere, the geothermal gradient is linear between the surface (0 ^{o}C) and the base of the continental lithosphere (at 125 km depth). The mantle potential temperature is assumed to be 1333 ^{o}C.

2. A pure-shear rifting event (50km total horizontal extension) between at 144Ma and 124Ma results a maximum stretching factor 1.4 over a total width of 200km, and no melting, in agreement with observations.

3. A Late Palaeocene extension and thinning event occurs. During this event 25km horizontal extension occurs in 1.25Myr. The flowfield, or mode of deformation is different for each model. In each of the six cases, total horizontal extension above and below the decoupling layer (if applicable) is constant so that total horizontal strain is conserved.

4. Deformation ceases after the Late Palaeocene event, and the lithosphere is allowed to cool.

An example model evolution (M5) is shown in Figure 10.4.

Some authors believe that breakup of the North Atlantic was accompanied by elevated mantle potential temperatures (e.g. White and McKenzie, 1989; White et al., 2008). Each model run is repeated assuming a mantle potential temperature of 1433^{o}C, in order to assess if predicted volumes of melt by each of the models with a relatively high mantle potential temperature are consistent with observations.

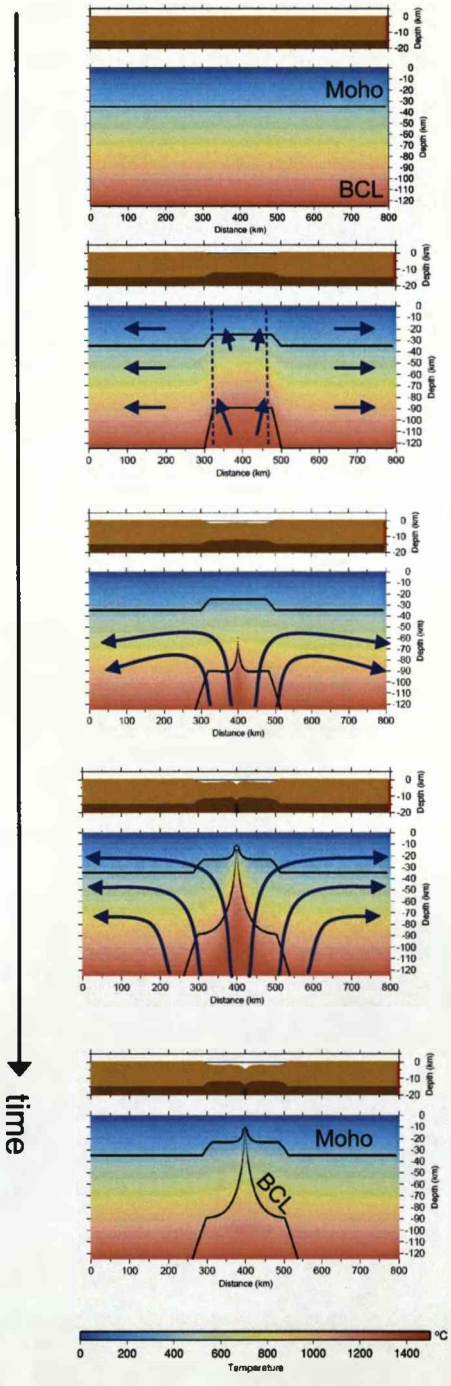

Initial conditions: 35 km thick crust, constant geotherm, mantle potential temperature 1333 °C.

144-124Ma: the whole lithosphere is thinned by pure-shear stretching over a total width of 200km. Maximum stretching factor = 1.4. (This is common to all models).

Palaeocene event (each model has a different mode of deformation)

Upwards-propagating upwelling-divergent flow initiates in the Early Palaeocene and propagates upwards to depth of 12.5km.

Horizontal extension begins in the Late Palaeocene. The upwelling-divergent flow operates below the mid-crust (12.5km depth), with a velocity ratio of one for 1.25Ma. The upper crust deforms by distributed pure-shear to balance extensional strain.

Flow-field ceases to operate in latest Palaeocene/Early Eocene, cooling until the present day. (Common to all models).

Figure 10.4: Example of evolution of forward model (M5).

10.3 Model results

The velocity vectors, temperature field, location of the Moho and base of the continental lithosphere, and finite strain ellipses for each model at the end of the Palaeocene lithospheric thinning event are shown in Figure 10.5. After the Palaeocene thinning event, the flowfield ceases to operate and the lithosphere cools. The resulting subsidence and heatflow history for each model (to present day) for various locations on the surface of the models is also shown in Figure 10.5. The total tectonic subsidence for each model is plotted in Figure 10.6a. This is the total tectonic subsidence since rifting began (assumed to be Late Jurassic times, ~144Ma). The subsidence caused by the Palaeocene thinning event can be split into two components: that which occurs during crustal and lithospheric thinning (Si), and that which occurs as a result of thermal subsidence after thinning processes have ceased to operate (St). The total subsidence caused by the Palaeocene thinning event (Si+St) for each model is shown in Figure 10.6b, and the post-rift subsidence (St) since Palaeocene thinning is shown in Figure 10.6c.

10.3.1 Post-Palaeocene subsidence

For each of the models, 25km of horizontal extension is assumed to occur during Palaeocene thinning, the distribution of that extension determines the resulting subsidence profile. The depth-dependent modes of extension and thinning (M2-M6) predict more subsidence in the centre of the basin (where thinning is focused) than on the flanks. For the same amount and distribution of late-Palaeocene upper crustal extension, the depth-dependent modes of thinning M2-M6 are able to explain much larger amounts of syn- and post-rift subsidence in the centre of the basin than the pure-shear model (M1).

The exact timing of lithospheric thinning in the FSB is not well understood: the paucity of post-end Palaeocene upper crustal faulting indicates that extension in the basin had ceased by end Palaeocene times, suggesting that the post-Palaeocene subsidence is mainly thermal subsidence. However, post end-Palaeocene preferential thinning of the

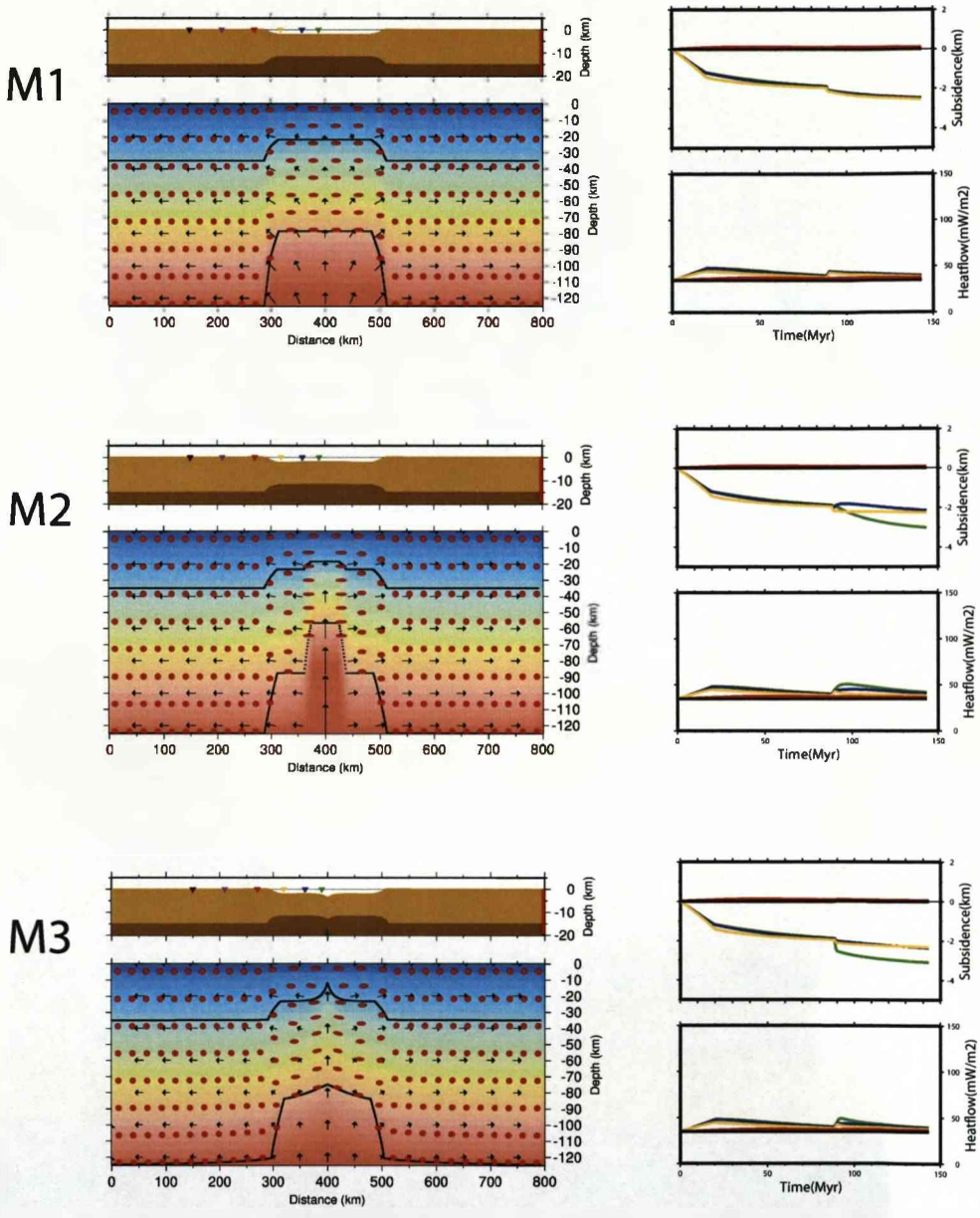

Figure 10.5: Forward modelling results for models M1,M2 and M3. Left side shows model predictions at the end of the Palaeocene lithosphere thinning event. The main panel shows a Eulerian plot of temperature, the velocity vectors, the position of the Moho and base of the continental lithosphere (BCL), red ellipses indicate direction and magnitude of strain since t=0; the upper panel shows the upper 20 km of the model, corrected for isostatic effects of thermal expansion, crustal thinning and water or air loading. Right side shows subsidence and heatflow history for selected pseudowell locations. The colour of the lines correspond to the location of the pseudowell (triangles on the left panels). Figure continued on next page.

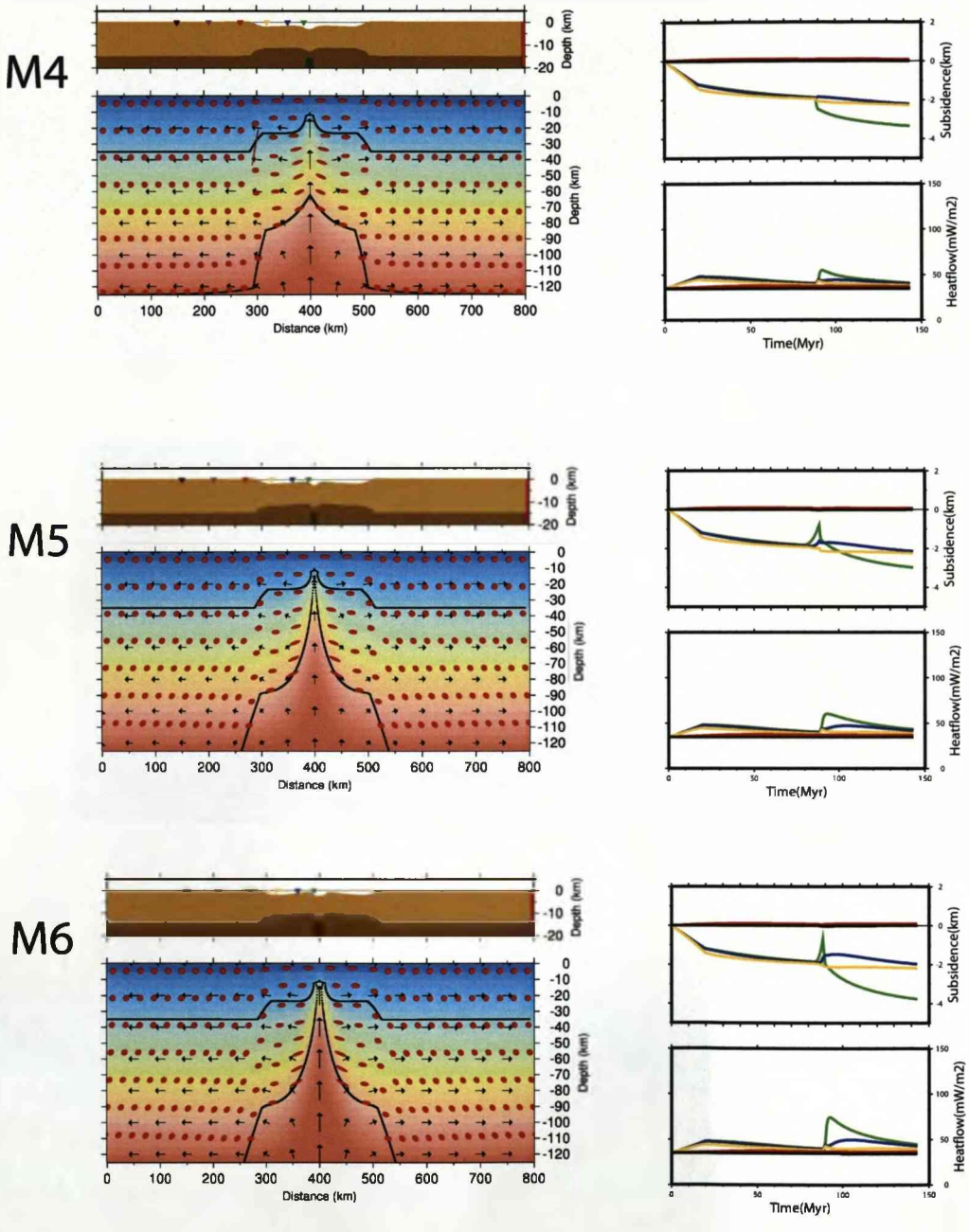

Figure 10.5: continued from previous page. Forward modelling results for models M4, M5 and M6. For explanation see previous page.

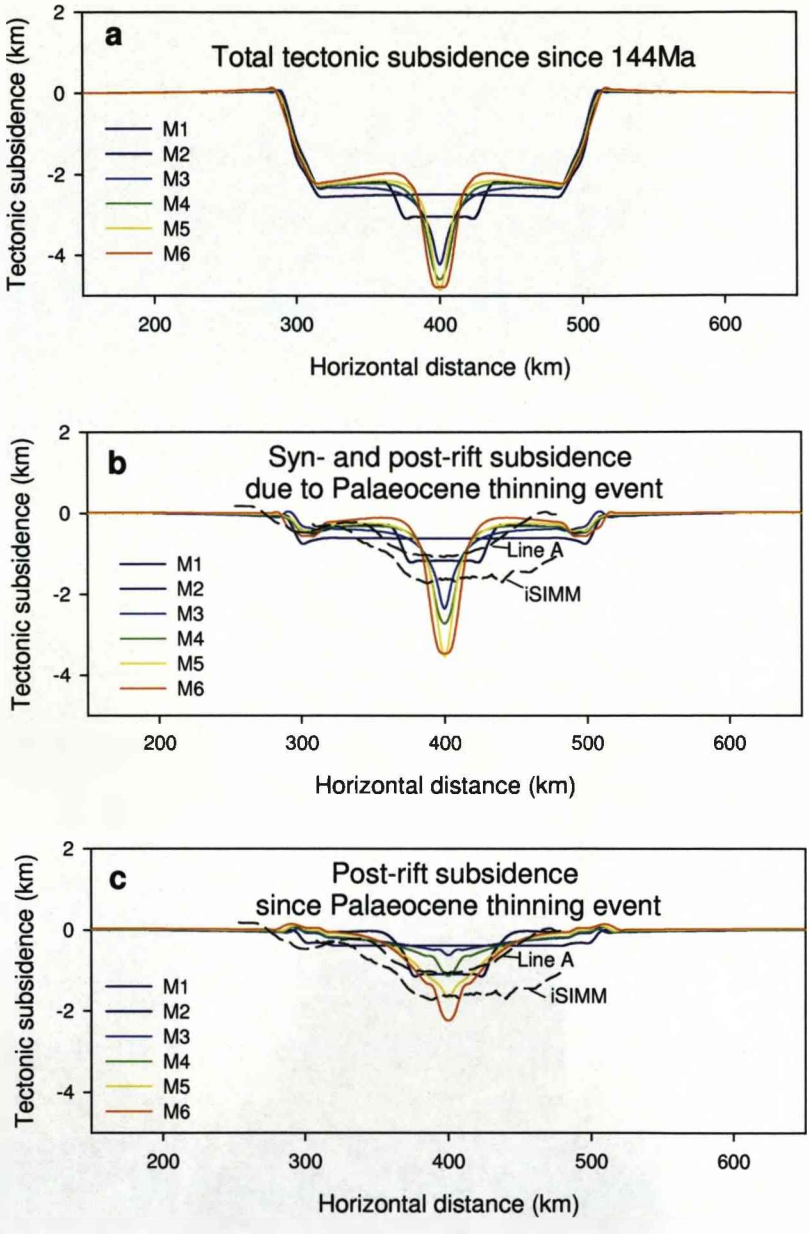

Figure 10.6: **(a)** Total tectonic subsidence since 144Ma predicted by models M1-M6. **(b)** Syn- and post-Palaeocene thinning tectonic subsidence (Si+St) predicted by models M1-M6. **(c)** Post-Palaeocene thinning tectonic subsidence (St) predicted by models M1-M6. In all plots effective elastic thickness is assumed to be zero (local isostasy). Black dashed lines are minimum tectonic subsidence profiles for line A and iSIMM (see Figure 10.3 for locations) calculated assuming that regional subsidence of 500m has occurred since the end of the Late Palaeocene. Note that the tectonic subsidence profiles calculated for line A and iSIMM are insensitive to the effective elastic thickness (Te) used during flexural backstripping.

lower crust and lithospheric mantle may have occurred, and the large magnitude of post-Palaeocene subsidence is difficult to explain by thermal subsidence without predicting large volumes of melt, as shown in Chapter 6 using 1–D models of instantaneous thinning. The models shown in this chapter are 2–D, of finite duration, and conserve extensional strain and so should provide a better test of the mode and relative timing of basin formation. The minimum observed post-Palaeocene subsidence on line A and the iSIMM line in the FSB (see Figure 10.3 for locations) is compared to the predicted syn- and post rift (Si+St), and the post-rift only (St) subsidence predicted by each of the models. The minimum post-Palaeocene subsidence is calculated assuming that 500m of regional subsidence occurred after the end of the Palaeocene in the FSB due to the relaxation of thermal uplift associated with a high mantle potential temperature or the presence of a mantle plume in the vicinity of the FSB at the time of breakup, or a mantle plume.

Both syn- and post-rift (Si+St) and post-rift subsidence only (St) profiles are calculated for each of the models assuming effective elastic thicknesses of 0km (local isostasy), 5km and 10km, and compared to the minimum post-Palaeocene subsidence in the basin in Figures 10.7 and 10.8 respectively.

Assuming local isostasy (Te=0km), the amount of syn- and post-rift subsidence (Si+St) predicted by the models is highly variable. The pure-shear model (M1) predicts a wider and shallower basin than observed. The decoupled pure-shear model predicts a basin of a similar width and magnitude as observed, whilst the UDF models M3-M6 predict a narrower and deeper basin than is observed. However, with the exception of the pure-shear model (M1), if the effective elastic thickness is assumed to be finite but relatively small (5-10km), all of the depth-dependent models M2-M6 can explain the magnitude and width of the post-Palaeocene subsidence in the southern part of the basin (along profile A). However, none of the models predict the magnitude of post-Palaeocene subsidence calculated for the northern part of the basin (along the iSIMM line).

The magnitude of post-rift subsidence in the basin (St) predicted by each of the models

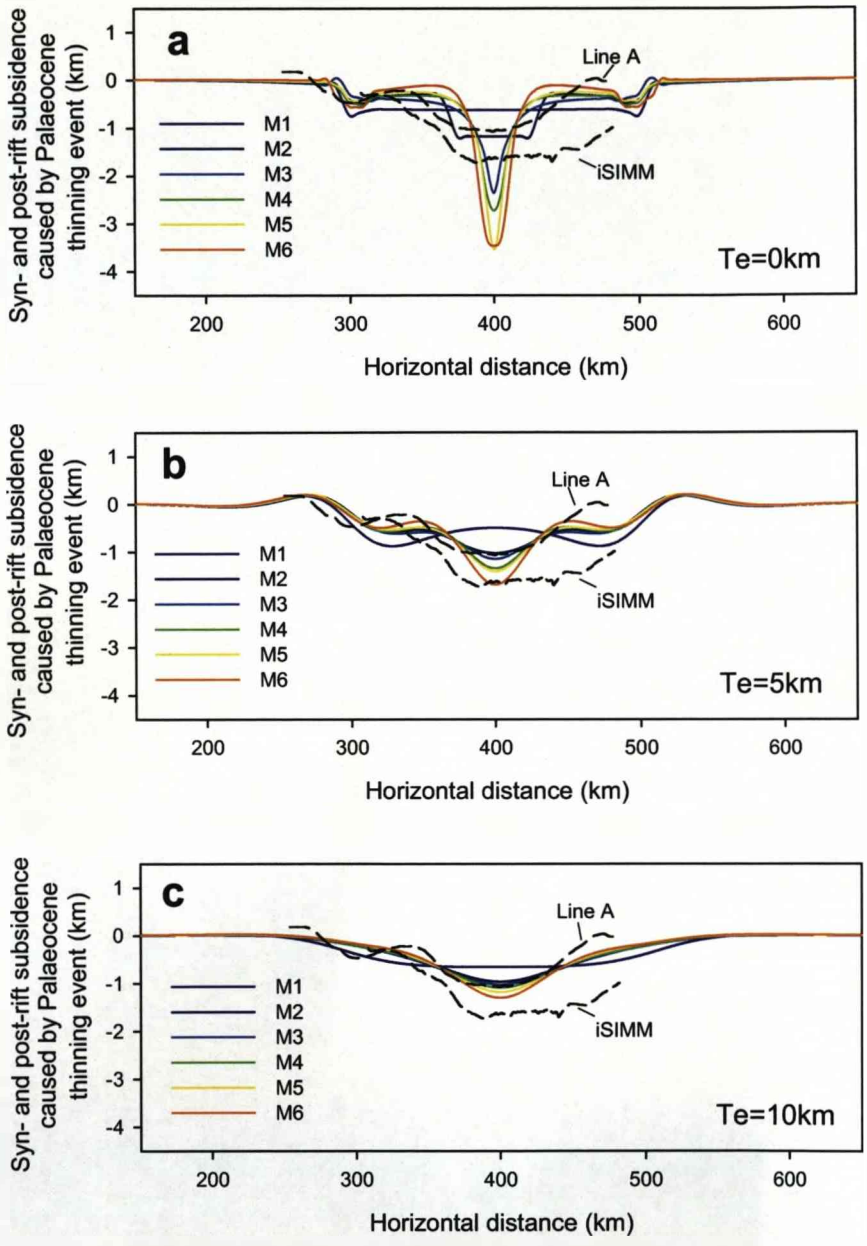

Figure 10.7: Predicted syn- and post-Palaeocene thinning subsidence (Si+St) for models M1 to M6, calculated assuming effective elastic thicknesses (Te) of **(a)** 0km (local isostasy), **(b)** 5km and **(c)** 10km. Black dashed lines are minimum tectonic subsidence profiles for line A and iSIMM (see Figure 10.3 for locations) calculated assuming that regional subsidence of 500m has occurred since the Late Palaeocene. Note that the tectonic subsidence profiles calculated for line A and iSIMM are insensitive to the effective elastic thickness (Te) assumed during flexural backstripping.

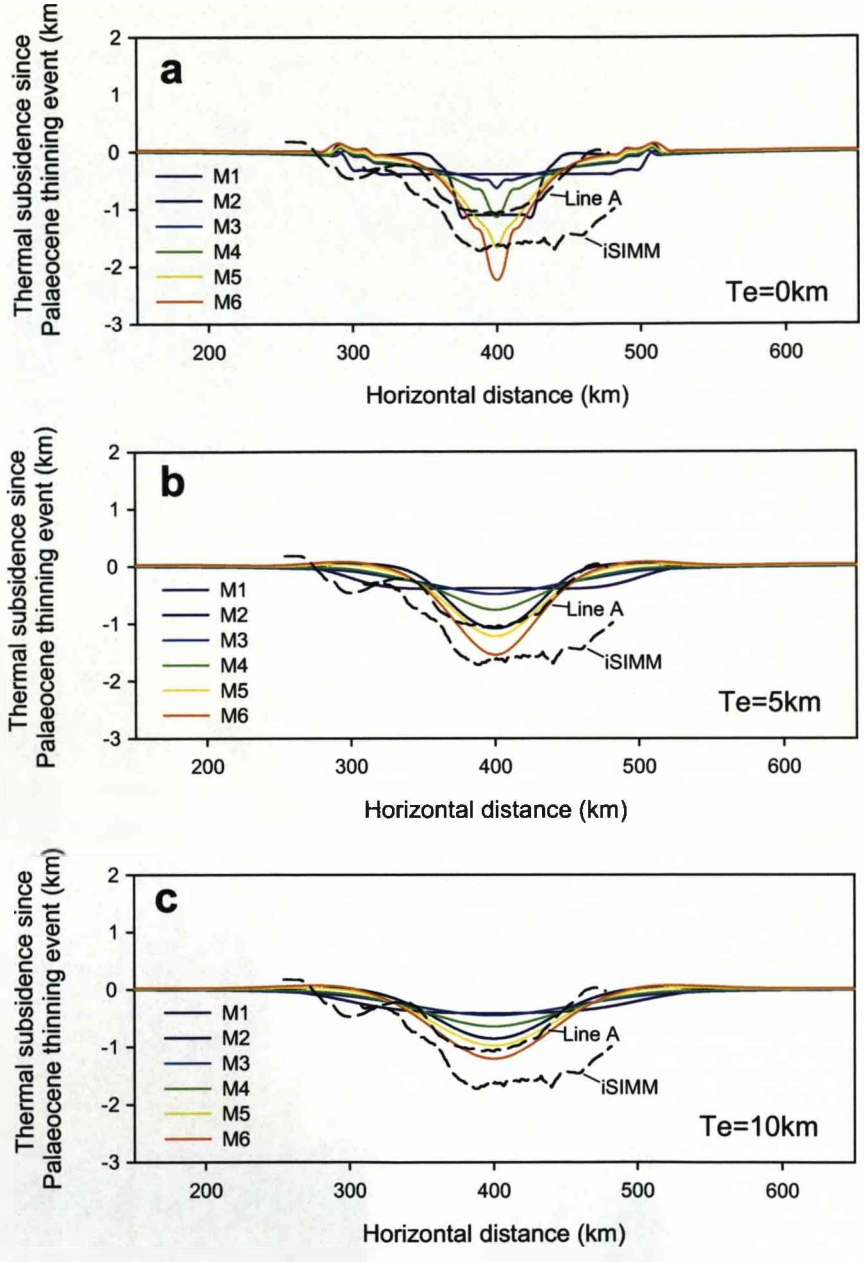

Figure 10.8: Predicted post-Palaeocene thinning subsidence (St) for models M1 to M6, calculated assuming effective elastic thicknesses Te of **(a)** 0km (local isostasy), **(b)** 5km and **(c)** 10km. Black dashed lines are minimum tectonic subsidence profiles for line A and iSIMM (see Figure 10.3 for locations) calculated assuming that regional subsidence of 500m has occurred since the Late Palaeocene. Note that the tectonic subsidence profiles calculated for line A and iSIMM are insensitive to the effective elastic thickness (Te) asumed during flexural backstripping.

varies more than the predicted syn- and post-rift subsidence (Si+St). The high velocity ratio upwards propagating upwelling-divergent flow model (M6) predicts the most post-rift thermal subsidence. This is due to model M6 being the most efficient model for advecting heat upwards during lithospheric thinning, and therefore post-thinning conductive cooling results in a large amount of thermal subsidence. Assuming an effective elastic thickness of 5 or 10km, the post-rift thermal subsidence (Si) predicted by models M2, M5 and M6 can explain the magnitude and width of the post-Palaeocene subsidence in the southern part of the basin (along profile A).

In summary, models M2, M5 and M6 can explain the post-Palaeocene subsidence in the southern part of the FSB as either syn- and post-rift subsidence (Si+St) or as post-rift subsidence only (St), if the lithosphere is considered to have a small but finite effective elastic thickness. Consequently it is not possible to discriminate between these models based on the predicted post-Palaeocene subsidence profiles. In the northern part of the basin the post-Palaeocene subsidence is deeper and wider than in the south, and none of the models shown easily account for this magnitude of post-Palaeocene subsidence; however model M6 can explain a very deep (but narrow) basin if post-Palaeocene subsidence is considered to comprise both syn- and post-rift subsidence (Si+St).

10.3.2 Subsidence and uplift history

The subsidence and heatflow history for 5 locations across the basin are shown for each model, assuming local isostasy, in Figure 10.5. Each model includes a Late Jurassic - Early Cretaceous pure-shear thinning event of maximum magnitude 1.4, therefore the subsidence and heatflow history of the basin prior to the Late Palaeocene thinning event is the same for each model. However the mode of Paleocene thinning affects the Palaeocene and later heatflow and subsidence history predicted by the model.

The pure-shear model (M1) predicts continuous subsidence throughout the basin evolution, with a period of rapid subsidence occurring during Palaeocene lithospheric thinning.

Extension within the decoupled pure-shear thinning model (M2) is depth-dependent

and predicts syn- and post- thinning subsidence in the centre of the basin which exceeds that which would be implied by upper crustal extension, if extension were assumed to be depth-uniform. A small amount (less than 100m) of syn-thinning uplift is predicted on the basin margin where thermal uplift locally exceeds subsidence due to crustal thinning. Post-rift thermal subsidence follows.

The static UDF model M3 (where the flowfield acts instantaneously throughout the whole continental lithosphere, and is fixed in the axial reference frame) predicts rapid Palaeocene subsidence in the centre of the basin during thinning, as the crustal thickness is rapidly reduced by the upwelling-divergent flowfield. Post-rift thermal subsidence follows.

Model M4 is similar to M3, differing only in that the velocity ratio of the upwelling divergent flow has a higher velocity ratio. During Palaeocene thinning rapid subsidence occurs in the centre of the basin, whilst a small amount (less than 100m) of syn-thinning uplift occurs on the basin flank due to a small amount of crustal thickening predicted by the high velocity ratio flow. Post-rift thermal subsidence follows.

The upwards propagating upwelling-divergent flow model M5 predicts that a period of uplift (up to 1100m) occurs as the lithospheric mantle is thinned. When the upwards-propagating flow begins to thin the crust, rapid subsidence occurs. When the upwelling divergent flow ceases, thermal subsidence follows, the rate of this thermal subsidence is greater than that predicted by the models M1, M2, M3 and M4, as the thermal perturbation at the end of thinning is relatively large.

For model M6, the upwards-propagating upwelling divergent flow model with a high velocity ratio, the maximum uplift during lithospheric mantle thinning increases to around 1300m close to the centre of the basin. As with model M5, rapid subsidence follows as the crust is thinned, and relatively rapid (thermal) subsidence continues after the lithospheric deformation field ceases. As illustrated in Figure 10.8, model M6 predicts the highest amount of post-thinning thermal subsidence, due to the large thermal perturbation in the basin at the end of rifting.

Subsidence histories calculated by backstripping in the Faroe-Shetland basin show that

the basin uplifted during the Late Palaeocene, and rapidly subsided at the end of the Palaeocene and in the Early Eocene (Smallwood and Gill, 2002; Champion et al., 2008, and see Chapters 4-6). The rapid subsidence began during Flett Formation times, approximately 1-2Myr before Top Balder times and continued into the Early Eocene. In Quad 204 of the basin at least 480m of uplift occurred in the Palaeocene (Champion et al., 2008, Figure 3.14), although it is not clear at present if this uplift was caused by a regional effect associated with a syn-breakup thermal anomaly or if it was partially or wholly a more localised effect. Each of the models presented predict rapid syn-thinning subsidence as the crust is thinned. The upwards-propagating models (M5 and M6) predict significant (thermal) uplift as the lithospheric mantle is first thinned followed by rapid subsidence as the lower crust is thinned. This result favours the upwards-propagating models of basin formation, as these models are able to explain uplift prior to rapid subsidence similar to that which is observed in the FSB (Figure 3.14).

Each of the depth-dependent models (M2-M5) predict higher maximum heatflow than the pure-shear model M1. This is due to the preferential thinning of the continental lithospheric mantle and the associated thermal perturbation. The heatflow maxima occurs slightly later for the depth-dependent models than for the depth-uniform stretching model due to the time-dependence of conduction of the depth-dependent thermal perturbation.

10.3.3 Melting

In all of the models shown in Figure 10.5, pressure-temperature conditions in the model did not cross the solidus, and no melting was predicted. The volume of melt is however sensitive to both the duration of deformation and the mantle potential temperature. More rapid, or instantaneous thinning would make melting more likely to occur, whilst the effects of conduction during slower thinning reduces the likelihood of melting. However, whilst the Palaeocene thinning in the FSB was probably rapid, the absolute timing is poorly constrained. Breakup of the Atlantic margin is widely thought to have occurred during times of increased mantle potential temperature (White and McKenzie,

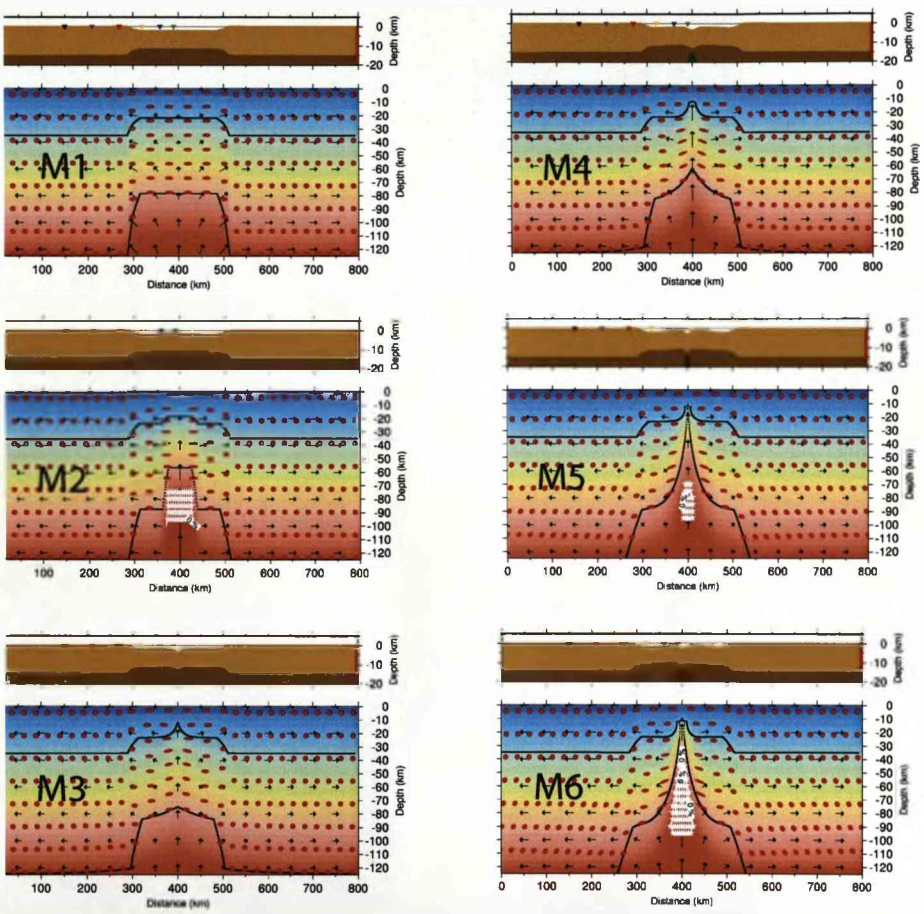

Figure 10.9: Melt production at end-Palaeocene times. Model predictions at the end of the lithospheric thinning event - assuming a hot mantle (potential temperature of 1433°C). The main panel shows a Eulerian plot of temperature, zone of melting at end of Palaeocene thinning event indicated in white. For other parameters see caption for Figure 10.5. Melt volumes (per km along strike) listed in the table in Figure 10.10.

1989, ~50-100 °C hotter than normal). The models shown in Figure 10.5 were calculated assuming a mantle potential temperature of 1333°C. When the mantle potential temperature was increased to 1433 °C, the decoupled pure-shear model (M2) and the upwards-propagating UDF models (M5 and M6) predict melting. Figure 10.9 shows the temperature field and the zone of melting at the end of the thinning event for models M1-M6 calculated with a mantle potential temperature of 1433°C. However, the volumes of melt predicted (if any), listed in the table in Figure 10.10, are low: less than 65km^3 per km along strike, or less than 0.5km in thickness if the melt is distributed over a 150km wide region. It is known that a small amount of melting occurred during the Late Palaeocene in the FSB, evidenced by sills, small intrusions and eruptive centres (Gatliff et al., 1984; Bell and Butcher, 2002; Trude et al., 2003), although the volumes are not well constrained. Seismic refraction profiles however do not indicate large volumes of volcanic addition or underplated crust in the basin, so it is unlikely that volcanic addition is more than a few km thick. Models M2, M5 and M6 are therefore consistent with a small amount of melting accompanying Palaeocene lithospheric thinning. However, if the modelled thinning duration was increased, melt volumes would decrease, and so considering the uncertainty regarding the duration and mantle potential temperature during Palaeocene thinning, it is not possible to discriminate between these models based on the volume of melt predicted.

10.3.4 Lithospheric geometry and finite deformation

With the exception of the pure-shear model (M1), each of the models predict depth-dependent stretching in the centre of the basin, where the upper crustal layer has been thinned much less than the lower crust and lithospheric mantle. Depth-dependent stretching was described for the FSB in Chapter 5: the magnitude of lithospheric thinning implied by the magnitude of post-Palaeocene subsidence far exceeds that implied by Palaeocene upper crustal extension, and so is incompatible with the pure-shear model.

The predicted Moho topography is dependent on the mode of thinning, each of the

depth-dependent models predict a narrow thinned zone in the basin axis, whilst the pure-shear model predicts a broad Moho upwarp. The minimum crustal thickness predicted by each of the models is listed in the table in Figure 10.10. The crust beneath the FSB is very thin; seismic data and gravity inversion results show that the top basement-Moho thickness is less than 15km in the axis of the basin, over a width of approximately 50km (Roberts, 2007, Figures 3.3 and 3.6). The width of lower crustal thinning observed in the FSB is greater than is predicted by any of the models presented, although this may be an artifact of the kinematic implementation of upwelling-divergent flow used in these models. The upwards-propagating, high velocity ratio model of lithosphere thinning (M6) is the most efficient mechanism for removing the lower crust. However, even at a upwelling to extension velocity ratio of 2, less lower crust is removed by model M6 than is implied from crustal thickness observations in the FSB. The possible fate of the lower crust and lithospheric mantle is discussed further in Section 10.4.

The basin geometry and finite strain of material beneath the basin predicted by each of the models varies (see Figure 10.5). The pure-shear model (M1) predicts that the upper crust, lower crust and lithospheric mantle are all thinned to the same degree, and finite strain is constant with depth. The decoupled pure-shear model (M2) predicts that beneath thinned crust, highly thinned (high finite strain with the long axis parallel to extension direction) lower crust and lithospheric mantle exist, i.e. the magnitude of finite strain increases with depth but the direction remains constant. The static (i.e. non-propagating) UDF models (M3 and M4) predict the presence of lithospheric mantle beneath thinned upper crust. Predicted finite strain in the lithospheric mantle for models M3 and M4 is non-parallel to the finite strain in the upper crust, and is dependent on the velocity ratio, with high velocity ratio flow predicting a higher magnitude of strain than the low velocity ratio flow. The upwards-propagating UDF models (M5 and M6) predict that asthenospheric mantle may underlie the thinned upper crustal lid. Predicted finite strain in the mantle for models M5 and M6 is non-parallel to the finite strain in the upper crust, and is dependent on the velocity ratio,

	Palaeocene horizontal extension (km)	Depth-dependent stretching predicted?	Post-Palaeocene subsidence explained as syn- and post-thinning subsidence?	Post-Palaeocene subsidence explained as post- thinning subsidence?	Melt predicted if T_m 1333°C (km^3 per km along strike)	Melt predicted if T_m 1433°C (km^3 per km along strike)	Basin uplift predicted?	Minimum crustal thickness (km)
M1	25	no	no	no	0	0	no	19.2
M2	25	yes	yes	no	0	30	<100m	17.2
M3	25	yes	yes	no	0	0	no	12.5
M4	25	yes	yes	no	0	0	<100m	12.5
M5	25	yes	yes	no	0	3.4	>1000m	12.5
M6	25	yes	yes	yes	0	61	>1000m	12.5

Figure 10.10: Table of key predictions made by each of the six forward models.

with high velocity ratio flow predicting a higher magnitude of strain than the low velocity ratio flow.

No observational data currently exist which distinguish the origin of the mantle (sub-continental or asthenospheric) or quantify the breakup-related finite strain beneath the FSB, therefore it is currently not possible to distinguish between the models based on these predictions. If new information regarding these things becomes available, the applicability of each model can be further tested.

10.4 Discussion

Late Palaeocene depth-dependent stretching in the FSB has been modelled using two-dimensional kinematic forward models of deformation. Each of the models assume that the lithosphere extended a total of 25km in the space of 1.25Myr at the end of the Palaeocene, but the mode of deformation differed in each case.

Each of the models makes different predictions of subsidence and uplift history, heat-flow, finite deformation and melt production in the basin, and of basin geometry. These

predictions were compared with observational constraints from the FSB where available. I suggest that an upwards-propagating upwelling divergent flow with a high velocity ratio (model M6, where V_z^0/V_x^0=2) best explains the process of depth-dependent stretching in the FSB. A schematic model of formation of the FSB is shown in Figure 10.11.

In this preferred model, Jurassic-Cretaceous pure-shear extension formed a wide basin. Subsequently, during the Palaeocene, upwelling-divergent flow initiated in the lower lithosphere of the FSB, propagating upwards to the mid-crust where it preferentially thinned the lower crust and lithospheric mantle for a short time before flow ceased and the basin thermally subsided. I suggest that Post-Paleocene thinning was occurring for a short time before and during deposition of the Top Balder formation (during the period of rapid subsidence), and that the post-Palaeocene subsidence in the FSB is post-rift thermal subsidence plus a component of syn-rift subsidence from a Late Palaeocene thinning event. Thus the thinning event was occurring immediately prior to and after SDR formation and the onset of seafloor spreading in the Norwegian basin. Thinning in the FSB ceased in the Early Eocene. I suggest that the Faroe-Shetland basin is a 'failed breakup basin', a basin which was thinned, but did not rupture, at around the same time as continental rupture occurred on the Atlantic margin.

The preferred model predicts a period of uplift of 1300m (whilst the lithospheric mantle is preferentially thinned) prior to a period of rapid subsidence (as the lower crust is thinned). This uplift-subsidence history is in qualitative agreement with that observed during the Late Palaeocene and early Eocene in the FSB. Additionally the preferred model predicts the highest amount of both syn- and post-rift (Si) and post-rift (St) subsidence due to the Palaeocene thinning event, and therefore (of all the models tested) best explains why the magnitude of post-Palaeocene subsidence in the FSB was large whilst the amount of upper crustal extension was minimal. The upwards-propagating upwelling divergent flow model (M6) also predicts a small volume of melt during thinning, if mantle potential temperatures are high ($\sim$ 1433°C), which is consistent with observations. The ages of the sills (c.53-55Ma, Hitchen and Ritchie, 1993; Trude et al.,

2003) and stratigraphic position of the volcanic centres in the basin are also consistent with maximum thinning in the basin occurring synchronously with breakup (formation of the SDRs) on the Faroes margin.

The crust beneath the FSB is highly thinned, with crustal basement less than 10km thick in places. The high velocity ratio, upwards propagating upwelling-divergent flow mode of deformation is the most efficient mechanism, of those tested, per unit of horizontal extension, of removing the lower crust. The mechanism implies that accommodation space in the basin was created by ductile lower crust and lithospheric mantle being pushed outwards, thickening (and uplifting) the flanks of the basin. Thickening and uplift of the basin flank areas caused by upwelling-divergent flow may be partially countered by thinning of the upper crust by distributed pure-shear. However, there is no evidence that the crust or lithosphere beneath the Shetland Platform was thickened in the Late Palaeocene. Uplift has occurred on the Faroes continental block, although that is thought to have occurred at a later time due to plate boundary reorganisation (Boldreel and Andersen, 1993; Andersen et al., 2000).

An alternative explanation regarding the fate of the lower continental crust requires that the formation of the FSB was a three-dimensional process, and large volumes of lower crust and lithosphere were pulled and moved into the Norwegian basin. It is however difficult to test whether such 3–D advection of continental lithosphere can or did occur. Further constraints on the subsidence and uplift history of the basin and the application of 3–D models to the basin may provide further answers on the fate of the lower crust and lithospheric mantle removed from the FSB during Palaeocene depth-dependent stretching.

Post-Palaeocene subsidence in the FSB increases to the northeast towards the Norwegian basin. The preferred model shown in this chapter is able to explain the tectonic subsidence in the southern part of the basin. The increased subsidence towards the northeast may indicate one or a number of the following: Total extension associated with Late Palaeocene thinning increased towards the northeast; the vigour of the upwelling-divergent flow (i.e. the velocity ratio) associated with the thinning increased

Jurassic-Cretaceous: Pure-shear extension. Upper crustal extension accommodated on brittle faults, ductile lower crustal and lithospheric mantle deformation.

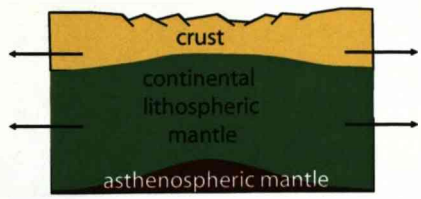

Cretaceous and Early Palaeocene: Post-rift thermal subsidence and sedimentation.

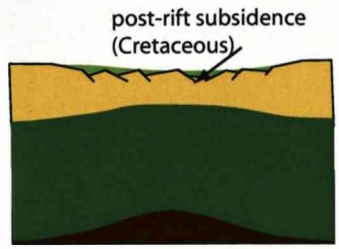

Palaeocene: Upwards-propagating upwelling-divergent flow thins the lithospheric mantle first, causing uplift in the basin.
Concurrent regional uplift (approx 500m) causes erosion of surrounding platform areas and rapid sedimentation in the basin.

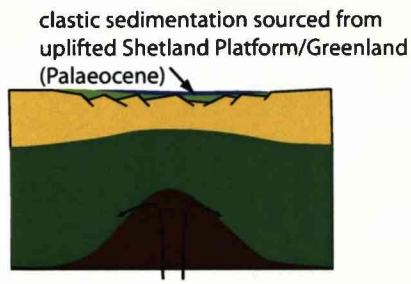

Late Palaeocene (Flett-Formation and Basalt Series times): Upwards-propagating upwelling-divergent flow thins the lower crust, causing rapid subsidence. The upwelling divergent flowfield acts in the lithospheric mantle and lower crust, whilst the upper crust extends by distributed pure shear on minor faults. Small amount of melt is produced in the basin. Continental lithospheric rupture at the Faroes margin.

Deformation in the Faroes-Shetland basin ceases shortly after Balder Formation times (i.e. shortly after the time of Seaward Dipping Reflector formation and the onset of seafloor spreading in the Norwegian basin).

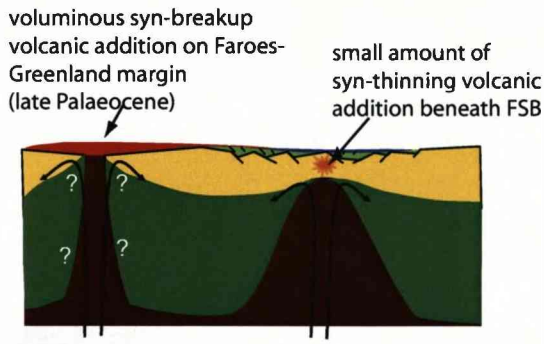

Eocene – Present Day: Thermal subsidence in the Faroe-Shetland Basin until present day. Continued spreading in the Norwegian basin until Miocene.

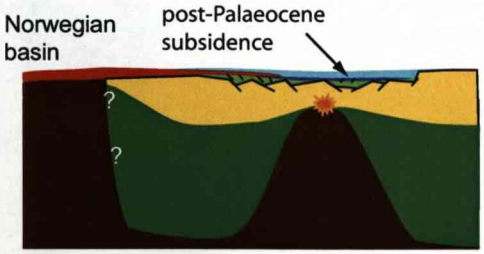

Figure 10.11: Schematic preferred model of development for the Faroe-Shetland basin.

towards the ocean basin; or that upwelling-divergent flow in the lithospheric mantle occurred to shallower depths in the northeast of the basin. All of these explanations are compatible with successful continental rupture and the initiation of seafloor spreading at the Møre margin, and that thinning of the FSB may have been at the tip of an incipient spreading centre, and is a 'failed breakup basin'. A decrease in crustal thickness to the northeast of the FSB indicated by gravity modelling (Figure 3.5 and Figure 3.6, Section 3.3) is consistent with the idea that preferential removal of the lower crust, possibly by a small-scale convection process within the continental mantle, occurred at progressively deeper levels away from the successful rupture of the lithosphere (i.e. towards the southwest).

A remaining question is why did lithospheric thinning, but not continental rupture not occur in the Faroe-Shetland basin in the Late Palaeocene? It is known that the integrated strength of the lithosphere under a basin can exceed that of unthinned continental lithosphere if the thermal perturbation associated with the basins formation has sufficiently cooled (e.g. England, 1983; Kusznir and Park, 1987; van Wijk and Cloetingh, 2002). Strengthening of the lithosphere in the FSB by earlier rift events may explain why continental rupture did not occur in the basin (England et al., 2005), but it does not explain why Palaeocene lithospheric and lower crustal thinning were able to occur.

A possible explanation for why thinning, but not breakup, occurred in the FSB in the Palaeocene was suggested in Chapter 6. A model was proposed where tensile forces associated with the opening of the Atlantic caused thinning to occur along more than one offset axis (i.e. the FSB and to the west of the Faroe Islands); these axes may have been associated with thermal (e.g. due to previous rifting) or compositional weaknesses. Continental breakup subsequently occurred to the west of the Faroes and at the Møre margin, with the Faroes margin acting as an oblique 'relay zone'. Active thinning and deformation in the FSB subsequently ceased, leaving a 'failed breakup basin'. The final location of breakup may be determined by a number of factors, including strength or melting heterogeneities in the lithospheric mantle or crust. Further 2–D and 3–D

models may enhance our understanding of the factors which influence the location of rifting and failed breakup basins.

The driving forces of continental breakup are often considered in terms of 'active' and 'passive' end-member model causative mechanism of lithospheric thinning, although much work has been done to show the importance of induced small-scale convection during the lithospheric thinning process (e.g. Keen, 1985; Buck, 1986; Huismans et al., 2001a). The mode of deformation suggested here for the development of the FSB is analogous to models of small-scale convection and enhanced upwelling during lithospheric thinning. In the next chapter dynamic models are employed to investigate the physics responsible for small scale convection in the lithospheric mantle and the conditions under which depth-dependent stretching of the continental lithosphere may occur.

Chapter 11

The role of wet melting and water-content heterogeneities during continental lithospheric thinning

11.1 Introduction

Many rift basins and rifted margins exhibit depth-dependent stretching, where the lithospheric mantle has been thinned significantly more than is implied by brittle faulting in the upper crust. One explanation for this is that small-scale convection in the continental mantle and lower crust, induced by upwelling, preferentially thins the continental mantle with respect to the upper crust (Keen, 1985; Huismans et al., 2001a; Huismans and Beaumont, 2008). Enhanced upwelling and small-scale convection during continental breakup may also explain the production of large volumes of melt during lithosphere thinning and early seafloor spreading at some volcanic margins (Mutter et al., 1988; van Wijk et al., 2001; Korenaga et al., 2002).

As discussed in Chapter 2 of this thesis, preferential thinning of the lithospheric mantle and lower crust with respect to the upper crust occurs prior to continental lithospheric

rupture and also occurs in continental rift basins which did not proceed to breakup (i.e. the Faroe-Shetland basin - see Chapters 6 and 10). The effect that upwelling-divergent flow may have in the development of rift basins and rifted margins was shown by the kinematic models described in Chapters 7 and 8. In the case of the FSB, which lies just inboard of the NE Atlantic margin (Figure 3.1), a Late Palaeocene thinning event, analogous to a small-scale convective event in the lithospheric mantle and lower crust, was suggested to have occurred in the basin synchronous with continental lithospheric rupture on the Møre and Faroes margins. This chapter aims to investigate some of the driving forces which may be responsible for preferential lithospheric thinning, specifically the role that melting and fertility heterogeneities may have on processes of continental thinning. This is done using a dynamic model.

Dynamic models of continental lithosphere thinning require that a heterogeneity is present for strain to localise; the nature of this heterogeneity will determine if a period of small-scale convection will occur during lithospheric thinning. Huismans et al. (2001a) and Huismans and Beaumont (2008) show that locally-thickened crust (and therefore a weaker lithospheric column) can cause strain to localise in the mantle lithosphere. Thermal buoyancy forces subsequently drive small-scale convection in the lithospheric mantle, resulting in preferential lithospheric thinning at the resulting margins. King and Anderson (1998) showed that a viscosity contrast caused by lateral variations in lithospheric thickness may also cause small-scale convective cells to occur. However, these models did not include the effects of melting on the development of the model.

The models of Boutilier and Keen (1999) and Nielsen and Hopper (2004) assume that strain localises within a narrow zone at the surface of the model and that the lithosphere has been pre-thinned prior to the onset of extension. Both of these sets of models predict a period of enhanced melt production due to small-scale convection, although Nielsen and Hopper (2004) suggest that a temperature anomaly may also be required to account for very thick syn- and early post-breakup melt thicknesses observed at some margins (e.g. East Greenland). However, the pre-thinning condition and focused surface extension applied in these models means that the small-scale convection does

not result in depth-dependent stretching (where the continental lithosphere is thinned more than the upper crust) beneath the rift axis.

Small-scale convection and enhanced upwelling has also been shown to be important beneath mid-ocean ridges. Braun et al. (2000) showed that buoyancy forces from deep damp melting, between the dry and wet solidii at 60-80km depth, can increase the upwelling velocity and therefore influence the predicted melt thicknesses, particularly at slow-spreading ridges. The results section of this chapter is split into two parts, and in the first results section of this chapter the role of deep damp melting on continental lithospheric thinning prior to breakup is investigated.

The continental lithosphere is usually considered to be more heterogeneous than the asthenosphere, in terms of temperature structure and composition. It is possible that the continental mantle has a heterogeneous water-content, inherited during the continental accretionary process or arising from rehydration during subduction. The presence of water in the continental lithosphere both weakens the mantle (Karato, 1986; Hirth and Kohlstedt, 1996) and increases its melt fertility (e.g. Katz et al., 2003); water-content heterogeneities may provide a viable mechanism by which strain may localise during continental thinning. In the second results section I assess the influence of melting heterogeneities on the dynamics of rifting.

A dynamic finite element- finite difference model is employed in this chapter to study the thinning and melting during continental lithospheric breakup, adapted from the model of Braun et al. (2000). Both the distribution of extension with depth and the volume of melt predicted by the models will be presented, and discussed in relation to general observations at rifted continental margins. This chapter is intended as a preliminary study into the role of melting, particularly wet melting and the effect of water-content (and thus fertility) heterogeneities on continental lithospheric thinning. A discussion of the limitations of the model and suggestions for further work is given at the end of the chapter.

The key questions which are addressed in this chapter are:

1. What conditions favour enhanced upwelling and small-scale convection beneath

or within the thinning continental lithosphere?

2. What is the effect of wet melting on lithospheric deformation during continental breakup? Can wet melting lead to instability and small-scale convection in the lithospheric mantle during rift basin and rifted margin formation?

3. Can water-content heterogeneities in the lithospheric mantle localise rifting and induce small-scale convection?

11.2 Method and model description

The models presented in this chapter are calculated using code adapted from the model described in Braun et al. (2000), which was designed to investigate the role of wet melting at mid-ocean ridges. Continental lithospheric thinning is a transient process, which evolves as the continental lithosphere is thinned or ruptured; consequentially the initial conditions and boundary conditions of the model were adapted in an attempt to better approximate realistic initial conditions for continental breakup. The model is first described in full, then the key adaptations which have been made to the model of Braun et al. (2000) are clarified.

11.2.1 Governing equations

The model is based on solutions to the following governing equations:

$$\frac{\partial u_i}{\partial x_i} = -\dot{M} \tag{11.1}$$

$$\frac{\partial T}{\partial t} = \kappa \nabla^2 T - u_i \frac{\partial T}{\partial x_i} - \frac{\triangle H_{fus}}{c_p} \dot{M} + H_c \tag{11.2}$$

$$-\frac{\partial p}{\partial x_i} + -\frac{\partial \tau_{ij}}{\partial x_i} + \rho g_i = 0 \tag{11.3}$$

$$\frac{\partial F}{\partial t} + u_i \frac{\partial F_i}{\partial x_i} = \dot{M} \tag{11.4}$$

from Braun et al. (2000) which express the conservation of mass, conservation of energy, mechanical equilibrium for variable viscosity and the production (due to melting) and advection of mantle depletion (F), respectively. In these equations u_i is the mantle velocity, $\dot{M}$ the rate of melt production, T is temperature, t is time, κ is thermal diffusivity, $\triangle H_{fus}$ is the latent heat of fusion, c_p is the specific heat at constant pressure, p is pressure, H_c is crustal radiogenic heat production. τ_{ij} is the deviatoric stress tensor defined as:

$$\tau_{ij} = 2\mu(\frac{\partial u_i}{\partial x_j} + \frac{\partial u_j}{\partial x_i}) \tag{11.5}$$

g_i is the acceleration due to gravity and μ is the apparent viscosity. The density, ρ, is a function of temperature, depletion, composition (i.e. whether the material is crust or mantle) and retained melt fraction (ϕ):

$$\rho = \rho_m(1 - \alpha T - yF) - \triangle\rho\phi \text{ in the mantle} \tag{11.6}$$

and

$$\rho = \rho_c(1 - \alpha T - yF) - \triangle\rho\phi \text{ in the crust} \tag{11.7}$$

where ρ_m is the reference density of the mantle, ρ_c is the reference density of the crust. α is the coefficient of thermal expansion, y is the ratio which accounts for the change in density of the residue owing to preferential extraction of iron versus magnesium during melting (Oxburgh and Parmentier, 1977) and $\triangle\rho$ is the density difference between solid and melt. A full table of parameters used in the equations in this chapter is given in Table 11.1.

11.2.2 Model configuration

Models of rifting are obtained numerically by a hybrid finite element - finite difference formulation, as described by Braun et al. (2000). Equations for buoyant viscous flow are solved using a standard penalty function method with linear rectangular elements. The equations for energy conservation and melt depletion are solved with second order

Variable	Meaning	value	units
A_p	Permeability constant	-	-
A	Viscosity constant for dry olivine[1]	$1.1X10^{-5}$	-
	for wet olivine[1]	90	-
A^*	Scaled viscosity constant	-	-
a	Coefficient of viscosity reduction	-	-
	due to melting	45	-
C_{OH}	Water-content	-	$OH/10^6Si$
C_{OHi}	Initial water-content	0-16000	$OH/10^6Si$
C_v	Equivalent crustal thickness	-	km
E^*	Activation energy for dry olivine:	530000	$Jmol^{-1}$
	for wet olivine:	480000	$Jmol^{-1}$
F	Depletion	-	-
F_{wet}	Degree of partial melting	-	-
	between wet and dry solidii	0-0.05	-
g	Gravitational acceleration	10	ms^{-2}
$\Delta H_{fus}/c_p$	Latent heat term - determines melt productivity	300	^oC
H_c	Crustal radiogenic heat production rate	$1X10^{-6}$	Wm^{-2}
K	Permeability	-	-
n	Stress exponent	3.5	-
$\dot{M}$	Rate of melt production	-	s-1
p	Pressure	-	Pa
r	Water concentration exponent	1.2	-
R	Ideal gas constant	8.31	$Jmol^{-1}K^{-1}$
Sc	Scaling viscosity coefficient	10^{-4}–10^{-6}	-

Table 11.0: Table of parameters. Continued on next page. [1] denotes that value is valid when calculated with stress in MPa and C_{OH} in $H/10^6Si$

Variable	Meaning	value	units
t	time	-	Myr
T	Temperature	-	^oC
T_{dry}	Dry solidus	-	^oC
T_{wet}	Wet solidus	-	^oC
u	Velocity	-	ms^{-1}
V_x^0	Model horizontal extension half-rate	2–40	$kmMyr^{-1}$
$V_x, V_x(x,z)$	Horizontal velocity component (at x,z)		$kmMyr^{-1}$
$V_z, V_z(x,z)$	Vertical velocity component (at x,z)		$kmMyr^{-1}$
V^*	Activation volume	$1.1X10^{-5}$	m^3mol^{-1}
y	Fractional density change due to depletion	$2.4X10^{-2}$	-
x	Horizontal distance	-	km
z	Depth	-	km
α	Coefficient of thermal expansion	$3.28X10^{-5}$	$^oC^{-1}$
β	Stretching factor	-	-
γ, gamma	Thinning factor	-	-
$\Delta\rho$	Fractional density change (solid to melt)	0.16	-
$\dot{\epsilon}$	strain rate	-	s^{-1}
κ	Thermal diffusivity	$1X10^{-6}$	-
μ	Apparent viscosity	-	Pas
ρ	Density	-	kgm^{-3}
ρ_m	Reference density of mantle	3300	kgm^{-3}
ρ_c	Reference density of crust	2900	kgm^{-3}
σ	Stress(second invariant)	-	MPa
τ	Deviatoric stress tensor	-	-
ϕ	Melt fraction in the matrix	-	-

Table 11.1: Table of parameters. Continued from previous page.

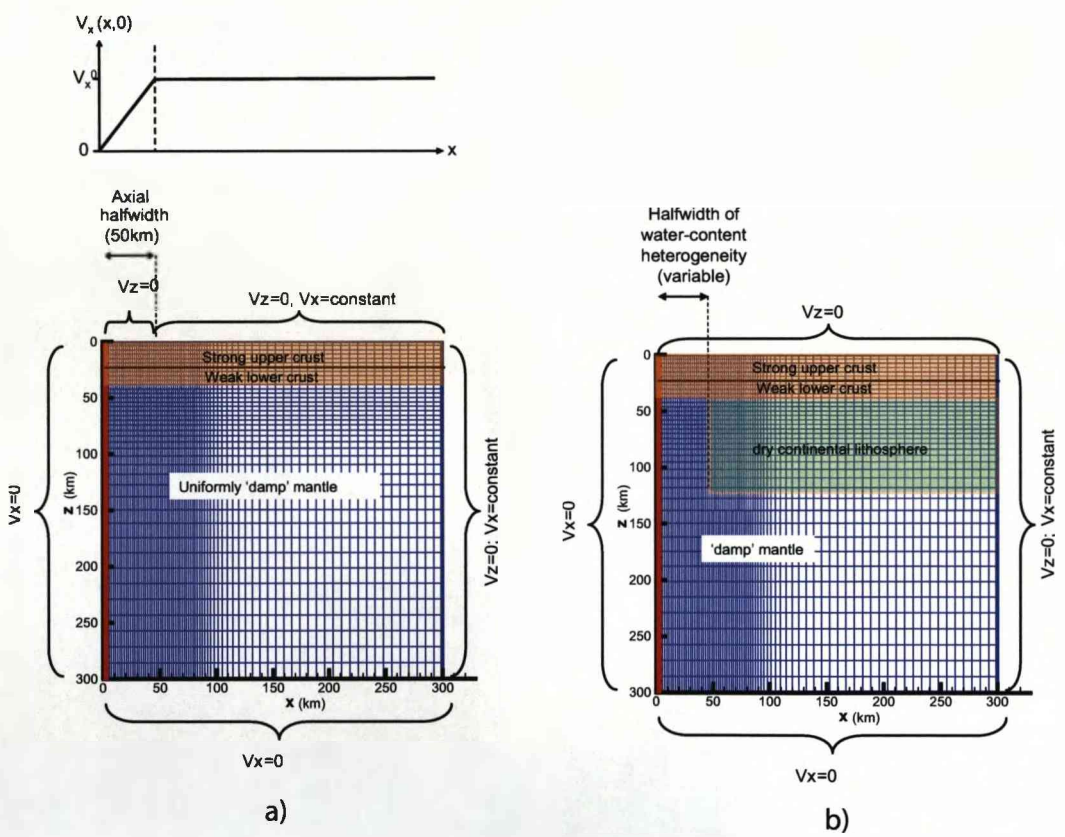

Figure 11.1: Initial and boundary conditions of the models. Blue mesh illustrates resolution. Red line denotes axis of symmetry, corresponding to the rift axis. (**a**) shows initial and boundary conditions and the velocity condition for the top boundary ($V_x(x,0)$) for models discussed in Section 11.3 (Results 1). (**b**) shows initial and boundary conditions for models discussed in Section 11.4 (Results 2).

finite difference approximations. Advection of material and scalar variables (e.g. temperature, depletion) is accomplished using an upwind-differencing method with high order corrections to reduce artificial diffusion. The model evolution is calculated on a 41 by 81 node mesh with non-uniform, rectangular elements within a vertical plane beneath a rift axis perpendicular to the axis. Node spacing decreases toward the rift axis from both depth and off-axis providing resolution of better than 2 km near the rift axis in a domain 300 km by 300 km (Braun et al., 2000, Figure 11.1).

11.2.3 Temperature calculation

The initial temperature profile is defined as an error function with an initial thermal age of 55Ma (Figure 11.2). The initial temperature profile is chosen to be very close to the wet solidus temperature so that only a small amount of extension is required to induce melting and is similar to the initial conditions assumed by Hernlund et al. (2008). The temperature of incoming material at the bottom is determined by a prescribed potential temperature (1350°C) and an adiabatic gradient (0.3°C/km). The temperature along the top boundary is set to 0°C. The temperature distribution is controlled by the competing effects of conductive heat loss from above, advective heat transport from below and radiogenic heat production (1×10^{-6}mWm^{-2}) in the upper 20km of crust (Equation 11.2).

11.2.4 Boundary conditions

In all models extension is driven by a constant velocity condition on the right-hand axis. This is the half-extension velocity V_x^0. Symmetry is assumed on the vertical boundary beneath the axis (the rift or ridge axis), so the full extension rate is $2V_x^0$. Material entering the base of the domain is assumed to be flowing only vertically, without resistance from the deeper mantle. The vertical velocity on the model surface is zero (Figure 11.1).

Two different boundary conditions are employed in this chapter for the surface velocity. These are shown in Figure 11.1. In the first set of models the mantle lithosphere and

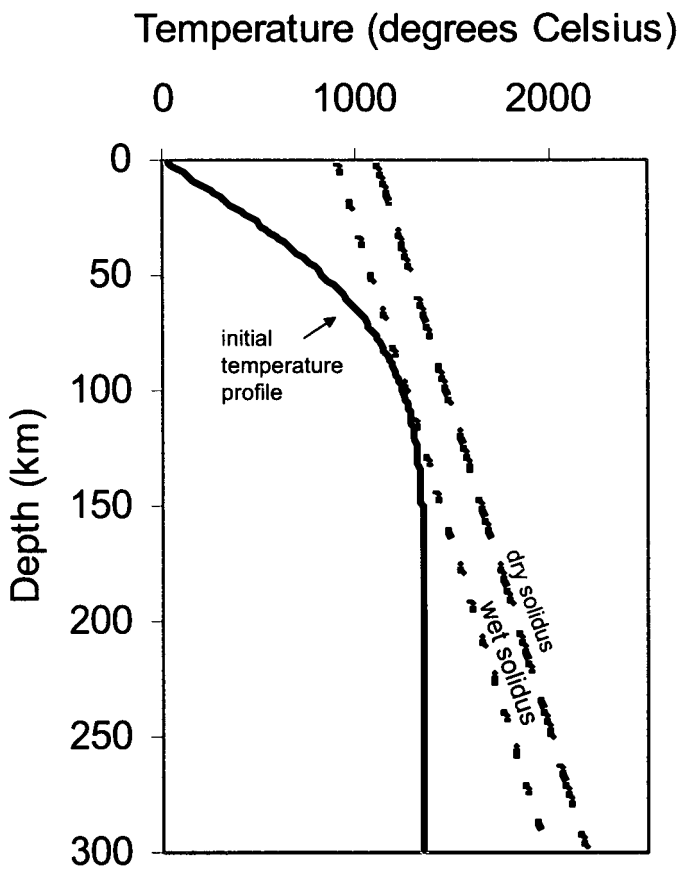

Figure 11.2: Initial temperature profile for all models, and wet and dry solidii. Note that at the start of the model (t=0) no lateral temperature variations exist.

asthenosphere is assumed to be homogeneous; in order for strain to localise a surface horizontal velocity condition is defined where extension occurs within a fixed axial region (Figure 11.1a). This boundary condition implies that the location of rifting is 'top-driven', determined by a weakness in the upper crust. In the second set of models the water-content, and consequentially the strength of the lithosphere, is heterogeneous and the surface horizontal velocity is not prescribed (Figure 11.1b). This initial condition implies that the location of rifting is determined by water-content heterogeneities in the continental lithospheric mantle.

11.2.5 Melting

Melting occurs when the temperature of the adiabatically upwelling solid exceeds the solidus temperature at a given pressure. The solidus temperature is a function of water-content (e.g. Asimow and Langmuir, 2003; Katz et al., 2003, and see Chapter 8). In this chapter the following simple melting functions are utilised for the calculation of melt fraction:

The dry and wet solidii are defined respectively as:

$$T_{dry} = 1100 + 3.6z \tag{11.8}$$

$$T_{wet} = 895 + 3.6z \tag{11.9}$$

where z is depth in km.

The degree of partial melting (F) caused by given amount of adiabatic decompression is given by:

$$F = F_{wet}(\frac{T - T_{wet}}{T_{dry} - T_{wet}}) \text{ above the wet solidus} \tag{11.10}$$

and

$$F = F_{wet}(\frac{\partial F}{\partial T})_p(T - T_{dry}) + F_{wet} \text{ above the dry solidus} \tag{11.11}$$

The maximum melt fraction produced in the wet melting region F_{wet} (between the wet and dry solidii) is assumed to be 5%. This is a higher fraction of wet melt than was

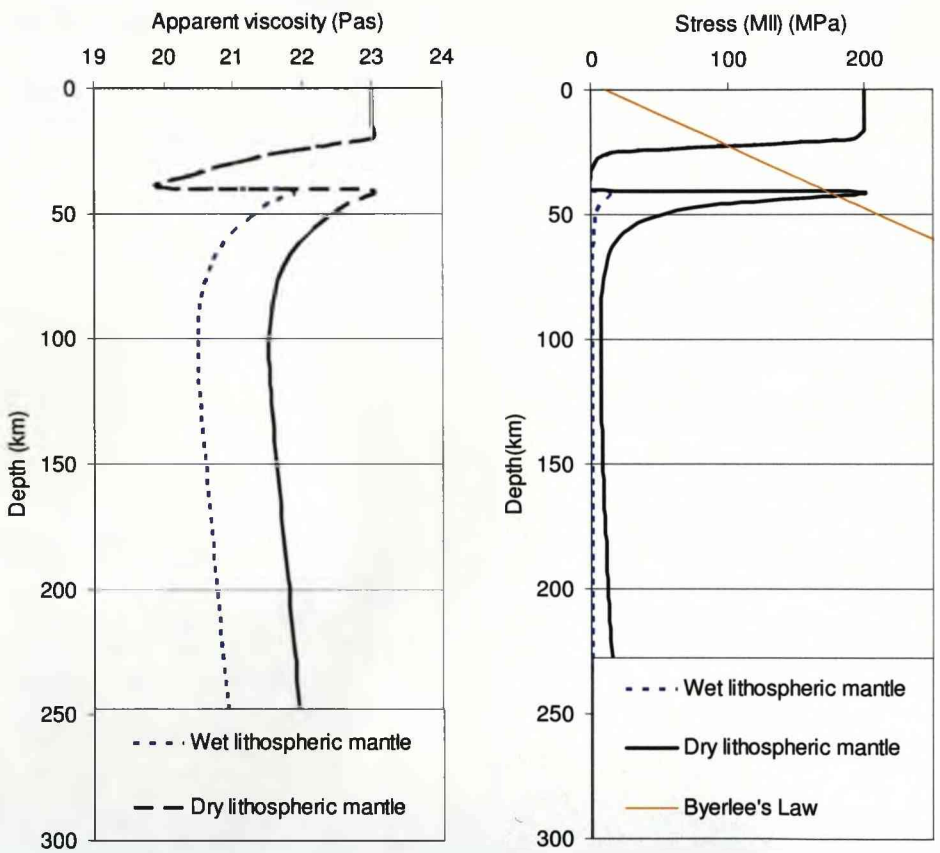

Figure 11.3: Example of initial apparent viscosity and maximum deviatoric stress profiles in 'wet' and 'dry' continental mantle. Apparent viscosity corresponds to the effective viscosity if the strain rate is $10^{-15}s^{-1}$. Scaling viscosity in this example is $10^{20.52}$ Pas. Byerlee's Law stress profile is shown for illustrative purposes only; this criterion was not included in these calculations.

assumed by Braun et al. (2000), but is still within the limits of mantle water capacity (e.g. Katz et al., 2003). A relatively high proportion of wet melting was chosen to accentuate the effect of wet melting on deformation. Where the mantle is 'dry', F_{wet} is set to zero. The amount of melt generated in the dry melting region may be adjusted through use of the isobaric melt productivity, $(\frac{\partial F}{\partial T})_{p\cdot}$; in this work melt productivity in the dry melting region was 2% /kbar. The total melt fraction was limited to 18 %, the fraction of melt produced prior to the exhaustion of clinopyroxene. The rate of melting $\dot{M}$ as a function of depth is calculated by (Braun et al., 2000):

$$\dot{M} = V_z(\frac{\partial F}{\partial z}) \tag{11.12}$$

where V_z is the upwelling rate

The total melt production rate for the whole model determines the equivalent melt thickness (C_v) which would be produced at the surface assuming that melt migration is perfectly efficient:

$$C_v = \frac{\rho_m}{\rho_c}\frac{1}{V_x^0}\int_{-\infty}^{0}\int_{0}^{+\infty}\dot{M}dxdz \tag{11.13}$$

The melt is assumed to migrate vertically through the mantle according to Darcy's law, so that the rate of melt extraction matches the production of melt (Braun et al., 2000):

$$\frac{K\triangle\rho g}{\mu} = \int_z \dot{M}dz \tag{11.14}$$

where $\triangle\rho$ is the density difference between the solid and the melt and K is the permeability, which is defined as

$$K = A_p\overline{\phi}^2 \tag{11.15}$$

where $\overline{\phi}$ is the mean melt fraction and A_p is a constant. The fraction of melt present in the matrix above the melting zone and the residence time of the melt (i.e. prior to extrusion) in the mantle is therefore dependent on the permeability of the mantle.

11.2.6 Viscosity

Viscosity (η) quantifies the resistance of a (viscous) material to deformation. Viscosity is defined as half the ratio of stress (σ, the second invariant of stress) to strain rate ($\dot{\epsilon}$) (e.g. Ranalli, 1995):

$$\eta = \frac{1}{2}\frac{\sigma}{\dot{\epsilon}} \tag{11.16}$$

In the lithosphere, viscosity is highly temperature-dependent, although pressure, grain size, strain rate, melt and water-content can also have a significant effect on viscosity. A general stress-strain rate relationship for viscous materials is:

$$\dot{\epsilon} = A^* \sigma^n d^{-P} (C_{OH})^r exp(a\phi) exp(-\frac{E^* + pV^*}{R(T + 273)}) \tag{11.17}$$

(Hirth and Kohlstedt, 2003), where A^* is a constant, n is the stress exponent, d is grain size, P is the grain size exponent, C_{OH} is water-content, r is the water-content exponent, ϕ is melt fraction, α is a constant, E^* is the activation energy, V^* is the activation volume, R is the gas constant and T is temperature. For a Newtonian fluid, n=1, and viscosity is not dependent on strain rate. In the lithosphere n=1 when deformation occurs by diffusion creep. When deformation occurs by dislocation creep, $n \approx 3.5$, and the apparent viscosity is dependent on strain rate, and the material is said to be 'non-linear'. For strain rate dependent rheology the apparent viscosity can be calculated by rearranging Equations 11.16 and 11.17. It is also worth pointing out that the rheology of olivine, both in the laboratory and in the Earth, is not completely understood, and there are uncertainties associated with all of the terms in the governing equations, in particular the effect of water (e.g. Korenaga and Karato, 2008).

In this chapter the viscosity of the lithospheric mantle and asthenosphere are calculated using constants from Hirth and Kohlstedt (2003) for olivine deforming by dislocation creep (n=3.5). All constants are listed in Table 11.1. The viscosity of the lithosphere is thus assumed to be independent of grain size. An additional scaling factor (Sc) is introduced in order to vary the relative influence of buoyancy forces on the models development:

$$A^* = ASc \tag{11.18}$$

Where A is the value of the viscosity constant for olivine from Hirth and Kohlstedt (2003) and A^* is the scaled viscosity constant used in Equation 11.17. The scaling factor has the effect of increasing or decreasing the viscosity of the entire model by the same amount. The scaling factor does not affect, for example, the viscosity gradient caused by a temperature gradient. However, the scaling viscosity does affect the relative influence of buoyancy forces on the development of the model; a high scaling factor increases the overall viscosity and therefore reduces the influence of buoyancy forces on the models development, and vice versa. Scaling factors of between 10^{-4} and 10^{-6} were used in this chapter, corresponding to a 1-2 order of magnitude change in the absolute value of viscosity of the whole model. When lower viscosities were used, buoyancy forces had a dominating influence on the deformation field, which became unstable. When higher viscosities were used, the effect of buoyancy forces on the deformation was negligible.
A scaling viscosity for each model is defined as the apparent viscosity of wet (1000 ppm) material which is 1350°C at a depth of 125km and is deforming at a strain rate of $10^{-15}s^{-1}$. The viscosity of the lower crust was calculated using the same equations, but viscosity is reduced by 2 orders of magnitude to approximate a weak lower crust. A maximum viscosity condition (of 10^{23}Pas) was also imposed.
In the first set of models, the continental lithosphere and asthenosphere are assumed to have an initially homogeneous water-content (C_{OHi}) of 16000 (1000 ppm). As melting occurs, the water is preferentially partitioned into the melt and the depleted mantle is dehydrated. A partition coefficient of 100 is assumed so that the water-content C_{OH} decreases with increasing depletion:

$$C_{OH} = C_{OHi}exp(-100 * F) \tag{11.19}$$

The viscosity of the mantle increases with depletion until it has the viscosity of 'dry'

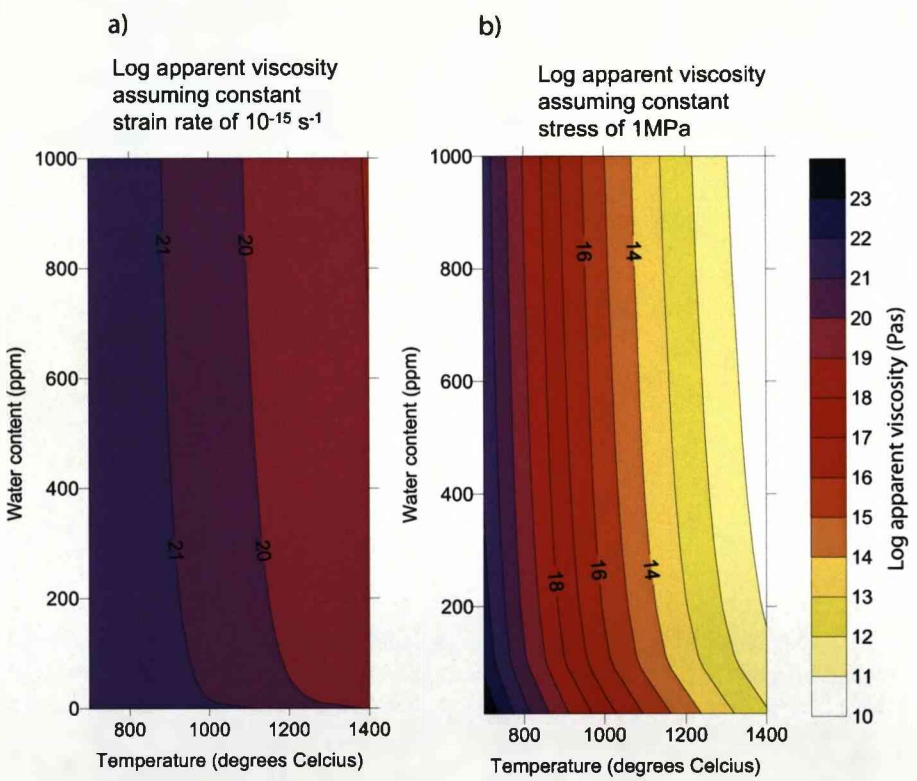

Figure 11.4: Effect of water-content and temperature on viscosity. (a) Log apparent viscosity (Pas) calculated for dislocation creep at constant strain rate of $\dot{\epsilon}$=10^{-15}s^{-1} at a depth of 80km. (b) Log apparent viscosity (Pas) calculated for dislocation creep at constant deviatoric stress of 1MPa at a depth of 80km.

mantle, this occurs at around 2.5% melting. For a constant strain rate, an initial water-content of 1000ppm results in a viscosity difference between 'wet' and 'dry' mantle of around one order of magnitude; for a constant deviatoric stress, an initial water-content of 1000ppm results in a viscosity difference between 'wet' and 'dry' mantle of around 2.5 orders of magnitude (Figure 11.4). Although a water-content of 1000ppm is within the limits of the storage capacity of the mantle (Hauri et al., 2006), it is much higher than that of average mantle (Hirth and Kohlstedt, 1996; Workman and Hart, 2005). The high water-content and high percentage of wet-melting were chosen so that the effects of wet melting in the lithosphere could be maximised. Figure 11.4 illustrates the effect of water-content on the apparent viscosity of the mantle, compared to the effect of temperature, calculated using the above equations. Even a small amount of water can significantly reduce the viscosity of the lithosphere, and Figure 11.4 suggests that water-content heterogeneities may have a bigger effect on lateral viscosity contrasts than temperature variations, particularly where dry mantle is close to damp or wet mantle. It is worth noting that the models presented here assume a non-linear rheology, and so the influence of dehydration on the viscosity may differ in detail to the influence of dehydration assumed by Braun et al. (2000) and Nielsen and Hopper (2004), who both assumed a linear rheology where complete dehydration (at 2% melting) caused a viscosity increase of two orders of magnitude.

In the first set of models, the initial water-content of the continental lithosphere is assumed to be homogeneous. In the second set of models, the initial water-content of the continental lithosphere is assumed to be heterogeneous. A column of the lithosphere is assumed to have a high water-content whilst the remainder of the continental lithosphere is assumed to be dry. Heterogeneities are envisaged to occur either during continental accretion or due to refertilisation caused by subduction. The asthenospheric mantle (defined as having an initial depth greater than 125km) is assumed to have a high water-content. This results in an initial viscosity and melt-fertility heterogeneity in the continental mantle (Figure 11.1b). The viscosity of the initially wet regions increases with depletion, as described above. The width and the water-content of the

heterogeneity and the extension velocity were varied in order to investigate the effect of these variables on the development of the model.

11.2.7 Calculation of thinning factors

The prediction of depth-dependent thinning is assessed by calculating thinning factors for the upper crust, the whole crust and the whole continental lithosphere. The initial thickness of each of these layers is assumed to be at 10km, 40km and 125km respectively. Thinning factors (γ) for each of the layers are calculated in the axial region using the following equation:

$$\gamma = 1 - 1/\beta \tag{11.20}$$

where β is the stretching factor which is calculated by

$$\beta = \frac{initial\ thickness}{present\ thickness} \tag{11.21}$$

For example if the whole crustal thickness in the axis of the model was 20km at a given time, then the stretching factor (β) would be 2 and the thinning factor (γ) 0.5.

11.2.8 Clarification of adaptations made to the model

This model was adapted from the model presented by Braun et al. (2000) in the following ways:

1. The velocity boundary conditions were altered. It is assumed that continental breakup is driven by far-field extensional forces and a constant horizontal velocity condition was imposed on the far boundary of the model. Two different top boundary conditions are investigated in this chapter, both allow thinning of the upper crust to occur over a wider area than allowed for the model of seafloor spreading of Braun et al. (2000). In the model of Braun et al. (2000), surface extension occurred within ~4km of the axis. In this model the surface extension can occur across a much wider area. This reflects the observation that rift basins typically exhibit extension over a width of more than 50km (e.g. Ziegler

and Cloetingh, 2004), in contrast to mid-ocean ridges where extension typically focuses into a zone less than 5km wide (e.g. Macdonald, 1982; Purdy and Detrick, 1986). In the first set of models, surface extension is accommodated within an axial zone which has a half-width of 50km. In the second set of models, surface extension may be accommodated across the whole width of the model.

2. The initial temperature profile is an error function profile which does not vary laterally. The temperature profile approximates lithosphere with a thermal age of 55Ma. The temperature profile was chosen so that no melting is initially predicted but, where the mantle is 'wet', only a small amount of extension is required to induce melting. In addition, radiogenic heating is assumed to occur in the upper continental crust.

3. The continental crust (assumed to be initially 40km thick) is less dense than the mantle. In addition, the lower crust (between 15km and 40km at time=0) has a viscosity two orders of magnitude weaker than olivine, which was chosen to approximate the viscosity of weak lower crust.

4. The rheology is non-linear, with a stress exponent of n=3.5. The rheology of the model in Braun et al. (2000) was linear (n=1). To this end, the viscosity calculation has been modified from that which is presented in Braun et al. (2000). The relative influence of temperature, melt and water-content on apparent viscosity is now dependent on the strain rate and stress fields.

11.3 Results 1: Continental lithosphere thinning - strain localisation caused by a surface velocity condition

11.3.1 Boundary conditions

In this section the continental and asthenospheric mantle are assumed to be initially homogeneous, with the rheology of wet olivine with a water-content of 1000ppm. Strain localisation during continental breakup is induced by a velocity condition at the surface

of the model. Surface extension is accommodated within an axial region that has a width of 100km (half-width of 50km). The accommodation of strain in the lower crust and lithospheric mantle depends on the evolution of the temperature and viscosity fields, and the magnitude of thermal and melt buoyancy forces. The role of buoyancy in the development of small-scale convective instabilities is demonstrated in this section, and the influence of melting on the progression of thinning in the lithosphere is investigated.

11.3.2 The role of buoyancy in small-scale convection induction in the continental lithosphere

Buoyancy forces in the lithosphere arise from density gradients caused by temperature gradients or the presence of melt. The effect of buoyancy on the deformation of the lithosphere depends on the magnitude of the density gradients and the viscosity of the material through which the buoyant material is trying to move (see Equation 11.3). Figure 11.5 shows the evolution of the temperature field and lithospheric geometry of three model of the continental lithosphere extending at a half-extension rate of 3mm/yr with a surface deformation zone 100km wide. Each model has a different scaling viscosity. In these models the viscosity is temperature and pressure dependent and only thermal buoyancy is considered (i.e. the buoyancy and viscosity effects of melting are not included in the viscosity calculation in these examples).

In Figure 11.6 axial thinning factors, equivalent melt thickness and the ratio between maximum upwelling velocity to the extensional velocity are plotted as a function of time. Observations from the Faroe-Shetland basin (Chapters 3-6 and 10 of this thesis)

Figure 11.5 *(following page)*: Evolution of lithospheric layers and temperature for 'top-driven' rift models (extensional half-velocity of 3mm/yr) for various scaling viscosities. Black lines are flow lines. Strain localisation occurs due to the surface velocity condition (boundary conditions are shown in Figure 11.1a). The effect of thermal buoyancy is included in these calculations, but the buoyancy and viscosity effects of melting are not. In each case the upper panels show the evolution of the rift basin or rifted margin geometry, and the lower panel shows the evolution of the temperature field. Axial thinning factors, maximum upwelling velocity and predicted equivalent melt thickness shown in Figure 11.6. Note that time-steps are calculated dynamically and so are different for each model run.

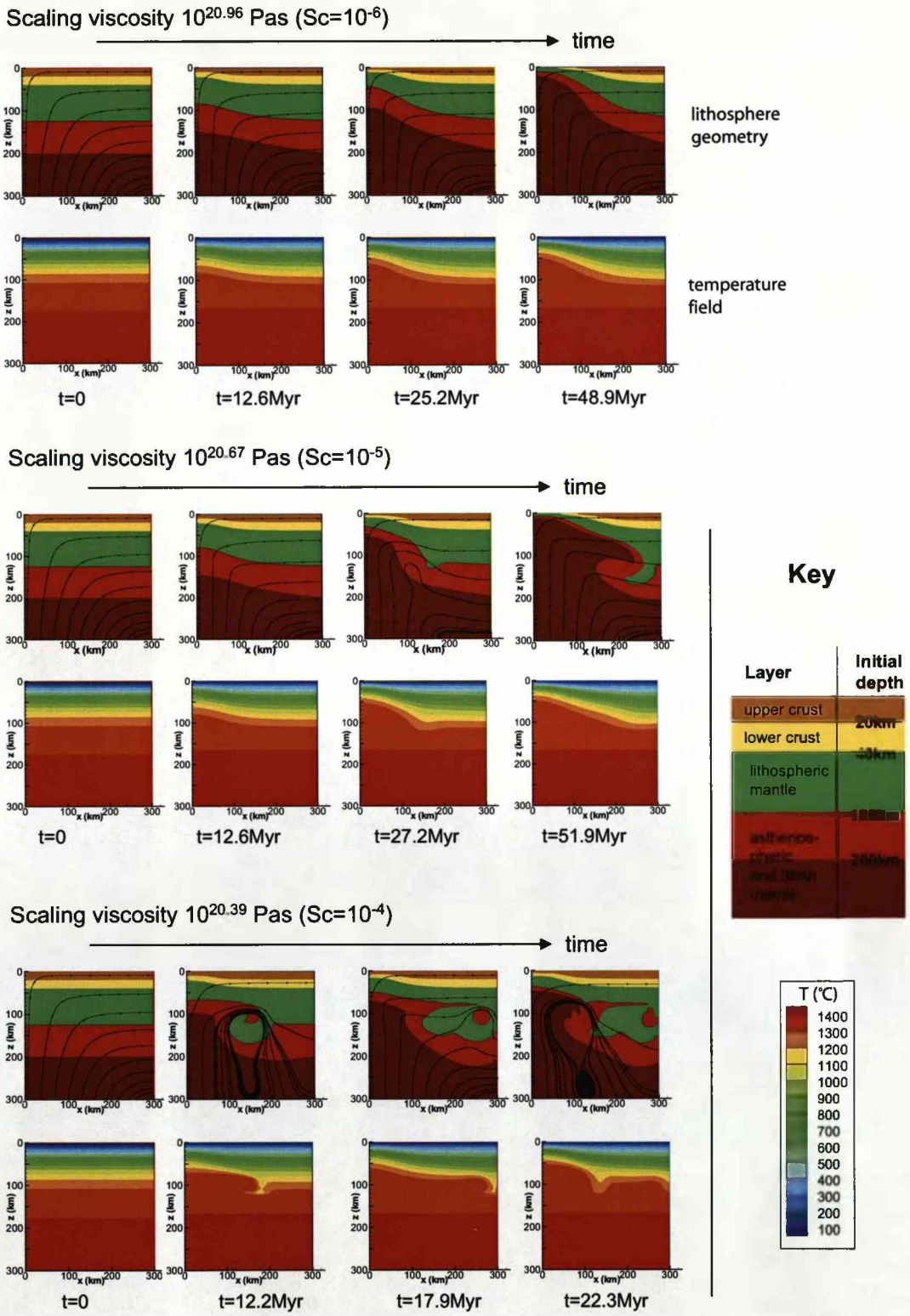
Scaling viscosity $10^{20.96}$ Pas (Sc=10^{-6})
time
lithosphere geometry
temperature field
t=0
t=12.6Myr
t=25.2Myr
t=48.9Myr
Scaling viscosity $10^{20.67}$ Pas (Sc=10^{-5})
time
t=0
t=12.6Myr
t=27.2Myr
t=51.9Myr
Scaling viscosity $10^{20.39}$ Pas (Sc=10^{-4})
time
t=0
t=12.2Myr
t=17.9Myr
t=22.3Myr
Key
Layer
Initial depth
upper crust
20km
lower crust
lithospheric mantle
T (°C)
1400
1300
1200
1100
1000
900
800
700
600
500
400
300
200
100

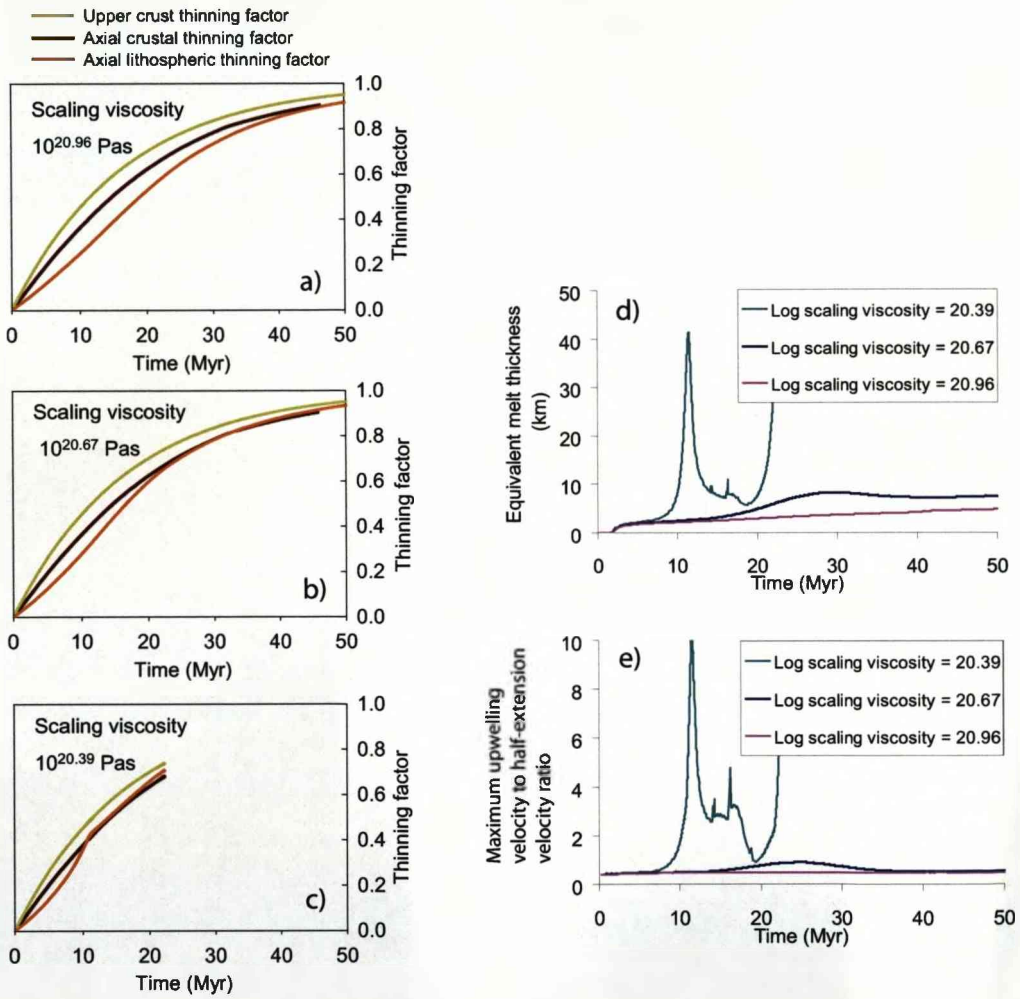

Figure 11.6: (**a-c**) Axial thinning factors, (**d**) predicted equivalent melt thickness and (**e**) maximum upwelling velocity to extension velocity ratio for 'top-driven' models shown in Figure 11.5.

suggest that preferential lithospheric thinning occurs along the rift axis of propagating or incipient rift tips prior to continental rupture. A focus of this work is to determine the driving forces and causes of processes which preferentially thin the upper lithosphere and lower crust along the axis of a rifting prior to continental breakup. Axial thinning factor plots will therefore illustrate if this can occur in a given model. Chapters 7 and 8 discussed the effect of the upwelling velocity to half-extensional velocity ratio during continental breakup on the resulting margin structure. If a transient small-scale convection event occurs then this would be reflected in a peak in the upwelling velocity to half-extensional velocity ratio plot. If this small-scale convection event occurs within the region of melting then a peak in the equivalent melt thickness plot would also be expected.

At a high scaling viscosity ($10^{20.96}$Pas, Sc=10^{-6}), the effect of buoyancy is suppressed as the buoyancy forces are low compared to the resistive viscous forces. Upper crustal thinning is forced to occur within the prescribed half-width, whilst the lower lithosphere deforms over a wider area. The plot of axial thinning factors against time (Figure 11.6a) shows that thinning of the upper crust exceeds that of the whole lithosphere for the duration of the model.

When the scaling viscosity is decreased, the upwards thermal buoyancy forces exert a greater control on the deformation of the lithosphere. At a scaling viscosity of $10^{20.67}$Pas (Sc=10^{-5}), the maximum upwelling velocity increases until around 25Myr as the magnitude of thermal buoyancy increases (Figure 11.6e). After 25Myr the maximum upwelling velocity decreases as the thermal perturbation becomes wider and lateral buoyancy and viscosity gradients are reduced. A peak in melt production is associated with the increased upwelling (Figure 11.6d). The increased upwelling velocity and melt production is the signature of small-scale convection in the lower lithosphere.

At an even lower scaling viscosity of $10^{20.39}$ (Sc=10^{-4}), buoyancy forces dominate the flowfield, and a vigorous small-scale convective cell is induced below around 90km. This convective cell migrates laterally beneath the higher viscosity lid, driven by lateral density variations until it reaches the edge of the model space (in Figure 11.5 this

occurred between 12.2 and 17.9Myr), after which time another convection cell initiates underneath the axis. A high degree of time-dependence is a feature of low-viscosity models which include buoyancy forces in their calculation (e.g. Nielsen and Hopper, 2004) as buoyancy forces are high with respect to viscous resistive forces. However, such time-dependent flow is usually considered unrealistic for the present-day Earth. The low-scaling viscosity model in Figure 11.5 predicts a wave of lithospheric thinning (and therefore uplift) away from the rift axis which is not generally observed. The flowfield predicted by the model is also significantly influenced by the lateral and vertical boundary conditions of the model and so cannot be meaningfully interpreted.

Axial thinning factor plots (Figure 11.6) show that lithospheric thinning in the axis of the models shown in Fgure 11.5 is less than that of the upper crust, even at low scaling viscosities. This is because the depth to which small-scale convection reaches is limited by the relatively high viscosity top-most mantle and crustal lid, and thinning of the upper part of the lithospheric mantle does not occur. The small-scale convection predicted by these models resulted in preferential thinning of the lithosphere off-axis (e.g. at a horizontal coordinate of around 200km at 51.9Myr for the model shown in Figure 11.5 with a scaling viscosity of $10^{20.67}$). However, observations from the Faroe-Shetland basin (Chapters 3-6) and from the Nam Con Son basin (Clift et al., 2001) suggest that preferential lithospheric thinning occurs along the rift axis of the propagating incipient rift tips. A focus of this work is to determine the driving forces and causes of processes which preferentially thin the upper lithosphere and lower crust along the axis of a rifting prior to continental breakup. In the next section the effects of melting on the development of the model are included in the calculation in order to assess whether the viscosity reduction and the increase in buoyancy forces associated with the presence of melt can induce small-scale convection in the upper continental mantle and lower crust.

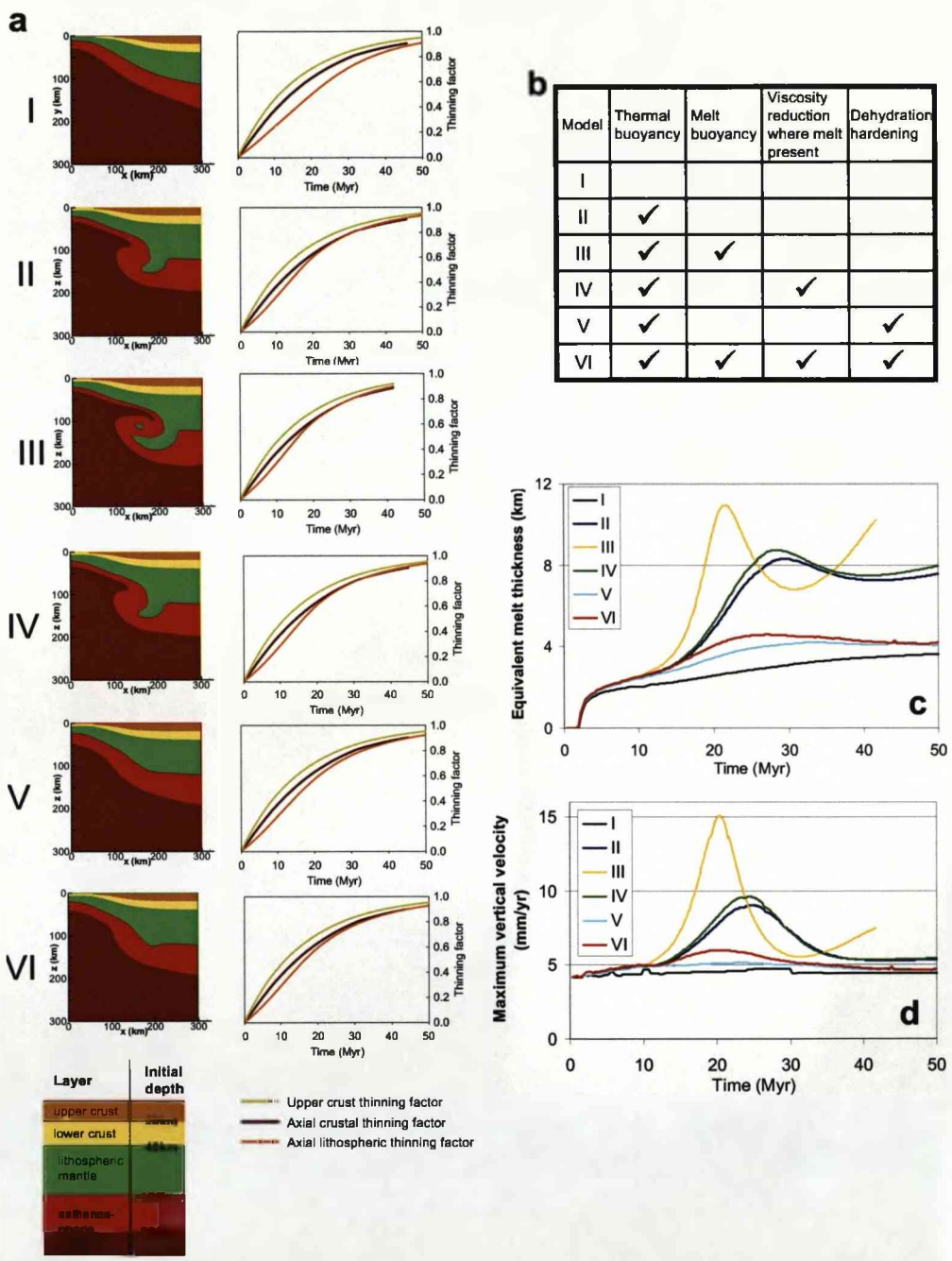

Model	Thermal buoyancy	Melt buoyancy	Viscosity reduction where melt present	Dehydration hardening
I				
II	✓			
III	✓	✓		
IV	✓		✓	
V	✓			✓
VI	✓	✓	✓	✓

Figure 11.7: The effect of thermal buoyancy and melting on continental lithosphere thinning. Models were run with a half-extension velocity of 3mm/yr. (**a**) Lithospheric geometry after ~100km extension. These show the relative influence of thermal buoyancy, melt buoyancy, viscosity reductions due to the presence of melt and viscosity increases due to dehydration on the resulting lithospheric geometry. The table (**b**) shows which effects were included in each model. (**c**) The maximum upwelling velocity and (**d**) equivalent melt thickness predicted by each of the models as a function of time.

11.3.3 The effect of melting on small-scale convection in the continental lithosphere during rifting

Partial melting affects the mantle viscosity and buoyancy forces in the mantle in three important ways:

1. The presence of melt and of depleted mantle enhances buoyancy forces because both melt and depleted mantle have a lower density than undepleted mantle.

2. The presence of melt reduces the viscosity of the mantle (Hirth and Kohlstedt, 1995).

3. The removal of water during melting increases the viscosity of depleted mantle (Karato, 1986; Hirth and Kohlstedt, 1996). This is termed dehydration hardening.

To assess the influence of each of these effects on the initiation of small-scale convection in the continental lithosphere, the effects of thermal buoyancy and melting are added separately to the model. The resulting lithospheric geometries after 100km half-extension (200km total extension) are shown for six different models in Figure 11.7. Each of the models has a different subset of the various effects of buoyancy and melting switched on. The maximum upwelling velocity and equivalent melt thicknesses are also plotted for each of the models. A scaling viscosity of $10^{20.67}$ is assumed, which was shown in Figure 11.5 to be low enough that (a relatively minor) small-scale convection may occur during thinning, but not too low so that the model evolution is influenced by the dimensions of the model.

In Model **I**, no buoyancy or melt effects are included in the calculation and no small scale convective event is induced. When thermal buoyancy is included in the calculations (Model **II**, which is also the model shown in Figure 11.5 with a scaling viscosity of $10^{20.67}$Pas), enhanced upwelling peaks at around 25Myr, and melt production at around 28Myr. When melt buoyancy is also included (Model **III**), the enhanced upwelling velocity ratio and maximum melt production occurs earlier and with an increased magnitude. However, the enhanced upwelling (small-scale convection) does not occur significantly shallower within the continental lithosphere and thinning of the

lithosphere at the axis still does not exceed thinning of the upper crust. The inclusion of a viscosity reduction where melt is present in the calculation (Model **IV**) also increases the maximum upwelling velocity, although the effect of a viscosity reduction where melt is present is less than the effect of the inclusion of melt buoyancy in the model. When dehydration hardening (Equation 11.19) is included in the calculation (Model **V**), the small-scale convection event is significantly suppressed. If thermal buoyancy and all of the effects of melting (buoyancy and viscosity effects) are included (Model **VI**), there is still a peak in upwelling velocity, which occurs at around 19 Myr, and a peak in melt production which occurs at around 24Myr. This result differs from the findings of Nielsen and Hopper (2004), who showed that whilst the presence of melt enhances upwelling and therefore syn-breakup small-scale convection, dehydration hardening almost completely suppresses the buoyant upwelling. In their models, no enhanced melt thicknesses are predicted unless a finite sub-lithospheric thermal anomaly is present. In this work a non-linear olivine rheology is used; Nielsen and Hopper (2004) used a linear rheology and so the effect on viscosity of melting and associated dehydration differ between the models. The use of the non-linear rheology may explain why, in this work, a (small) pulse of volcanism and small-scale convection is predicted during continental thinning in these models without the presence of a sub-lithospheric thermal anomaly.

For Model **VI** (in which all of the thermal buoyancy and melt effects are included), a plot of thinning factor across the resulting margin structure (after ~100km of half-extension) is shown in Figure 11.8. Beneath the flanks of the margin the small-scale convection event has preferentially thinned the lithospheric mantle with respect to the upper crust. However, at the axis, thinning of the lithospheric mantle never exceeds that of the upper crust (Figure 11.7). Wet melting in the lower lithosphere during continental lithospheric thinning can induce some small-scale convection, but the depth of this convection cell is limited by a high viscosity lid and so cannot explain depth-dependent stretching (preferential lithospheric thinning with respect to the upper crust) in the axis of propagating rift tips.

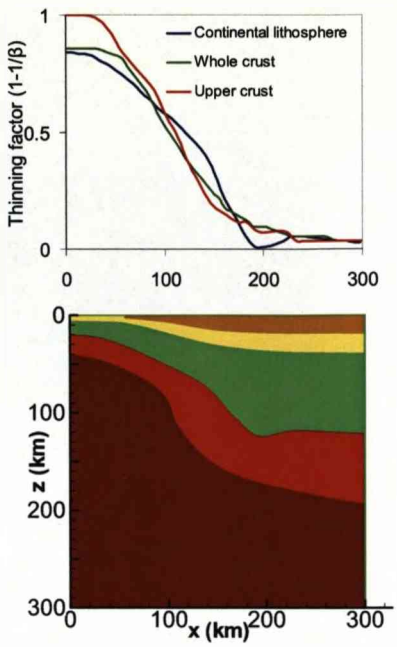

Figure 11.8: Lithospheric thinning factors across a modelled rifted margin. Upper crustal, whole crustal and whole lithosphere thinning factors across model **VI** after ~100km half-extension as a function of distance.

11.3.4 Summary of Results 1

In the models described in this section, strain focussing occurs due to a surface velocity condition: extension in the upper crust was accommodated within a region of fixed width (this condition is used as a proxy for an upper crustal heterogeneity). This condition caused thinning of the lower lithosphere beneath this upper crustal heterogeneity, initially over a broader area. The models show that thermal and melt buoyancy and the effects of melting on viscosity can cause a period of small-scale convection and enhanced upwelling to occur beneath the axial region during continental lithospheric thinning. The enhanced upwelling, which is caused by lateral density gradients, is suppressed as extension and thinning proceed and the thermal and melt perturbation becomes wider. The small-scale convection event may be an inherent part of the rifting process, and is able to predict a (small) pulse of enhanced volcanism without the presence of a thermal heterogeneity.

Small-scale convection in the lower continental lithospheric mantle did result in preferential lithospheric thinning (with respect to upper crustal thinning) on the flanks of the thinned region. However, the models presented in this section do not predict preferential lithospheric and lower crustal thinning in the axis of the rift. Although melting in the models initiated soon after the onset of extension (~2Myr), the maximum upwelling velocity did not occur until 19Myr (after 57km of half-extension, corresponding to stretching factors in the weak zone of the upper crust of more than 3), and the small-scale convection was limited below a relatively high viscosity lid in the lower lithospheric mantle.

The models described in this section are 'top-driven', the rift location was determined by a surface velocity condition. In the next section the potential implications of a strength heterogeneity in the continental mantle on the development of small-scale convection and preferential lithospheric thinning are investigated, to determine whether such heterogeneities may explain observations of depth-dependent stretching at rifted continental margins and propagating rift tips. The viscosity (and strength) profile of the continental lithosphere is dependent on a number of factors, including its thermotectonic age, composition, crustal and lithospheric thickness and previous rifting or continental collision history (e.g. Ziegler and Cloetingh, 2004). In the next section the continental lithosphere weakness is assumed to be a water-content heterogeneity.

11.4 Results 2. Continental lithosphere thinning - the role of compositional heterogeneities in inducing small-scale convection during continental thinning

11.4.1 Initial setup and boundary conditions

In this section the effect of compositional (water-content) heterogeneities in the continental lithosphere on thinning processes is investigated. Water-content heterogeneities are envisaged to occur in the continental lithosphere during continental accretion of heterogeneous mantle, and by refertilisation of the mantle wedge during subduction.

Heterogeneities (pre-existing structures and thickness variations) have previously been shown to influence deformation in the continental lithosphere (King and Anderson, 1995; Vauchez et al., 1997, 1998; Corti et al., 2003), and furthermore, a number of rifts are thought to occur at, or close to lithospheric-scale boundaries or ancient sutures (e.g. the North Atlantic (Wilson, 1966), the Iberian-Newfoundland conjugate margins (Muntener and Manatschal, 2006), the Main Ethiopian Rift (Cornwell, 2008)).

In the models described in this section, areas of 'wet' (high water-content) and 'dry' (low water-content) mantle were defined on the initial grid (see Figure 11.1b), and advected according to the velocity field. The viscosity of the wet and dry areas evolved according to Equation 11.17 so that if the 'wet' regions partially melt, the viscosity can increase up to that defined for 'dry' mantle. The calculation of melt fraction for wet and dry regions are calculated as described by Equations 11.10 and 11.11 respectively. The model is driven by a constant velocity condition on the right-hand side of the model, although, in contrast to the models described in the previous section, no horizontal velocity condition is imposed on the upper surface of the model (see Figure 11.1). Consequentially strain localisation occurs as a result of the water-content heterogeneity. The initial temperature structure is the same as described for the previous model.

An example of the evolution of a model with an initial water-content heterogeneity is shown in Figure 11.9. The continental lithosphere is assumed to be initially 'dry' except for within a zone 100km wide (50km half-width), where it has a water-content of 1000ppm. The asthenospheric mantle is also assumed to be 'wet'. The 'wet' zone is consequentially initially weaker than the 'dry' lithosphere.

As extension begins (at a half-extension rate of 3mm/yr), strain accommodation occurs preferentially within the 'wet' zone in the lower lithosphere, but is distributed across the whole model at the level of the upper crust. As a consequence lithospheric thinning is depth-dependent: preferential axial lower lithosphere thinning occurs in the wet zone. As thermal and melt buoyancy forces increase within the zone of thinning the maximum upwelling velocity increases and an enhanced upwelling small-scale convection event may initiate, amplifying the depth-dependent stretching and causing a period of

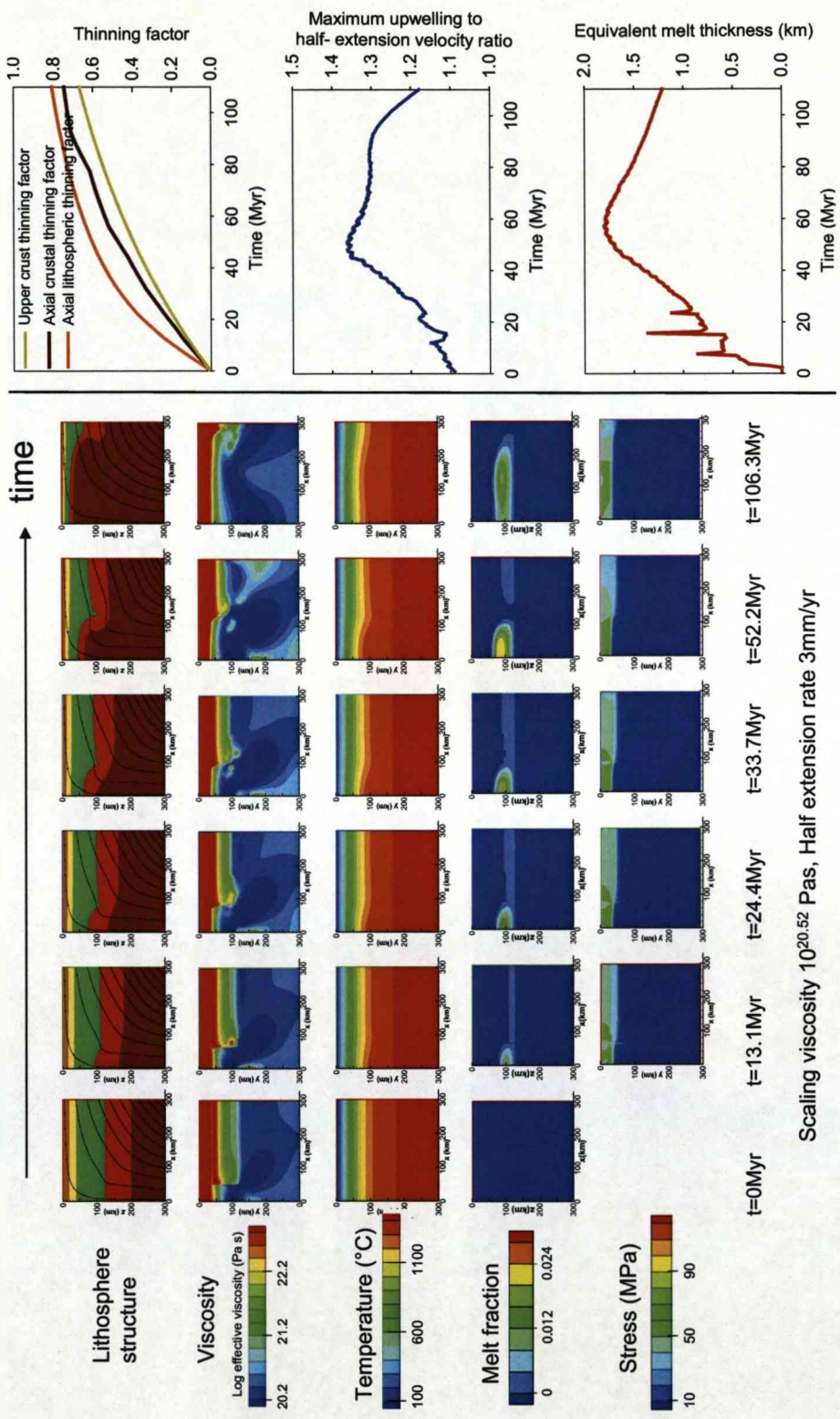

Figure 11.9: Evolution of rifting initiated at a water-content heterogeneity. Axial thinning factors, maximum upwelling velocity and equivalent melt thickness through time also shown.

enhanced melt production. The small-scale convection is limited by the width of the heterogeneity, and flow becomes more passive (and the maximum upwelling velocity to half-extension velocity reduces) as viscosity and buoyancy gradients are reduced. In the example shown in Figure 11.9 the maximum upwelling velocity to half spreading velocity ratio occurs at around 50Myr, after half-extension of 150km (total extension of 300km). Peak melt production occurs after around 55Myr (165km half-extension or 330km total extension). These values of extension are relatively high compared with measurements of total upper crustal extension at continental margins, and very high compared with the amount of upper crustal extension which is thought to accompany depth-dependent stretching at propagating rifts and failed breakup basins. For example the FSB experienced depth-dependent stretching, where the continental lithosphere and lower crust were thinned significantly more than the upper crust, with very minor upper crustal extension (less than a few tens of km), and in a much shorter time than is predicted by this model. However, the timing and magnitude and depth of the small-scale convection and the resulting deformation history are likely to be dependent on the values used in each of the governing equations, as well as on the equations used and relationships which have been assumed. The effect of the scaling viscosity, the extension velocity and the width and magnitude of the water-content heterogeneity on the timing and magnitude of small-scale convection events are discussed further here, although this list of variables is not exhaustive.

The timing and magnitude of the maximum upwelling velocity and peak melt production is dependent on the scaling viscosity of the model (Figure 11.10). A scaling viscosity of $20^{20.52}$ is used for the remainder of these tests, low enough that small-scale convection can occur but not too low that the system becomes unstable.

For the model shown in Figure 11.9 the locus of thinning migrates laterally as small-scale convection is strongest where there is a viscosity contrast close to the edge of the heterogeneity (cf. King and Anderson, 1995). Although the model is symmetric, in the Earth any heterogeneity is likely to be asymmetric, and so the migration of the locus of thinning towards a heterogeneity boundary may partially explain the asymmetry which

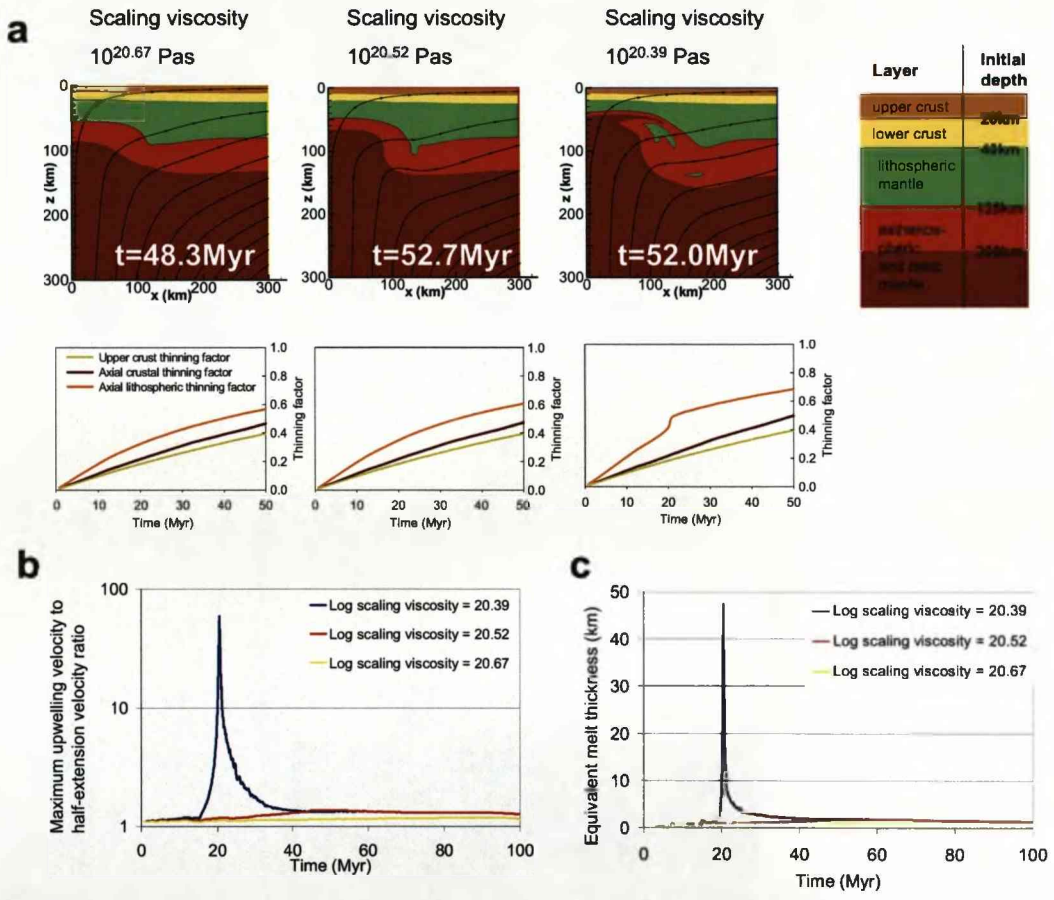

Figure 11.10: Dependence on scaling viscosity of the evolution of rifting at a water-content heterogeneity. (**a**) Lithospheric geometry shown after approx 150km half-extension and axial thinning factors through time calculated for various scaling viscosities. Each model was driven by a constant velocity boundary condition (3mm/yr). Maximum upwelling velocity to half-extension velocity ratio (**b**) and equivalent melt thickness (**c**) through time also shown.

is observed at some margins.

In the models presented in this section, a maximum viscosity criterion is used for the upper lithosphere and crust, and extension is generally distributed evenly across the top of the model. However, this condition means that strain does not localise in the upper lithosphere, and consequentially the lithosphere does not reach a point of 'rupture' (commonly defined by a critical thinning factor, which is usually localised). In the Earth, the upper crust deforms by brittle deformation. Brittle faulting in the upper crust occurs when stress exceeds the maximum stress defined by the Byerlee criteria (Byerlee, 1978), and can be approximated numerically by iteratively reducing the viscosity in the upper crust so that this stress is not exceeded (e.g. Chen and Morgan, 1990; Pérez-Gussinyé et al., 2006). Deformation in the lower lithosphere may increase stresses in the upper crust to the point of rupture. Unfortunately the code used in this chapter became unstable when the Byerlee criteria was included.

Nevertheless, plots of stress (e.g. in Figure 11.9) indicate where stresses in the crust may become high enough that brittle failure would occur. For the model shown in Figure 11.9, high stresses are induced above the region of enhanced upwelling. As extension continues, the maximum upper crustal stress migrates along the surface of the model (above the locus of thinning) close to the viscosity discontinuity. Brittle faulting in the regions of high upper crustal stress may cause focused thinning of the crust, further weakening and eventually rupture of the crust. The stress fields calculated for the model in Figure 11.9 suggest that if crustal rupture occurs during small-scale convection the resulting margin will be approximately symmetric, whilst if crustal rupture occurs later than around 50Myr, rupture may not occur at the axis but approximately above the lateral heterogeneity and the margins may be asymmetric. Further development of the model to include brittle failure is required to test these ideas.

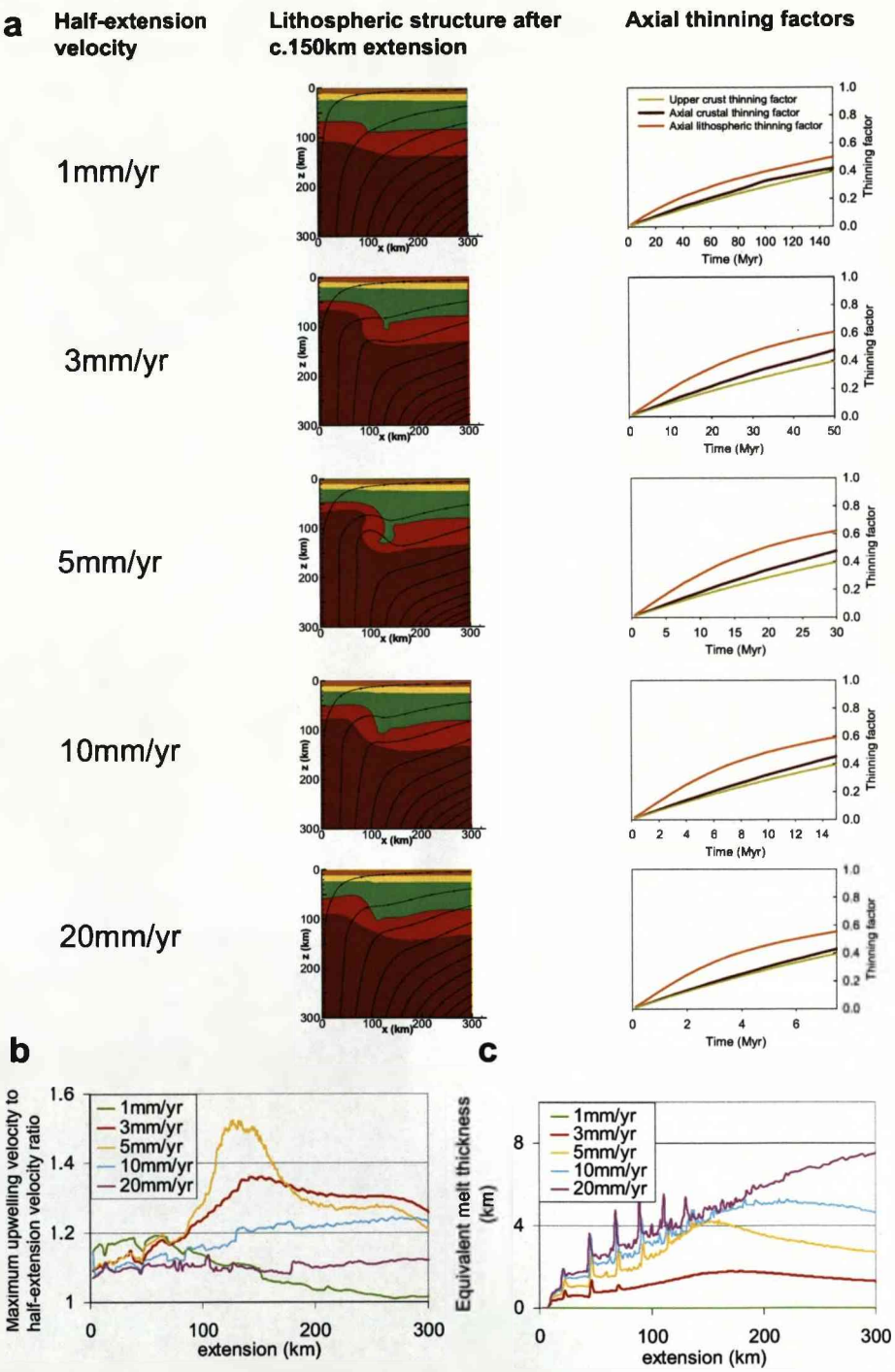

Figure 11.11: Rifting at a water-content heterogeneity - dependence on half-extension rate. (**a**) Lithospheric geometry shown after approx 150km half-extension, and axial thinning factors through time for various half-extension rates. Maximum upwelling velocity: half-extension rate (**b**) and equivalent melt thickness (**c**) through time also shown.

11.4.2 Sensitivity of continental lithospheric thinning to half-extension velocity

The example model shown in Figure 11.9 was repeated for a variety of extension velocities. The lithospheric geometry after around 150km of half-extension, and thinning factors, maximum upwelling velocity to half-extension velocity ratio and melt production through time is plotted in Figure 11.11. At a half-extension velocity of 1mm/yr, thinning still preferentially occurs within the weak zone, but conductive cooling suppresses the thermal perturbation associated with thinning, no melting is predicted, and buoyancy forces are low. At 1mm/yr the water-content heterogeneity does not induce enhanced upwelling or small-scale convection. As the half-extension velocity is increased up to 5mm/yr, feedback between preferential lithospheric thinning, thermal and melt buoyancy causes an increase in the maximum upwelling velocity, and a small-scale convection event occurs. For half-spreading rates of 10mm/yr and 20mm/yr, thinning of the lithosphere preferentially occurs in the axis of the weakened zone, but no high velocity ratio or melt thickness peak occurs. In these models enhanced upwelling and an early melt production peak therefore seems to be most likely to occur at relatively slow half-spreading rates of around 3-5mm/yr. Braun et al. (2000) showed that enhanced upwelling beneath mid-ocean ridges was greatest at slow-spreading rates, as the effect of melt buoyancy from deep melting had the greatest relative effect on lateral buoyancy force gradients. A similar explanation may apply here.

Figure 11.12 *(following page)*: Rifting at a water-content heterogeneity - dependence on concentration of water. (**a**) Lithospheric geometry shown after approx 150km half-extension, and axial thinning factors through time for models run with various water-contents. In each case the viscosity of the 'wet' mantle and lithosphere is the same, but the viscosity of the 'dry' region varies. $\Delta\mu^*$ denotes the difference in viscosity at the base of the lithosphere. However in each case the 'wet' region is also more fertile. For the model where the water-content heterogeneity is 0ppm, there is still a melt-fertility heterogeneity, although the effect of this does not localise thinning on its own. For melt production calculations for the 'wet' and 'dry' regions see Equations 11.10 and 11.11. (**b**) Maximum upwelling velocity and (**c**) and equivalent melt thickness through time.

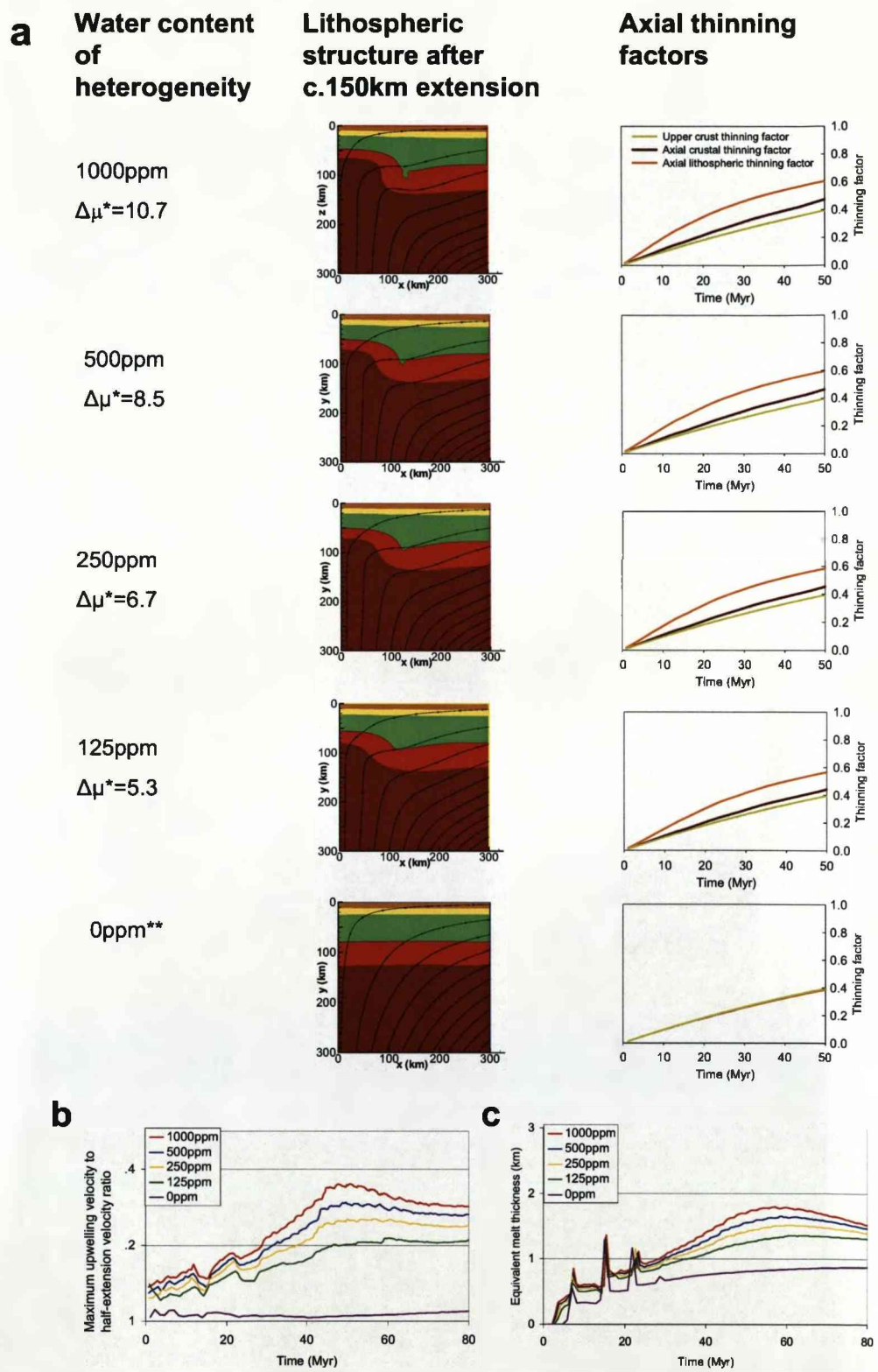
a
Water content of heterogeneity
Lithospheric structure after c.150km extension
Axial thinning factors
1000ppm
Δμ*=10.7
500ppm
Δμ*=8.5
250ppm
Δμ*=6.7
125ppm
Δμ*=5.3
0ppm**
Upper crust thinning factor
Axial crustal thinning factor
Axial lithospheric thinning factor
Thinning factor
Time (Myr)
z (km)
y (km)
x (km)
b
Maximum upwelling velocity to half-extension velocity ratio
c
Equivalent melt thickness (km)
1000ppm
500ppm
250ppm
125ppm
0ppm

11.4.3 Sensitivity of continental lithospheric thinning to magnitude of water-content heterogeneity

In the model presented above, the water-content of the 'wet' region in the continental lithosphere was very high (1000ppm). A high water-content was chosen in order to maximise the melting and water-effects on the model. The model has been repeated for water-content heterogeneities of 500ppm, 250ppm and 125ppm. Figure 11.12 shows the lithospheric geometry after around 150km of half-extension, axial thinning factors, ratio of maximum upwelling velocity ratio and equivalent melt thickness for these models. The viscosity of the wet region is scaled so that the initial viscosity of the wet region is the same for each model, but the contrast in viscosity between 'wet' and 'dry' lithosphere is varied. The wet and dry solidii and melt production calculations are not changed. Additionally, the results of a model run with no water-content heterogeneity ('0ppm') is also shown; the initial viscosity of this model does not vary laterally. However in this model the axial region (50km half-width) has the melting properties of wet mantle, whilst the rest of the model has the melting properties of dry mantle. The model deforms by evenly distributed pure-shear; the increase in buoyancy forces associated with wet melting within this heterogeneity are insufficient to localise extension. The model demonstrate that lithospheric deformation occurs by evenly distributed pure-shear in the absence of a viscosity heterogeneity.

A peak in the maximum upwelling velocity and melt production, indicative of a small-scale convection event, is predicted even when the water-content heterogeneity is as low as 125ppm. The extent of preferential lithospheric thinning increases with the magnitude of the water-content heterogeneity, as the magnitude of the water-content heterogeneity determines the magnitude of the viscosity contrast, which enables small-scale convection to occur. As the magnitude of the water-content heterogeneity is increased, the small-scale convection also occurs to a shallower depth, and therefore more melt is produced during the small-scale convection.

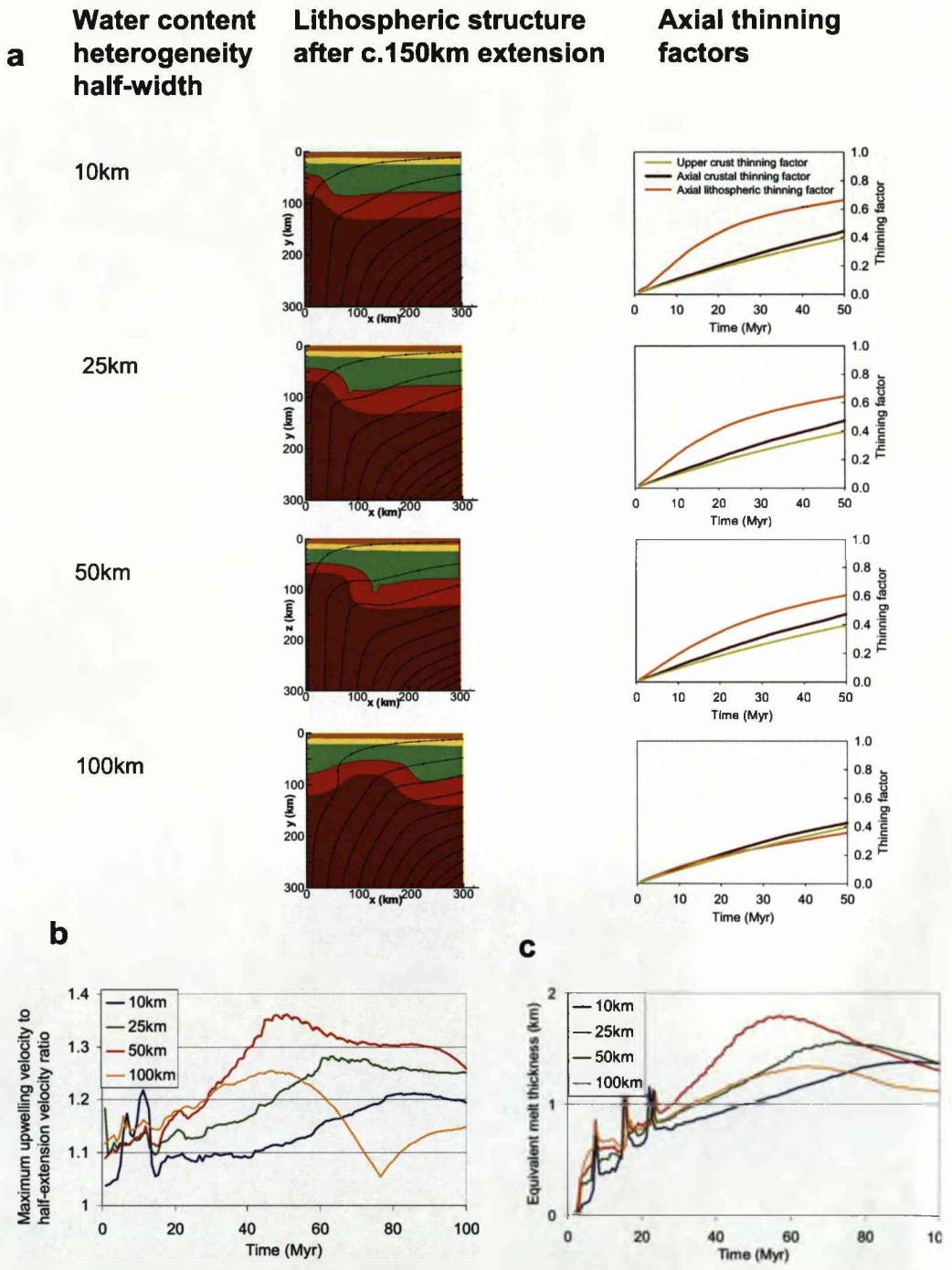

Figure 11.13: Rifting at a water-content heterogeneity - dependence on the half-width of the heterogeneity. (**a**) Lithospheric geometry shown after approx 150km half-extension, and axial thinning factors for various width heterogeneities. (**b**) Maximum upwelling velocity to half-extension rate rate and (**c**) equivalent melt thickness predicted by each of the models.

11.4.4 Sensitivity of continental lithospheric thinning to width of water-content heterogeneity

A series of models were run to assess the effect on model evolution of the width of a water-content heterogeneity. In Figure 11.13 model geometry is shown after 150km of extension for models with heterogeneities with half-widths of 10km, 25km, 50km and 100km. The axial thinning factors show that even when the heterogeneity is only 20km wide (10km half-width), significant preferential thinning occurs within the wet, weak zone, and a peak in the maximum upwelling velocity occurs after around 80Myr. As the width of the heterogeneity is increased up to 100km (50km half-width), the maximum upwelling velocity in the model increases, and occurs earlier in the model development, reflecting an increase in the vigour of small-scale convection. For the model run with a heterogeneity width of 200km (half-width 100km), the locus of thinning is off-axis after 150km extension, at the edge of the heterogeneity where the viscosity contrast is greatest. The maximum upwelling velocity to half-extension velocity ratio and the largest peak in melt production occurred for the model with a heterogeneity width of 100km (half-width 50km). This may reflect an optimum wavelength for small-scale convection in the continental lithosphere for the model parameters used in this section.

11.4.5 Summary of Results 2

In this set of models, strain focusing occurred during continental rifting due to a water-content heterogeneity within the continental lithosphere. A transient period of enhanced upwelling and melt production was predicted for many of the models. Enhanced upwelling, preferential lithospheric thinning and melt production was most pronounced when the water-content heterogeneity was large, around 100km in width and the full extension rate was around 10mm/yr.

11.5 Discussion

Observations of rift basins and rifted margins suggest that depth-dependent stretching is an inherent part of continental lithospheric thinning. A number of authors have shown that small-scale convection in the lithospheric mantle during thinning may explain depth-dependent stretching, anomalous melt production and enhanced rift-shoulder uplift (e.g. Keen, 1985; Mutter, 1985; Buck, 1986; Huismans et al., 2001a; van Wijk et al., 2001; Nielsen and Hopper, 2004) at rift basins and at rifted margins. Although positive temperature anomalies can enhance melt production during continental breakup, a number of authors have shown that small-scale convection does not require the presence of temperature anomalies or mantle plumes (e.g. Huismans et al., 2001a; van Wijk et al., 2001); small-scale convection and enhanced thinning and melt production may be initiated due to entirely 'passive' driving forces, as density and viscosity gradients in the lower lithosphere become unstable and induce secondary convection as extensional forces act on the continental lithosphere.

For strain localisation to occur in any model, a heterogeneity is required. In a numerical model a heterogeneity may be introduced as an initial condition within the model space or as a boundary condition. After initial thinning, initiation of small-scale convection requires that buoyancy forces are large compared to the resistive viscous forces. Under certain conditions, a transient period of enhanced upwelling and small-scale convection may begin shortly after the onset of thinning when lateral buoyancy and viscosity are high, and become suppressed as these gradients are reduced as thinning continues.

Few previous models have included the effects of melting on the development of lithospheric thinning. The presence of melt increases buoyancy forces and reduces viscosity which enhance upwelling, although depletion of the mantle increases the viscosity. When compared to a model where only thermal buoyancy forces are considered, including the effects of melting causes the maximum upwelling to occur sooner, although the effects of melting also suppress the magnitude of the upwelling and small-scale convection. However, it should also be remembered that dehydration hardening (which

suppresses the small-scale convection) also stabilises flow as seafloor spreading develops, and reduces the excessive time-dependence of the flow predicted by models where the scaling viscosity is relatively low (Boutilier and Keen, 1999; Nielsen and Hopper, 2004).

In this chapter, two boundary condition-initial condition combinations were applied to the continental lithosphere in order for thinning to localise. In the first models strain was focussed at the surface within a prescribed half-width. In these models a transient period of enhanced upwelling was predicted as an inherent part of the lithospheric thinning process, however, the depth of the small-scale convection was limited by the viscosity of the upper continental mantle. Depth-dependent stretching, where the lithospheric mantle is preferentially thinned with respect to the upper crust was predicted on the flanks of the rift basin, however depth-dependent stretching in the axis of the model (i.e. that which is observed at propagating rift tips and failed breakup basins) was not predicted. These results suggest that the onset of melting alone cannot explain the initiation of small-scale convection and preferential lithospheric thinning.

In the second set of models, strain focusing occurred due to a water-content heterogeneity within the continental lithosphere. The presence of water both weakens (reduces the viscosity) and increases the melt productivity of the lithospheric mantle. No horizontal velocity conditions were imposed on the surface of the model, and consequentially, upper crustal extension was distributed over a wider area than lithospheric thinning, and preferential thinning of the lithospheric mantle was predicted in the axis of the model. A transient period of enhanced upwelling and melt production was also predicted for many of the models. This may be the first time that both preferential lithospheric thinning and enhanced melt production has been predicted by a dynamic numerical model. Enhanced upwelling, lithospheric thinning and melt production were most pronounced when the water-content heterogeneity was large (due to the large lateral viscosity discontinuity), around 100km in width and the full extension rate was around 10mm/yr. The water-content heterogeneity was assumed to take the form of a vertical column of wet mantle juxtaposed against a dry lithosphere. In the Earth, heterogeneities may be

more gradational, and may be more patchy than has been assumed here. The viscosity of the continental lithosphere is also affected by its thermal structure, which may also be laterally variable, due to previous rifting events, the effect of thermal blanketing (if thick radiogenic crust is present), or the presence of mantle plumes.

This work has shown that heterogeneities in the continental lithosphere and crust can influence the development of small-scale convection and preferential lithospheric thinning during rift basin and margin formation. Heterogeneities may also explain the migration or abandonment of rift basins. If thinning of the lower lithosphere can initiate due to the presence of a compositional or thermal weakness, then it is possible that a strong (e.g. depleted) region in the upper lithosphere or lower crust may resist continued extension, allowing the locus of thinning to migrate to a weaker, more fertile region. This explanation is analogous (but alternative) to the idea that rift migration occurs when thinned continental lithosphere has become stronger than unthinned continental lithosphere following a period of cooling (England, 1983; Kusznir and Park, 1987; van Wijk and Cloetingh, 2002). More work is required to assess the likely distribution and magnitude of heterogeneities in the continental lithosphere, and the potential role of inherited heterogeneities in causing rift basin migration and abandonment.

Some of the models presented in this chapter predicted axial lithospheric thinning factors which exceeded those of the upper crust due to small-scale convection in the lithospheric mantle. However, at many rifted margins and in rift basins where depth-dependent stretching is observed, the lower crust appears to have also been preferentially thinned. Small-scale convection in the uppermost continental mantle and lower crust was limited in these models by the viscosity of the upper mantle, lower crustal flow is also resisted by crustal buoyancy. The strength (and therefore viscosity) profile of continental lithosphere is the subject of current debate, particularly the strength of the uppermost continental mantle. Most workers agree that the upper crust and upper mantle are both strong, whilst the lower crust is weak (e.g. Burov and Watts, 2006, and references therein). However, Maggi et al. (2000) show that earthquakes beneath Tibet occur in the lower crust, not in the continental mantle, and Jackson (2002) concludes

that the upper mantle must be relatively weak. A weaker upper mantle could, in these models, allow small-scale convection to thin the upper lithospheric mantle, which may then enhance thinning of the lower crust. To test this would require a change in the initial temperature structure of the model or a change to the calculation of viscosity so that the upper mantle is initially weaker than has been assumed in this work.

A major shortcoming of this work is that the top-most crust and top-most lithospheric mantle are modelled as high viscosity lids. The upper crust deforms by brittle processes, and deformation occurs when stress levels exceed that defined by the Byerlee criteria. Including a condition for brittle deformation in the model may cause thinning to localise at the level of the upper crust. Such deformation would influence the continued deformation of the model and allow the model to evolve into a model of seafloor spreading flanked by rifted margins. The plots of stress in Figure 11.9 suggest that crustal rupture may occur above the small-scale convective event or close to the edge of the heterogeneity. Unfortunately the model became unstable when a brittle failure criterion was introduced, although it may become possible if the resolution of the model is increased. I would suggest that including the brittle failure criteria to the model is the next stage in the development of this work.

11.6 Summary

A transient period of small-scale convection may be responsible for depth-dependent stretching and enhanced melting during continental lithospheric thinning prior to continental breakup. This phenomenon may be an inherent part of the rifting process. In this chapter the role of wet melting and water-content heterogeneities on deformation of the continental lithosphere during extension were investigated. Wet melting had previously been shown to enhance upwelling at slow-spreading ocean ridges (Braun et al., 2000), and it was hypothesised that the onset of deep, damp melting could be a trigger mechanism for continental lithospheric thinning and breakup. As shown by Nielsen and Hopper (2004), this work illustrates that although melting enhances buoyancy and

reduced viscosity, dehydration hardening significantly suppresses small-scale convection during lithospheric thinning, although in contrast to that of Nielsen and Hopper (2004), this work suggests that dehydration hardening may not completely suppress an upwelling and melt production peak. However, in the first set of models (where the continental lithosphere is homogeneous), small-scale convection induced by wet melting is limited to the lower part of the lithosphere, and it appears that wet melting alone cannot explain preferential thinning of the lithospheric mantle.

Results from the second set of models presented in this chapter suggest that water-content heterogeneities may provide sufficient weakness in the continental lithosphere for thinning to localise and for preferential thinning of the lithospheric mantle to occur as soon as extension begins. The presence of water both reduces the viscosity and the solidus of olivine, and the feedback between preferential thinning, melting and viscosity allows small-scale convection to occur. The viscosity of 'wet' mantle increases to that of 'dry' mantle after a few percent of melting and this effect reduces the lateral viscosity contrast so that the small-scale convection ceases, and deformation becomes more passive. The model therefore predicts both preferential lithospheric thinning and a period of enhanced melting during continental breakup. This model requires that the continental lithosphere is heterogeneous in water-content. Inherited variations in composition, as well as refertilisation of the continental mantle during previous subduction events may explain such heterogeneities. A conceptual model for induced small-scale convection at an inherited water-content heterogeneity is given in Figure 11.14. Inherited heterogeneities may also provide an explanation for the migration or abandonment of rifts, although further work is required to test this.

11.7 Suggestions for further and follow-up work

As is the case with all numerical models, many assumptions have been made in terms of the initial conditions and the relationships between variables used in these models. Further work may increase the understanding of the behavior of the model, which should enhance the understanding of the driving forces and processes responsible for

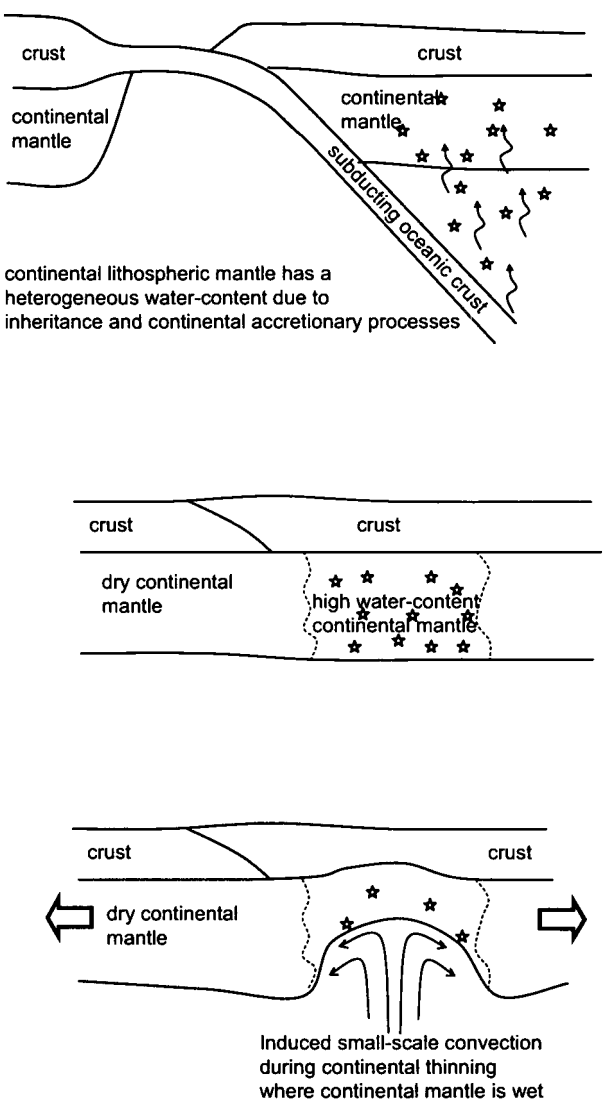

Figure 11.14: Conceptual diagram of induced small-scale convection during continental lithospheric thinning caused by inherited water-content heterogeneities.

lithospheric thinning, lithospheric rupture and the onset of seafloor spreading. In particular I would suggest that the following items be addressed, in approximately this order

1. The model should be made both bigger and higher resolution. In some of the models presented here, small-scale convection was influenced by the boundary conditions, particularly the right hand side vertical axis. This was particularly noticeable at low scaling viscosities, and partially determined the scaling viscosities which were used whilst investigating the effects of other variables. Additionally, plots of maximum upwelling velocity to half-extension velocity ratio and equivalent melt thickness showed some high frequency 'noise' on top of the overall trends (e.g. Figure 11.12). It is likely that this noise is a function of the relatively low resolution grid used in these models.

2. The crust and upper mantle should be allowed to deform according to the Byerlee criteria (see Figure 11.3). Unfortunately the model became unstable when the criteria was included for the model presented, but a higher resolution model may reduce numerical artifacts and allow the Byerlee criteria to be imposed. Including this criteria may enable the strain to focus in the upper crust as a result of preferential thinning, cause the continental lithosphere to 'rupture' and allow the model to develop into a model of seafloor spreading.

3. The distribution of compositional heterogeneities should be looked at in more detail to further assess the possibility that the location and style of rifting may be influenced by water-content heterogeneities, and also to assess the possibility that rift migration and rift abandonment may be influenced by realistic heterogeneities in the lithosphere.

4. Temperature heterogeneities could be invoked as an alternative starting condition for the model, to assess their potential influence on the initiation of small-scale convection.

5. The results of the models presented here were only qualitatively compared with

observations of lithospheric thinning and melt production at rift basins and at rifted margins. The models shown here generally predicted the onset of small-scale convection and enhanced upwelling after tens of Myr or hundreds of km of extension. In the Earth, depth-dependent stretching has been observed at rifted margins where total extension is much less than this, as well as at propagating rift tips where total extension is only a few tens of km. Additionally the peaks in the maximum upwelling velocity to half-extension velocity predicted here are relatively low in comparison to the voluminous melt volumes observed at some volcanic margins. Further work and sensitivity tests to variables including mantle potential temperature will enable quantitative comparisons to observations where they are available. This will allow the nature and size of heterogeneities required to account for observations to be constrained, and the likelihood of the presence of such heterogeneities to be assessed in more detail.

Chapter 12

Discussion and Conclusions

12.1 Introduction

The aim of this thesis was to investigate the processes and mechanisms which thin the continental lithosphere during rift basin and rifted margin formation, prior to the onset of 'normal' seafloor spreading.

12.2 Depth-dependent stretching in the Faroe-Shetland basin

In Chapters 3-6 I investigated the Tertiary development of the Faroe Shetland basin (NE Atlantic margin), a candidate for a failed breakup basin - a fossil propagating rift tip. The basin lies along strike from the Møre basin and Møre margin, inboard of the NE Atlantic continent-ocean boundary. The Faroe-Shetland basin (FSB) comprises large Mesozoic fault blocks, and is often considered to be a Mesozoic rift basin. The Mesozoic history of the basin is consistent with a model of rift basin formation by pure-shear. However, the basin experienced large amounts of post-Palaeocene water-loaded tectonic subsidence, which suggests that a rift event, with an apparent stretching factor of more than 3, occurred in the Palaeocene. Only relatively minor Palaeocene or post-Paleocene upper crustal extension is observed, with stretching factors of less than 1.1. The excess post-Palaeocene subsidence maximum occurs along the axis of the basin

and cannot be explained by post-plume subsidence, underplating or inversion.

This analysis shows that depth-dependent stretching occurred in the FSB during the Palaeocene, at the same time as continental rupture occurred at the Møre and Faroes margins (see Figure 12.1 for summary diagram). This result demonstrates that depth-dependent stretching can occur in continental lithosphere where breakup does not subsequently occur. The result also supports the hypothesis that depth-dependent stretching is a syn-breakup process (Clift and Lin, 2001; Kusznir et al., 2004), rather than being a result of early seafloor spreading.

The timing and magnitude of subsidence and heatflow and the amount of melting predicted by depth-dependent modes of thinning are different to those predicted by the pure-shear (depth-uniform) model. Consequently, errors may be made when predicting palaeobathymetry and heatflow if depth-uniform stretching is assumed for a region where thinning was actually depth-dependent. Where the lithospheric mantle is thinned preferentially with respect to the upper crust, then subsidence, heatflow peaks and the amount of melt produced are greater than would be expected if upper crustal thinning factors are assumed to represent the magnitude of depth-uniform thinning.

12.2.1 Timing of depth-dependent stretching in the Faroe-Shetland basin

This analysis indicates that depth-dependent stretching (preferential thinning of the lithospheric mantle and lower crust with respect to the upper crust) occurred in the Faroe-Shetland basin between the Late Palaeocene and earliest Eocene, at the same time as the voluminous volcanism and the emplacement of seaward dipping reflectors (SDRs) on the Faroes margin. At this time, the basin was also subject to a regional uplift event of approximately 500m, associated with voluminous volcanism and breakup of the Atlantic. This regional uplift (and subsequent subsidence) somewhat obscures the uplift-subsidence signal from depth-dependent stretching in the basin. However, the magnitude of post-Palaeocene subsidence (which is also post-continental breakup on the Faroes margin), is not easily explained as post-thinning thermal subsidence

Jurassic-Cretaceous: Pure-shear extension. Upper crustal extension accommodated on brittle faults, ductile lower crustal and lithospheric mantle deformation.

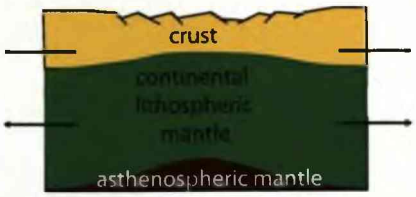

Cretaceous and Early Palaeocene: Post-rift thermal subsidence and sedimentation.

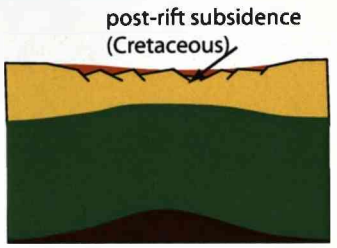

Palaeocene: Upwards-propagating upwelling-divergent flow thins the lithospheric mantle first, causing uplift in the basin.
Concurrent regional uplift (approx 500m) causes erosion of surrounding platform areas and rapid sedimentation in the basin.

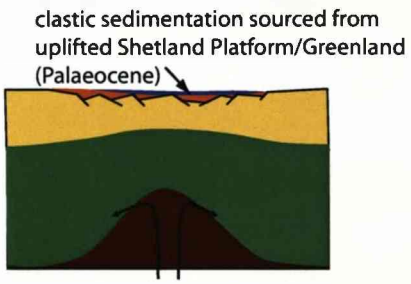

Late Palaeocene (Flett-Formation and Basalt Series times): Upwards-propagating upwelling-divergent flow thins the lower crust, causing rapid subsidence. The upwelling divergent flowfield acts in the lithospheric mantle and lower crust, whilst the upper crust extends by distributed pure shear on minor faults. Small amount of melt is produced in the basin. Continental lithospheric rupture at the Faroes margin.

Deformation in the Faroes-Shetland basin ceases shortly after Balder Formation times (i.e. shortly after the time of Seaward Dipping Reflector formation and the onset of seafloor spreading in the Norwegian basin).

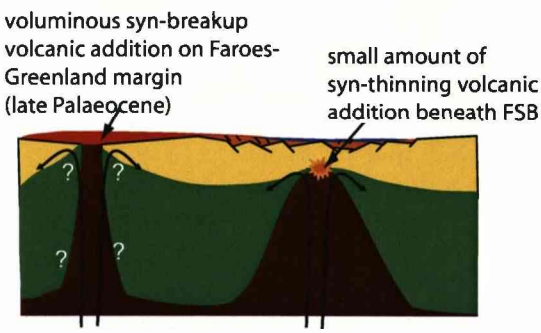

Eocene – Present Day: Thermal subsidence in the Faroe-Shetland Basin until present day. Continued spreading in the Norwegian basin until Miocene.

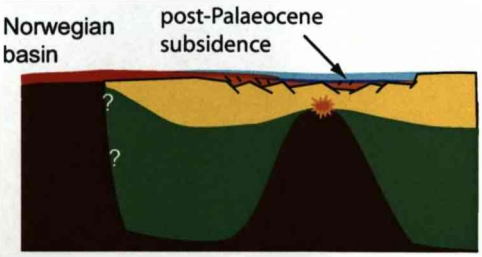

Figure 12.1: Schematic preferred model for formation of the Faroe-Shetland basin.

only, suggesting that lithospheric mantle and lower crustal thinning beneath the FSB continued until after continental breakup had occurred on the Faroes margin. This timing is also consistent with 1–D subsidence analysis and the (minor) volumes of Late Palaeocene-age volcanic addition, the sills and volcanic centres of the basin. The results suggest that continental lithospheric thinning can occur along multiple offset or segmented axes prior to breakup, leaving a 'failed breakup basin' once seafloor spreading begins (Figure 12.2).

12.2.2 The mode of deformation in the FSB

At late Palaeocene times the FSB lay approximately along strike from the location of the Møre margin, and represents a failed continuation of the zone of lithospheric thinning which ruptured to form the Atlantic Ocean. In Chapter 10 forward kinematic models were assessed to determine the mode of deformation responsible for the Tertiary development of the FSB. The preferred model of basin formation is one in which the continental lithospheric mantle is thinned from its base upwards by an upwards-propagating, upwelling-divergent flowfield. This type of deformation can explain (Palaeocene) uplift as the lithospheric mantle is first thinned, followed by rapid subsidence as the lower crust is then thinned. The upwards-propagating upwards-divergent flowfield model is analogous to models of induced small-scale convection in the continental lithosphere. In the case of the FSB, I suggest that small-scale convection occured in the lower crust and lithospheric mantle whilst the upper crust experienced only minor extension. The amount of subsidence predicted by the model is able to explain large amounts of post-Palaeocene subsidence with only minor upper crustal extension, in agreement with observations.

The magnitude of post-Palaeocene water-loaded tectonic subsidence in the FSB increases towards the north, where the basin opens out into the Norwegian basin. This suggests that the mode of deformation responsible for the depth-dependent stretching in the basin thinned the northern axis of the FSB more than the southern axis of the basin, consistent with the successful breakup at the Møre margin. In terms of the

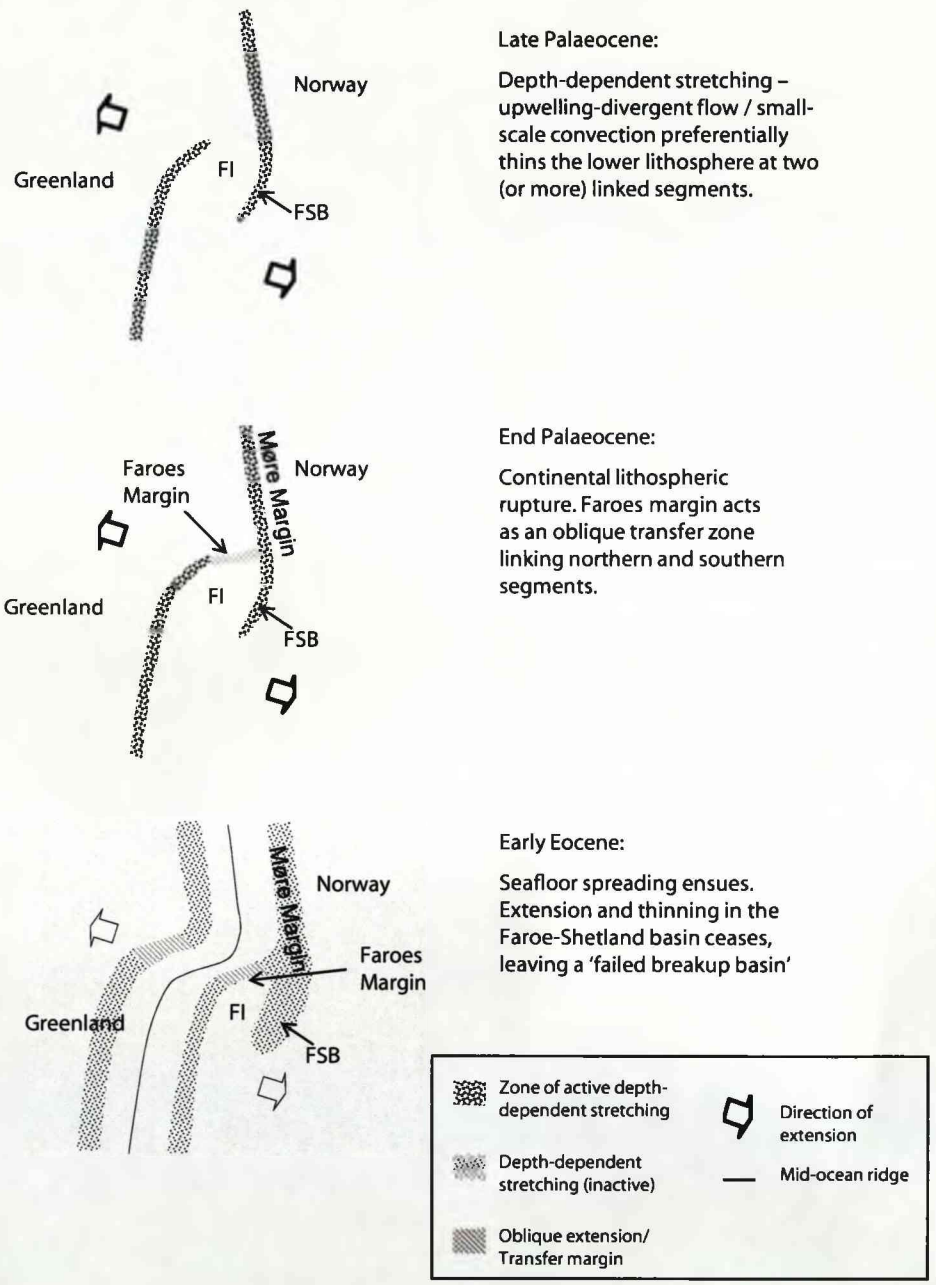

Figure 12.2: Conceptual plan-view of breakup of the North Atlantic in the vicinity of the Faroe-Shetland basin.

model presented in Chapter 10, this may be explained if the upwelling divergent flow was able to penetrate to shallower depths in the north of the basin, and succeeded in rupturing the lithosphere at the Møre margin.

12.3 The mode of deformation during continental lithosphere thinning and breakup. Pure-shear and upwelling-divergent flow models.

The magnitude of stretching and thinning at rift basins and rifted continental margins is usually quantified using a stretching factor (β). If the continental lithosphere is assumed to stretch and thin by a factor of β by a pure-shear mode of deformation (McKenzie, 1978), then subsidence, heatflow, finite strain and the volume and composition of melt can be predicted (McKenzie, 1978; Jarvis and McKenzie, 1980; McKenzie and Bickle, 1988; Bown and White, 1995).

However, whilst rift basins with relatively minor extension can often be successfully modelled using the pure-shear model, this and other works have shown that stretching and thinning of the continental lithosphere can be depth-dependent (e.g. Royden and Keen, 1980; Driscoll and Karner, 1998; Davis and Kusznir, 2004). Consequently using the pure-shear model to predict subsidence, heatflow, finite strain and the volume and composition of melt may be inappropriate. Depth-dependent modes of thinning may be particularly important as the continental lithosphere proceeds to breakup (i.e. at rifted margins and failed breakup basins such as the Faroe-Shetland basin).

The model of continental lithospheric thinning by upwelling-divergent flow was proposed by Davis and Kusznir (2004) to explain observations of depth-dependent stretching at rifted continental margins. The upwelling-divergent flow (UDF) model is similar to models of seafloor spreading, and therefore the UDF model evolves into a simple model of seafloor spreading and does not require a sudden change in the mode of deformation during the continental breakup process. The deformation field of the UDF models presented in Chapters 7-10 uses the analytical cornerflow solution of Batchelor

(1967). The flowfield can be defined by an upwelling velocity (V_z^0) and half-spreading rate (V_x^0) boundary conditions, which is applied to initially undeformed continental lithosphere. The values of the upwelling and half-spreading velocities are variable.

In Chapters 7 and 8 the pure-shear and upwelling divergent flow models of continental lithospheric thinning, continental breakup and the onset of seafloor spreading were compared in terms of resulting margin geometry, subsidence, heatflow, finite strain and volcanic addition (e.g. see Figure 12.3). The subsidence and heat-flow histories predicted by the UDF models of continental lithosphere thinning and rifted margin formation are more varied and complex than those predicted by the pure-shear model. The models are kinematic and therefore do not explicitly address the driving forces responsible for continental lithospheric thinning. However, the pure-shear model implies that lithospheric thinning and upwelling occurs as a passive response to horizontal extension, whilst the UDF model implies that thermal buoyancy forces drive the lithospheric and asthenospheric convection in the continental lithosphere soon after the onset of extension in the continental lithosphere.

12.3.1 Volcanism at rifted margins

Rifted margins are often classified in terms of the volume of volcanic addition which accompanied breakup. Commonly, where melt volumes at rifted margins are different to those predicted by the model of continental breakup by pure-shear, anomalously hot or cool mantle, or depleted or enriched mantle has been invoked to explain the apparent discrepancy (e.g. White and McKenzie, 1989; Bown and White, 1995; Minshull et al., 2001; Reston and Morgan, 2004). In Chapter 8, a number of intrinsic variables were shown to affect the subsidence, heatflow history, as well as the volume and composition of volcanism during continental lithospheric thinning. Factors which bring forward the onset of melting and increase the thickness of melt produced are:

1. Faster spreading rates

2. Increased mantle potential temperature

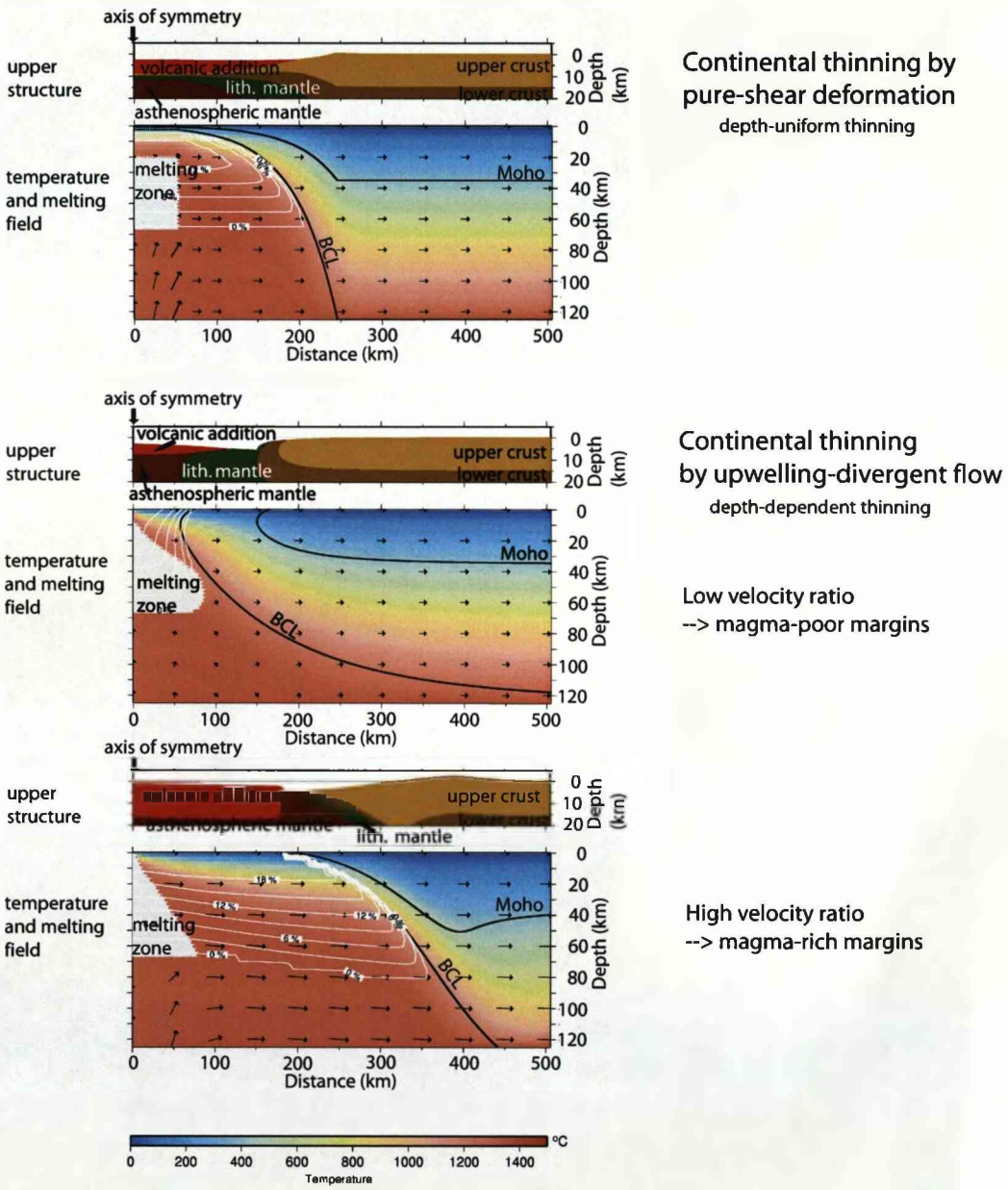

Figure 12.3: Comparison of margin geometry and volcanic addition predicted by pure-shear and upwelling-divergent flow model.

3. Thinner lithosphere
4. High clinopyroxene content of the mantle / other compositional heterogeneity
5. High mantle water-content

Assuming that the thinning of the lithosphere at rifted margins occurs by pure-shear, only increased mantle potential temperature (by 100-200^{o}C) can easily explain very thick (up to 20km) volcanic addition.

Factors which retard the onset of melting and decrease the thickness of melt produced are:

1. Slower extension rates
2. Lower mantle potential temperature
3. Thicker lithosphere
4. Lower clinopyroxene content / other compositional heterogeneity
5. Melt retention (or re-freezing) in the mantle

Slow extension rates, low mantle potential temperature or melt retention can explain very thin (or absent) volcanism during pure-shear thinning of the continental lithosphere.

However, the volume of melt produced during continental breakup is also dependent on the mode of deformation, if the lithosphere does not thin by pure-shear deformation, then the volume (and composition) of melt may appear anomalous when compared to expectations from the pure shear model.

For the upwelling-divergent flow (UDF) model, the ratio between the axial upwelling (V_z^0) to the half-spreading (V_x^0) velocity can be varied to give a range of lithospheric structures: Models with low velocity ratios (V_z^0/V_x^0) predict that wide zones of lower continental crust and continental mantle are exhumed prior to the onset of melting during continental breakup, and are considered appropriate to non-volcanic margins. High velocity ratio UDF models predict that melting begins soon after deformation begins

and that thick volcanic addition may be present close to the continental margin, and are considered appropriate to volcanic margins (Figure 12.3). All UDF models predict depth-dependent stretching. The UDF model predicts a range of margin structures and a wide range in volcanic addition at rifted margins without requiring that temperature or compositional anomalies are present.

Observations of volcanic addition thickness and composition, finite deformation, subsidence and heatflow history, and extension rate may be used to constrain the mode of deformation and the conditions of continental lithosphere thinning or rupture. A good fit between observations and model predictions suggests that the model input variables (e.g. mode of deformation, mantle potential temperature) are appropriate to the basin or margin. Where datasets are incomplete, the models make predictions which are testable when new data become available. Forward modelling was carried out for two case-studies in this thesis: the Faroe-Shetland basin (described above) and the Iberian margin (discussed in next section).

Continental lithosphere thinning probably occurs by both pure-shear and upwelling-divergent flow deformation mechanisms and the importance of each mechanism may vary with depth and time. Further case-studies and more complete datasets will improve our understanding of the relative role that these modes of deformation play during thinning of the continental lithosphere, and offer insights into the driving forces responsible for continental lithosphere thinning and breakup.

12.3.2 Continental lithospheric thinning at the Iberian continental margin

In Chapter 9 the pure-shear and upwelling-divergent flow models were compared in their ability to explain the formation of the Iberian margin. The Iberian margin is particularly well studied example of a magma-poor, or non-volcanic margin, and a wide zone of exhumed continental mantle (ZECM) is observed between unequivocal continental and oceanic crust (Boillot et al., 1987, 1989; Pickup et al., 1996; Dean et al., 2000). Pure-shear models of continental lithosphere thinning generally predict melt

generation before continental break-up at the Iberian margin, unless anomalously cool asthenosphere temperatures (Minshull et al., 2001) or depleted mantle source (Pérez-Gussinyé et al., 2006) are invoked. If continental lithospheric thinning at the Iberian margin is assumed to have occurred due to a low velocity ratio upwelling-divergent flow, then no mantle potential temperature or compositional heterogeneity is required to explain the lack of volcanism in the ZECM. The model predicts a wide zone of exhumed lower crust and continental lithospheric mantle, which is in agreement with the overall lithospheric structure of the margin. Thus I suggest that upwelling-divergent flow played an important role in the formation of the Iberian margin.

12.4 Causes of depth-dependent continental lithospheric thinning: Induced small-scale convection at a water-content heterogeneity?

In Chapter 11 I used dynamic models to investigate the potential role of water in inducing upwelling in the continental lithosphere during continental breakup. It is envisaged that the continental lithospheric mantle has a heterogeneous water content due to inheritance as well as continental accretion and subduction-related refertilisation. A water-content heterogeneity in the lithospheric mantle may sufficiently weaken the mantle so that extension is accommodated by localised lithospheric thinning in a 'wet' region (Figure 12.4). Viscosity contrasts caused by water-content heterogeneities may also induce small-scale convection in the lithospheric mantle, producing an associated melt peak. The small-scale convection event was self-limiting as the lateral viscosity contrasts were reduced by the small-scale convection.

The small-scale convection event predicted by the model resulted in both depth-dependent stretching (preferential thinning of the lithospheric mantle with respect to the upper crust) and a (small) melt production peak during continental lithospheric thinning. Qualitatively, these predictions are consistent with observations of depth-dependent stretching at rift basins and rifted margins, and of enhanced melt production at some

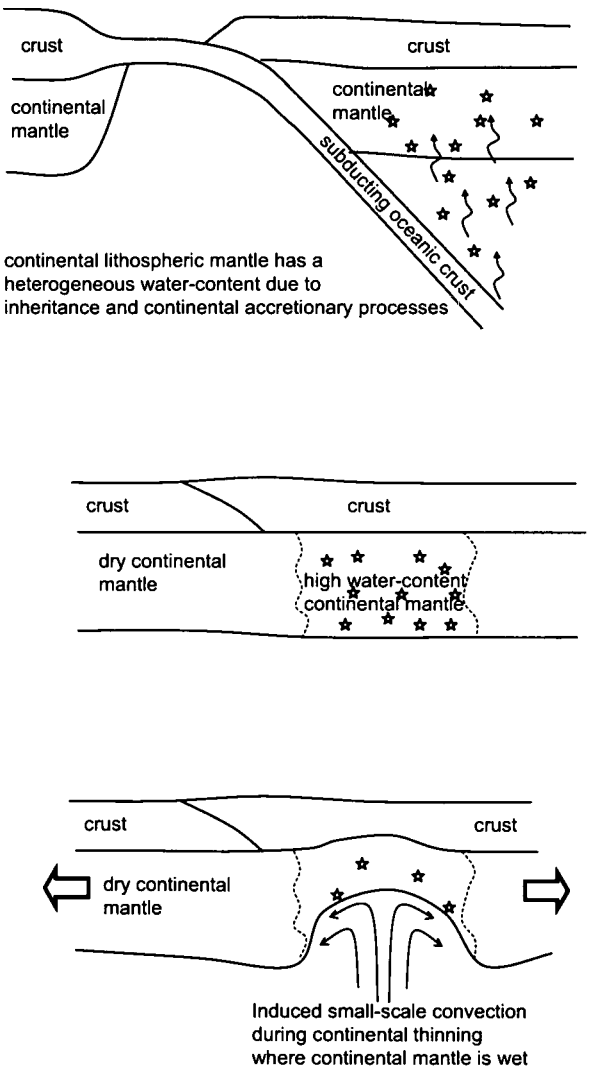

Figure 12.4: Conceptual diagram of induced small-scale convection during continental lithospheric thinning caused by inherited water-content heterogeneities.

volcanic margins. However, the small-scale convection did not predict preferential thinning of the lower crust, which is observed at rift basins (e.g. the Faroe-Shetland basin) and at rifted margins. Further development of the model to include brittle deformation as well as ductile deformation, and of a wider range of initial conditions and rheologies, may quantitatively explain observations where they are available. This will allow the nature and size of water-content heterogeneities required to account for observations of depth-dependent stretching to be constrained, and the likelihood of the presence of such heterogeneities to be assessed in more detail.

Inherited water-content heterogeneities provide a causative initial condition for depth-dependent continental lithospheric thinning to occur as a result of horizontal extensional forces, providing a weak zone at which continental thinning can initiate, and inducing small-scale convection and preferential thinning of the lower continental lithosphere prior to continental breakup.

Bibliography

Abrahamsen, N. (2006). Palaeomagnetic results from the Lopra-1/1a re-entry well, Faroe Islands. *Geological Survey of Denmark and Greenland Bulletin*, **9**, 51–65.

Ahern, J. L. and Turcotte, D. L. (1979). Magma migration beneath an ocean ridge. *Earth And Planetary Science Letters*, **45**(1), 115–122.

Allen, P. A. and Allen, J. R. (2005). *Basin Analysis*. Blackwell Publishing.

Andersen, M. S., Nielsen, T., Sorensen, A. B., Boldreel, L. O., and Kuijpers, A. (2000). Cenozoic sediment distribution and tectonic movements in the Faroe region. *Global And Planetary Change*, **24**(3-4), 239–259.

Anderson, D. L. (2006). Speculations on the nature and cause of mantle heterogeneity. *Tectonophysics*, **416**(1-4), 7–22.

Artemieva, I. M. (2006). Global 1 degrees x 1 degrees thermal model tc1 for the continental lithosphere: Implications for lithosphere secular evolution. *Tectonophysics*, **416**(1-4), 245–277.

Artemjev, M. E. and Artyushkov, E. (1971). Structure and isostasy of Baikal rift and mechanism of rifting. *Journal Of Geophysical Research*, **76**(5), 1197–.

Asimow, P. D. and Langmuir, C. H. (2003). The importance of water to oceanic mantle melting regimes. *Nature*, **421**(6925), 815–820.

Asimow, P. D., Dixon, J. E., and Langmuir, C. H. (2004). A hydrous melting and fractionation model for mid-ocean ridge basalts: Application to the mid-Atlantic ridge near the azores. *Geochemistry Geophysics Geosystems*, **5**.

Barton, P. and Wood, R. (1984). Tectonic evolution of the north-sea basin - crustal stretching and subsidence. *Geophysical Journal Of The Royal Astronomical Society*, **79**(3), 987–1022.

Bassi, G. (1991). Factors controlling the style of continental rifting - insights from numerical modeling. *Earth And Planetary Science Letters*, **105**(4), 430–452.

Batchelor, G. (1967). *An Introduction to Fluid Dynamics*. Cambridge University Press, New York.

Beattie, P. (1993). Uranium thorium disequilibria and partitioning on melting of garnet peridotite. *Nature*, **363**(6424), 63–65.

Bell, B. and Butcher, H. (2002). On the emplacement of sill complexes: evidence from the Faroe-Shetland Basin. *Geological Society, London, Special Publications*, **197**(1), 307–329.

Beslier, M. O., Royer, J. Y., Girardeau, J., Hill, P. J., Boeuf, E., Buchanan, C., Chatin, F., Jacovetti, G., Moreau, A., Munschy, M., Partouche, C., Robert, U., and Thomas, S. (2004). A wide ocean-continent transition along the south-west Australian margin: first results of the margau/md110 cruise. *Bulletin De La Societe Geologique De France*, **175**(6), 629–641.

Blackman, D. K., Kendall, J. M., Dawson, P. R., Wenk, H. R., Boyce, D., and Morgan, J. P. (1996). Teleseismic imaging of subaxial flow at mid-ocean ridges: Traveltime effects of anisotropic mineral texture in the mantle. *Geophysical Journal International*, **127**(2), 415–426.

Blackman, D. K., Wenk, H. R., and Kendall, J. M. (2002). Seismic anisotropy of the upper mantle 1. factors that affect mineral texture and effective elastic properties. *Geochemistry Geophysics Geosystems*, **3**.

Bohnhoff, M. and Makris, J. (2004). Crustal structure of the southeastern Iceland-Faeroe ridge (ifr) from wide aperture seismic data. *Journal Of Geodynamics*, **37**(2), 233–252.

Boillot, G., Recq, M., Winterer, E. L., Meyer, A. W., Applegate, J., Baltuck, M., Bergen, J. A., Comas, M. C., Davies, T. A., Dunham, K., Evans, C. A., Girardeau, J., Goldberg, G., Haggerty, J., Jansa, L. F., Johnson, J. A., Kasahara, J., Loreau, J. P., Lunasierra, E., Moullade, M., Ogg, J., Sarti, M., Thurow, J., and Williamson, M. (1987). Tectonic denudation of the upper mantle along passive margins - a model based on drilling results (ODP leg-103, western Galicia margin, Spain). *Tectonophysics*, **132**(4), 335–342.

Boillot, G., Feraud, G., Recq, M., and Girardeau, J. (1989). Undercrusting by serpentinite beneath rifted margins. *Nature*, **341**(6242), 523–525.

Boldreel, L. O. and Andersen, M. S. (1993). Late-Paleocene to Miocene compression in the Faeroe-rockall area. *In Parker, J.R. (ed.) Petroleum Geology of Northwest Europe: Proceedings of the 4th conference.*, pages 1025–1034.

Boldreel, L. O. and Andersen, M. S. (1998). Tertiary compressional structures on the Faroe-Rockall plateau in relation to northeast Atlantic ridge-push and Alpine foreland stresses. *Tectonophysics*, **300**(1-4), 13–28.

Bonatti, E. and Michael, P. J. (1989). Mantle peridotites from continental rifts to ocean basins to subduction zones. *Earth And Planetary Science Letters*, **91**(3-4), 297–311.

Booth, J., Swiecicki, T., and Wilcockson, P. (1993). The tectono-stratigraphy of the solan basin, west of Shetland. *In Parker, J.R. (ed.) Petroleum Geology of Northwest Europe: Proceedings of the 4th conference.*, pages 987–998.

Boutilier, R. R. and Keen, C. E. (1999). Small-scale convection and divergent plate boundaries. *Journal Of Geophysical Research-Solid Earth*, **104**(B4), 7389–7403.

Bown, J. W. and White, R. S. (1995). Effect of finite extension rate on melt generation at rifted continental margins. *Journal Of Geophysical Research-Solid Earth*, **100**(B9), 18011–18029.

Braun, M. G., Hirth, G., and Parmentier, E. M. (2000). The effects of deep damp melting on mantle flow and melt generation beneath mid-ocean ridges. *Earth And Planetary Science Letters*, **176**(3-4), 339–356.

Brodie, J. and White, N. (1994). Sedimentary basin inversion caused by igneous underplating - northwest European continental-shelf. *Geology*, **22**(2), 147–150.

Buck, W. and Su, W. (1989). Focused mantle upwelling below mid-ocean ridges due to feedback between viscosity and melting. *Geophysical Research Letters*, **16**(7), 641–644.

Buck, W. R. (1986). Small-scale convection induced by passive rifting - the cause for uplift of rift shoulders. *Earth And Planetary Science Letters*, **77**(3-4), 362–372.

Buck, W. R., Lavier, L. L., and Poliakov, A. N. B. (1999). How to make a rift wide. *Philosophical Transactions Of The Royal Society Of London Series A-Mathematical Physical And Engineering Sciences*, **357**(1753), 671–690.

Burov, E. B. and Diament, M. (1995). The effective elastic thickness (Te) of continental lithosphere - what does it really mean. *Journal Of Geophysical Research-Solid Earth*, **100**(B3), 3905–3927.

Burov, E. B. and Watts, A. B. (2006). The long-term strength of continental lithosphere: jelly sandwich or creme brulee? *GSA Today*, **16**(1), 4–10.

Byerlee, J. (1978). Friction of rocks. *Pure Applied Geophysics*, **116**, 615–626.

Cannat, M. (1996). How thick is the magmatic crust at slow spreading oceanic ridges? *Journal Of Geophysical Research-Solid Earth*, **101**(B2), 2847–2857.

Ceramicola, S., Stoker, M., Praeg, D., Shannon, P. M., De Santis, L., Hoult, R., Hjelstuen, B. O., Laberg, S., and Mathiesen, A. (2005). Anomalous Cenozoic subsidence along the 'passive' continental margin from Ireland to mid-Norway. *Marine And Petroleum Geology*, **22**(9-10), 1045–1067.

Champion, M. E. S., White, N. J., Jones, S. M., and Lovell, J. P. B. (2008). Quantifying transient mantle convective uplift: An example from the Faroe-Shetland basin. *Tectonics*, **27**(1).

Chazot, G., Charpentier, S., Kornprobst, J., Vannucci, R., and Luais, B. (2005). Lithospheric mantle evolution during continental break-up: The west Iberia non-volcanic passive margin. *Journal Of Petrology*, **46**(12), 2527–2568.

Chen, Y. S. and Morgan, W. J. (1990). A nonlinear rheology model for midocean ridge axis topography. *Journal Of Geophysical Research-Solid Earth And Planets*, **95**(B11), 17583–17604.

Chenet, P., Montadert, L., Gairaud, H., and Roberts, D. (1982). Extension ratio measurements on the Galicia, Portugal, and northern Biscay continental margins: implications for evolutionary models of passive continental margins. In *Studies in Continental Margin Geology*, volume 34 of *Memoirs*, pages 703–715. American Association of Petroleum Geologists.

Chian, D. P., Keen, C., Reid, I., and Louden, K. E. (1995). Evolution of nonvolcanic rifted margins - new results from the conjugate margins of the Labrador sea. *Geology*, **23**(7), 589–592.

Chian, D. P., Louden, K. E., Minshull, T. A., and Whitmarsh, R. B. (1999). Deep structure of the ocean-continent transition in the southern Iberia Abyssal Plain from seismic refraction profiles: Ocean Drilling Program (legs 149 and 173) transect. *Journal Of Geophysical Research-Solid Earth*, **104**(B4), 7443–7462.

Clift, P. and Lin, J. (2001). Preferential mantle lithospheric extension under the south china margin. *Marine and Petroleum Geology*, **18**(8), 929–945.

Clift, P. D. and Turner, J. (1998). Paleogene igneous underplating and subsidence anomalies in the rockall-Faeroe-Shetland area. *Marine And Petroleum Geology*, **15**(3), 223–243.

Clift, P. D., Lin, J., and ODP Leg 184 Scientific, P. (2001). Patterns of extension and magmatism along the continent-ocean boundary, south China margin. *Geological Society, London, Special Publications*, **187**(1), 489–510.

Cochran, J. R. and Karner, G. D. (2007). Constraints on the deformation and rupturing of continental lithosphere of the Red Sea: the transition from rifting to drifting. *Geological Society, London, Special Publications*, **282**(1), 265–289.

Cooper, M. M., Evan, A. C., Lynch, D. J., Neville, G., and Newley, T. (1999). The foinaven field: managing reservoir development uncertainty prior to start-up. *In Fleet, A.J and Boldy, S.A.R. (eds) Petroleum Geology of Northwest Europe: Proceedings of the 5th Conference*, pages 675–682.

Cordoba, D., Banda, E., and Ansorge, J. (1987). The Hercynian crust in northwestern Spain - a seismic survey. *Tectonophysics*, **132**(4), 321–333.

Cornwell, D. G. (2008). *Magma-assisted continental rift margins: the Ethiopian rift.* Ph.D. thesis, University of Leicester.

Corti, G., Van Wijk, J., Bonini, M., Sokoutis, D., Cloetingh, S., Innocenti, F., and Manetti, P. (2003). Transition from continental break-up to punctiform seafloor spreading: How fast, symmetric and magmatic. *Geophysical Research Letters*, **30**(12).

Cox, K. G. (1993). Continental magmatic underplating. *Philosophical Transactions Of The Royal Society Of London Series A-Mathematical Physical And Engineering Sciences*, **342**(1663), 155–166.

Davies, R., Cartwright, J., Pike, J., and Line, C. (2001). Early oligocene initiation of North Atlantic Deep Water formation. *Nature*, **410**(6831), 917–920.

Davies, R., Cloke, I., Cartwright, J., Robinson, A., and Ferrero, C. (2004). Post-breakup compression of a passive margin and its impact on hydrocarbon prospectivity: An example from the Tertiary of the Faeroe-Shetland basin, united kingdom. *Aapg Bulletin*, **88**(1), 1–20.

Davis, M. and Kusznir, N. J. (2004). Depth-dependent lithospheric stretching at rifted continental margins. In G. Karner, editor, *Proceedings of NSF Rifted Margins Theoretical Institute*, pages 92–136. Columbia University Press,.

Davis, M. J. (1999). *Lithospheric stretching at rifted continental margins.* Ph.D. thesis, University of Liverpool.

Dean, K., McLachlan, K., and Chambers, A. (1999). Rifting and the development of the Faeroe-Shetland basin. *In Fleet, A.J and Boldy, S.A.R. (eds) Petroleum Geology of Northwest Europe: Proceedings of the 5th Conference*, pages 533–544.

Dean, S. M., Minshull, T. A., Whitmarsh, R. B., and Louden, K. E. (2000). Deep structure of the ocean-continent transition in the southern Iberia Abyssal Plain from seismic refraction profiles: The IAM-9 transect at 40 degrees 20 ' N. *Journal Of Geophysical Research-Solid Earth*, **105**(B3), 5859–5885.

Dick, H. J. B., Lin, J., and Schouten, H. (2003). An ultraslow-spreading class of ocean ridge. *Nature*, **426**(6965), 405–412.

Doré, A. G., Lundin, E., Jensen, L. N., Birkeland, O., Eliassen, P. E., and Fichler, C. (1999). Principal tectonic events in the evolution of the northwest European Atlantic margin. *In Fleet, A.J and Boldy, S.A.R. (eds) Petroleum Geology of Northwest Europe: Proceedings of the 5th Conference*, pages 41–61.

Driscoll, N. W. and Karner, G. D. (1998). Lower crustal extension across the northern Carnarvon basin, Australia: Evidence for an eastward dipping detachment. *Journal Of Geophysical Research-Solid Earth*, **103**(B3), 4975–4991.

Dunbar, J. A. and Sawyer, D. S. (1989). How preexisting weaknesses control the style of continental breakup. *Journal Of Geophysical Research-Solid Earth And Planets*, **94**(B6), 7278–7292.

Earle, M. M., Jankowski, E. J., and Vann, I. R. (1989). Structural and stratigraphic evolution of the Faeroe-Shetland channel and northern rockall trough. *AAPG Memoir*, **46**, 461–469.

Ebdon, C., Granger, P., Johnson, H., and Evans, A. (1995). Early Tertiary evolution and sequence stratigraphy of the Faeroe-Shetland basin: Implications for hydrocarbon prospectivity. *In Scrutton, R.A., Stoker, M.S., Shimmield, G.B. and Tudhope, A.W. The Tectonics, Sedimentation and Palaeoceanography of the North Atlantic Region. Geological Society, London, Special Publications*, **90**, 51–69.

Eldholm, O. and Grue, K. (1994). North-Atlantic volcanic margins - dimensions and production-rates. *Journal Of Geophysical Research-Solid Earth*, **99**(B2), 2955–2968.

Ellis, D., Bell, B. R., Jolley, D. W., and O'Callaghan, M. (2002). The stratigraphy, environment of eruption and age of the Faroes lava group, NE Atlantic ocean. *Special Publications*, **197**, 253–269.

Ellis, D., Bell, B., Jolley, D., and Passey, S. (2005). Faroe islands field excursion 2005: Transfer zones, clastic sedimentation and volcanism. *None, Internal Statoil Document.*

England, P. (1983). Constraints on extension of continental lithosphere. *Journal Of Geophysical Research*, **88**(NB2), 1145–1152.

England, R. W., McBride, J. H., and Hobbs, R. W. (2005). The role of Mesozoic rifting in the opening of the NE Atlantic: evidence from deep seismic profiling across the Faroe-Shetland trough. *Journal Of The Geological Society*, **162**, 661–673.

Féraud, G., Beslier, M. O., and G. Cornen, G. (1996). ^{40}Ar-^{39}Ar dating of gabbros from the ocean-continent transition of the western Iberia margin: preliminary results. In R. B. Whitmarsh, D. S. Sawyer, A. Klaus, and D. G. Masson, editors, *Proceedings of the Ocean Drilling Program, Scientific Results.*, volume 149, pages 489–495. Ocean Drilling Program, College Station, Texas.

Fischer, K. M., Parmentier, E. M., Stine, A. R., and Wolf, E. R. (2000). Modeling anisotropy and plate-driven flow in the Tonga subduction zone back arc. *Journal Of Geophysical Research-Solid Earth*, **105**(B7), 16181–16191.

Forsyth, D. and Uyeda, S. (1975). Relative importance of driving forces of plate motion. *Geophysical Journal Of The Royal Astronomical Society*, **43**(1), 163–200.

Fouch, M. J., Fischer, K. M., Parmentier, E. M., Wysession, M. E., and Clarke, T. J. (2000). Shear wave splitting, continental keels, and patterns of mantle flow. *Journal Of Geophysical Research-Solid Earth*, **105**(B3), 6255–6275.

Foulger, G. R. and Anderson, D. L. (2005). A cool model for the Iceland hotspot. *Journal Of Volcanology And Geothermal Research*, **141**(1-2), 1–22.

Funck, T., Hopper, J. R., Larsen, H. C., Louden, K. E., Tucholke, B. E., and Holbrook, W. S. (2003). Crustal structure of the ocean-continent transition at Flemish Cap: Seismic refraction results. *Journal Of Geophysical Research-Solid Earth*, **108**(B11).

Gallagher, J. W. and Dromgoole, P. (2007). Exploring below the basalt, offshore Faroes: a case history of sub-basalt imaging. *Petroleum Geoscience*, **13**, 213–225.

Gatliff, R. W., Hitchen, K., Ritchie, J. D., and Smythe, D. K. (1984). Internal structure of the Erlend Tertiary volcanic complex, north of Shetland, revealed by seismic reflection. *Journal of the Geological Society*, **141**(3), 555–562.

Green, D. H. and Ringwood, A. E. (1967). The genesis of basaltic magmas. *Contributions to Mineralogy and Petrology*, **15**(2), 103–190.

Greenhalgh, E. and Kusznir, N. (2008). Post-breakup rifted margin hinterland uplift predicted from a geodynamic model of continental lithosphere thinning and breakup. *EGU Abstracts*.

Greenhalgh, E. E. and Kusznir, N. J. (2007). Evidence for thin oceanic crust on the extinct aegir ridge, Norwegian basin, NE Atlantic derived from satellite gravity inversion. *Geophysical Research Letters*, **34**(6).

Haq, B. U., Hardenbol, J., and Vail, P. R. (1987). Chronology of fluctuating sea levels since the triassic. *Science*, **235**(4793), 1156–1167.

Harry, D. L. and Bowling, J. C. (1999). Inhibiting magmatism on nonvolcanic rifted margins. *Geology*, **27**(10), 895–898.

Haszeldine, R. S., Ritchie, J. D., and Hitchen, K. (1987). Seismic and well evidence for the early development of the Faeroe-Shetland basin. *Scottish Journal Of Geology*, **23**, 283–300.

Hauri, E., Gaetani, G. A., and Green, T. H. (2006). Partitioning of water during melting of the Earth's upper mantle at H2O-undersaturated conditions. *Earth and Planetary Science Letters*, **248**(3-4), 715–734.

Healy, D. and Kusznir, N. J. (2007). Early kinematic history of the Goban Spur rifted margin derived from a new model of continental breakup and sea-floor spreading initiation. *Geological Society, London, Special Publications*, **282**(1), 199–215.

Hernlund, J. W., Tackley, P. J., and Stevenson, D. J. (2008). Buoyant melting instabilities beneath extending lithosphere: 1. Numerical models. *Journal Of Geophysical Research-Solid Earth*, **113**(B4).

Hirschmann, M., Aubaud, C., and Withers, A. (2005). Storage capacity of H2O in nominally anhydrous minerals in the upper mantle. *Earth and Planetary Science Letters*, **236**(1-2), 167–181.

Hirth, G. and Kohlstedt, D. L. (1995). Experimental constraints on the dynamics of the partially molten upper mantle 2. deformation in the dislocation creep regime. *Journal of Geophysical Research*, **100**, 15441–15450.

Hirth, G. and Kohlstedt, D. L. (1996). Water in the oceanic upper mantle: Implications for rheology, melt extraction and the evolution of the lithosphere. *Earth And Planetary Science Letters*, **144**(1-2), 93–108.

Hirth, G. and Kohlstedt, D. L. (2003). Rheology of the upper mantle and the mantle wedge: A view from the experimentalists. *Inside the subduction factory. Geophysical Monograph*, **138**, 83–105.

Hitchen, K. and Ritchie, J. D. (1993). New k-ar ages, and a provisional chronology, for the offshore part of the British Tertiary Igneous Province. *Scottish Journal Of Geology*, **29**, 73–85.

Hooper, R. J. and Walker, I. (2002). The Mesozoic and early Tertiary opening of the North Atlantic and its impact on the development of the Faeroe-Shetland basin system. *Annual Meeting Expanded Abstracts - American Association of Petroleum Geologists, vol.2002*, page 80.

Hopper, J. R., Funck, T., Tucholke, B. E., Louden, K. E., Holbrook, W. S., and Larsen, H. C. (2006). A deep seismic investigation of the Flemish Cap margin: implications for the origin of deep reflectivity and evidence for asymmetric break-up between Newfoundland and Iberia. *Geophysical Journal International*, **164**(3), 501–515.

Huismans, R. S. and Beaumont, C. (2008). Complex rifted continental margins explained by dynamical models of depth-dependent lithospheric extension. *Geology*, **36**(2), 163–166.

Huismans, R. S., Podladchikov, Y. Y., and Cloetingh, S. (2001a). Dynamic modeling of the transition from passive to active rifting, application to the Pannonian basin. *Tectonics*, **20**(6), 1021–1039.

Huismans, R. S., Podladchikov, Y. Y., and Cloetingh, S. (2001b). Transition from passive to active rifting: Relative importance of asthenospheric doming and passive extension of the lithosphere. *Journal Of Geophysical Research-Solid Earth*, **106**(B6), 11271–11291.

Hurst, N., Kusznir, N., and Roberts, A. (2004). Late Palaeocene mantle plume uplift on the Fugloy ridge, NE Faroes. *EOS Transactions*, **85**, T23B–0587.

Hurst, N. W. (2006). *Crustal Thinning and Subsidence on the NW European Atlantic Margin.* Ph.D. thesis, University of Liverpool.

Jackson, J. (2002). Strength of the continental lithosphere: Time to abandon the jelly sandwich? *GSA Today*, **12**(9), 4–10.

Jagoutz, O., Muntener, O., Manatschal, G., Rubatto, D., Peron-Pinvidic, G., Turrin, B. D., and Villa, I. M. (2007). The rift-to-drift transition in the North Atlantic: A stuttering start of the MORB machine? *Geology*, **35**(12), 1087–1090.

Jarvis, G. T. and McKenzie, D. P. (1980). Sedimentary basin formation with finite extension rates. *Earth And Planetary Science Letters*, **48**(1), 42–52.

Jolley, D. W. and Bell, B. R. (2002). Genesis and age of the Erlend volcano, NE Atlantic margin. *Geological Society, London, Special Publications*, **197**, 95–109.

Jolley, D. W. and Widdowson, M. (2005). Did paleogene North Atlantic rift-related eruptions drive early Eocene climate cooling? *Lithos*, **79**(3-4), 355.

Karato, S. (1986). Does partial melting reduce the creep strength of the upper mantle? *Nature*, **319**(6051), 309.

Karner, G. D. and Watts, A. B. (1982). On isostasy at Atlantic-type continental margins. *Journal Of Geophysical Research*, **87**(NB4), 2923–2948.

Katz, R. F., Spiegelman, M., and Langmuir, C. H. (2003). A new parameterization of hydrous mantle melting. *Geochemistry Geophysics Geosystems*, **4**.

Keen, C. E. (1985). The dynamics of rifting - deformation of the lithosphere by active and passive driving forces. *Geophysical Journal Of The Royal Astronomical Society*, **80**(1), 95–120.

King, S. D. and Anderson, D. L. (1995). An alternative mechanism of flood basalt formation. *Earth And Planetary Science Letters*, **136**(3-4), 269–279.

King, S. D. and Anderson, D. L. (1998). Edge-driven convection. *Earth And Planetary Science Letters*, **160**(3-4), 289–296.

Kiørboe, L. (1999). Stratigraphic relationships of the lower Tertiary of the Faeroe basalt plateau and the Faeroe-Shetland basin. *In Fleet, A.J and Boldy, S.A.R. (eds) Petroleum Geology of Northwest Europe: Proceedings of the 5th Conference*, pages 559–572.

Klein, E. (2003). Earth science - Spread thin in the Arctic. *NATURE*, **423**(6943), 932–933.

Klein, E. M. and Langmuir, C. H. (1987). Global correlations of ocean ridge basalt chemistry with axial depth and crustal thickness. *Journal Of Geophysical Research-Solid Earth And Planets*, **92**(B8), 8089–8115.

Klemperer, S. L. (1988). Crustal thinning and nature of extension in the northern North-Sea from deep seismic-reflection profiling. *Tectonics*, **7**(4), 803–821.

Knott, S., Burchell, M., Jolley, E. J., and Fraser, A. J. (1993). Mesozoic to Cenozoic plate reconstructions of the North Atlantic and hydrocarbon plays of the Atlantic margins. *In Parker, J.R. (ed.) Petroleum Geology of Northwest Europe: Proceedings of the 4th conference.*, pages 953–974.

Kohlstedt, D. L., Evans, B., and Mackwell, S. J. (1995). Strength of the lithosphere - constraints imposed by laboratory experiments. *Journal Of Geophysical Research-Solid Earth*, **100**(B9), 17587–17602.

Korenaga, J. and Karato, S. I. (2008). A new analysis of experimental data on olivine rheology. *Journal Of Geophysical Research-Solid Earth*, **113**(B2).

Korenaga, J., Kelemen, P., and Holbrook, W. (2002). Methods for resolving the origin of large igneous provinces from crustal seismology. *Journal of Geophysical Research-Solid Earth*, **107**(B9).

Kusznir, N., Hunsdale, R., Roberts, A. M., and iSIMM Team (2005). Timing and magnitude of depth-dependent lithosphere stretching on the southern Lofoten and northern Vøring continental margins offshore mid-Norway: implications for subsidence and hydrocarbon maturation at volcanic rifted margins. In A. Dore and B. Vining, editors, *Petroleum Geology: Northwest Europe and Global perspectives - Proceedings of the 6th Petroleum Geology Conference*, pages 757–783. Geological Society, London.

Kusznir, N. J. and Karner, G. D. (2007). Continental lithospheric thinning and breakup in response to upwelling divergent mantle flow: application to the woodlark, Newfoundland and Iberia margins. In G. D. Karner, G. Manatschal, and L. M. Pinheiro, editors, *Imaging, Mapping and Modelling Continental Lithosphere Extension and Breakup*, volume 282 of *Special Publications*, pages 389–419. Geological Society, London.

Kusznir, N. J. and Park, R. G. (1982). Intraplate lithosphere strength and heat flow. *Nature*, **299**(5883), 540.

Kusznir, N. J. and Park, R. G. (1987). The extensional strength of the continental lithosphere: its dependence on geothermal gradient, and crustal composition and thickness. *Geological Society, London, Special Publications*, **28**(1), 35–52.

Kusznir, N. J., Marsden, G., and Egan, S. S. (1991). A flexural-cantilever simple-shear/pure-shear model of continental lithosphere extension: applications to the Jeanne d'Arc Basin, Grand Banks and Viking Graben, North Sea. *Geological Society, London, Special Publications*, **56**(1), 41–60.

Kusznir, N. J., Roberts, A. M., and Morley, C. K. (1995). Forward and reverse modelling of rift basin formation. *Geological Society, London, Special Publications*, **80**(1), 33–56.

Kusznir, N. J., Hunsdale, R., and Roberts, A. M. (2004). Timing of depth-dependent lithosphere stretching on the S. Lofoten rifted margin offshore mid-Norway: pre-breakup or post-breakup? *Basin Research*, **16**(2), 279–296.

Lamers, E. and Carmichael, S. M. M. (1999). The paleocene deepwater sandstone play west of Shetland. *In Fleet, A.J and Boldy, S.A.R. (eds) Petroleum Geology of Northwest Europe: Proceedings of the 5th Conference*, pages 645–659.

Larsen, H. C. and Marcussen, C. (1992). Sill-intrusion, flood basalt emplacement and deep crustal structure of the Scoresby Sund region, East Greenland. *Geological Society, London, Special Publications*, **68**(1), 365–386.

Latin, D. and White, N. (1990). Generating melt during lithospheric extension - pure shear vs simple shear. *Geology*, **18**(4), 327–331.

Lavier, L. L. and Manatschal, G. (2006). A mechanism to thin the continental lithosphere at magma-poor margins. *Nature*, **440**(7082), 324–328.

Leach, H. M., Herbert, N., Los, A., and Smith, R. (1999). The schiehallion development. *In Fleet, A.J and Boldy, S.A.R. (eds) Petroleum Geology of Northwest Europe: Proceedings of the 5th Conference*, pages 683–692.

Lemoine, M., Tricart, P., and Boillot, G. (1987). Ultramafic and gabbroic ocean-floor of the ligurian tethys (alps, corsica, apennines) - in search of a genetic model. *Geology*, **15**(7), 622–625.

Lizarralde, D., Gaherty, J. B., Collins, J. A., Hirth, G., and Kim, S. D. (2004). Spreading-rate dependence of melt extraction at mid-ocean ridges from mantle seismic refraction data. *Nature*, **432**(7018), 744–747.

Macdonald, K. C. (1982). Mid-ocean ridges - fine scale tectonic, volcanic and hydrothermal processes within the plate boundary zone. *Annual Review Of Earth And Planetary Sciences*, **10**, 155–190.

Macdonald, K. C. and Fox, P. J. (1983). Overlapping spreading centres: new accretion geometry on the East Pacific Rise. *Nature*, **302**(5903), 55.

Mackay, L. M., Turner, J., Jones, S. M., and White, N. J. (2005). Cenozoic vertical motions in the Moray Firth basin associated with initiation of the Iceland plume. *Tectonics*, **24**(5).

Maggi, A., Jackson, J. A., Priestley, K., and Baker, C. (2000). A re-assessment of focal depth distributions in southern Iran, the Tien Shan and northern India: do earthquakes really occur in the continental mantle? *Geophysical Journal International*, **143**(3), 629–661.

Manatschal, G. (2004). New models for evolution of magma-poor rifted margins based on a review of data and concepts from west Iberia and the Alps. *International Journal Of Earth Sciences*, **93**(3), 432–466.

Manatschal, G. and Bernoulli, D. (1999). Architecture and tectonic evolution of nonvolcanic margins: Present-day Galicia and ancient Adria. *Tectonics*, **18**(6), 1099–1119.

Marsden, G., Yielding, G., Roberts, A. M., and Kusznir, N. J. (1990). Application of a flexural cantilever simple-shear/pure-shear model of continental lithosphere extension to the formation of the northern North Sea basin. In *Tectonic Evolution of the North Sea Rifts*, pages 241–261. Clarendon Press, Oxford.

Matthews, S. J., Fraser, A. J., Lowe, S., Todd, S. P., and Peel, F. J. (1997). Structure, stratigraphy and petroleum geology of the SE Nam Con Son Basin, offshore Vietnam. *Geological Society, London, Special Publications*, **126**(1), 89–106.

McKenzie, D. (1978). Some remarks on the development of sedimentary basins. *Earth And Planetary Science Letters*, **40**(1), 25–32.

McKenzie, D. (1979). Finite deformation during fluid-flow. *Geophysical Journal Of The Royal Astronomical Society*, **58**(3), 689–715.

McKenzie, D. (1984). A possible mechanism for epeirogenic uplift. *Nature*, **307**(5952), 616.

McKenzie, D. (1989). Some remarks on the movement of small melt fractions in the mantle. *Earth And Planetary Science Letters*, **95**(1-2), 53–72.

McKenzie, D. and Bickle, M. J. (1988). The volume and composition of melt generated by extension of the lithosphere. *Journal Of Petrology*, **29**(3), 625–679.

Minshull, T. A., Dean, S. M., White, R. S., and Whitmarsh, R. B. (2001). Anomalous melt production after continental break-up in the southern Iberia Abyssal Plain. In R. C. Wilson, R. B. Whitmarsh, B. Taylor, and N. Frotzheim, editors, *Non-volcanic Rifting of Continental Margins: A Comparison of Evidence from Land and Sea*, volume 187 of *Special Publications*, pages 537–550. Geological Society, London.

Mitchell, S., Beamish, G., Wood, M., Malacek, S., Armentrout, J., Damuth, J., and Olson, H. (1993). Paleogene sequence stratigraphic framework of the Faeroe basin. *In Parker, J.R. (ed.) Petroleum Geology of Northwest Europe: Proceedings of the 4th conference.*, pages 1011–1023.

Morgan, J. P., Parmentier, E. M., and Lin, J. (1987). Mechanisms for the origin of midocean ridge axial topography - implications for the thermal and mechanical structure of accreting plate boundaries. *Journal Of Geophysical Research-Solid Earth And Planets*, **92**(B12), 12823–12836.

Mosar, J., Torsvik, T. H., and the BAT team (2002). Opening of the Norwegian and Greenland seasa: plate tectonics in mid Norway since the late Permian. *In Eide, E. A. (ed.) BATLAS - Mid Norway plate reconstructions with global and Atlantic perspectives*, pages 48–59.

Mudge, D. C. and Bujak, J. P. (2001). Biostratigraphic evidence for evolving palaeoenvironments in the lower paleogene of the Faeroe-Shetland basin. *Marine And Petroleum Geology*, **18**(5), 577–590.

Muller, R. D., Roest, W. R., Royer, J. Y., Gahagan, L. M., and Sclater, J. G. (1997). Digital isochrons of the world's ocean floor. *Journal Of Geophysical Research-Solid Earth*, **102**(B2), 3211–3214.

Muntener, O. and Manatschal, G. (2006). High degrees of melt extraction recorded by spinel harzburgite of the Newfoundland margin: The role of inheritance and consequences for the evolution of the southern North Atlantic. *Earth And Planetary Science Letters*, **252**(3-4), 437–452.

Muntener, O., Pettke, T., Desmurs, L., Meier, M., and Schaltegger, U. (2004). Refertilization of mantle peridotite in embryonic ocean basins: trace element and nd isotopic evidence and implications for crust-mantle relationships. *Earth And Planetary Science Letters*, **221**(1-4), 293–308.

Mutter, J. (1985). Seaward dipping reflectors and the continent ocean boundary at passive continental margins. *Tectonophysics*, **114**(1-4), 117–131.

Mutter, J. C., Buck, W. R., and Zehnder, C. M. (1988). Convective partial melting.1. a model for the formation of thick basaltic sequences during the initiation of spreading. *Journal Of Geophysical Research-Solid Earth And Planets*, **93**(B2), 1031–1048.

Nadin, P. A. and Kusznir, N. J. (1995). Paleocene uplift and Eocene subsidence in the northern north-sea basin from 2d forward and reverse stratigraphic modeling. *Journal Of The Geological Society*, **152**, 833–848.

Nadin, P. A., Kusznir, N. J., and Cheadle, M. J. (1997). Early Tertiary plume uplift of the North Sea and Faeroe-Shetland basins. *Earth And Planetary Science Letters*, **148**(1-2), 109–127.

Naylor, P. H., Bell, B. R., Jolley, D. W., Durnall, P., and Fredsted, R. (1999). Paleogene magmatism in the Faeroe-Shetland basin: influences on uplift history and sedimentation. *In Fleet, A.J and Boldy, S.A.R. (eds) Petroleum Geology of Northwest Europe: Proceedings of the 5th Conference*, pages 545–558.

Nicolas, A. and Poirier, J. P. (1976). *An Introduction to Fluid Dynamics*. Wiley, London.

Nielsen, T. K. and Hopper, J. R. (2002). Formation of volcanic rifted margins: Are temperature anomalies required? *Geophysical Research Letters*, **29**(21).

Nielsen, T. K. and Hopper, J. R. (2004). From rift to drift: Mantle melting during continental breakup. *Geochemistry Geophysics Geosystems*, **5**.

Olsen, K. H. and Morgan, P. (1995). Progress in understanding continental rifts. In K. H. Olsen, editor, *Developments in Geotectonics*, volume 25, pages 3–26. Elsevier Science.

Oxburgh, E. R. and Parmentier, E. M. (1977). Compositional and density stratification in oceanic lithosphere-causes and consequences. *Journal of the Geological Society*, **133**(4), 343–355.

Perez-Gussinye, M., Ranero, C. R., Reston, T. J., and Sawyer, D. (2003). Mechanisms of extension at nonvolcanic margins: Evidence from the Galicia Interior basin, west of Iberia. *Journal Of Geophysical Research-Solid Earth*, **108**(B5).

Pérez-Gussinyé, M., Morgan, J. P., Reston, T. J., and Ranero, C. R. (2006). The rift to drift transition at non-volcanic margins: Insights from numerical modelling. *Earth And Planetary Science Letters*, **244**(1-2), 458–473.

Peron-Pinvidic, G., Manatschal, G., Minshull, T. A., and Sawyer, D. S. (2007a). Tectonosedimentary evolution of the deep Iberia-Newfoundland margins: Evidence for a complex breakup history. *Tectonics*, **26**(2).

Peron-Pinvidic, G., Manatschal, G., Minshull, T. A., and Sawyer, D. S. (2007b). Tectonosedimentary evolution of the deep Iberia-Newfoundland margins: Evidence for a complex breakup history. *Tectonics*, **26**(2).

Petrini, K., Connolly, J. A. D., and Podladchikov, Y. Y. (2001). A coupled petrological-tectonic model for sedimentary basin evolution: the influence of metamorphic reactions on basin subsidence. *Terra Nova*, **13**(5), 354–359.

PhippsMorgan, J. (1987). Melt migration beneath mid-ocean spreading centers. *Geophysical Research Letters*, **14**(12), 1238–1241.

Pickup, S. L. B., Whitmarsh, R. B., Fowler, C. M. R., and Reston, T. J. (1996). Insight into the nature of the ocean-continent transition off west Iberia from a deep multichannel seismic reflection profile. *Geology*, **24**(12), 1079–1082.

Press, W. H., Teukolsky, S. A., Vetterling, W. T., and Flannery, B. P. (1992). *Numerical Recipes in FORTRAN: The Art of Scientific Computing*. Cambridge University Press, New York, 1992.

Purdy, G. M. and Detrick, R. S. (1986). Crustal structure of the mid-Atlantic ridge at 23-degrees-n from seismic refraction studies. *Journal Of Geophysical Research-Solid Earth And Planets*, **91**(B3), 3739–3762.

Ranalli, G. (1995). *Rheology of the Earth*. Springer, second edition.

Rasmussen, J. and Noe-Nygaard, A. (1970). *Geology of the Faeroe Islands.*, volume 25. Geological Survey of Denmark 1 series.

Raum, T., Mjelde, R., Berge, A. M., Paulsen, J. T., Digranes, P., Shimamura, H., Shiobara, H., Kodaira, S., Larsen, V. B., Fredsted, R., Harrison, D. J., and Johnson, M. (2005). Sub-basalt structures east of the Faroe islands revealed from wide-angle seismic and gravity data. *Petroleum Geoscience*, **11**(4), 291–308.

Reid, I. and Jackson, H. R. (1981). Oceanic spreading rate and crustal thickness. *Marine Geophysical Researches*, **5**(2), 165–172.

Reston, T. (2007). Extension discrepancy at North Atlantic nonvolcanic rifted margins: Depth-dependent stretching or unrecognized faulting? *Geology*, **35**(4), 367–370.

Reston, T. J. and Morgan, J. P. (2004). Continental geotherm and the evolution of rifted margins. *Geology*, **32**(2), 133–136.

Reston, T. J., Krawczyk, C. M., and Klaeschen, D. (1996). The S reflector west of Galicia (Spain): Evidence from prestack depth migration for detachment faulting during continental breakup. *Journal Of Geophysical Research-Solid Earth*, **101**(B4), 8075–8091.

Ribe, N. M. (1992). On the relation between seismic anisotropy and finite strain. *Journal Of Geophysical Research-Solid Earth*, **97**(B6), 8737–8747.

Richardson, K. R., Smallwood, J. R., White, R. S., Snyder, D. B., and Maguire, P. K. H. (1998). Crustal structure beneath the Faroe islands and the Faroe-Iceland ridge. *Tectonophysics*, **300**(1-4), 159.

Richardson, K. R., White, R. S., England, R. W., and Fruehn, J. (1999). Crustal structure east of the Faroe islands: mapping sub-basalt sediments using wide-angle seismic data. *Petroleum Geoscience*, **5**(2), 161–172.

Riisager, P., Riisager, J., Abrahamsen, N., and Waagstein, R. (2002). New paleomagnetic pole and magnetostratigraphy of Faroe Islands flood volcanics, North Atlantic igneous province. *Earth and Planetary Science Letters*, **201**(2), 261–276.

Ritchie, J. D., Gatliff, R. W., and Richards, P. C. (1999). Early Tertiary magmatism in the offshore NW UK margin and surrounds. *In Fleet, A.J and Boldy, S.A.R. (eds) Petroleum Geology of Northwest Europe: Proceedings of the 5th Conference*, pages 573–584.

Ritchie, J. D., Johnson, H., and Kimbell, G. S. (2003). The nature and age of Cenozoic contractional deformation within the NE Faroe-Shetland basin. *Marine And Petroleum Geology*, **20**(5), 399–409.

Roberts, A. (2007). *Crustal structure of the Faroes North Atlantic margin from wide-angle seismic data.* Ph.D. thesis, University of Cambridge.

Roberts, A. M., Lundin, E. R., and Kusznir, N. J. (1997). Subsidence of the Vøring basin and the influence of the Atlantic continental margin. *Journal Of The Geological Society*, **154**, 551–557.

Roberts, A. M., Kusznir, N. J., Yielding, G., and Styles, P. (1998). 2d flexural backstripping of extensional basins: the need for a sideways glance. *Petroleum Geoscience*, **4**(4), 327–338.

Roberts, A. M., Corfield, R. I., Kusznir, N. J., Matthews, S. J., Hansen, E.-K., and Hooper, R. J. (2009). Mapping palaeostructure and palaeobathymetry along the Norwegian Atlantic continental margin: More and Voring basins. *Petroleum Geoscience*, **15**(1), 27–43.

Roberts, D. G., Backman, J., Morton, A. C., Murray, J. W., and Keene, J. B. (1984). Evolution of volcanic rifted margins; synthesis of leg 81 results on the west margin of rockall plateau. *In: Initial reports of the Deep Sea Drilling Project*, **81**, 883–911.

Roberts, D. G., Thompson, M., Mitchener, B., Hossack, J., Carmichael, S., and Bjø rnset, H.-M. (1999). Palaeozoic to Tertiary rift and basin dynamics: mid-Norway to the bay of Biscay - a new context for hydrocarbon prospectivity in the deep water frontier. *In Fleet, A.J and Boldy, S.A.R. (eds) Petroleum Geology of Northwest Europe: Proceedings of the 5th Conference*, pages 7–40.

Rowley, D. B. and Sahagian, D. (1986). Depth-dependent stretching; a different approach. *Geology*, **14**(1), 32–35.

Roy, R. F., Decker, E. R., Blackwell, D. D., and Birch, F. (1968). Heat flow in United States. *J. Geophys. Res.; Vol/Issue: 73:16*, pages Pages: 5207–21.

Royden, L. and Keen, C. E. (1980). Rifting process and thermal evolution of the continental-margin of eastern Canada determined from subsidence curves. *Earth And Planetary Science Letters*, **51**(2), 343–361.

Rumph, B., Reaves, C. M., Orange, V. G., and Robinson, D. (1993). Structuring and transfer zones in the Faeroe basin in a regional tectonic context. *In Parker, J.R. (ed.) Petroleum Geology of Northwest Europe: Proceedings of the 4th conference.*, pages 999–1009.

Russell, S. M. and Whitmarsh, R. B. (2003). Magmatism at the west Iberia non-volcanic rifted continental margin: evidence from analyses of magnetic anomalies. *Geophysical Journal International*, **154**(3), 706–730.

Salters, V. J. M. and Hart, S. R. (1989). The hafnium paradox and the role of garnet in the source of mid-ocean-ridge basalts. *Nature*, **342**(6248), 420–422.

Saunders, A. D., Fitton, J. G., Kerr, A. C., Norry, M. J., and Kent, R. W. (1997). The North Atlantic igneous province. *in Large Igneous Provinces: Continental, Oceanic, and Planetary Flood Volcanism, edited by J. J. Mahoney and M. F. Coffin*, pages pp. 45–93.

Sawyer, D. S. (1986). Effects of basement topography on subsidence history analysis. *Earth And Planetary Science Letters*, **78**(4), 427–434.

Sclater, J. G. and Christie, P. A. F. (1980). Continental stretching - an explanation of the post-mid-cretaceous subsidence of the central north-sea basin. *Journal Of Geophysical Research*, **85**(NB7), 3711–3739.

Scotchman, I. C., Marais-Gilchrist, G., de Souza, F. G., Chaves, F. F., Atterton, L. A., Roberts, A., and Kusznir, N. J. (2006). A failed sea-floor spreading centre, Santos basin, Brazil. *In: Rio Oil and Gas Expo and Conference 2006 Annals.*

Shen, Y. and Forsyth, D. W. (1992). The effects of temperature-dependent and pressure-dependent viscosity on 3-dimensional passive flow of the mantle beneath a ridge-transform system. *Journal Of Geophysical Research-Solid Earth*, **97**(B13), 19717–19728.

Sibuet, J. C., Srivastava, S., and Manatschal, G. (2007). Exhumed mantle-forming transitional crust in the Newfoundland-Iberia rift and associated magnetic anomalies. *Journal Of Geophysical Research-Solid Earth*, **112**(B6).

Skogseid, J., Pedersen, T., Eldholm, O., and Larsen, B. T. (1992). Tectonism and magmatism during NE Atlantic continental break-up: the Vøring Margin. *Geological Society, London, Special Publications*, **68**(1), 305–320.

Skogseid, J., Planke, S., Faleide, J. I., Pedersen, T., Eldholm, O., and Neverdal, F. (2000). NE Atlantic continental rifting and volcanic margin formation. *Geological Society, London, Special Publications*, **167**(1), 295–326.

Smallwood, J. R. and Gill, C. E. (2002). The rise and fall of the Faroe-Shetland basin: evidence from seismic mapping of the balder formation. *Journal Of The Geological Society*, **159**, 627–630.

Smallwood, J. R. and Kirk, W. J. (2005). Paleocene exploration in the Faroe-Shetland channel:disappointments and discoveries. *In Dore, A.G. and Vining, B.A. (eds). Petroleum Geology: Northwest Europe and Global perspectives -Proceedings of the 6th Petroleum Geology Conference*, pages 977–991.

Smallwood, J. R., Towns, M. J., and White, R. S. (2001). The structure of the Faeroe-Shetland trough from integrated deep seismic and potential field modelling. *Journal Of The Geological Society*, **158**, 409–412.

Sorensen, A. B. (2003). Cenozoic basin development and stratigraphy of the Faroes area. *Petroleum Geoscience*, **9**(3), 189–207.

Sotin, C. and Parmentier, E. M. (1989). Dynamical consequences of compositional and thermal density stratification beneath spreading centers. *Geophysical Research Letters*, **16**(8), 835–838.

Spiegelman, M. and McKenzie, D. (1987). Simple 2-D models for melt extraction at midocean ridges and island arcs. *Earth And Planetary Science Letters*, **83**(1-4), 137–152.

Srivastava, S. P., Sibuet, J. C., Cande, S., Roest, W. R., and Reid, I. D. (2000). Magnetic evidence for slow seafloor spreading during the formation of the Newfoundland and Iberian margins. *Earth And Planetary Science Letters*, **182**(1), 61–76.

Steckler, M. S. and Watts, A. B. (1978). Subsidence of Atlantic-type continental-margin off new-york. *Earth And Planetary Science Letters*, **41**(1), 1–13.

Steckler, M. S., Berthelot, F., Lyberis, N., and Lepichon, X. (1988). Subsidence in the Gulf of Suez - implications for rifting and plate kinematics. *Tectonophysics*, **153**(1-4), 249–270.

Stewart, J. H. (1971). Basin and Range structure - system of horsts and grabens produced by deep-seated extension. *Geological Society Of America Bulletin*, **82**(4), 1019–1043.

Taylor, B., Goodliffe, A., Martinez, F., and Hey, R. (1995). Continental rifting and initial sea-floor spreading in the woodlark basin. *Nature*, **374**(6522), 534–537.

ter Voorde, M., van Balen, R. T., Bertotti, G., and Cloetingh, S. (1998). The influence of a stratified rheology on the flexural response of the lithosphere to (un)loading by extensional faulting. *Geophysical Journal International*, **134**(3), 721–735.

Trude, J., Cartwright, J., Davies, R. J., and Smallwood, J. (2003). New technique for dating igneous sills. *Geology*, **31**(9), 813–816.

Tsikalas, F., Faleide, J., and Eldholm, O. (In Press). The NE Atlantic conjugate margins. In *Roberts, D.G. and Bally, A.W. (eds) Principles of Phanerozoic Regional Geology.* Elsevier Publ.

Tucholke, B. E., Sawyer, D. S., and Sibuet, J. C. (2007). Breakup of the Newfoundland Iberia rift. *Geological Society, London, Special Publications*, **282**(1), 9–46.

Turcotte, D. and Schubert, G. (2002). *Geodynamics.* Cambridge University Press, second edition.

Turner, J. and Scrutton, R. (1993). Subsidence patterns in western margin basins: evidence from the Faeroe-Shetland basin. *In Parker, J.R. (ed.) Petroleum Geology of Northwest Europe: Proceedings of the 4th conference.*, pages 975–983.

Tymms, V. J. (2006). *Numerical Modelling of Rifted Continental Margin Formation.* Ph.D. thesis, University of Liverpool.

Vagnes, E., Gabrielsen, R. H., and Haremo, P. (1998). Late cretaceous-Cenozoic intraplate contractional deformation at the Norwegian continental shelf: timing, magnitude and regional implications. *Tectonophysics*, **300**(1-4), 29.

van Wijk, J., Huismans, R., ter Voorde, M., and Cloetingh, S. (2001). Melt generation at volcanic continental margins: no need for a mantle plume? *Geophysical Research Letters*, **28**(20), 3995–3998.

van Wijk, J. W. and Cloetingh, S. (2002). Basin migration caused by slow lithospheric extension. *Earth And Planetary Science Letters*, **198**(3-4), 275–288.

Vauchez, A., Barruol, G., and Tommasi, A. (1997). Why do continents break up parallel to ancient orogenic belts? *Terra Nova*, **9**, 62–66.

Vauchez, A., Tommasi, A., and Barruol, G. (1998). Rheological heterogeneity, mechanical anisotropy, and tectonics of the continental lithosphere. *Tectonophysics*, **296**, 61–86.

Vitorello, I. and Pollack, H. N. (1980). Variation of continental heat flow with age and the thermal evolution of continents. *J. Geophys. Res.; Vol/Issue: 85:B2*, pages Pages: 983–996.

Waagstein, R. (1988). Structure, composition and age of the Faeroe basalt plateau. *Geological Society, London, Special Publications*, **39**(1), 225–238.

Waagstein, R. (1995). Radiometric dating of the basalts in and around the lopra-1 well, Faeroe islands. *DGU Service report*, **42**.

Walsh, J., Watterson, J., and Yielding, G. (1991). The importance of small-scale faulting in regional extension. *Nature*, **351**(6325), 391–393.

Watts, A. W. (2001). *Isostasy and flexure of the lithosphere.* Cambridge University Press.

Wernicke, B. (1985). Uniform-sense normal simple shear of the continental lithosphere. *Canadian Journal of Earth Sciences*, **22**(1), 108–125.

White, N. and Latin, D. (1993). Subsidence analyses from the north-sea triple-junction. *Journal Of The Geological Society*, **150**, 473–488.

White, N. and McKenzie, D. (1988). Formation of the steers head geometry of sedimentary basins by differential stretching of the crust and mantle. *Geology*, **16**(3), 250–253. ISI Document Delivery No.: M6561 Times Cited: 91 Cited Reference Count: 34 English Article 0091-7613.

White, R. and McKenzie, D. (1989). Magmatism at rift zones - the generation of volcanic continental margins and flood basalts. *Journal Of Geophysical Research-Solid Earth And Planets*, **94**(B6), 7685–7729.

White, R. S., McKenzie, D., and Onions, R. K. (1992). Oceanic crustal thickness from seismic measurements and rare-earth element inversions. *Journal Of Geophysical Research-Solid Earth*, **97**(B13), 19683–19715.

White, R. S., Minshull, T. A., Bickle, M. J., and Robinson, C. J. (2001). Melt generation at very slow-spreading oceanic ridges: Constraints from geochemical and geophysical data. *Journal Of Petrology*, **42**(6), 1171–1196.

White, R. S., Smith, L. K., Roberts, A. W., Christie, P. A. F., Kusznir, N. J., and iSIMM Team (2008). Lower-crustal intrusion on the North Atlantic continental margin. *Nature*, **452**(7186), 460–U6.

Whitmarsh, R. B. and Miles, P. R. (1995). Models of the development of the west Iberia rifted continental-margin at 40-degrees-30N deduced from surface and deep-tow magnetic-anomalies. *Journal Of Geophysical Research-Solid Earth*, **100**(B3), 3789–3806.

Whitmarsh, R. B., White, R. S., Horsefield, S. J., Sibuet, J. C., Recq, M., and Louvel, V. (1996). The ocean-continent boundary off the western continental margin of Iberia: Crustal structure west of Galicia Bank. *Journal Of Geophysical Research-Solid Earth*, **101**(B12), 28291–28314.

Whitmarsh, R. B., Dean, S. M., Minshull, T. A., and Tompkins, M. (2000). Tectonic implications of exposure of lower continental crust beneath the Iberia Abyssal Plain, northeast Atlantic Ocean: Geophysical evidence. *Tectonics*, **19**(5), 919–942.

Whitmarsh, R. B., Manatschal, G., and Minshull, T. A. (2001a). Evolution of magma-poor continental margins from rifting to seafloor spreading. *Nature*, **413**(6852), 150–154.

Whitmarsh, R. B., Minshull, T. A., Russell, S. M., Dean, S. M., Louden, K. E., and Chian, D. (2001b). The role of syn-rift magmatism in the rift-to-drift evolution of the west Iberia continental margin: geophysical observations. In R. C. Wilson, R. B. Whitmarsh, B. Taylor, and N. Frotzheim, editors, *Non-volcanic Rifting of Continental Margins: A Comparison of Evidence from Land and Sea*, volume 187 of *Special Publications*, pages 107–124. Geological Society, London.

Wilson, D., Aster, R., West, M., Ni, J., Grand, S., Gao, W., Baldridge, W. S., Semken, S., and Patel, P. (2005). Lithospheric structure of the Rio Grande rift. *Nature*, **433**(7028), 851.

Wilson, J. T. (1966). Did Atlantic close and then re-open? *Nature*, **211**(5050), 676–670.

Workman, R. K. and Hart, S. R. (2005). Major and trace element composition of the depleted MORB mantle (DMM). *Earth And Planetary Science Letters*, **231**(1-2), 53–72.

Ziegler, P. A. and Cloetingh, S. (2004). Dynamic processes controlling evolution of rifted basins. *Earth-Science Reviews*, **64**(1-2), 1–50.